Comptes Rendus
de l'Académie des sciences

1878-1535 (electronic)

Physique

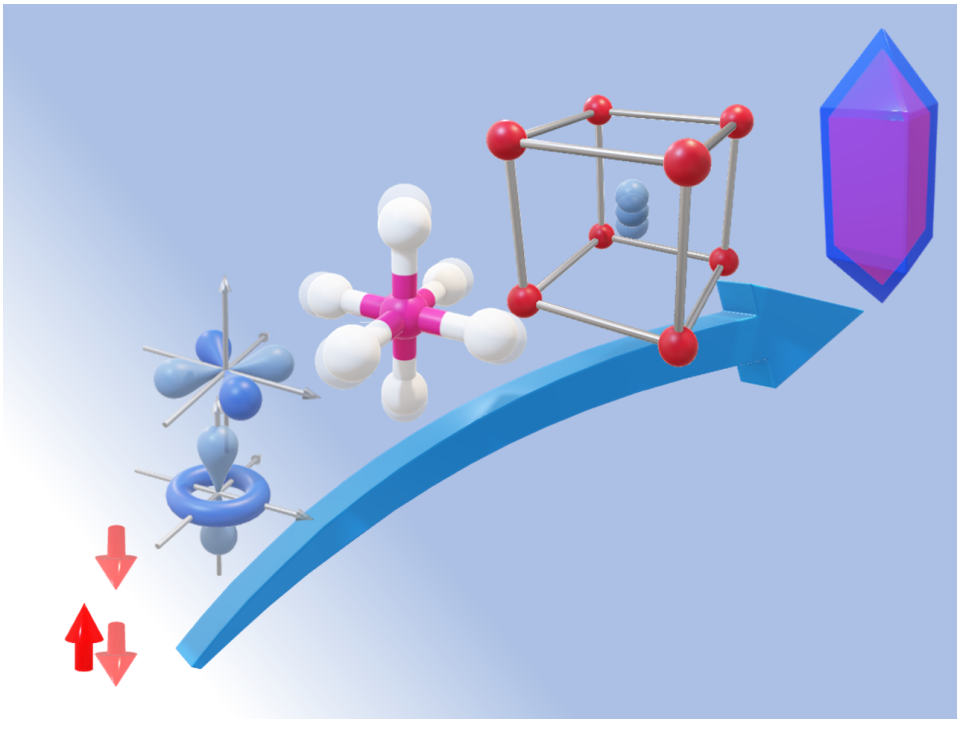

Volume 22, Special Issue S2, 2021

Special issue / *Numéro thématique*

Physics of ultra-fast phenomena / *Physique des phénomènes ultra-rapides*

Guest editors / *Rédacteurs en chef invités*

Éric Collet, Sylvain Ravy

Académie des sciences — Paris

INSTITUT DE FRANCE
Académie des sciences

CENTRE MERSENNE

Comptes Rendus

Physique

Objective of the journal

Comptes Rendus Physique is a peer-reviewed electronic journal of international standing, covering all fields of physics and astrophysics. It publishes mainly thematic issues, but also original research articles, preliminary announcements, review articles, historical perspectives, pedagogical texts or conference proceedings, without length limit, in English or in French. It also publishes special issues devoted to certain recent and/or significant aspects of the discipline, whose authors are chosen from among the most active researchers on the subject and whose coordination is assured by guest editors.

Comptes Rendus Physique is published according to a virtuous policy of diamond open access, free for authors (no publication fees) as well as for readers (immediate and permanent open access).

About the journal

All journal's information, including the text of published articles, which is fully open access, is available from the journal website at https://comptes-rendus.academie-sciences.fr/physique/.

Author enquiries

For enquiries relating to the submission of articles, please visit this journal's homepage at https://comptes-rendus.academie-sciences.fr/physique/.

Contact

Académie des sciences
23, quai de Conti, 75006 Paris, France
Tel: (+33) (0)1 44 41 43 72
CR-Physique@academie-sciences.fr

Comptes Rendus
Physique
2021, 22, nº S2

Contents / *Sommaire*

Comptes Rendus
Physique
2021, 22, nº S2, p. 1-2
https://doi.org/10.5802/crphys.90

Physics of ultra-fast phenomena / *Physique des phénomènes ultra-rapides*

Guest editors

Rédacteurs invités

Éric Collet

Sylvain Ravy

Eric Collet is a professor at the University of Rennes 1, specializing in the study of systems with coupled electronic and structural instabilities, such as neutral-ionic transitions, spin transitions or the charge transfer transitions. After a post-doctorate at the Léon Brillouin laboratory at CEA Saclay and a stay in Japan, he was recruited in 2001 at the University of Rennes 1, to initiate a new activity on photoinduced phase transitions. Within the framework of his appointment at the Institut Universitaire de France, he conducts research on molecular materials exhibiting ultra-fast photoinduced phase transitions. He develops photo-crystallography experiments and uses optical spectroscopies and ultra-fast structural analyses on synchrotron and X-FEL by X-ray diffraction and XANES. He is also interested in all non-equilibrium mechanisms driven by laser excitation where the response of materials depends on the excitation wavelength and can be non-linear. He received the Louis Ancel prize from the French Physical Society in 2017 and the CNRS silver medal in 2020. Since 2017, he is deputy director of the Institut de Physique de Rennes and leads an international laboratory with Japan, focused on the study of ultrafast photoinduced phase transitions.

Eric Collet *est Professeur à l'Université de Rennes 1. Ce physicien de la matière condensée est spécialisé dans l'étude de systèmes présentant des instabilités électroniques et structurales couplées, telles que la transition neutre-ionique, la transition de spin ou la transition à transfert de charge. Après un post-doctorat au laboratoire Léon Brillouin au CEA Saclay et un séjour au Japon, il est recruté en 2001 à l'Université de Rennes 1, pour initier une nouvelle activité portant sur les transitions de phase photoinduites. Dans le cadre de sa nomination à l'Institut Universitaire de*

France, il mène des recherches sur les matériaux moléculaires présentant des transitions de phases photoinduites ultra-rapides. Il développe des expériences de photo-cristallographie et utilise les spectroscopies optiques et les analyses structurales ultra-rapides sur synchrotron et X-FEL par diffraction des rayons X et XANES. Il s'intéresse aussi à l'ensemble des mécanismes hors équilibre pilotés par excitation laser où la réponse des matériaux dépend de la longueur d'onde d'excitation et peut être non-linéaire. Il a reçu le prix Louis Ancel de la société française de physique en 2017 et la médaille d'argent du CNRS en 2020. Depuis 2017, il est directeur adjoint de l'Institut de Physique de Rennes et il dirige un laboratoire international avec le Japon, centré sur l'étude des transitions de phase photoinduites ultra-rapides.

Sylvain Ravy, 60, is a condensed matter physicist specialized in X-ray diffraction. A CNRS researcher, he first joined the Laboratoire de Physique des Solides d'Orsay (LPS), where he worked on structural phase transitions through the analysis of "X-ray diffuse scattering", which allows the study of disorder effects in condensed matter, such as those appearing in the precursor effects of phase transitions. After a two-year stay in the USA, where he conducted photoelectron spectroscopy experiments at the Berkeley Synchrotron, he joined the SOLEIL synchrotron in 2004, to set up a diffraction beamline, CRISTAL. This line is dedicated to crystallography, in particular to studies using the coherence of X-rays (coherent scattering) and time-resolved scattering. After 11 years at SOLEIL, he became director of the LPS in 2015, where he continues to work on time-resolved diffraction, particularly on so-called "charge density wave" compounds. Indeed, these compounds are particularly sensitive to ultrafast laser pulses which induce insulator-to-metal phase transitions, with associated structural effects. Since 2021, he is Deputy Scientific Director at the "Institut de Physique du CNRS", in charge of the research infrastructures, mainly photon and neutron sources.

***Sylvain Ravy**, 60 ans, est un physicien de la matière condensée spécialisé dans la diffraction des rayons X. Chercheur CNRS, il a d'abord rejoint le Laboratoire de Physique des Solides d'Orsay (LPS), où il a travaillé sur les transitions de phase structurales par l'analyse de la « diffusion diffuse des rayons X », qui permet d'étudier les effets de désordres dans la matière condensée, comme ceux apparaissant dans les effets précurseurs des transitions de phase. Après un séjour de deux ans aux USA, où il mène des expériences de spectroscopie de photo-électrons au Synchrotron de Berkeley, il rejoint le synchrotron SOLEIL en 2004, pour y monter une ligne de lumière, CRISTAL. Cette ligne est dédiée à la cristallographie, en particulier aux études utilisant la cohérence des rayons X (diffusion cohérente) et la diffusion en temps résolu. Après 11 ans passés à SOLEIL, il devient en 2015 directeur du LPS, où il continue à travailler sur la diffraction en temps résolu, particulièrement sur les composés dits à « onde de densité de charge ». En effet, ceux-ci sont particulièrement sensibles aux impulsions laser ultra-rapides qui y induisent des transitions de phase isolant-métal, avec des effets structuraux associés. Depuis 2021, il est Directeur Adjoint Scientifique à l'Institut de Physique du CNRS, en charge des infrastructures de recherche suivies par cet institut, principalement les sources de photons et de neutrons.*

Comptes Rendus
Physique
2021, 22, nº S2, p. 3-14
https://doi.org/10.5802/crphys.88

Foreword / *Avant-propos*

Foreword: Ultrafast Phenomena in condensed matter physics

Avant-propos : Phénomènes ultra-rapides en physique de la matière condensée

Eric Collet *, [a] **and Sylvain Ravy** *, [b]

[a] Univ Rennes, CNRS, IPR (Institut de Physique de Rennes) - UMR 6251, F-35000 Rennes, France
URL: https://ipr.univ-rennes1.fr/interlocuteurs/eric-collet

[b] Université Paris-Saclay, CNRS, Laboratoire de Physique des Solides, 91405, Orsay, France
URL: https://www.lps.u-psud.fr/spip.php?article531

E-mails: eric.collet@univ-rennes1.fr (E. Collet), sylvain.ravy@universite-paris-saclay.fr (S. Ravy)

Abstract. Matter is dynamic and changes under the effect of various external constraints, in particular light. The development of ultra-fast techniques now makes it possible to study the elementary mechanisms of ultrafast photoinduced phenomena, in particular by following the dynamics of electronic and structural degrees of freedom of matter. These studies provide a better understanding of these non-equilibrium processes in order to control the physical properties of molecules and materials by light. In this introductory article we discuss different aspects of studying ultra-fast condensed matter phenomena.

Résumé. La matière est dynamique et se transforme sous l'effet de différentes contraintes extérieures, en particulier la lumière. Le développement de techniques ultra-rapides permet à présent d'étudier les mécanismes élémentaires de phénomènes photoinduits ultra-rapides, en particulier en suivant les dynamiques des degrés de libertés électroniques et structuraux de la matière. Ces études permettent de mieux comprendre ces processus hors équilibre pour envisager un contrôle des propriétés physiques de molécules et matériaux par la lumière. Dans cet article d'introduction nous abordons différents aspects de l'étude de phénomènes ultra-rapide en matière condensée.

Keywords. Condensed matter, Molecules, Materials, Ultra-fast phenomena, Out-of-equilibrium, Spectroscopies, Diffraction.

Mots-clés. Matière Condensée, Molécules, Matériaux, Phénomènes ultra-rapides, Hors équilibre, Spectroscopies, Diffraction.

* Corresponding authors.

For understanding the physical properties of molecules or materials, it is necessary to investigate how the constituting degrees of freedom (spin, charge, orbital, molecular structure or crystalline packing, Figure 1) equilibrate and get ordered at microscopic scales. At thermal equilibrium, these orders may change under the effect of external parameters such as pressure and temperature, which may transform molecules or drive phase transitions. More recently, new challenges have emerged to direct the functionality of condensed matter, as excitation with an ultrashort laser pulse allows for driving ultrafast photoinduced molecular transformations or phase transitions. Advances in sophisticated technologies and instrumentation in ultrafast science make it now possible to drive ultrafast transformations by stimulating selectively a responsive degree of freedom [1, 2]. In addition, various time-resolved techniques allow for probing selectively the ultrafast and out-of-equilibrium dynamics, the equilibration and the coupling of different degrees of freedom coming into play [3–8]. Directing the functionality of materials towards a desired outcome at the relevant length, time and energy scales is a current challenge in materials' science.

Watching the elementary processes driving the transformation of matter, including electronic and structural dynamics, requires the use of techniques with a temporal resolution approaching the femtosecond range (1 fs = 10^{-15} s) with sub-Ångström spatial resolution. In this way, A. H. Zewail pioneered femtochemistry by developing fs pump–probe spectroscopy to study photochemical processes [9]. Pump–probe techniques use a pump laser pulse to trigger the transformation of molecules or materials and a probe pulse to measure the state of the system at a given time dt after photo-excitation (Figure 1).

The last decades witnessed unprecedented controls of Photo-Induced Phase Transitions (PIPT) [1] through the use of femtosecond (1 fs = 10^{-15} s) UV or visible laser pulses, which excite and reorganize electronic structure and modify the equilibrium atomic coordinates in the crystalline structure. The pumping energy determines the excited degrees of freedom: optical (≈1 eV) photons mainly cause inter-band electronic transitions, whereas mid-IR or THz excitations (≈1–100 meV) can resonantly activate phonon modes. These two kinds of excitations are fundamentally different: the first one promotes the system to an electronically excited state, whereas the second modifies the system within its electronic ground state. Pump–probe experiments spread over a growing community of scientists studying ultrafast phenomena, as new technological developments allow for generating not only ultrashort electromagnetic pulses in the THz, infrared (IR), visible (VIS), ultraviolet (UV) and X-ray range but also pulses of electrons [1, 4, 10–14]. Optical pump–probe spectroscopies, using IR, VIS or UV pulses are home-based experiments that can now routinely operate on a daily basis. However, radiation in the IR–VIS–UV domain does not provide information about the evolution of the atomic structure of matter, except in rare cases of simple systems for which the dependence of potential energy curves on the structural dynamics is known. It was therefore necessary to develop ultra-short pulses of X-ray or electron to perform measurements allowing for watching directly structural dynamics [4, 5, 15–19]. This broad spectrum of techniques allows now for monitoring the temporal evolution of the probed degrees of freedom on their intrinsic timescales, including spin, charge, molecular, lattice and crystalline structure.

Delocalized optical electronic excitation has been studied in hard-condensed matter, with insulators and semi-metals for example. This process modifies the relative electronic population of bonding and anti-bonding bands and the fraction of excited electrons n_e is the control parameter that can continuously reshape the potential energy surface (PES, Figure 2a) because the ultrafast thermalisation of electrons modifies the Fermi-Dirac distribution. This drives collective degrees of freedom of the lattice, such as an optical lattice phonon mode Q_{L}, moving the system over long-range order to a new equilibrium structure. The study of the excitation of the coherent phonon in Bismuth was an important step in the development of ultrafast science [14,20–22]. The crystalline

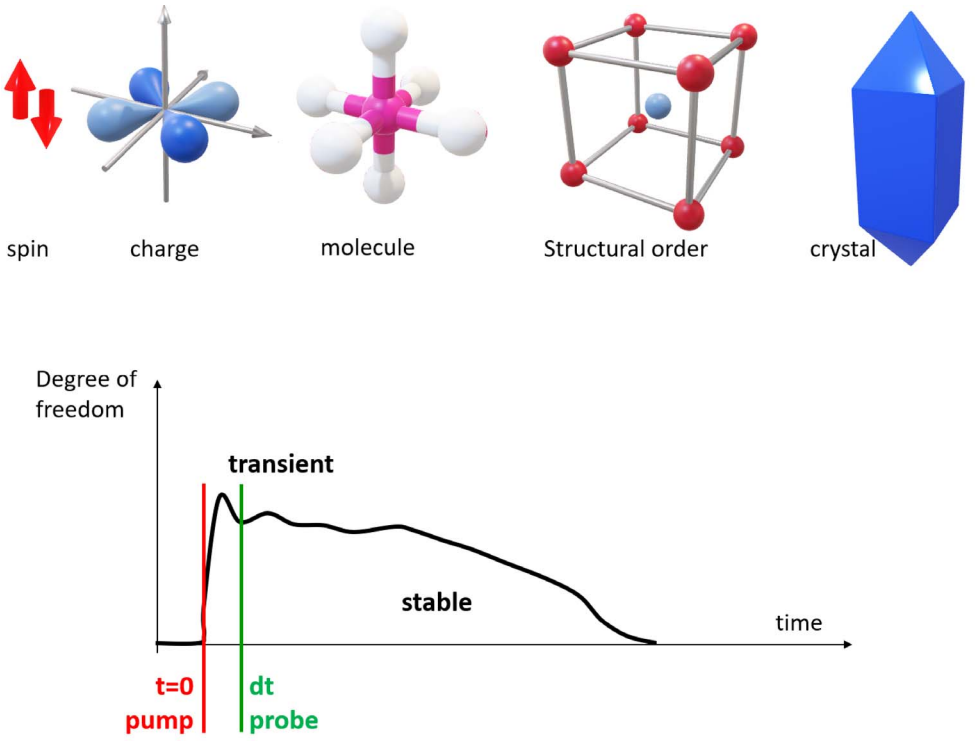

Figure 1. Schematic representation of different degrees of freedom involved in photoinduced processes. Pump–probe techniques allow for monitoring in time the evolution of a degree of freedom.

structure of Bismuth is rhombohedral, with two Bi atoms per unit cell, packed along the large diagonal of the cell with alternating short (X) and long ($1-X$) Bi–Bi interatomic distances. This equilibrium crystalline structure is governed by the electronic population of more or less bonding states (Figure 2a). The optical excitation of Bi populates less bonding electronic states, which modifies the equilibrium distance X. The inter-atomic potential is mainly governed by the thermalization of the electrons, which occurs on a fast timescale. Therefore, after photoexcitation, the potential is changed on a timescale much shorter than the phonon period and the atoms move coherently towards the new equilibrium position. The activation and damping of this coherent phonon Q_L were investigated by various techniques sensitive to the change of electronic state and/or structure [14, 20, 21, 23]. A thermodynamical model based on the two-temperature approach, the one of the electrons and the one of the lattice, evidenced that the coherent atomic motion is and entropy-driven process [24]. In addition, a lattice instability may appear above the critical value $n_e > n_c$ as the PES changes from double to single well, i.e. towards a higher symmetry. However, such processes require a lot of energy: the initial electronic temperature can reach 1000 K. In addition, only a small amount of the optical energy is coherently transferred to Q_L because of energy transfers through electron–phonon and phonon–phonon couplings towards many other degrees of freedom. For some systems, structural reorganization along Q_L can switch physical properties from insulating to metallic state for example [25] and even towards hidden phases [26].

Similar coherent structural dynamics was reported in molecular crystals. The family of $(EDOTTF)_2XF_6$ systems, where X stands for counter anions As, Sb or P, corresponds to 1/4 filled

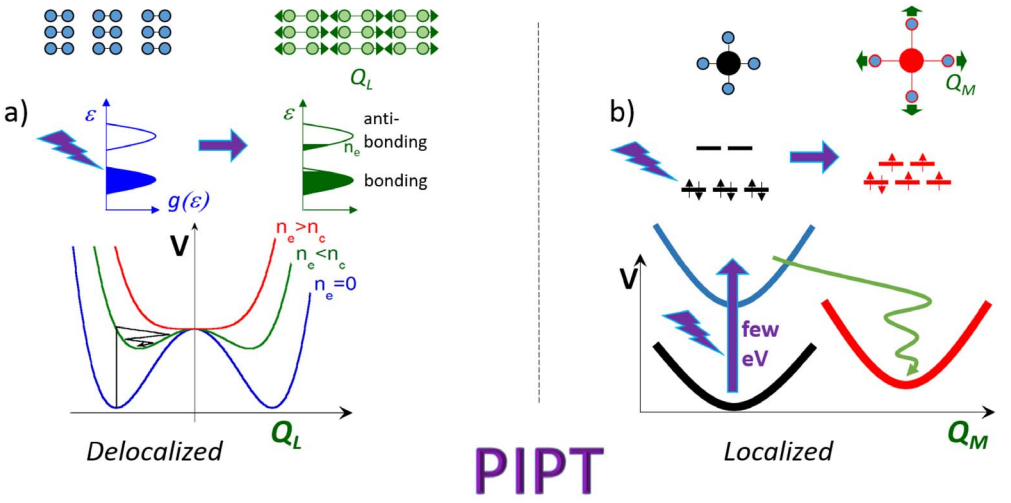

Figure 2. (a) PIPT driven by electronic excitation for delocalized electronic population of antibonding bands modifies the equilibrium of the lattice along Q_L. (b) Electronic excitation localized at the molecular level results in another PES for the new electronic state with different equilibrium structure of the molecule along Q_M.

molecular conductors (in terms of holes), which exhibit charge order in the insulating low temperature phase [27, 28] and the associated symmetry breaking corresponds to a doubling of the unit cell as neutral-bent and ionic-flat $(EDOTTF)_2$ dimers alternate. Those materials display a gigantic response to femtosecond laser excitation in the insulating phase, modulating so optical reflectivity up to 120%. The dynamics is associated with coherent structural reorganization and time-resolved electron diffraction evidenced the molecular motions involved in the process [29]. This is also the case for the molecular crystal $Me_4P[Pt(dmit)_2]_2$ [6], which exhibits a photoinduced charge transfer. Femtosecond electron diffraction studies allowed one to directly observe the coherent molecular motions involved in the process, and clearly identified them as due to a dimer expansion and a librational mode.

PIPTs driven by optical excitation were studied in molecular materials. Some initial processes are local and can be described at the molecular scale. The molecular entity is here the relevant building block: different and discrete PES correspond to discrete molecular electronic states (Figure 2b). The excitation from a ground state (black) to an electronic excited state (blue) may decay and be trapped in a less bonding and metastable state (red) by the structural reorganisation along a molecular mode Q_M. The coupling between electronic excitation and structural reorganizations is also an important aspect responsible for the appearance of light-induced excited spin state trapping (LIESST) in many transition metal complexes with electronic configuration d^4–d^7 and capable of spin crossover [12,30,31]. In these bistable molecular materials, the metal bonded to the ligand (L) may have two spin states in the case of a d^6 configuration: the LS state of electronic configuration ($S = 0$, $t_{2g}^6 e_g^0 L^0$) and the HS state ($S = 2$, $t_{2g}^4 e_g^2 L^0$). The LIESST effect consists in exciting by light a system in the LS state in order to switch it to the HS state. The structural trapping of the photoinduced HS state occurs at the time scale of elementary atomic movements and involves a reorganization of the molecular structure, linked to the variation of the iron-ligand (Fe–L) bond length, which accompanies the population of anti-bonding e_g states. X-ray absorption spectroscopy is a powerful technique for monitoring such local transformation occurring around the metal ion. A recent XANES study performed at the LCLS X-ray free electron laser

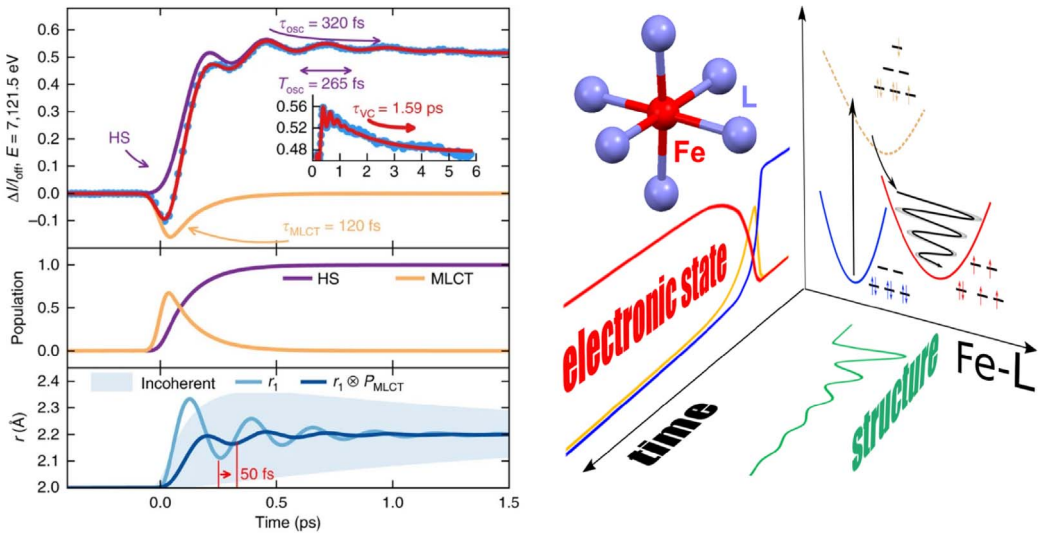

Figure 3. Evolution of the X-ray absorption signal (left) of a spin transition system after fs optical laser excitation, reprinted with permission from [12]. The signal decomposes in terms of electronic state change and structural dynamics with the evolution of the Fe–L distance r (right).

(X-FEL) [12] with a temporal resolution of ~25 fs, made it possible to directly observe the coherent structural dynamics of the ligand during the LIESST effect (Figure 3). XANES also allowed for discriminating the mean change of electronic state and the structural dynamics. The optical excitation $t_{2g} \rightarrow L$ induces a state of metal-ligand charge transfer (MLCT $t_{2g}^5 e_g^0 L^1$), and this change from Fe^{2+} to Fe^{3+} decreases the absorption of X-rays. This state then relaxes towards the HS state via activation and damping of the breathing mode, corresponding to an elongation of the Fe–L bonds, which is characterized by an increase and oscillation of the X-rays absorption. It is then possible to disentangle the electronic and structural dynamics, as shown in Figure 3.

Some molecular systems exhibit intermediate situation, in which the electronic excitation involves several molecules. This is the case for charge-transfer systems undergoing insulator-metal [6] or para- to ferroelectric [32] phase transitions. The past 15 years witnessed development of a broad and expanding spectrum of complementary optical and X-ray techniques, including spectroscopy and diffraction [4]. These techniques have delivered new insights into the dynamics of molecular systems and solids, by investigating how an ultrafast and intense optical pulse drives the transformation process, and how electronic and structural degrees of freedom are coupled, and evolve in real time. For condensed matter, the topics concern a broad variety of mechanisms including coherent structural dynamics [4, 6, 12, 31, 32], cooperative transformation [30], charge-orbital orders [33], etc.

A recent study of a photomagnetic CoFe Prussian blue analogue investigated how coupled charge-transfer and spin transition evolve in time [34]. These systems are coordination networks where cyanide groups connect the Co and the Fe ions in octahedral crystal fields. There are two bistable electronic–structural configurations (Figure 4) linked to a charge transfer (CT) between Fe and Co: the ground $Co^{III}(S = 0)Fe^{II}(S = 0)$ state or the photoinduced $Co^{II}(S = 3/2)Fe^{III}(S = 1/2)$. In the HS $Co^{II}Fe^{III}$ state, the population of anti-binding Co (e_g) orbitals lengthens Co–N bonds by ≈0.2 Å and this spin transition (ST) on the Co is the main reaction coordinate. The photoinduced

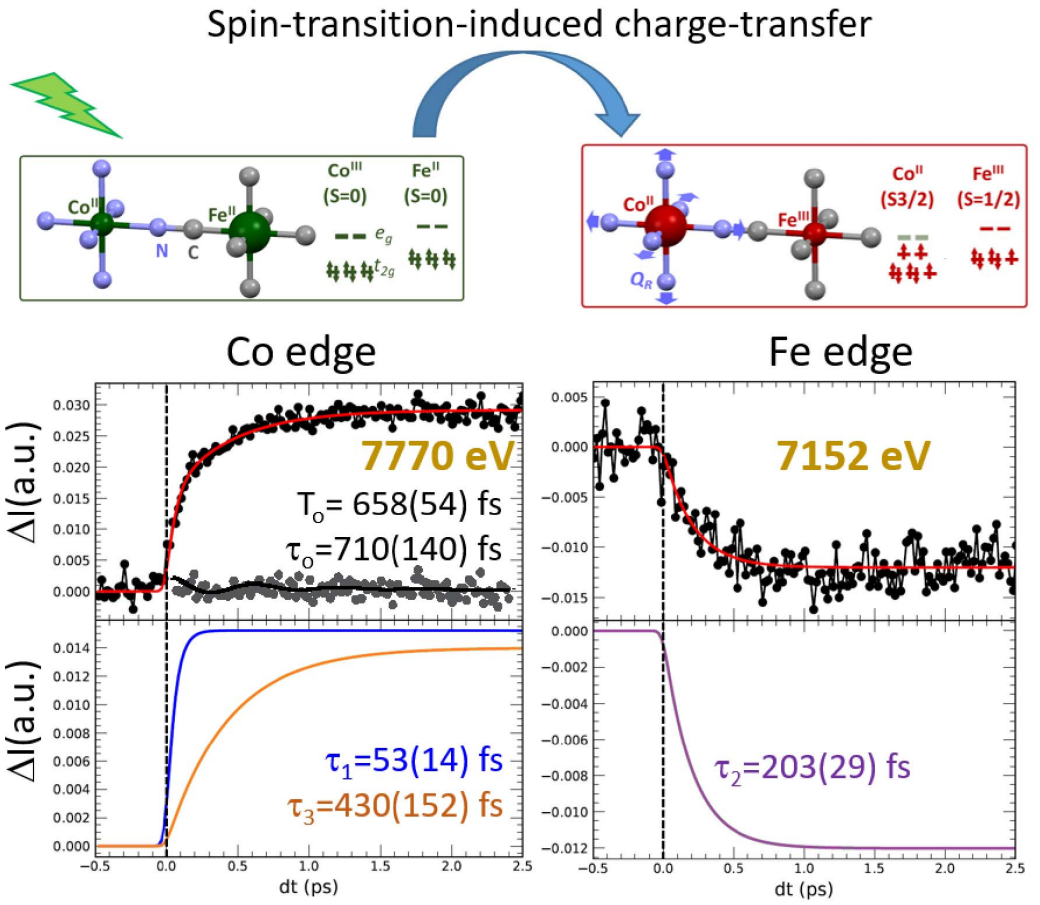

Figure 4. Photomagnetic transition between low and high spin states [34]. XANES spectroscopy measurements show that it is the photoinduced spin transition (ST) around the Co, occurring within ~50 fs as observed at 7770 eV, which induces the charge transfer (CT) within ~200 fs, as observed around the Fe edge (7152 eV), thus following the transformation path STICT.

Fe → Co charge transfer process remained inaccessible and it was then considered that the path followed during the transformation is a photoinduced charge transfer, which induces its turn the spin transition (CTIST transformation lane). The time-resolved XANES measurements performed at the X-FEL LCLS with ≈25 fs time resolution allowed probing selectively the dynamics of electronic and structural degrees of freedom around Fe and Co ions [34]. These results provided a direct insight into electronic and structural dynamics: the Co^{III} (t_{2g}) → Co^{III} (e_g) optical excitation induces the spin transition on Co and elongates the Co–N bonds within ≈50 fs, as characterized by a rapid variation in absorption above the threshold Co (7770 eV, Figure 4). XANES, which is a technique of choice for measuring changes in the oxidation state of metals, revealed that the Fe → Co (CT) charge transfer takes place in a second step within ≈200 fs, as characterized by the spectral shift at the Fe absorption edge (7152 eV). These results provide a clear answer to a question debated for decades, by demonstrating that in this photoexcited prototype CoFe compound, the transformation pathway is a photoactivated spin transition, which induces charge transfer (STICT in Figure 4).

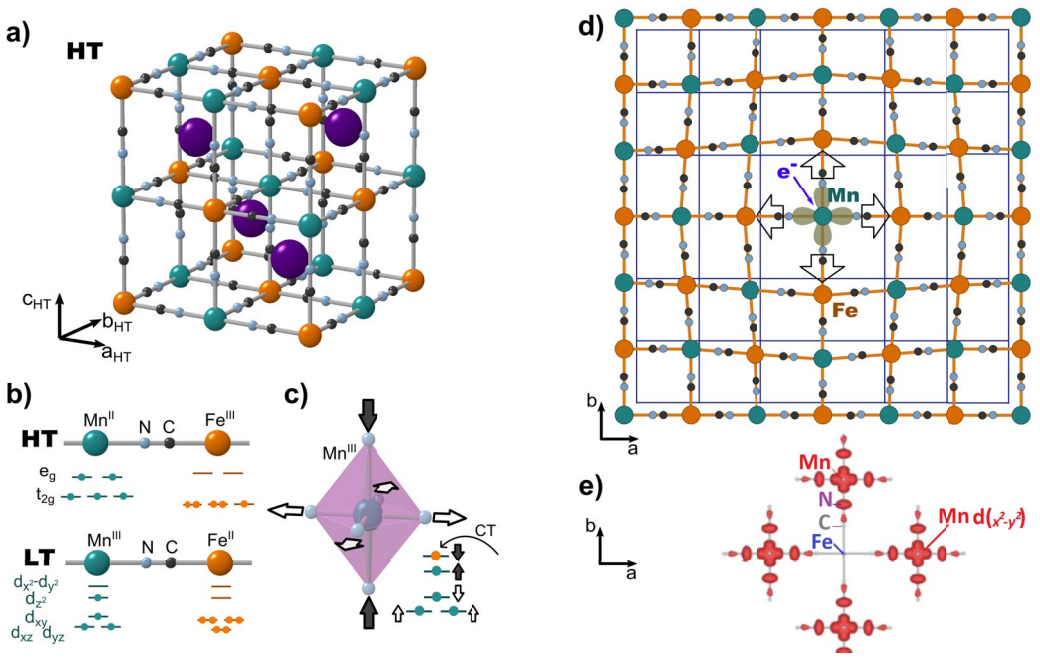

Figure 5. (a) Crystalline structure of RbMnFe PBA in the cubic HT phase. (b) Schematic valence states and electronic configurations in the LT $Mn^{III}Fe^{II}$ and HT $Mn^{II}Fe^{III}$ phases. (c) The $Mn^{III}Fe^{II} \rightarrow Mn^{II}Fe^{III}$ charge transfer, populating the antibonding Mn $d(x^2 - y^2)$ state, is stabilized by the reverse Jahn–Teller distortion elongating Mn–N bonds along a and b and shrinking the ones along c. (d) Schematic representation of the lattice expansion in the (a, b) plane distortion due to the CT small-polaron. (e) The CT populates the Mn $d(x^2 - y^2)$ state and is self-trapped by Mn–N bond elongation. Reprinted with permission from [35].

$RbMn[Fe(CN)_6]$ Prussian blue analogues also exhibit diverse CT-based functionalities [36–38]. The additional complexity comes the fact that the bistability between the high-temperature cubic (HT) $Mn^{II}(S = 5/2)Fe^{III}(S = 1/2)$ state and the low-temperature (LT) $Mn^{III}(S = 2)Fe^{II}(S = 0)$ state is also coupled to a symmetry breaking towards a tetragonal lattice, due to Jahn–Teller distortion around the Mn^{III} [39, 40]. Since CT couples to Jahn–Teller distortion, the nature of the photoinduced process was questioned: is it a Jahn–Teller-induced CT or a CT-induced structural trapping? Femtosecond optical pump–probe spectroscopy revealed that two photoswitching pathways exist, depending on the excitation pump wavelength, which is confirmed by band structure calculations [41]. Photoexcitation of α spins corresponds to the Mn(d–d) band, which drives reverse Jahn–Teller distortion through the population of antibonding Mn–N orbitals, and induces CT within ~190 fs. Photoexcitation of β spins drives intervalence Fe → Mn CT towards non-bonding states and results in a slower dynamic. Time resolved X-ray diffraction studies also revealed the anisotropic out-of-equilibrium lattice dynamics triggered by the self-trapping of photo-induced $Mn^{III}Fe^{II} \rightarrow Mn^{II}Fe^{III}$ CT [35]. The observed dynamics evidenced a decoupling in time of the lattice expansion and the ferroelastic Jahn–Teller distortion. The anisotropic out-of-equilibrium lattice dynamics is triggered by the self-trapping of photo-induced $Mn^{III}Fe^{II} \rightarrow Mn^{II}Fe^{III}$CT. The impulsive lattice response is driven by the local Jahn–Teller reorganization, which elongates the a and b lattice parameters and shrinks the c axis (Figure 5). The structural reorganization is stabilized by a displacive volume expansion, controlled by the long-lived

photo-induced CT small-polarons. Indeed, CT populates the lowest unoccupied crystalline orbital, with electronic density highly localized on antibonding Mn($d_{x^2-y^2}$) and N orbitals. This change of electronic state elongates Mn–N bonds in the (a, b) lattice plane and is therefore responsible for the anisotropic volume expansion.

Photoinduced phenomena are often multi-scale processes. The recent study by Mariette *et al.* [36], based on femtosecond X-ray diffraction experiments, revealed how electronic and structural precursor phenomena generate strain waves and coherent macroscopic transformation pathway for the semiconducting-to-metal transition in bistable Ti_3O_5 nanocrystals [42]. The authors have measured the lattice deformation in the photoinduced phase transition as a function of time, and monitored the intra-cell distortions around the light absorbing metal dimer and the long-range deformations governed by acoustic waves. The photoinduced phase propagates from the laser-exposed surface.

The scale of energy involved in optical excitation is the limiting factor in many of the previous studies. The energy difference between the starting and the final phases in bistable systems for instance is of the order of thermal energy ($k_B T < 30$ meV at $T = 300$ K), which is much lower than the energy of optical photons (eV) [1]. PIPTs driven by optical excitation are then often dominated by heat dissipation, which hinders establishment of ordered state or destroys the coherent dynamics. Temperature rise inevitably favors states of higher entropy and higher symmetry. Since emergence of functions like ferro-electricity is related to symmetry breaking, and hence to lower entropy states, a new suitable control method is required. By acting on lattice vibration modes at a resonant and relevant energy scale (10–250 meV), the nonlinear phononics (NLP) is a potential candidate method for tuning materials along a transformation pathway while allowing to circumvent the above-mentioned limitations (Figure 6). It preserves all advantages intrinsic to the ultrafast time-scales while alleviating the shortcomings of electronic excitations, whereby electron–phonon couplings are not controlled, and selectively activates a highly responsive phonon mode. NLP is based on a strong and resonant excitation of low-energy IR phonon Q_{IR} (frequency Ω_{IR}) by high-power femtosecond mid-IR lasers (1000 s·cm^{-1}). A. Cavalleri's group demonstrated that NLP can favors superconductivity or drive insulator-metal transition [43–48]. According to the theory of nonlinear phononics developed by Subedi and Georges [43, 49] the intense laser field $F(t)$ of the IR pulse populates a significant quanta of Q_{IR} phonons ($n \gg 1$) with large amplitude $\langle Q_{IR}^2 \rangle$. The non-linear coupling to a phonon mode Q_{TS} moves its equilibrium position by $\propto F^2(\Omega_{IR}/\Omega_{TS})^2$. NLP allows then to tune the potential V_{TS} along a transformation pathway, towards another phase of different structural-electronic orders. Some recent uses of NLP via mid-IR phonon excitations in hard condensed matter include large perturbations of orbital [50], magnetic [51–53] and ferroelectric [54] orders. Hence, NLP promises capabilities insofar unachieved in PIPT, as the ultrafast modification of the potential, occurring on a few Q_{IR} phonon periods, will drive coherent and collective transformations.

The field of ultrafast phenomena in condensed matter is rapidly expending, with a large variety of topics and techniques, and this special issue perfectly illustrates this diversity. Recent advances allowing monitoring ultrafast phenomena are presented by Chong-Yu Ruan *et al.* for ultrafast electron diffraction and Michael Wulff *et al.* for X-ray techniques at synchrotron and X-FEL. Yoichi Okimoto *et al.* show how time-resolved Raman spectroscopy can be used to study the picosecond dynamics of the photo-excited charge-ordered perovskite-type cobalt oxides. Marino Marsi *et al.* present time-resolved Angle Resolved Photoemission Spectroscopy ARPES, which allows for visualizing directly on the femtosecond time scale the evolution of band dispersion of photoexcited solids. Stefan Haacke *et al.* revisit with optical spectroscopy the sub-picosecond photo-isomerization process. Claire Laulhé *et al.* use X-ray diffraction to investigate to ultrafast photoinduced dynamics of an incommensurate charge density wave in 1T–TaS_2. Alaska Subedi is reviewing the emerging field of non-linear phononics and its underlying theory.

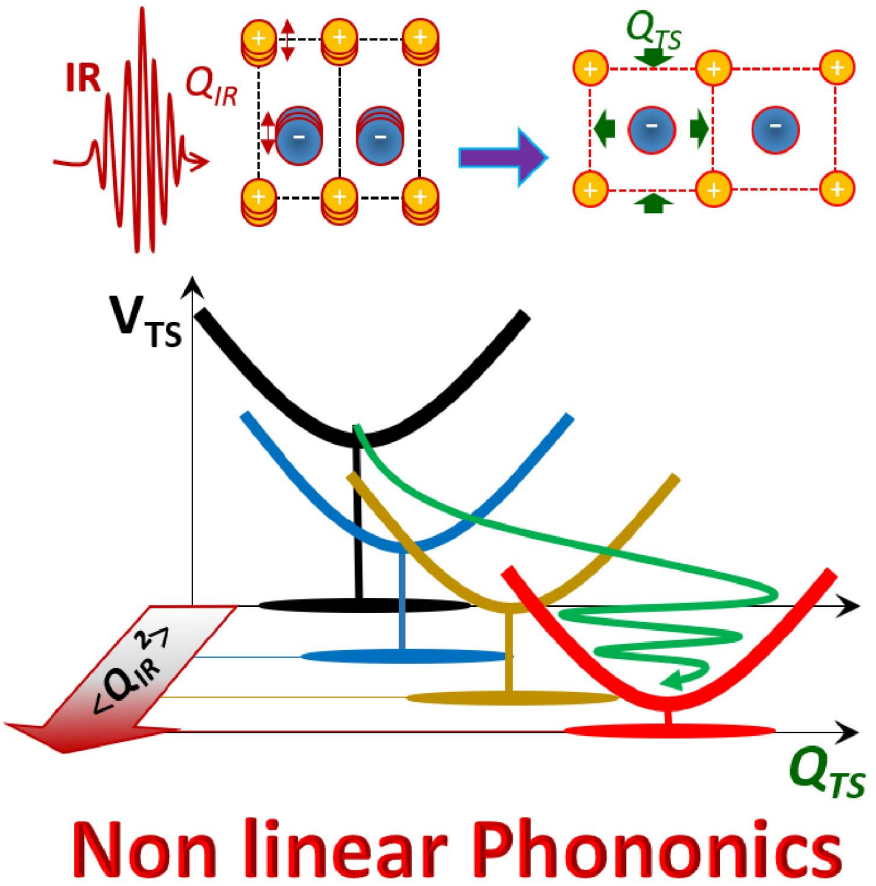

Figure 6. Nonlinear phononics drives transformation in the electronic ground state: a highly excited $\langle Q_{\mathrm{IR}}^2 \rangle$ anharmonically couples to a totally symmetric mode Q_{TS}, rectifies its potential V_{TS} and drives a structural reorganisation by modifying the equilibrium position of Q_{TS}.

References

[1] D. N. Basov, R. D. Averitt, D. Hsieh, "Towards properties on demand in quantum materials", *Nat. Mater.* **16** (2017), p. 1077-1088.

[2] K. Nasu, *Photoinduced Phase Transitions*, World Scientific, Singapore, Hackensack, NJ, 2004.

[3] A. H. Zewail, "Chemistry at the uncertainty limit", *Angew. Chem. Int. Ed.* **40** (2001), p. 4371-4375.

[4] M. Chergui, E. Collet, "Photoinduced structural dynamics of molecular systems mapped by time-resolved X-ray methods", *Chem. Rev.* **117** (2017), p. 11025-11065.

[5] E. Collet, "Dynamical structural science", *Acta Crystallogr. A* **66** (2010), p. 133-134.

[6] T. Ishikawa, S. A. Hayes, S. Keskin, G. Corthey, M. Hada, K. Pichugin, A. Marx, J. Hirscht, K. Shionuma, K. Onda, Y. Okimoto, S.-y. Koshihara, T. Yamamoto, H. Cui, M. Nomura, Y. Oshima, M. Abdel-Jawad, R. Kato, R. J. D. Miller, "Direct observation of collective modes coupled to molecular orbital–driven charge transfer", *Science* **350** (2015), p. 1501-1505.

[7] F. Schmitt, P. S. Kirchmann, U. Bovensiepen, R. G. Moore, L. Rettig, M. Krenz, J. H. Chu, N. Ru, L. Perfetti, D. H. Lu, M. Wolf, I. R. Fisher, Z. X. Shen, "Transient electronic structure and melting of a charge density wave in $TbTe_3$", *Science* **321** (2008), p. 1649-1652.

[8] C. Boeglin, E. Beaurepaire, V. Halte, V. Lopez-Flores, C. Stamm, N. Pontius, H. A. Durr, J. Y. Bigot, "Distinguishing the ultrafast dynamics of spin and orbital moments in solids", *Nature* **465** (2010), p. 458-461.

[9] A. H. Zewail, F. C. d. Schryver, S. D. Feyter, G. Schweitzer, *Femtochemistry: with the Nobel Lecture of A. Zewail*, Wiley-VCH, Weinheim New York, 2001.

[10] T. Kampfrath, K. Tanaka, K. A. Nelson, "Resonant and nonresonant control over matter and light by intense terahertz transients", *Nat. Photonics* **7** (2013), p. 680-690.

[11] K. Zhang, R. Ash, G. S. Girolami, J. Vura-Weis, "Tracking the Metal-centered triplet in photoinduced spin crossover of $Fe(phen)_3^{(2+)}$ with tabletop femtosecond M-Edge X-ray absorption near-edge structure spectroscopy", *J. Am. Chem. Soc.* **141** (2019), no. 43, p. 17180-17188.

[12] H. T. Lemke, K. S. Kjær, R. Hartsock, T. Brandt van Driel, M. Chollet, J. M. Glownia, S. Song, D. Zhu, E. Pace, S. F. Matar, M. N. Nielsen, M. Benfatto, K. J. Gaffney, E. Collet, M. Cammarata, "Coherent structural trapping through wave packet dispersion during photoinduced spin state switching", *Nat. Commun.* **8** (2017), article no. 15342.

[13] S. Zerdane, L. Wilbraham, M. Cammarata, O. Iasco, E. Rivière, M. L. Boillot, I. Ciofini, E. Collet, "Comparison of structural dynamics and coherence of d–d and MLCT light-induced spin state trapping", *Chem. Sci.* **8** (2017), p. 4978-4986.

[14] J. Faure, J. Mauchain, E. Papalazarou, M. Marsi, D. Boschetto, I. Timrov, N. Vast, Y. Ohtsubo, B. Arnaud, L. Perfetti, "Direct observation of electron thermalization and electron-phonon coupling in photoexcited bismuth", *Phys. Rev. B* **88** (2013), article no. 075120.

[15] M. Chergui, A. H. Zewail, "Electron and X-ray methods of ultrafast structural dynamics: advances and applications", *Chemphyschem* **10** (2009), p. 28-43.

[16] T. Graber, S. Anderson, H. Brewer, Y. S. Chen, H. S. Cho, N. Dashdorj, R. W. Henning, I. Kosheleva, G. Macha, M. Meron, R. Pahl, Z. Ren, S. Ruan, F. Schotte, V. Srajer, P. J. Viccaro, F. Westferro, P. Anfinrud, K. Moffat, "BioCARS: a synchrotron resource for time-resolved X-ray science", *J. Synchrotron Radiat.* **18** (2011), p. 658-670.

[17] Y. Jiang, L. C. Liu, H. M. Müller-Werkmeister, C. Lu, D. Zhang, R. L. Field, A. Sarracini, G. Moriena, E. Collet, R. J. D. Miller, "Structural dynamics upon photoexcitation in a spin crossover crystal probed with femtosecond electron diffraction", *Angew. Chem. Int. Ed.* **56** (2017), p. 7130-7134.

[18] L. X. Chen, X. Zhang, M. L. Shelby, "Recent advances on ultrafast X-ray spectroscopy in the chemical sciences", *Chem. Sci.* **5** (2014), p. 4136-4152.

[19] M. Cammarata, L. Eybert, F. Ewald, W. Reichenbach, M. Wulff, P. Anfinrud, F. Schotte, A. Plech, Q. Kong, M. Lorenc, B. Lindenau, J. Rabiger, S. Polachowski, "Chopper system for time resolved experiments with synchrotron radiation", *Rev. Sci. Instrum.* **80** (2009), article no. 015101.

[20] K. Sokolowski-Tinten, C. Blome, J. Blums, A. Cavalleri, C. Dietrich, A. Tarasevitch, I. Uschmann, E. Forster, M. Kammler, M. Horn-von Hoegen, D. von der Linde, "Femtosecond X-ray measurement of coherent lattice vibrations near the Lindemann stability limit", *Nature* **422** (2003), p. 287-289.

[21] D. M. Fritz, D. A. Reis, B. Adams, R. A. Akre, J. Arthur, C. Blome, P. H. Bucksbaum, A. L. Cavalieri, S. Engemann, S. Fahy, R. W. Falcone, P. H. Fuoss, K. J. Gaffney, M. J. George, J. Hajdu, M. P. Hertlein, P. B. Hillyard, M. H. V. Hoegen, M. Kammler, J. Kaspar, R. Kienberger, P. Krejcik, S. H. Lee, A. M. Lindenberg, B. McFarland, D. Meyer, T. Montagne, E. D. Murray, A. J. Nelson, M. Nicoul, R. Pahl, J. Rudati, H. Schlarb, D. P. Siddons, K. Sokolowski-Tinten, T. Tschentscher, D. von der Linde, J. B. Hastings, "Ultrafast bond softening in bismuth: Mapping a solid's interatomic potential with X-rays", *Science* **315** (2007), p. 633-636.

[22] S. L. Johnson, P. Beaud, E. Vorobeva, C. J. Milne, E. D. Murray, S. Fahy, G. Ingold, "Non-equilibrium phonon dynamics studied by grazing-incidence femtosecond X-ray crystallography", *Acta Crystallogr. A* **66** (2010), p. 157-167.

[23] T. Garl, E. G. Gamaly, D. Boschetto, A. V. Rode, B. Luther-Davies, A. Rousse, "Birth and decay of coherent optical phonons in femtosecond-laser-excited bismuth", *Phys. Rev. B* **78** (2008), article no. 134302.

[24] Y. Giret, A. Gellé, B. Arnaud, "Entropy driven atomic motion in laser-excited bismuth", *Phys. Rev. Lett.* **106** (2011), article no. 155503.

[25] A. Cavalleri, C. Toth, C. W. Siders, J. A. Squier, F. Raksi, P. Forget, J. C. Kieffer, "Femtosecond structural dynamics in VO_2 during an ultrafast solid-solid phase transition", *Phys. Rev. Lett.* **8723** (2001), article no. 237401.

[26] H. Ichikawa, S. Nozawa, T. Sato, A. Tomita, K. Ichiyanagi, M. Chollet, L. Guerin, N. Dean, A. Cavalleri, S.-i. Adachi, T.-h. Arima, H. Sawa, Y. Ogimoto, M. Nakamura, R. Tamaki, K. Miyano, S.-y. Koshihara, "Transient photoinduced "hidden" phase in a manganite", *Nat. Mater.* **10** (2011), p. 101-105.

[27] M. Chollet, L. Guerin, N. Uchida, S. Fukaya, H. Shimoda, T. Ishikawa, K. Matsuda, T. Hasegawa, A. Ota, H. Yamochi, G. Saito, R. Tazaki, S.-i. Adachi, S.-y. Koshihara, "Gigantic Photoresponse in $\frac{1}{4}$-Filled-Band Organic Salt $(EDO\text{-}TTF)_2PF_6$", *Science* **307** (2005), p. 86-89.

[28] M. Servol, N. Moisan, E. Collet, H. Cailleau, W. Kaszub, L. Toupet, D. Boschetto, T. Ishikawa, A. Moréac, S. Koshihara, M. Maesato, M. Uruichi, X. Shao, Y. Nakano, H. Yamochi, G. Saito, M. Lorenc, "Local response to light excitation in the charge-ordered phase of$(EDO\text{-}TTF)_2SbF_6$", *Phys. Rev. B* **92** (2015), article no. 024304.

[29] M. Gao, C. Lu, H. Jean-Ruel, L. C. Liu, A. Marx, K. Onda, S. Y. Koshihara, Y. Nakano, X. Shao, T. Hiramatsu, G. Saito, H. Yamochi, R. R. Cooney, G. Moriena, G. Sciaini, R. J. Miller, "Mapping molecular motions leading to charge delocalization with ultrabright electrons", *Nature* **496** (2013), p. 343-346.

[30] R. Bertoni, M. Lorenc, H. Cailleau, A. Tissot, J. Laisney, M. L. Boillot, L. Stoleriu, A. Stancu, C. Enachescu, E. Collet,

"Elastically driven cooperative response of a molecular material impacted by a laser pulse", *Nat. Mater.* **15** (2016), p. 606-610.

[31] M. Cammarata, R. Bertoni, M. Lorenc, H. Cailleau, S. Di Matteo, C. Mauriac, S. F. Matar, H. Lemke, M. Chollet, S. Ravy, C. Laulhe, J. F. Letard, E. Collet, "Sequential activation of molecular breathing and bending during spin-crossover photoswitching revealed by femtosecond optical and X-ray absorption spectroscopy", *Phys. Rev. Lett.* **113** (2014), article no. 227402.

[32] E. Collet, M. H. Lemee-Cailleau, M. Buron-Le Cointe, H. Cailleau, M. Wulff, T. Luty, S. Y. Koshihara, M. Meyer, L. Toupet, P. Rabiller, S. Techert, "Laser-induced ferroelectric structural order in an organic charge-transfer crystal", *Science* **300** (2003), p. 612-615.

[33] P. Beaud, A. Caviezel, S. O. Mariager, L. Rettig, G. Ingold, C. Dornes, S. W. Huang, J. A. Johnson, M. Radovic, T. Huber, T. Kubacka, A. Ferrer, H. T. Lemke, M. Chollet, D. Zhu, J. M. Glownia, M. Sikorski, A. Robert, H. Wadati, M. Nakamura, M. Kawasaki, Y. Tokura, S. L. Johnson, U. Staub, "A time-dependent order parameter for ultrafast photoinduced phase transitions", *Nat. Mater.* **13** (2014), p. 923-927.

[34] M. Cammarata, S. Zerdane, L. Balducci, G. Azzolina, S. Mazerat, C. Exertier, M. Trabuco, M. Levantino, R. Alonso-Mori, J. Glownia, S. Song, L. Catala, T. Mallah, S. F. Matar, E. Collet, "Charge transfer driven by ultrafast spin transition in a CoFe Prussian blue analogue", *Nat. Chem.* **13** (2021), p. 10-14.

[35] G. Azzolina, R. Bertoni, C. Mariette, M. Cammarata, E. Trzop, C. Ecolivet, M. Sander, M. Levantino, H. Tokoro, K. Imoto, M. Yoshikiyo, S. Ohkoshi, E. Collet, "Out-of-equilibrium lattice response to photo-induced charge-transfer in a MnFe Prussian blue analogue", *J. Mater. Chem. C* **9** (2021), p. 6773-6780.

[36] H. Tokoro, S. Ohkoshi, "Multifunctional Material: Bistable Metal–Cyanide Polymer of Rubidium Manganese Hexacyanoferrate", *Bull. Chem. Soc. Jpn.* **88** (2015), p. 227-239.

[37] K. Kato, Y. Moritomo, M. Takata, M. Sakata, M. Umekawa, N. Hamada, S. Ohkoshi, H. Tokoro, K. Hashimoto, "Direct observation of charge transfer in double-perovskite-like $RbMnFe(CN)_6$", *Phys. Rev. Lett.* **91** (2003), article no. 255502.

[38] S. Ohkoshi, H. Tokoro, M. Utsunomiya, M. Mizuno, M. Abe, K. Hashimoto, "Observation of spin transition in an octahedrally Coordinated Manganese(II) compound", *J. Phys. Chem. B* **106** (2002), p. 2423-2425.

[39] H. Tokoro, S. Ohkoshi, T. Matsuda, K. Hashimoto, "A large thermal hysteresis loop produced by a charge-transfer phase transition in a rubidium manganese hexacyanoferrate", *Inorg. Chem.* **43** (2004), p. 5231-5236.

[40] G. Azzolina, R. Bertoni, C. Ecolivet, H. Tokoro, S. Ohkoshi, E. Collet, "Landau theory for non-symmetry-breaking electronic instability coupled to symmetry-breaking order parameter applied to Prussian blue analog", *Phys. Rev. B* **102** (2020), article no. 134104.

[41] G. Azzolina, H. Tokoro, K. Imoto, M. Yoshikiyo, S.-i. Ohkoshi, E. Collet, "Exploring ultrafast photoswitching pathways in RbMnFe Prussian Blue Analogue", *Angew. Chem. Int. Ed.* (2021).

[42] C. Mariette, M. Lorenc, H. Cailleau, E. Collet, L. Guérin, A. Volte, E. Trzop, R. Bertoni, X. Dong, B. Lépine, O. Hernandez, E. Janod, L. Cario, V. Ta Phuoc, S. Ohkoshi, H. Tokoro, L. Patthey, A. Babic, I. Usov, D. Ozerov, L. Sala, S. Ebner, P. Böhler, A. Keller, A. Oggenfuss, T. Zmofing, S. Redford, S. Vetter, R. Follath, P. Juranic, A. Schreiber, P. Beaud, V. Esposito, Y. Deng, G. Ingold, M. Chergui, G. F. Mancini, R. Mankowsky, C. Svetina, S. Zerdane, A. Mozzanica, A. Bosak, M. Wulff, M. Levantino, H. Lemke, M. Cammarata, "Strain wave pathway to semiconductor-to-metal transition revealed by time-resolved X-ray powder diffraction", *Nat. Commun.* **12** (2021), article no. 1239.

[43] A. Subedi, A. Cavalleri, A. Georges, "Theory of nonlinear phononics for coherent light control of solids", *Phys. Rev. B* **89** (2014), article no. 220301.

[44] D. Nicoletti, A. Cavalleri, "Nonlinear light–matter interaction at terahertz frequencies", *Adv. Opt. Photonics* **8** (2016), p. 401-464.

[45] M. Forst, C. Manzoni, S. Kaiser, Y. Tomioka, Y. Tokura, R. Merlin, A. Cavalleri, "Nonlinear phononics as an ultrafast route to lattice control", *Nat. Phys.* **7** (2011), p. 854-856.

[46] J. Zhang, R. D. Averitt, "Dynamics and control in complex transition metal oxides", *Annu. Rev. Mater. Res.* **44** (2014), p. 19-43.

[47] R. Mankowsky, A. Subedi, M. Forst, S. O. Mariager, M. Chollet, H. T. Lemke, J. S. Robinson, J. M. Glownia, M. P. Minitti, A. Frano, M. Fechner, N. A. Spaldin, T. Loew, B. Keimer, A. Georges, A. Cavalleri, "Nonlinear lattice dynamics as a basis for enhanced superconductivity in $YBa_2Cu_3O_{6.5}$", *Nature* **516** (2014), p. 71-73.

[48] M. Liu, H. Y. Hwang, H. Tao, A. C. Strikwerda, K. Fan, G. R. Keiser, A. J. Sternbach, K. G. West, S. Kittiwatanakul, J. Lu, S. A. Wolf, F. G. Omenetto, X. Zhang, K. A. Nelson, R. D. Averitt, "Terahertz-field-induced insulator-to-metal transition in vanadium dioxide metamaterial", *Nature* **487** (2012), p. 345-348.

[49] A. Subedi, "Midinfrared-light-induced ferroelectricity in oxide paraelectrics via nonlinear phononics", *Phys. Rev. B* **95** (2017), article no. 134113.

[50] R. I. Tobey, D. Prabhakaran, A. T. Boothroyd, A. Cavalleri, "Ultrafast electronic phase transition in $La_{1/2}Sr_{3/2}MnO_4$ by coherent vibrational excitation: evidence for nonthermal melting of orbital order", *Phys. Rev. Lett.* **101** (2008), article no. 197404.

[51] M. Först, R. I. Tobey, S. Wall, H. Bromberger, V. Khanna, A. L. Cavalieri, Y. D. Chuang, W. S. Lee, R. Moore, W. F.

Schlotter, J. J. Turner, O. Krupin, M. Trigo, H. Zheng, J. F. Mitchell, S. S. Dhesi, J. P. Hill, A. Cavalleri, "Driving magnetic order in a manganite by ultrafast lattice excitation", *Phys. Rev. B* **84** (2011), article no. 241104.

[52] M. Forst, A. D. Caviglia, R. Scherwitzl, R. Mankowsky, P. Zubko, V. Khanna, H. Bromberger, S. B. Wilkins, Y. D. Chuang, W. S. Lee, W. F. Schlotter, J. J. Turner, G. L. Dakovski, M. P. Minitti, J. Robinson, S. R. Clark, D. Jaksch, J. M. Triscone, J. P. Hill, S. S. Dhesi, A. Cavalleri, "Spatially resolved ultrafast magnetic dynamics initiated at a complex oxide heterointerface", *Nat. Mater.* **14** (2015), p. 883-888.

[53] T. F. Nova, A. Cartella, A. Cantaluppi, M. Först, D. Bossini, R. V. Mikhaylovskiy, A. V. Kimel, R. Merlin, A. Cavalleri, "An effective magnetic field from optically driven phonons", *Nat. Phys.* **13** (2017), p. 132-136.

[54] R. Mankowsky, A. von Hoegen, M. Forst, A. Cavalleri, "Ultrafast reversal of the ferroelectric polarization", *Phys. Rev. Lett.* **118** (2017), article no. 197601.

Comptes Rendus
Physique
2021, 22, nº S2, p. 15-73
https://doi.org/10.5802/crphys.86

Physics of ultra-fast phenomena / *Physique des phénomènes ultra-rapides*

Toward nonthermal control of excited quantum materials: framework and investigations by ultrafast electron scattering and imaging

Xiaoyi Sun [a], **Shuaishuai Sun** [a] **and Chong-Yu Ruan** [*, a]

[a] Department of Physics and Astronomy, Michigan State University, East Lansing, MI 48825, USA

E-mails: sunxia14@msu.edu (X. Sun), sunshuai@msu.edu (S. Sun), ruanc@msu.edu (C.-Y. Ruan)

Abstract. Quantum material systems upon applying ultrashort laser pulses provide a rich platform to access excited material phases and their transformations that are not entirely like their equilibrium counterparts. The addressability and potential controls of metastable or long-trapped out-of-equilibrium phases have motivated interests both for the purposes of understanding the nonequilibrium physics and advancing the quantum technologies. Thus far, the dynamical spectroscopic probes eminently focus on microscopic electronic and phonon responses. For characterizing the long-range dynamics, such as order parameter fields and fluctuation effects, the ultrafast scattering probes offer direct sensitivity. Bridging the connections between the microscopic dynamics and macroscopic responses is central toward establishing the nonequilibrium physics behind the light-induced phases. Here, we present a path toward such understanding by cross-examining the structure factors associated with different dynamical states obtained from ultrafast electron scattering, imaging, and modeling. We give the basic theoretical framework on describing the non-equilibrium scattering problems and briefly describe how such framework relates to the out-of-equilibrium phenomena. We give effective models outlining the emergences of nonthermal critical points, hidden phases, and non-equilibrium relaxational responses from vacuum-suspended rare-earth tritellurides, tantalum disulfides thin films, and vanadium dioxide nanocrystalline materials upon light excitations.

Keywords. Photoinduced phase transitions, Interaction quench, Quantum materials nonequilibrium many-body systems, Ultrafast electron diffraction, Ultrafast electron microscopy.

Available online 28th September 2021

* Corresponding author.

1. Introduction

The interests for exploring light-induced new functional phases or properties of matters are motivated by practical endeavors, dubbed as materials on demand [1,2], as a new direction of material research. The desire to harness the functionalities beyond the conventional metals or semiconductors has drawn significant attentions for exploring quantum materials [3]. The quantum materials, also referred to as strongly correlated electron materials, are featured by their complex phase diagrams where multiple electronic phases often occur adjacently. While such complexity is rooted in the active interactions between multiple microscopic degrees of freedom—lattice, charge, spin, and orbital—competing ground states are of macroscopic nature [2,4] and their evolutions over the external control parameters can be discussed much without the detailed knowledge at the microscopic scales [5]. The physics of phase transitions can often be encapsulated in generalized order parameters that either explicitly breaks or implicitly connects to the symmetry-breaking processes. Much of the success in developing predicative models owes to phenomenological models based on the order parameter concept [6–8], which has been demonstrated in contexts [9] ranging from condensed matter physics to cosmology [10].

Much anticipated are the successful models for nonequilibrium phase transitions in the quantum materials. A number of important developments have emerged in recent years concerning this topic. One can now rely on the growing capabilities of the ultrafast techniques to give increasingly more details of the nonequilibrium transformations between quantum phases; see for example the recent reviews [11–14]. Indeed, many recent ultrafast pump–probe studies of quantum matters also led to surprising results that cannot be identified from the equilibrium states [15–23], often referred to as the hidden state problem [24, 25]. Second, studying the nonequilibrium collective state evolution in quantum materials involves fundamental concept of nonequilibrium many-body physics [26–30]. Especially, understanding how a nonequilibrium system self-organizes into a broken-symmetry phase is a problem of broad interests from condensed matter [31–33] to high-energy physics [34–36]. It is widely believed that the generic responses of an isolated many-body system upon quench is to evolve towards the equilibrium state. However, before the system could fully equilibrate, novel behaviors may occur. The confluence of new experiments and theoretical frameworks has prompt synergistic developments. For example, the nonequilibrium phase transitions have also been intensively researched under controlled settings using the trapped cold atoms as the quantum material simulators [37–42].

In this article, we will attempt to establish a unified framework to treat ultrafast scattering from the nonequilibrium states of quantum materials. In this case, the system we refer to is the broken-symmetry order expressed in the lattice field with distinct order parameter that can be measured by the scattering approach. The pump–probe platform offers new opportunities for studying nonequilibrium physics. In the nonequilibrium physics context, the ultrafast light excitation couples to the system through a perturbation that changes the system parameters. More specifically, we ask how a quantum material containing long-range broken-symmetry states may effectively switch under an ultrafast "quench" [13, 43] enforced by laser pulse in routes distinctively different from a thermal state [44, 45]. In this central aspect, excited quantum material transformation is akin to the femtochemistry problem [46] where the ultrafast electronic excitation sets the new bonding landscape before the heavier molecular nuclear dynamics can follow. Given the separation of the timescale, the impulsive unveiling of the new potential energy landscape sets forth the ensuing molecule conformational dynamics where the dynamics of electrons follow those of the nuclei adiabatically. This scenario is referred to as the impulse-adiabatic approximation. Meanwhile, the inability for a many-body system to instantaneously thermalize offers intriguing aspect of controlling quantum material phase transition out of equilibrium.

Scattering from a nonequilibrium system contains information on both the microscopic dynamics and macroscopic state evolution, and properly extracting such information in a controlled nonequilibrium quantum material will offer valuable insight on the symmetry-breaking properties and the nonequilibrium effects. Three prototypical quantum material systems: rare-earth tritellurides, tantalum disulfides, and vanadium dioxide will be discussed under this framework. We also examine the pump and material settings required for the controlled experiments. Facing the challenging issues with the multiscale dynamics, the technological aspects of the multi-messenger approaches based on a unified framework of ultrafast electron microscopy system will also be discussed. Our goals here are twofold. One is to understand the still mysterious hidden phase phenomena in nonequilibrium quantum materials. The second is to explore the ideas of using the light-excited quantum material as a platform to study the nonequilibrium physics.

2. Description of non-equilibrium phase transition

Quantum phases are macroscopic states that exist at a finite temperature with quantum mechanism in origin but often behave semi-classically [2, 4]. They often emerge by breaking the existing symmetry of the underpinning Hamiltonian defining the microscopic states [8]. In doing so, they distinguish themselves from the microstate evolution, and the collective state properties typically are described by a very small number of long-scale order parameters, in which the microscopic dynamics are coarse-grained [9]. Ultrafast pump–probe approaches utilize the temporal resolution and pump control to explore hidden or transient metastable phases as a means to unveil the underpinning complex landscape of macroscopic quantum phases and to study the nonequilibrium physics.

Based on defining a local order parameter, the Landau–Ginzburg mean-field theory successfully captures a system undergoing a phase transition in which some symmetry is broken [6, 7]. The scattering techniques, which can provide direct evidence of the symmetry change and the properties of the order parameters, have been instrumental for the success of developing Landau–Ginzburg theory for quantum materials [6, 47–49]. The main focus of this article is to examine how nonequilibrium quantum materials involving multiple broken-symmetry ground states evolve upon applying laser quench. The process typically involves nonequilibrium state of the order parameters. Ultrafast electron scattering is used as a sensitive probe to characterize the dynamical order parameter fields.

For the experimental examples discussed in this paper, the macroscopic systems we refer to are the broken-symmetry orders expressed in the lattice field with distinct order parameter. In these cases, the phase evolution is characterized by the long-wave responses on much greater length scale than the periodicity of the mean atomic positions. The scale difference allows different physical principles governing the order parameters and the microscopic dynamics to be separated. For example, macrostate evolution is decoupled dynamically from the local vibrational excitations around the mean positions. Therefore, it is natural for the impulse-adiabatic description of the femtochemistry problems to apply to the nonequilibrium phase transition of quantum materials under the ultrafast quench—a paradigmatic scenario has been given for the photoinduced phase transition (PIPT) problems concerning the strongly correlated molecular solids; see the review [25]. Here, the Landau–Ginzburg free-energy equation serves to describe the long-scale property, i.e., a general functional of the coarse-grained order parameter, which is registered in coherent scattering structural factor; whereas the microscopic processes are encoded in the diffuse and inelastic scattering.

For illustrating the correspondence between the order-parameter field and the scattering functions, we start with the case of a singular order parameter $\eta = |\eta|e^{i\theta}$ associated with a

continuous phase transition. Typically, only the amplitude and its gradient will change the free-energy density, written as:

$$f = \frac{1}{2}a(T - T_c)|\eta|^2 + \frac{1}{4}A_4|\eta|^4 + \frac{1}{2}\alpha_{ij}\frac{\partial\eta}{\partial x_i}\frac{\partial\eta}{\partial x_j}. \tag{1}$$

For a uniform order parameter, the potential surface described by the first two terms on the righthand side (RHS) has the stationary points that give the coordinate for the broken-symmetry state ($|\eta| > 0$). For the broken-symmetry state typically residing at low temperature, a and A_4 are positive. With the phase rigidity tensor $\alpha_{ij} > 0$, the third term raises the free energy for a system being inhomogeneous. This simple mean-field depiction captures the universal laws governing the system when it approaches the critical point, with the temperature difference $|T_c - T|$ as the control parameter. For $T < T_c$, $f_{\eta\eta} = 2a(T - T_c)$, i.e., approaching the broken-symmetry state from above the free energy changes from a parabolic uphill to a double well potential. The nonanalyticity at T_c and the ensuing BCS-type onset of the order parameter are given by following the stationary point as a function of temperature:

$$|\eta(T)| = \sqrt{\frac{a}{A_4}}(T_c - T)^{1/2}. \tag{2}$$

The Landau–Ginzburg equation also gives the right description for the pre-transitional instabilities probed by the diffuse scattering, which provides additional information about the phase rigidity. To see this, we express the long-range parameter variations with the fluctuation waves components:

$$\delta\eta(r) = \sum_{\mathbf{k}} \eta_{\mathbf{k}} e^{i\mathbf{k}\cdot\mathbf{r}}, \tag{3}$$

where $\eta_{\mathbf{k}}$ and $\mathbf{k}$ represent the amplitude and the momentum wavevector. The least work required to produce the variation $\delta\eta$ according to (1) is

$$\delta\eta(\mathbf{r}) = \frac{1}{2}f_{\eta\eta}(\delta\eta)^2 + \frac{1}{2}\alpha_{ij}\frac{\partial f}{\partial x_i}\frac{\partial f}{\partial x_j}. \tag{4}$$

We can calculate the mean-square Fourier component of the fluctuation wave at momentum $\mathbf{k}$:

$$\langle\eta_{\mathbf{k}}\eta^*_{\mathbf{k}}\rangle = \frac{k_B T}{V}\left(\frac{1}{f_{\eta\eta} + \alpha_{ij}k_i k_j}\right). \tag{5}$$

Equation (5) gives the Lorentzian line shape of the anomalous spectrum of diffuse scattering near T_c. From (1) and (2), we establish for $T > T_c$, $f_{\eta\eta} = a(T - T_c)$. Rearranging (5), we obtain $\langle\eta_{\mathbf{k}}\eta^*_{\mathbf{k}}\rangle = (k_B T/V)(1/\alpha_{\parallel}k_{\parallel}^2 + \alpha_{\perp}k_{\perp}^2 + a(T - T_c))$ for $T > T_c$, with the Lorentz line width $\Delta k_{\parallel,\perp} = (a(T - T_c)/\alpha_{\parallel,\perp})^{1/2}$.

Thus far, only the statics of the Landau–Ginzburg equation is discussed. For considering the nonequilibrium phase transition, connections to the microscopic physics must be made. To give a microscopic picture, we consider a single-wavevector charge-density wave (CDW) system [50]. Here, the specific ordering formation is by breaking the translational symmetry over a specific wave-vector $\mathbf{Q}$, typically driven by the electronic instabilities at the relevant length scale ($2\pi/\mathbf{Q}$) coupled to the lattice field [51]. In this case, the order parameter has the amplitude and phase components and can be written as $\eta = |\eta|e^{i(\mathbf{Q}\cdot\mathbf{r}+\phi)}$ with $|\eta|$ and ϕ representing the amplitude and phase fields. The order parameter fields can be probed via their connection to the distorted lattice, or lattice periodic distortion wave (LDW). At each lattice site $\mathbf{L}$, the distorted amplitude is described by

$$\mathbf{u}_{\mathbf{L}}(r) = u_0\hat{e}\sin(\mathbf{Q}\cdot\mathbf{L} + \phi), \tag{6}$$

where $\hat{e}$ and u_0 represent the polarization vector and amplitude. The order parameter and LDW are related by $u_0 = |\eta|A_{\eta u}$ with $A_{\eta u}$ a constant that can be probed under the steady state prior to applying quench, where the order parameter $|\eta|$ is typically set to be 1 by convenience.

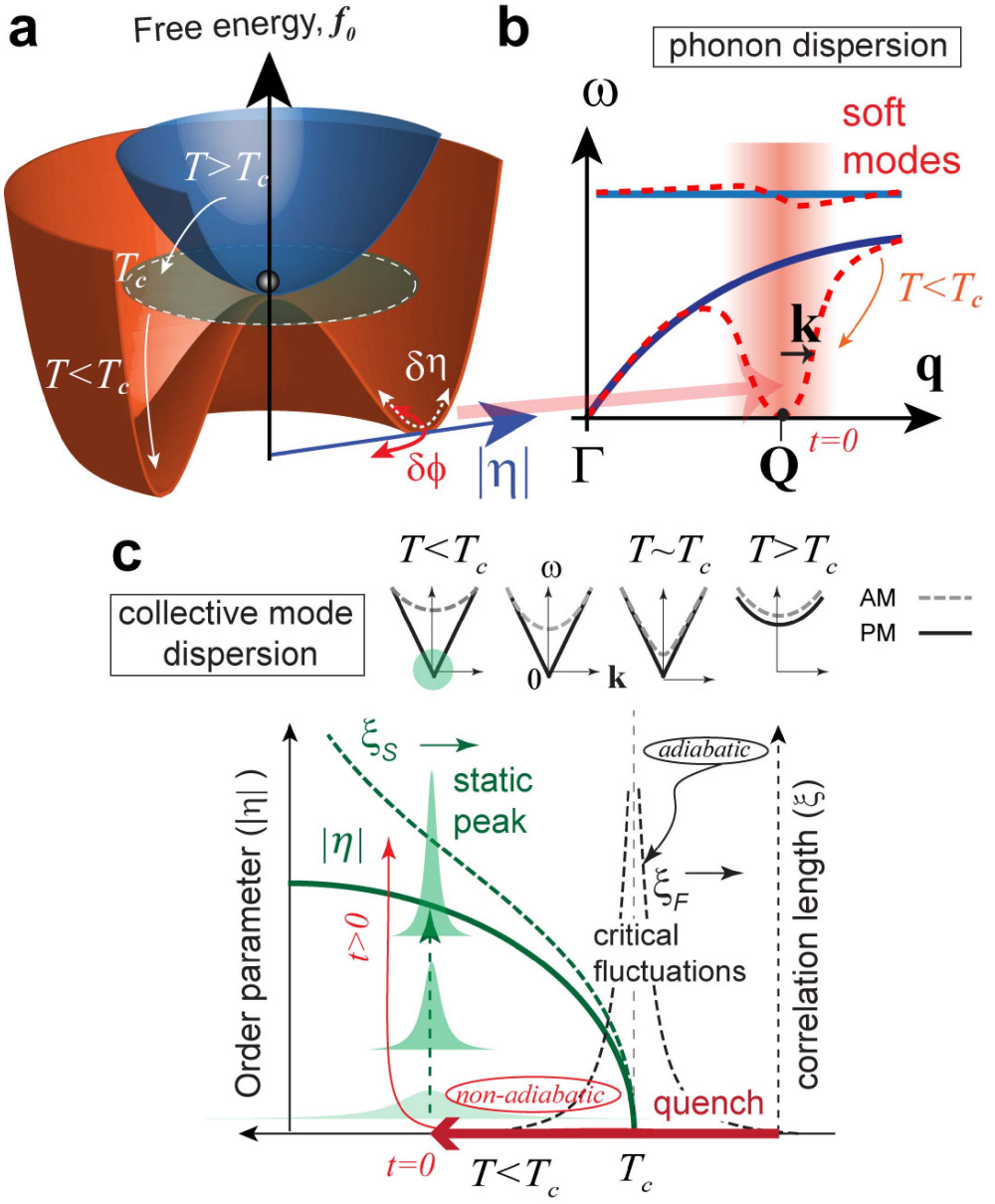

Figure 1. Landau–Ginzburg free-energy surface for spontaneous symmetry breaking and the order parameter dynamics. (a) The 2D free-energy landscape that defines the order parameter field at different temperatures. The arrow directions show temperature quench. The field fluctuations are depicted in the change of the amplitude ($\delta\eta$) and the phase ($\delta\phi$). (b) The corresponding lattice phonon dispersion curves that couple to the landscape modification. The lattice softening, driven by the temperature quench, occurs at momentum wavevector **Q** of the long-range state. (c) The phase ordering kinetics orchestrated by the fluctuation fields. The near-equilibrium scenario is depicted in black curves. The nonequilibrium one, depicted in green, is driven by a deep quench, where $T \ll T_c$. The dispersion curves for the amplitude (AM) and phase mode (PM) of the CDW state are depicted at the top. Adapted with permission from Ref. [23].

We first give a hypothetical scenario of a swift system-wide temperature quench to below T_c to drive spontaneous phase ordering. For a complex order parameter, this process is now described on a two-dimensional (2D) landscape of the order parameter fields (amplitude and phase); see Figure 1a. Driving the order parameter evolution is the free-energy potential which unfolds from the uphill into the Mexican-hat shape of the broken-symmetry phase. After choosing a phase, the amplitude ($|\eta|$) dynamics is deterministic as a ball falling from the top of the hill to a location in the trough, i.e. a spontaneous symmetry breaking (SSB). However, nonequilibrium scenarios appear with the underlying separation of scales in the physical CDW system. This can be understood by mapping the unfolding energy landscape involving the long-wave state evolution to the corresponding changes in the lattice field. The relevant lattice dynamics are governed by the momentum-dependent lattice potential expressed in the phonon dispersion curves (Figure 1b), which shift from those of the normal ($T > T_c$; solid lines) state to the broken-symmetry phase ($T < T_c$; dashed lines) with a mode softening at phonon momentum wavevector $\mathbf{q} \sim \mathbf{Q}$ which may be probed via the inelastic and diffuse scattering spectrum [52–59]. As the lattice potential changes leveled at the electronic scale is assumed to be nearly instantaneous, the soft modes in the critical regime (colored in red where the dispersion curves drop in frequency, ω) cannot respond adiabatically. This inherent nonadiabicity between the potential energy shift and the long-wave soft collective mode response is prominent for any photoinduced phase transition driven by a quench [23].

Two types of collective modes are involved in the phase change dynamics [50, 60]. One is the amplitude modes (AM), represented by the amplitude fluctuation $\delta|\eta|$ as depicted in Figure 1a. The AM would be generally gapped within the broken-symmetry ground state as it costs energy to increase or decrease the amplitude $|\eta|$. Meanwhile, the incommensurate CDW state also hosts the ungapped phase mode (PM) [50], as also depicted in Figure 1a where the level of the free energy surface does not change over phase variation, $\delta\phi$; in this case PM is referred to as the Goldstone mode [50, 61–63]. In Figure 1c, we depict the dispersion curves for the AM and PM modes as a function of the temperature. It is easy to see that the AM would be always gapped with the exception at the critical point, whereas the PM becomes ungapped after establishing the new broken symmetry phase. These soft modes are dynamically connected with the field instabilities only at the bottom of the free energy. The asymptotic slope of the dispersion curve determines the "sound speed" of the fluctuation wave.

In the ultrafast scattering experiments, the order parameter is mapped into the LDW amplitude and probed via the time-dependent two-point equal-time correlation function:

$$S_\eta(\mathbf{r}-\mathbf{r}';t) \sim \langle u(\mathbf{r};t)u(\mathbf{r}';t)\rangle, \tag{7}$$

where the bracket denotes the spatial and ensemble averaging over the probed volume and the acquisition time window. The Fourier transformation of the (7) gives the structure factor $S_\eta(\mathbf{q};t)$ which results in satellites for the ordered states in the reciprocal space. As will be discussed in Section 4, Equation (5) gives the diffuse scattering component of $S_\eta(\mathbf{q};t)$. Hence, we can extract the ξ_F, the correlation length for the critical fluctuations, from the line shape of the diffuse scattering, i.e. $\xi_F = 1/\Delta k_{\parallel,\perp}$, and deduce the rigidity based on the T-dependence:

$$\frac{\alpha_{\parallel,\perp}}{a} = (T - T_c)\xi_F^2. \tag{8}$$

It is instructive to point out that the bandwidth of the phonon softening probed by inelastic scattering is typically much larger than the anomalous linewidth of the diffuse scattering. This is because only those stochastic soft-phonon modes near the CDW **Q** vector will eventually condense into the static CDW order. The order parameter field fluctuations may be described over the Mexican hat energy surface.

These long-wave and low-energy excitations are considered as the hydrodynamic modes [61] or fluctuation waves [49], with wavelength $\lambda = 2\pi/|\mathbf{k}|$, where typically the momentum wavevector $|\mathbf{k}| \ll |\mathbf{Q}|$, the wave vector of the CDW/LDW. Such field fluctuations must be created by joining two soft phonon modes from the lattice field. It has been shown by Overhauser [50, 62] that to form a collective mode with momentum $\mathbf{k}$, either AM or PM, two soft phonons with momentum $\mathbf{q} = \mathbf{k} \pm \mathbf{Q}$, must be coherently jointed [50]; conversely, upon quenching the order parameters, the excited collective mode decays by dissociating into a pair of phonons. The dissociation process would be most relevant in discussing the overdamped dynamics following the impulsive suppression of a pre-existing CDW order.

Now we concern how the order parameter of the nonequilibrium state will manifest physically. We expect in potential-driven dynamics the system will be attracted to a minimum energy basin. The simplest nonequilibrium dynamical model is relaxational for a non-conserved order parameter $\eta(\mathbf{r}; t)$, such as the CDW system and with a stochastic contribution, often referred to as time-dependent Ginzburg–Landau equation [9, 27, 64]:

$$\frac{\partial \eta}{\partial t} = -\Gamma \frac{\delta f}{\delta \eta} + \varsigma = -\Gamma \left[\frac{\delta f_0}{\delta \eta} - \alpha \nabla^2 \eta \right] + \varsigma(\mathbf{r}, t). \tag{9}$$

Here f_0 is the effective potential energy (excluding the gradient term), Γ is a relaxation constant and $\varsigma(\mathbf{r}, t)$ is the noise source. One can often take the noise as random and for a Gaussian white noise $\langle \varsigma(\mathbf{r}, t) \rangle = 0$ and the noise correlator $\langle \varsigma(\mathbf{r}, t) \varsigma(\mathbf{r}', t') \rangle = 2T\Gamma\delta(\mathbf{r} - \mathbf{r}')\delta(t - t')$ [9, 27].

We can now connect this expression to the phenomenological description of SSB. Under a deep quench with the eventual $T \ll T_c$, a large shift of the local curvature of the potential is induced as depicted in Figure 1a. In the initial amplitude dynamics, the first term on the RHS is most important. However, the phase space of the order parameter is broadened by its coupling to the stochastic background (the 3rd term), but only in the soft phonon mode regions due to the scale matching. The nonlinear coupling to phonons leads to a rectification allowing the amplitude mode to build up as the system move from the hill to the low-energy basin. When reaching the bottom of the basin where $\delta f_0/\delta\eta \sim 0$, the second term will now become more important. This means the nonequilibrium system will undergo pattern formation, driven by the positive rigidity favoring long-range ordering. The (9) can be simplified to [1]

$$\frac{\partial \eta}{\partial t} = \mathrm{D}\nabla^2 \eta + \varsigma, \tag{10}$$

where $D = \Gamma\alpha$ is the diffusion constant [27] and defines a characteristic timescale $t_D \sim \xi_S^2/D$ for the coarsening where ξ_s is the size of the coherent domain created. It is easy to see that in this case the relaxational dynamics for the coarsening follows a universal scaling law [65, 66]. The size of the domain increases at velocity $\sim \partial\xi_s(t)/\partial t = 2\mathrm{D}/\xi_s(t)$. This implies that the characteristic length scale $\xi_s(t) = \sqrt{2\mathrm{D}t}$ grows as $t^{1/2}$ [65].

In the following, we will go beyond the hypothetic scenario of temperature quench. The temperature quench is inherently impractical to implement as such a process is physically slow and is prone to generate inhomogeneous phase ordering due to the presence of interfaces for cooling the system from outside. The more effective approach to implement the physical quench is instead via driving the system interaction parameters rather than changing the temperature of the system [43]. This will require additional order parameter(s) to couple with the present one—a scenario of cooperativity or competitions described in a multi-parameter free-energy equation, which is in fact a characteristic feature of quantum material phase transitions [31, 32, 67, 68]. As

[1] Private communication with M. Maghrebi.

will be discussed in the experimental studies, rich scenarios as those involve competitive broken-symmetry orders, vestigial orders, and the intertwined ground states could be identified, leading to intriguing nonequilibrium states and hidden phases; see Section 6.

3. Light-induced hidden phases through competitions

While one expects that there should always be a corresponding critical threshold directly linked to a thermal phase transition according to (2), there have been many reports that the experimentally identified thresholds are significantly less than the thermodynamic requirements. In many cases, an additional low energy threshold is linked to the appearance of a light-induced hidden state without entirely melting the pre-existing ordered phase. Indeed, the threshold behavior with a sub-thermal activation energy density has been the hallmarks of PIPT phenomena [25].

We now consider a multi-component free-energy surface in which the order parameters are coupled to account for phase transitions where different broken-symmetry orders coexist or compete in quantum materials. In particular, in strongly correlated electron systems, the competing orbital, spin, and lattice interactions yield a multiplicity of nearly degenerate broken-symmetry phases and complex phase diagrams [2,11,69,70]. For example, within the high-critical temperature superconductors, such as iron-based and cuprates, superconductivity is often found to compete with a density-wave order. A prototypical case concerning the competitive SSB within the density-wave systems is recently discussed and observed in the rare-earth telluride compounds [22,23].

A generic Landau–Ginzburg expression that applies to the broad range of physical phenomena concerning competitions is [31,71,72]

$$f_0(\eta_1,\eta_2,\ldots)=\frac{1}{2}\sum_i a_i(T^{(i)}-T_{c,i})|\eta_i|^2+\frac{1}{4}\sum_i A_{4,i}|\eta_i|^4+\frac{1}{2}\sum_{ij}\tilde{A}_{ij}|\eta_i|^2|\eta_j|^2, \tag{11}$$

where the first two terms represent the free energy from the individual phase that will undergo SSB at the respective critical temperature $T_{c,i}$. The third term gives the coupling energy where a competitive scenario has $\tilde{A}_{ij}>0$. One can apply this multi-component potential energy surface to (9) to determine the order parameter dynamics. Of concern here is the nonequilibrium phase competitions driven predominantly by the laser interaction quench. Generally, the stochastic effects propagating to the long-range degree of freedom are slow to manifest. The microscopic physics depends on "local" momentum-dependent coupling between the excited hot carriers and the lattice modes, to establish the initial bath that is expected to be inhomogeneous in effective temperatures. Nonetheless, we expect the post-quench immediate response to be potential-driven. We first discuss here the truly competitive SSB scenario, applying to the rare-earth tritelluride system [23,72], in which T_c is shared among the two order parameters η_1 and η_2.

While much of the ordering dynamics involving complex order parameters will depend on the microscopic details of the experimental settings, here we focus on the phenomenology of amplitude dynamics, i.e. $|\eta_1|$ and $|\eta_2|$. The competition here precludes the thermal phase of $|\eta_2|$ from appearing below T_c if $|\eta_1|$ is selected by SSB. This is described in Figure 2, where f_0 is expressed in two dimensions along $|\eta_1|$ and $|\eta_2|$. For a model simulation the parameters here are chosen for $|\eta_1|=1$ to be the sole minimum at an initial temperature T_1 (black curve), before applying laser quench. Within the reversible thermodynamic pathway, i.e. via adiabatically tuning the temperature that is homogeneous system-wide, the $|\eta_1|$ remains the dominate phase as represented by the sole minimum basin in the global energy surface. This can be seen by taking the derivative over $|\eta_1|$, which we assume to be the thermodynamically preferred state at the low temperature. We then obtain $|\eta_1|=\sqrt{(a_1(T_c-T)-\tilde{A}|\eta_2|^2)/A_{4,1}}$, i.e. $|\eta_1|$ naturally takes a non-zero value when $|\eta_2|=0$ at $T<T_c$. This thermal route is depicted in blue on the right side of

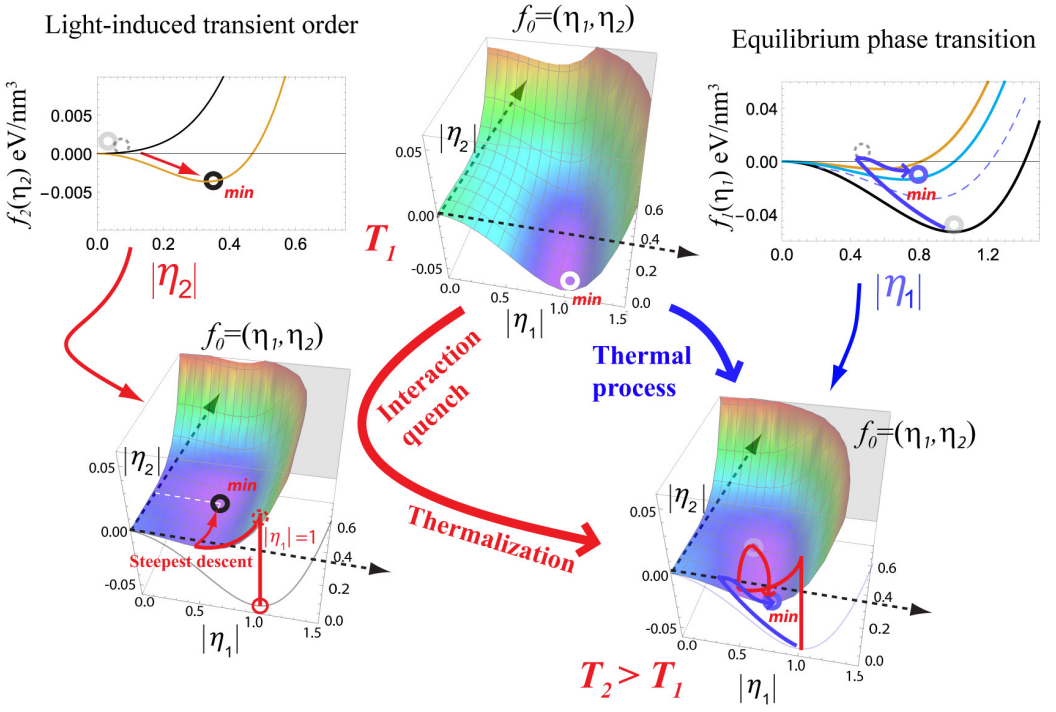

Figure 2. Light-induced changes of the Landau–Ginzburg free-energy landscape involving two order parameters η_1 and η_2. The non-equilibrium pathway (depicted in the left route) involves the formation of a bi-directional hidden state with order parameter η_2 when the repulsive coupling potential is suppressed by a swift reduction of the preeminent order parameter η_1. In contrast, in the thermal pathway (right) the global free energy minimum remains in the condition where $|\eta_2| = 0$, namely the CDW is uniaxial. Adapted with permission from Ref. [23].

Figure 2. In the model calculation, $|\eta_1|$ reaches a new minimum at 0.6 (brown curve) due to heating. Conversely, a stable new static broken-symmetry order (i.e., $\langle\eta_2\rangle > 0$) could appear at $T < T_c$ if $a_2(T - T_c) + \tilde{A}|\eta_1|^2$ becomes negative. To achieve this naturally, one needs to supply an amplitude quench of the initial order to a level beyond:

$$|\eta_{\text{th}}| = \sqrt{\frac{a_2(T_c - T)}{\tilde{A}}}, \tag{12}$$

namely a threshold behavior emerges. However, by requiring $|\eta_1|$ to be dominant, i.e. $a_1/A_{4,1} > a_2/\tilde{A}$, one can see this is prohibited if the quenched system were to maintain the thermal equilibrium condition. Therefore, the light-induced hidden state scenario shall occur in a nonequilibrium process in which one can suppress $|\eta_1|$ transiently through an interaction quench that initially couples only to a subset of lattice modes.

This scenario is described on the left side of Figure 2. A nonthermal quench of $|\eta_1|$ to ~0.5 leads to a minimum in the subspace of the free energy for $|\eta_2|$ at ~0.36 (see the black circle). Here, we assume the field of the new order parameter, being decoupled from the high-temperature bath created by quench, has a temperature of the ambient. Meanwhile, the order parameter field of the present order, being driven directly by the quench, has a higher local temperature, i.e., $T^{(2)} \ll T^{(1)}$ in the initial period. Following this, it is possible for the new order parameter

to undergo a threshold onset at a critical laser fluence F_c, which is much smaller than what is required to completely melt the existing order [19, 23]. However, if the system were to regain thermal equilibrium, i.e. $T^{(2)} \sim T^{(1)}$, then one can show the free energy again has the global minimum over a non-zero $|\eta_1|$, i.e. the hidden state is removed from the order parameter field when the system thermalizes.

4. Mapping the dynamical order parameter with ultrafast scattering

Optical excitations can result in a departure from the thermal responses making the modeling of the scattering factor, Debye–Waller effects, and the diffuse signatures quite different from the conventional approaches for the equilibrium states. In this section, we focus on understanding the different lattice responses to the nonequilibrium excitation that go into the structure factor function. The analyses here are based on momentum-resolved structure factor $S(\mathbf{q}, t)$ or their momentum integration $m(\mathbf{Q}, t)$, which can be directly compared with the ultrafast electron scattering experiments. The goals are to derive directly from the experimental measurements the nonequilibrium systems, including the evolution of the static order parameters and the associated order-parameter field fluctuations of the quantum phases. However, in a nonequilibrium phase transition, such as SSB driven by a quench, these long-range parameters are rooted in the microscopic excitations. While there has been extended literature dedicated to the scattering by the phonon processes [73, 74] and by the long-ranged broken-symmetry state with periodic lattice distortions [50, 52, 75], the discussions were often partial to one aspect only and aimed at the near-equilibrium processes. The goal here is to lay out the scattering formalism to treat the two as well as the quasi-static order parameter evolution in a self-contained framework.

The nonequilibrium phases created by the impulsive excitation involve two types of lattice dynamical effects: the incoherent microscopic responses of the lattice, i.e. the phonons, and the long-range parameter fluctuation waves of the cooperative states. To be more specific, we refer to these two types of excited lattice wave manifolds as $\{\mathbf{q}\}$ and $\{\mathbf{k}\}$ based on their respective momentum wavevectors. The signatures from the soft modes that belong in $\{\mathbf{q}\}$ and the those of the collective modes that belong in $\{\mathbf{k}\}$ can be differentiated experimentally. In the spectroscopy experiments, because of the momentum conservation, the probe photon does not directly couple to the soft mode at a finite momentum $\mathbf{q}$. However, it can couple to the collective modes at the long-wavelength limit: $\mathbf{k} = \mathbf{q} - \mathbf{Q} \to 0$. In contrast, in the scattering experiments, one detects both effects at different parts of the momentum space. We shall attempt to capture these two types of lattice excitations in the scattering formalism. In ultrafast scattering, one probes the time-dependent structural factor around the reciprocal lattice $\mathbf{G}_{hkl}$ at the momentum transfer wavevector, $\mathbf{s} = \mathbf{q} + \mathbf{G}_{hkl}$:

$$S(\mathbf{s}, t) = \int \mathrm{e}^{-\mathrm{i}\mathbf{s}\cdot(\mathbf{r}-\mathbf{r}')} \langle \rho(\mathbf{r}, t)\rho(\mathbf{r}', t)\rangle \, \mathrm{d}\mathbf{r}\, \mathrm{d}\mathbf{r}', \tag{13}$$

which is the Fourier counterpart of the correlation function $\langle \rho(\mathbf{r}, t)\rho(\mathbf{r}', t)\rangle\langle\cdots\rangle$ denoting spatial and ensemble-averaging of the probed volume set by the experimental conditions. One can show for a sufficiently long-ranged order parameter on a periodic lattice $\mathbf{L} = n_1\mathbf{a}_1 + n_2\mathbf{a}_2 + n_3\mathbf{a}_3$ with n_1, n_2, n_3 being integers $(0, \pm1, \pm2\ldots)$, the integral is simplified into

$$S(\mathbf{s}, t) = \langle F(\mathbf{s}, t) F^*(\mathbf{s}, t)\rangle,$$

where $F(\mathbf{s}, t) = \int \sum_{\mathbf{L}} f_{\mathbf{L}} \delta(\mathbf{r} - \mathbf{L} - \mathbf{u}_L(t)) \mathrm{e}^{-\mathrm{i}\mathbf{s}\cdot\mathbf{r}} \, \mathrm{d}\mathbf{r} = \sum_{\mathbf{L}} f_{\mathbf{L}} \mathrm{e}^{-\mathrm{i}\mathbf{s}\cdot(\mathbf{L}+\mathbf{u}_L(t))}$ is the Fourier spectrum of the lattice. The term $f_{\mathbf{L}}$ equal to $\sum_i \rho_i \mathrm{e}^{-\mathrm{i}\mathbf{s}\cdot\boldsymbol{\varrho}_i}$ represents the unit cell scattering form factor where $\boldsymbol{\varrho}_i$ is the mean unmodified relative position of the atom in the unit cell. Here, $\mathbf{u}_{\mathbf{L}}(t)$ is the displacement from the mean position at each lattice site, which may originate either from the long-range parameter or fluctuations due to phonons or collective modes.

More specifically here, we consider a single long-range parameter η present in the system, e.g. introduced by a charge-density or orbital order (6). We write down the general form of $\mathbf{u}_{\mathbf{L}}$ considering phonons $\mathbf{u}_q(\mathbf{r},t) = \sum_{\mathbf{q}} u_{\mathbf{q},0}\hat{e}_{\mathbf{q}}\sin(\mathbf{q}\cdot\mathbf{r}-\omega_{\mathbf{q}}t+\phi_{\mathbf{q}})$ and the contributions from the LDW $\mathbf{u}_\eta(\mathbf{r}) = u_{0,\eta}\hat{e}_\eta\sin[\mathbf{Q}\cdot\mathbf{r}+\phi_\eta]$, with $u_{i,0}$, $\hat{e}_i$ and ϕ_i denoting the respective amplitude, polarization directional vector and phase. For describing the fluctuations of the order parameter, we include in $\mathbf{u}_\eta$ the associated collective excitations in terms of the phase and amplitude fluctuations in $\delta\phi(r,t) = \sum_{\mathbf{k}}\phi_{0,\mathbf{k}}\sin(\mathbf{k}\cdot\mathbf{r}-\omega_{\mathbf{k}}t)$ and $\delta\hat{A}(\mathbf{r},t) = \sum_{\mathbf{k}'}\hat{A}_{0,\mathbf{k}'}\sin(\mathbf{k}'\cdot\mathbf{r}-\omega_{\mathbf{k}'}t)$. We then have $\mathbf{u}_{\mathbf{q}}(\mathbf{r},t) = \sum_{\mathbf{q}} u_{\mathbf{q},0}\hat{e}_{\mathbf{q}}\sin(\mathbf{q}\cdot\mathbf{r}-\omega_{\mathbf{q}}t+\phi_{\mathbf{q}})$ for the phonons, and $\mathbf{u}_\eta(\mathbf{r},t) = \mathbf{u}_{0,\eta}\hat{e}_\eta(1+\delta\hat{A}(\mathbf{r},t))\sin[\mathbf{Q}\cdot\mathbf{r}+\delta\phi(\mathbf{r},t)]$ for the displacement associated with long-range parameter. Following this, the overall displacement at each lattice site is

$$\mathbf{u}_{\mathbf{L}}(t) = \sum_{\mathbf{q}}\mathbf{u}_{\mathbf{q}}(\mathbf{L},t) + u_{0,\eta}\hat{e}_\eta(1+\delta\hat{A}(\mathbf{L},t))\sin[\mathbf{Q}\cdot\mathbf{L}+\delta\phi(\mathbf{L},t)]. \tag{14}$$

Equation (14) has all key ingredients to describe the dynamics of the excited states with soft modes and collective modes in a broken-symmetry state. To simplify the derivation without losing generality, we first drop the amplitude fluctuations $\delta\hat{A}$ and expand the equation based on the momentum-dependent displacement $\mathbf{u} = \mathbf{u}_{\mathbf{q}} + \mathbf{u}_{\mathbf{k}}$, with the order-parameter fluctuations dominated by the phase modes [50]. In this case, the distribution function is written as:

$$\rho(\mathbf{r},t) = \sum_{\mathbf{L}}\delta\left\{\mathbf{r}-\mathbf{L}-\sum_{\mathbf{q}}u_{\mathbf{q}}\hat{e}_{\mathbf{q}}(\mathbf{L},t) - u_\eta\hat{e}_\eta\sin(\mathbf{Q}\cdot\mathbf{L}+\sum_{\mathbf{k}}\phi_{\mathbf{k}}\sin(\mathbf{k}\cdot\mathbf{L}-\omega_{\mathbf{k}}t))\right\}. \tag{15}$$

The system form factor is given:

$$\begin{aligned} F(\mathbf{s},t) &= \int\rho(\mathbf{r},t)\mathrm{e}^{-\mathrm{i}\mathbf{s}\cdot\mathbf{r}}\,\mathrm{d}\mathbf{r} \\ &= \sum_{\mathbf{L}} f_{\mathbf{L}}\mathrm{e}^{-\mathrm{i}\mathbf{s}\cdot(\mathbf{L}+\sum_{\mathbf{q}}u_q\hat{e}_{\mathbf{q}}(\mathbf{L})+u_\eta\hat{e}_\eta\sin(\mathbf{Q}\cdot\mathbf{L}+\sum_{\mathbf{k}}\phi_{\mathbf{k}}\sin(\mathbf{k}\cdot\mathbf{L}-\omega_{\mathbf{k}}t)))} \\ &= \sum_{\mathbf{L}} f_{\mathbf{L}}\mathrm{e}^{-\mathrm{i}\mathbf{s}\cdot\mathbf{L}}\left\{\mathrm{e}^{-\mathrm{i}\mathbf{s}\cdot(\sum_{\mathbf{q}}u_{\mathbf{q}}\hat{e}_{\mathbf{q}}(\mathbf{L}))}\right\}\{\mathrm{e}^{-\mathrm{i}\mathbf{s}\cdot u_\eta\hat{e}_\eta\sin(\mathbf{Q}\cdot\mathbf{L}+\sum_{\mathbf{k}}\phi_{\mathbf{k}}\sin(\mathbf{k}\cdot\mathbf{L}-\omega_{\mathbf{k}}t))}\}. \end{aligned} \tag{16}$$

The first bracket on RHS is simply the scattering by lattice phonons. We have

$$\mathrm{e}^{-\mathrm{i}\mathbf{s}\cdot(\sum_{\mathbf{q}}u_{\mathbf{q}}\hat{e}_{\mathbf{q}}(\mathbf{L}))} = \prod_{\mathbf{q}}\mathrm{e}^{-\mathrm{i}\mathbf{s}\cdot\mathbf{u}_{\mathbf{q},0}\sin(\mathbf{q}\cdot\mathbf{L}-\omega_{\mathbf{q}}t)}.$$

Using the Jacobi–Anger generating function:

$$\mathrm{e}^{-\mathrm{i}z\sin\phi} = \sum_{n=0}^{\infty}\mathrm{e}^{-\mathrm{i}n\phi}J_n(z), \tag{17}$$

we have

$$\mathrm{e}^{-\mathrm{i}\mathbf{s}\cdot(\sum_{\mathbf{q}}\mathbf{u}_{\mathbf{q}}\hat{e}_{\mathbf{q}}(\mathbf{L}))} = \prod_{\mathbf{q}}\sum_{l}\mathrm{e}^{-\mathrm{i}l(\mathbf{q}\cdot\mathbf{L}-\omega_{\mathbf{q}}t)}J_l(\mathbf{s}\cdot\mathbf{u}_{\mathbf{q},0}).$$

The second bracket on RHS gives the scattering from the order parameter static wave with phase fluctuations. By twice applying the Jacobi–Anger generating function, we can derive

$$\begin{aligned} \mathrm{e}^{-\mathrm{i}\mathbf{s}\cdot u_{\eta,0}\hat{e}_\eta\sin(\mathbf{Q}\cdot\mathbf{L}+\sum_{\mathbf{k}}\phi_{\mathbf{k}}\sin(\mathbf{k}\cdot\mathbf{L}-\omega_{\mathbf{k}}t))} &= \left\{\sum_m\mathrm{e}^{-\mathrm{i}m\mathbf{Q}\cdot\mathbf{L}}J_m(\mathbf{s}\cdot\mathbf{u}_{\eta,0})\right\}\mathrm{e}^{-\mathrm{i}\sum_{\mathbf{k}}m\phi_{\mathbf{k}}\sin(\mathbf{k}\cdot\mathbf{L}-\omega_{\mathbf{k}}t)} \\ &= \left\{\sum_m\mathrm{e}^{-\mathrm{i}m\mathbf{Q}\cdot\mathbf{L}}J_m(\mathbf{s}\cdot\mathbf{u}_{\eta,0})\right\}\left\{\prod_{\mathbf{k}}\sum_n\mathrm{e}^{-\mathrm{i}n(\mathbf{k}\cdot\mathbf{L}-\omega_{\mathbf{k}}t)}J_n(m\phi_{\mathbf{k}})\right\} \\ &= \prod_{\mathbf{k}}\sum_{m,n}\mathrm{e}^{-\mathrm{i}(m\mathbf{Q}+n\mathbf{k})\cdot\mathbf{L}}\mathrm{e}^{\mathrm{i}n\omega_{\mathbf{k}}t}J_m(\mathbf{s}\cdot\mathbf{u}_{\eta,0})J_n(m\phi_{\mathbf{k}}). \end{aligned}$$

Putting together, we obtain

$$F(\mathbf{s},t) = \sum_{\mathbf{L}} f_{\mathbf{L}}\left\{\prod_{\mathbf{q}}\sum_l\mathrm{e}^{-\mathrm{i}(\mathbf{s}+l\mathbf{q})\cdot\mathbf{L}}\mathrm{e}^{\mathrm{i}l\omega_q t}J_l(\mathbf{s}\cdot\mathbf{u}_{\mathbf{q},0})\prod_{\mathbf{k}}\sum_{m,n}\mathrm{e}^{-\mathrm{i}(m\mathbf{Q}+n\mathbf{k})\cdot\mathbf{L}}\mathrm{e}^{\mathrm{i}n\omega_{\mathbf{k}}t}J_m(\mathbf{s}\cdot\mathbf{u}_{\eta,0})J_n(m\phi_{\mathbf{k}})\right\}.$$

With the understanding that each $\mathbf{q}$ and $\mathbf{k}$ component is distinct and incoherent with respect to each other, we can describe them separately in the form factor:

$$\begin{aligned} F(\mathbf{s},t;\mathbf{q},\mathbf{k}) &= \sum_{\mathbf{L},l,m,n} f_{\mathbf{L}}\{e^{-i(\mathbf{s}+l\mathbf{q}+m\mathbf{Q}+n\mathbf{k})\cdot\mathbf{L}} e^{il\omega_{\mathbf{q}}t} e^{im\omega_{\mathbf{k}}t} J_l(\mathbf{s}\cdot\mathbf{u}_{\mathbf{q},0}) J_m(\mathbf{s}\cdot\mathbf{u}_{\eta,0}) J_n(m\phi_{\mathbf{k}})\} \\ &= \sum_{l,m,n} f_{\mathbf{L}}\delta(\mathbf{s}-\mathbf{G}_{hkl}-l\mathbf{q}-m\mathbf{Q}-n\mathbf{k}) e^{il\omega_{\mathbf{q}}t} e^{im\omega_{\mathbf{k}}t} J_l(\mathbf{s}\cdot\mathbf{u}_{\mathbf{q},0}) J_m(\mathbf{s}\cdot\mathbf{u}_{\eta,0}) J_n(m\phi_{\mathbf{k}}). \quad (18) \end{aligned}$$

Now, we are in a position to consider scattering weight transfer under different excitation scenarios.

4.1. *Case A: Debye–Waller effect and diffusive scattering from lattice phonons*

Here, we consider the effective "heating" of the lattice, resulting in the Debye–Waller effect and the diffuse scattering around the main lattice Bragg peak at $\mathbf{s}=\mathbf{G}_{hkl}$ and simplify (7) by assuming there is no static distortion wave present i.e. $l=m=n=0$, however, the effect of phonons is included. Then the structure factor for the main lattice Bragg peak

$$S_0^{(0)}(\mathbf{G}_{hkl}) = FF^* = \delta(\mathbf{s}-\mathbf{G}_{hkl})|f_{\mathbf{L}}J_0(\mathbf{s}\cdot\mathbf{u}_{\mathbf{q},0})|^2. \quad (19)$$

One can simplify the equation with $J_0(\mathbf{s}\cdot\mathbf{u}_{\mathbf{q},0})$ well approximated by $1-(\mathbf{s}\cdot\mathbf{u}_{\mathbf{q},0})^2/4$, justified since $\mathbf{s}\cdot\mathbf{u}_{\mathbf{q},0}\ll 1$ with $\mathbf{u}_{\mathbf{q},0}\sim 0.01$ Å. Then by taking logarithm on both sides, one can derive

$$e^{-i\mathbf{s}\cdot\left(\sum_{\mathbf{q}} u_{\mathbf{q}}\hat{e}_{\mathbf{q}}(\mathbf{L})\right)} = e^{-\sum_{\mathbf{q}}\frac{1}{4}(\mathbf{s}\cdot\mathbf{u}_{\mathbf{q},0})^2} = e^{-M_q},$$

where $M_q=\sum_{\mathbf{q}} 1/4(\mathbf{s}\cdot\mathbf{u}_{\mathbf{q},0})^2$. This gives $S_0^{(0)}=\delta(\mathbf{s}-\mathbf{G}_{hkl})|f_{\mathbf{L}}|^2e^{-2M_q}$, with e^{-2M_q} simply the conventional phonon Debye–Waller factor (DWF), although in this form one does not require the system to be in thermal equilibrium.

Experimentally, the DWF is deduced for individual Bragg peak at $\mathbf{G}_{hkl}$. Equation (19) gives the projected mean-square (ms) value of lattice vibration from all independent vibrational modes

$$u_{hkl}^2 = 2M_q/|\mathbf{G}_{hkl}|^2, \quad (20)$$

according to the projection of the respective polarization vector $\hat{e}_{\mathbf{q}}$ onto $\mathbf{G}_{hkl}$. The excitation of phonons that leads to the suppression of the main Bragg peak intensity as described in (18) also gives rise to diffuse scattering around the main Bragg peak at $\mathbf{s}=\mathbf{G}_{hkl}+\mathbf{q}$. Here, one may assume that the scattering by phonon at different $\mathbf{q}$ is incoherent, hence allowing the cross terms to be dropped. Considering the 1st order diffuse scattering, the structure factor becomes

$$S_1^{(0)}(\mathbf{q}) = FF^* = |f_{\mathbf{L}}|^2e^{-2M_q}\sum_{\mathbf{q}}\delta(\mathbf{s}-\mathbf{G}_{hkl}-\mathbf{q})|J_1(\mathbf{s}\cdot\mathbf{u}_{\mathbf{q},0})|^2. \quad (21)$$

$|J_1(\mathbf{s}\cdot\mathbf{u}_{\mathbf{q},0})|^2$ can be similarly well approximated by $(\mathbf{s}\cdot\mathbf{u}_{\mathbf{q},0}/2)^2=1/2G_{\mathbf{q}}$, where $G_{\mathbf{q}}=1/2(\mathbf{s}\cdot\mathbf{u}_{\mathbf{q},0})^2$. Hence, one obtains

$$S_1^{(0)}(\mathbf{q}) \cong |f_{\mathbf{L}}|^2e^{-2M_q}\sum_{\mathbf{q}} G_{\mathbf{q}}\delta(\mathbf{s}-\mathbf{G}_{hkl}-\mathbf{q}). \quad (22)$$

Similarly, from the 2nd-order phonon diffuse scattering ($l=2$)

$$\begin{aligned} S_2^{(0)}(\mathbf{q}) &= |f_{\mathbf{L}}|^2e^{-2M_q}\sum_{\mathbf{q}}\delta(\mathbf{s}-\mathbf{G}_{hkl}-2\mathbf{q})|J_2(\mathbf{s}\cdot\mathbf{u}_{\mathbf{q},0})|^2 \\ &\cong |f_{\mathbf{L}}|^2e^{-2M_q}\sum_{\mathbf{q}} 1/2(G_{\mathbf{q}})^2\delta(\mathbf{s}-\mathbf{G}_{hkl}-2\mathbf{q}). \quad (23) \end{aligned}$$

By substituting $\sum_{\mathbf{q}} G_{\mathbf{q}}=2M_q$ and including contribution from $S_0^{(0)}$, a conservation law is obtained for the integrated intensity near $\mathbf{G}_{hkl}$: $m_{\mathbf{G}_{hkl}}=\sum_l S_l^{(0)}=|f_{\mathbf{L}}|^2e^{-2M_q}(1+2M_q+1/2(2M_q)^2+\cdots)=|f_{\mathbf{L}}|^2$. Hence, the effect from scattering by phonons can be regarded as transferring the scattering weight from $\mathbf{G}_{hkl}$ to $\mathbf{G}_{hkl}+l\mathbf{q}$, resulting in the creation of the diffuse background. On one hand, this allows one to sum up the effects from all vibrational modes into the lattice DWF. On the

other hand, the diffuse scattering techniques measure the momentum distribution of the phonon structure factors [52, 74] and in a wide angle setting such measurements can be conducted along with coherent scattering experiments to unpack the dynamics of phonons in the ultrafast X-ray and electron diffraction; for example, see Refs [57–59]. We point out the scattering formalism discussed here applies to both thermal and nonthermal scenarios. Taking only the dominant one-phonon contribution, the diffuse scattering $S^{(0)}_{\rm diff}(\mathbf{q})$ is given by summing the phonon structure factor from different vibrational state occupancy $n(\mathbf{q})$:

$$S^{(0)}_{\rm diff}(\mathbf{q}) = \sum_{\mathbf{q}} \frac{n(\mathbf{q})+1}{\omega(\mathbf{q})} |S^{(0)}_1(\mathbf{q}, \hat{e}_{\mathbf{q}})|. \tag{24}$$

Normally, in the equilibrium experiment, $n(\mathbf{q}) = \coth(\hbar\omega_{\mathbf{q}}/2k_BT)$ and a Gaussian vibrational state from the equilibrium Boltzmann statistics [74] and hence allowing one to map DWF into temperature assuming the deposited energy is equipartitioned among all active modes [52, 73]. Whereas this assumption is no longer guaranteed in the experimental conditions at far-from-equilibrium regime [76], neither (22) nor (23) is restricted to the Boltzmann statistics, hence they will apply to the nonequilibrium experiments as a way to track the kinetics of vibrational energy flow from the initially strongly coupled modes into the rest to establish the lattice phonon baths.

4.2. *Case B: Evaluating order parameter evolution and fluctuation effects by phase modes*

Now, we look at the scattering by the superlattice, namely the LDW, at $\mathbf{s} = \mathbf{G}_{hkl} + \mathbf{Q}$, but also recognizing the existence of phonons in the system. Here, the scenario has $m = 1$, $n = 0$, and (18) gives the structure factor for the 1st-order satellite associated with the static wave:

$$S^{(1)}_0(\mathbf{k}) = |f_{\mathbf{L}}|^2 e^{-2M_q} \delta(\mathbf{s} - \mathbf{G}_{hkl} - \mathbf{Q} - \mathbf{k}) |J_1(\mathbf{s}\cdot\mathbf{u}_{\eta,0})|^2 \prod_{\mathbf{k}} |J_0(\phi_{\mathbf{k}})|^2. \tag{25}$$

Applying the same argument in *case A*, one can write down the equivalence of the DWF for the scattering at $\mathbf{Q}$ as $e^{-2M_\phi} = \prod_{\mathbf{k}} |J_0(\phi_{\mathbf{k}})|^2$, where $2M_\phi = \sum_{\mathbf{k}} 1/2\phi^2_{\mathbf{k}}$. This gives the scattering by the superlattice

$$S^{(1)}_0(\mathbf{Q}) = |f_{\mathbf{L}}|^2 e^{-2M_q} e^{-2M_\phi} \delta(\mathbf{s} - \mathbf{G}_{hkl} - \mathbf{Q}) |J_1(\mathbf{s}\cdot\mathbf{u}_{\eta,0})|^2. \tag{26}$$

Again we consider each phase fluctuation component as independent and write the structure factor for the 1st-order fluctuation wave: $S^{(1)}_1 = |f_{\mathbf{L}}|^2 \sum_{\mathbf{k}} e^{-2M_q} \delta(\mathbf{s} - \mathbf{G}_{hkl} - \mathbf{Q} - \mathbf{k}) |J_1(\mathbf{s}\cdot\mathbf{u}_{\mathbf{q},0})|^2 |J_1(\phi_{\mathbf{k}})|^2$. The scenario is very similar to the main lattice diffuse scattering case, and by considering also higher-order fluctuation waves, the total satellite scattering at $\mathbf{Q}$: $\sum_m S^{(1)}_m = |f_{\mathbf{L}}|^2 e^{-2M_q} |J_1(\mathbf{s}\cdot\mathbf{u}_{\mathbf{q},0})|^2 e^{-2M_\phi}(1 + 2M_\phi + 1/2(2M_\phi)^2 + \cdots) = |f_{\mathbf{L}}|^2 e^{-2M_q} |J_1(\mathbf{s}\cdot\mathbf{u}_{\mathbf{q},0})|^2$, which is conserved; the effect of phase fluctuations can be considered as transferring the scattering weight from $\mathbf{Q}$ to $\mathbf{Q} + l\mathbf{k}$. But unlike in the case of main lattice DWF [52, 73], the phase fluctuations play a much more significant role here given the phase modes are ungapped (or low-energy modes), especially when considering an incommensurate wave state [50, 62]. This, from (18), leads to peak broadening in the structure factor $S_{\mathbf{Q}}(\mathbf{k})$. Nonetheless, from the conservation law, fully integrating contributions from both the static and the fluctuational components, $m_{\mathbf{Q}} = \int S_{\mathbf{Q}}(\mathbf{k})\, d\mathbf{k}$, allows one to still retrieve the order parameter amplitude $u_{\eta,0}$ from an evolving CDW structure factor:

$$m_{\mathbf{Q}} = |f_{\mathbf{L}}|^2 e^{-2M_q} |J_1(\mathbf{s}\cdot\mathbf{u}_{\eta,0})|^2. \tag{27}$$

The situation is more complex for the main lattice Bragg peak if there are more than one CDW states present in the system (denoted by l). The momentum integration of $S_{\mathbf{G}}$ gives:

$$m_{\mathbf{G}_{hkl}} = |f_{\mathbf{L}}|^2 e^{-2M_q} \prod_l |J_0(\mathbf{G}_{hkl}\cdot\hat{e}_{\eta_l} u_{0,\eta_l}(t))|^2. \tag{28}$$

4.3. *Case C: Fluctuation effects by amplitude modes*

Here we consider diffuse scattering by amplitude fluctuations of the distortion wave at $\mathbf{s} = \mathbf{G}_{hkl} + n\mathbf{Q} \pm \mathbf{k}$. Given that the AM is in general gapped (except at the critical point of a continuous phase transition), it has a much less impact when compared to the PM. To see this, we again assume that the AM and the PM are independent. The effect from amplitude fluctuations is formulated in the density modulations

$$\rho(\mathbf{r}, t) = \sum_{\mathbf{L}} \delta \left\{ \mathbf{r} - \mathbf{L} - \sum_{\mathbf{q}} u_{\mathbf{q}} \hat{e}_{\mathbf{q}}(\mathbf{L}) - u_\eta (1 + \delta\eta) \hat{e}_\eta \sin(\mathbf{Q}\cdot\mathbf{L} + \phi) \right\},$$

where $\delta\eta$ is expanded with the Fourier components $\delta\eta = \sum_{\mathbf{k}} \eta_{\mathbf{k}} \sin(\mathbf{k}\cdot\mathbf{L} - \omega_{\mathbf{k}} t)$. Let us look at the contribution from only one "$\mathbf{k}$" component: $J_n[\mathbf{s}\cdot\mathbf{u}_\eta(1 + \eta_{\mathbf{k}} \sin(\mathbf{k}\cdot\mathbf{L} - \omega_{\mathbf{k}} t))]$. In the limit of small distortion, i.e. $\mathbf{s}\cdot\mathbf{u}_\eta \ll 1$, the expression is simplified using the recursion relation:

$$\begin{aligned} &J_n[\mathbf{s}\cdot\mathbf{u}_\eta(1 + \eta_{\mathbf{k}} \sin(\mathbf{k}\cdot\mathbf{L} - \omega_{\mathbf{k}} t))] \\ &\quad = J_n(\mathbf{s}\cdot\mathbf{u}_\eta) \left\{ 1 + |n| \eta_{\mathbf{k}} \sin(\mathbf{k}\cdot\mathbf{L} - \omega_{\mathbf{k}} t) + \frac{|n|(|n|-1)}{2} \eta_{\mathbf{k}}^2 \sin^2(\mathbf{k}\cdot\mathbf{L} - \omega_{\mathbf{k}} t) \right\}. \end{aligned}$$

We expand $\sin(\mathbf{k}\cdot\mathbf{L} - \omega_{\mathbf{k}} t) = 1/2\{e^{i(\mathbf{k}\cdot\mathbf{L} - \omega_{\mathbf{k}} t)} + e^{-i(\mathbf{k}\cdot\mathbf{L} - \omega_{\mathbf{k}} t)}\}$ and similarly for $\sin^2(\mathbf{k}\cdot\mathbf{L} - \omega_{\mathbf{k}} t)$, to obtain the form factor for the fluctuation wave with momentum wavevector $\mathbf{k}$ to the second order:

$$\begin{aligned} F(\mathbf{s};\mathbf{k}) \;=\; & e^{-M_q} \sum_{\mathbf{L},n} e^{-i(\mathbf{s}+n\mathbf{Q})\cdot\mathbf{L}} J_n(\mathbf{s}\cdot\mathbf{u}_\eta) \left\{ 1 + \frac{|n|}{2i} \eta_{\mathbf{k}} \left[e^{i(\mathbf{k}\cdot\mathbf{L} - \omega_{\mathbf{k}} t)} + e^{-i(\mathbf{k}\cdot\mathbf{L} - \omega_{\mathbf{k}} t)} \right] \right. \\ & \left. - \frac{|n|(|n|-1)}{8} \eta_{\mathbf{k}}^2 \left[2 + e^{i(2\mathbf{k}\cdot\mathbf{L} - 2\omega_{\mathbf{k}} t)} + e^{-i(2\mathbf{k}\cdot\mathbf{L} - 2\omega_{\mathbf{k}} t)} \right] \right\} \\ =\; & e^{-M_q} \delta(\mathbf{s} - \mathbf{G}_{hkl} - n\mathbf{Q}) J_n(\mathbf{s}\cdot\mathbf{u}_\eta) \left(1 - \frac{|n|(|n|-1)}{4} \eta_{\mathbf{k}}^2 \right) \\ & + e^{-M_q} \delta(\mathbf{s} - \mathbf{G}_{hkl} - n\mathbf{Q} - \mathbf{k}) e^{-i\omega_{\mathbf{k}} t} J_n(\mathbf{s}\cdot\mathbf{u}_\eta) \left(1 - \frac{|n|}{2i} \eta_{\mathbf{k}} \right) \\ & + e^{-M_q} \delta(\mathbf{s} - \mathbf{G}_{hkl} - n\mathbf{Q} + \mathbf{k}) e^{+i\omega_{\mathbf{k}} t} J_n(\mathbf{s}\cdot\mathbf{u}_\eta) \left(1 - \frac{|n|}{2i} \eta_{\mathbf{k}} \right) \\ & - e^{-M_q} \delta(\mathbf{s} - \mathbf{G}_{hkl} - n\mathbf{Q} - 2\mathbf{k}) e^{-i2\omega_{\mathbf{k}} t} J_n(\mathbf{s}\cdot\mathbf{u}_\eta) \frac{|n|(|n|-1)}{8} \eta_{\mathbf{k}}^2 \\ & - e^{-M_q} \delta(\mathbf{s} - \mathbf{G}_{hkl} - n\mathbf{Q} + 2\mathbf{k}) e^{+i2\omega_{\mathbf{k}} t} J_n(\mathbf{s}\cdot\mathbf{u}_\eta) \frac{|n|(|n|-1)}{8} \eta_{\mathbf{k}}^2. \end{aligned}$$

When $n = 0$, the first term on RHS: $S_0^{(0)} = |f_{\mathbf{L}}|^2 e^{-2M_q} |J_0(\mathbf{s}\cdot\mathbf{u}_\eta)|^2$ gives the intensity at the lattice Bragg peak, which is the same as before the collective excitations; both PM and AM do not alter the main lattice peak structure factor. Note, when $n = 1$, the excitations of AM do not change the 1st-order satellite intensity at $\mathbf{s} = \mathbf{G}_{hkl} + \mathbf{Q}$, which is unlike the case for PM. The amplitude fluctuations do contribute to the diffuse scattering around the satellite intensity at $\mathbf{G}_{hkl} + n\mathbf{Q}$, for $n \geq 1$; see the remaining terms on the RHS. While the AM excitation adds to the diffuse background, its gapped nature makes such contribution much smaller than the effect from PM, away from the critical point.

4.4. *Case D: Scattering weight transfer between static wave fluctuations and lattice phonons during phase transitions*

Tracking the dynamical transfer of scattering weight between the microscopic and macroscopic systems driven by an ultrafast quench is at the core of discussing the nonequilibrium physics of phase transitions [26,35,66,77–79]. For the prototypical case of SSB upon quench, the free energy landscape with a nonzero $\langle\eta\rangle$ would involve phase and amplitude modes; see Figure 1c. Here, in

a physical text we consider the Peierls-type SSB to form an incommensurate CDW, in which the unfolding of the order parameter landscape is preceded by the lattice softening in the normal state. The CDW wavevector is determined by a maximum of the full electronic susceptibility χ enhanced by the Fermi surface nesting and the associated electron-lattice interactions at $\mathbf{Q}_\chi$. The same conditions also lead to the softening in the phonon dispersion curve [80], with the phonon frequency $\omega_{\mathbf{q}} \to 0$ as $\mathbf{q} \to \mathbf{Q}_\chi$. The fluctuation waves and soft phonons are intricately connected by $\mathbf{q} = \mathbf{k} \pm \mathbf{Q}$. One can see this by considering a phase fluctuational wave (phase mode) at $\mathbf{k}$. It manifests in the lattice vibration $\mathbf{u}_{\phi,k}(\mathbf{L}, t) = \mathbf{u}_{Q,0} \sin(\mathbf{Q}\cdot\mathbf{L} + \delta\phi_k(t))$, with $\delta\phi_k(t) = \phi_{k,0}\sin(\mathbf{k}\cdot\mathbf{L} - \omega t)$. For a small amplitude, $\phi_{k,0} \ll 1$, $\sin(\mathbf{Q}\cdot\mathbf{L} + \delta\phi_k(t)) = \sin(\mathbf{Q}\cdot\mathbf{L})\cos(\delta\phi_k(t)) + \sin(\delta\phi_k(t))\cos(\mathbf{Q}\cdot\mathbf{L}) \sim \sin(\mathbf{Q}\cdot\mathbf{L}) + \delta\phi_k(t)\cos(\mathbf{Q}\cdot\mathbf{L})$, and one arrives at $\mathbf{u}_{\phi,k}(\mathbf{L}, t) = \mathbf{u}_{Q,0}\sin(\mathbf{Q}\cdot\mathbf{L}) + \boldsymbol{\phi}_{k,0}\sin(\mathbf{k}\cdot\mathbf{L} - \omega t)\cos(\mathbf{Q}\cdot\mathbf{L})$. The first term is simply the unperturbed static distortion wave. The second term can be rewritten as $\delta\boldsymbol{\phi}_{\eta,k} = 1/2\boldsymbol{\phi}_{k,0}\{\sin[(\mathbf{k}+\mathbf{Q})\cdot\mathbf{L} - \omega t] + \sin[(\mathbf{k}-\mathbf{Q})\cdot\mathbf{L} - \omega t]\}$, which constitutes a "coherent superposition" of two phonon modes having wavevector $\mathbf{k}+\mathbf{Q}$ and $\mathbf{k}-\mathbf{Q}$. Similarly, one can look at the amplitude mode at $\mathbf{k}$ and writes $\delta\mathbf{u}_{\eta,k} = \mathbf{u}_{k,0}\sin(\mathbf{k}\cdot\mathbf{L} - \omega t)\sin(\mathbf{Q}\cdot\mathbf{L}) = 1/2\mathbf{u}_{k,0}\{\cos[(\mathbf{k}+\mathbf{Q})\cdot\mathbf{L} - \omega t] + \cos[(\mathbf{k}-\mathbf{Q})\cdot\mathbf{L} - \omega t]\}$, thus comes to the same conclusion [50].

The derivation here illustrates the direct connection between the soft phonon modes and the CDW collective modes, which would necessitate an interplay between the structure factors of the CDW and the main lattice peaks. The pairing and unpairing dynamics attributed to the scattering weight transfer are embedded in the nonequilibrium dynamics of phase transitions. Figure 3 discusses the two scenarios encountered experimentally where we look at the interconversion between two types of the lattice dynamics through the changes in the dispersion curves that are coupled to the free-energy landscape changes. Of concern is how one can decouple the DWF from the symmetry-associated contribution pertaining to the phase transition. To this end, with proper consideration of multi-**Q** contributions one can independently obtain the respective order parameter dynamics via evaluating $h(t) = m_{Q_l}(t)/m_G(t)$ and $g(t) = m_{Q_a}(t)/m_{Q_c}(t)$, where the contribution from DWF is eliminated. Specifically,

$$h(t) = \frac{|J_1(\mathbf{G}_{hkl}\cdot\hat{e}_{\eta_l}u_{0,\eta_l}(t))|^2}{\prod_l |J_0(\mathbf{G}_{hkl}\cdot\hat{e}_{\eta_l}u_{0,\eta_l}(t))|^2} \tag{29}$$

and

$$g(t) = \left|\frac{J_1(\mathbf{G}_{hkl}\cdot\hat{e}_{\eta_a}u_{0,\eta_a})}{J_1(\mathbf{G}_{hkl}\cdot\hat{e}_{\eta_c}u_{0,\eta_c})}\right|^2. \tag{30}$$

Given the polarization of the CDW state $\hat{e}_{\eta_l}$, the order parameter $u_{0,\eta_l}(t)$ can be retrieved and used to deduce the DWF at $\mathbf{G}_{hkl}$.

5. Multi-messenger ultrafast electron scattering and imaging experiments

We now consider the practical aspects of implementing these measurements through the ultrafast scattering and imaging techniques. First, we discuss the ultrafast electron diffraction (UED) approach. A central thesis for the success of using the scattering-detected order parameter dynamics to reconstruct the free-energy landscape is the separation of scales as discussed in Section 2. While this approach reduces the complex nonequilibrium phase transitions to problems just involving few macroscopic degrees of freedom (order parameters), the validity of the impulse-adiabatic approximation behind this approach needs to be examined in the experiments.

The event sequences from the microscopic excitations to the macroscopic transitions, as highlighted in Figure 3, are intrinsically multi-stepped and multi-perspective, but can be efficiently probed with recent significant advances of the fs spectroscopy and X-ray scattering techniques;

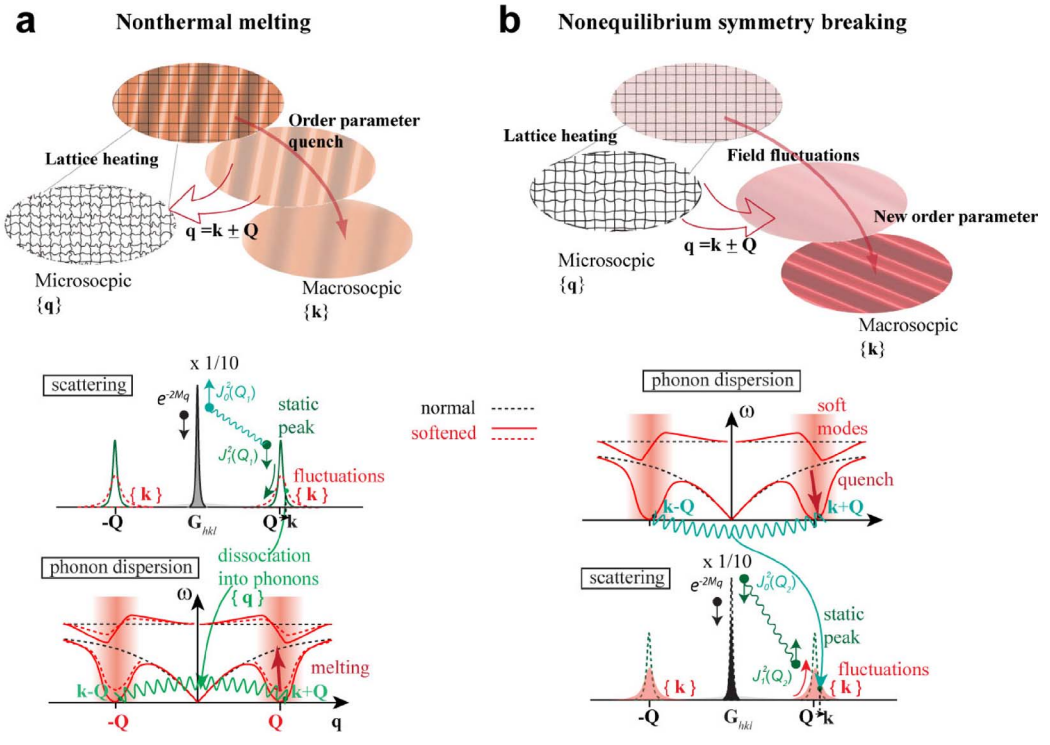

Figure 3. Nonequilibrium phonon dynamics and fluctuation waves in the CDW system during light-induced melting and order formation. The connection between the two dynamics upon the laser interaction quench is viewed through the changes in the phonon dispersion curves, which are coupled to the change of the order-parameter free energy landscape driving the fluctuation waves of the system. The two signatures are manifested in the scattering structure factors of the main lattice ($S_{\mathbf{G}}$) and the CDW superstructures ($S_{\mathbf{Q}}$) at $\mathbf{G}_{hkl}$ and $\mathbf{Q}$ respectively. Here, h, k and l represent the Miller indices. The transfer of the scattering weight between $S_{\mathbf{G}}$ and $S_{\mathbf{Q}}$ occurs as a CDW order is created or destroyed. The excitations of the lattice modes contribute to the dynamical DWF, expressed in e^{-2M_q}. On the other hand, the symmetry breaking or recovery (i.e. the melting of CDW) modifies $S_{\mathbf{G}}$ and $S_{\mathbf{Q}}$ respectively with the Bessel functions: J_1 and J_2, which are anti-correlated with each other. The manifolds of fluctuation waves and phonons involved in the phase transitions are denoted by their momentum wavevector in $\{\mathbf{k}\}$ and $\{\mathbf{q}\}$.

for recent reviews, see [11–14]. Similarly, the development of the electron-based ultrafast electron scattering [81–92] and microscopy [93–108] techniques is also in full swing in recent years. Upon applying the laser pulses, the excitation energy is initially stored in the photo-excited hot carriers, setting off the nonequilibrium microscopic dynamics through couplings to the lattice modes. Ultrafast spectroscopy techniques have investigated these initial relaxations and found clear signatures of more than one decay channel [13]. Hot carriers decay nearly instantaneously through internal relaxations establishing an effective electron temperature, T_e. But the electronic energy relaxation into the lattice can only efficiently occur within a small part of phonon branches, referred to as the strongly coupled phonons (SCP), often within the higher energy optical branches most connected with the electronic excitations. Then the energy is spread to other modes loosely defined as the weakly coupled phonons (WCP). The exchange of kinetic energies between the

three sub-systems is typically described by a three-temperature model (3TM) [13, 109–112].

Meanwhile, the ordering over the long-range scale does not directly couple to the microscopic processes due to a large mismatch in the momentum and energy states active at the shortest time. The dynamics of the order parameter are driven by the shift of the energy landscape established by the momentum-dependent electron–phonon coupling (EPC) matrix. The EPC is shaped by electronic instabilities at the Fermi surface (FS) and electron correlation effects, which can be altered significantly upon applying optical excitations. The shifting of the energy landscape thus can occur on a very short timescale, which, from the perspective of the long-range order parameter, represents a nonthermal interaction quench.

One of the main goals of UED is to capture the dynamics of the order parameter following the quench. Only the average structure can be obtained by the intensity of the Bragg peaks whereas the structural fluctuations resulted from the symmetry-breaking and recovery processes (see Figure 3) shall be retrieved as well from features beyond the central coherent peak. Of concern is also the soft modes and the pre-transitional phonon dynamics [113–116], properties of the lattice elastic energy landscape supporting the symmetry breaking [9, 117, 118]. These events partially overlap in time with the microscopic processes probed by the ultrafast spectroscopy techniques. The signatures of such are obtained from the **q**-resolved fine structure of the coherent structure factors as well as the diffuse scattering surrounding the Bragg peaks. Only through the combination of the scattering signals (coherent and incoherent) gathered from the different reciprocal subspaces of the Brillouin zone a deeper understanding of the nonequilibrium phenomenon of phase transition can be gained. To this end, a strong advantage of UED lies in its large Ewald sphere, making the retrieval of the different **q**-dependent features at once possible from a large momentum-scale diffraction pattern—typically as many as 10–100 Bragg peaks can be observed simultaneously in a single diffraction pattern, in contrast to the X-ray diffraction approach.

In principle, the simple geometry of the conventional UED approaches makes it well suited to compare with results obtained by ultrafast spectroscopy [11–14]. An important problem concerns the comparison between the volume excited and the parts probed by different techniques [13,25]. When applying an optical or near-infrared laser pulse, the excitation transforms the materials on a finite absorption penetration depth, typically within 100 nm. The very large cross-section of the electron scattering means that small volume samples, such as thin films or nanocrystals in the range of 10s nm scale (depending on the beam energy) can be used. This feature partially relieves the concerns of sampling inhomogeneously excited regions and unpacking information—an issue to be addressed in Section 6.3.

Meanwhile, the advantage of UED might turn into a disadvantage as the scattered signal can be dispersed into a large momentum space with a relatively poor **q** resolution. This calls for an increase of the beam flux and a decrease of the sample lateral size to improve the **q** resolution, however at the expense of signal strength. A challenge of UED as well as the ultrafast electron microscopy (UEM) approach has been to balance the requirement of the resolution versus the dose afforded under a repetition rate set by the recovery time of the excited quantum material systems, typically in the kHz and sub-kHz ranges [13, 120, 121]. There is an apparent limitation, setting the resolution affordable under a specific dose, by the space-charge-led pulse lengthening, referred to as the space-charge effect (SCE) [122–129]. Fortunately, looking deeper into this SCE issue, one can find a way to overcome this SCE even in a significant way, by properly manipulating the beams in its 6-dimensional collective phase space through electron-optical means. Key knowledge about this came from studying the dynamical phase space structures of the pulses as a function of the particle number, $N_{e,0}$, controlled by the extraction field F_a, both experimentally and theoretically.

The electron pulses used in the UED systems are typically created by applying the fs ultraviolet laser pulses on a cathode through the photoelectric effect [122]. From the multi-level fast multiple

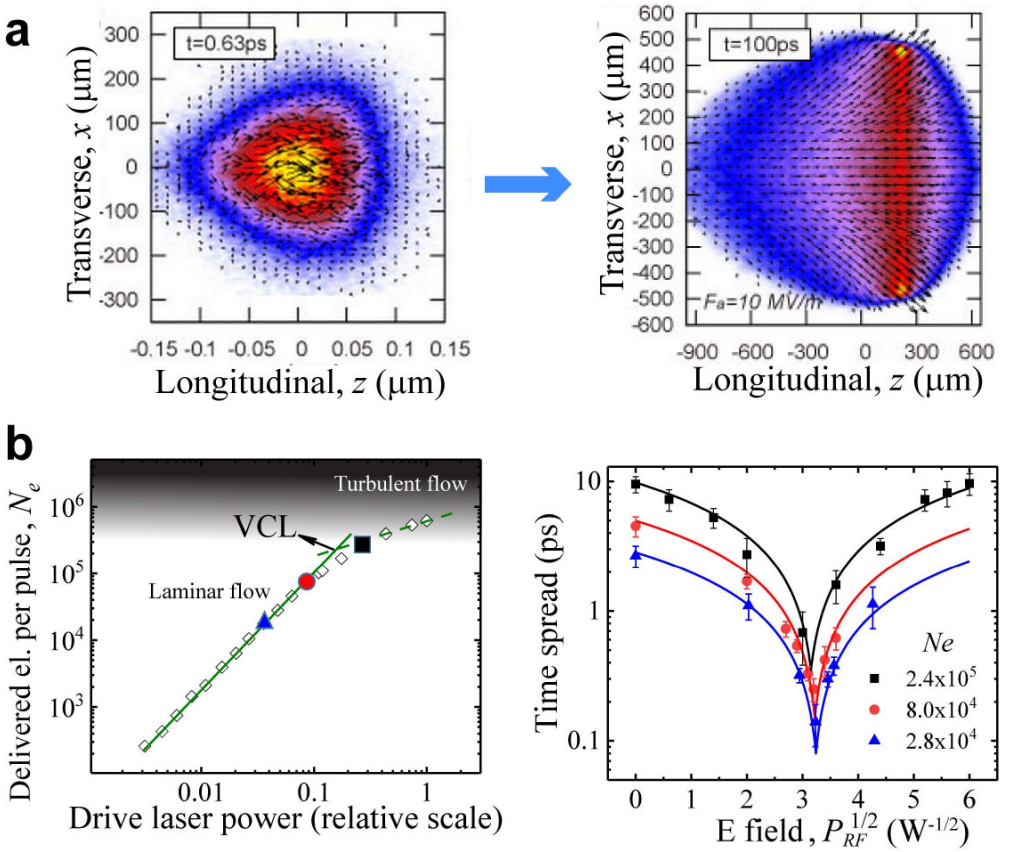

Figure 4. The brightness-limited performance in the electron bunch compression. (a) The multi-level fast-multiple model (ML-FMM) simulation of the structures of the electron pulse extracted under a field F_a = 10 MV/m from a photocathode at two different times. (b) The number of particles in the electron bunches, N_e, obtained at the specimen of the UEM system as a function of the ultrafast ultraviolet drive laser power. This number is typically a small fraction (~5–10%) of the particle number $N_{e,0}$ generated at the cathode due to the slicing by the alignment apertures in the beamline. One obtains the virtual cathode limit (VCL) from the slope change. The right panel shows the pulse duration characteristics under the tuning of the longitudinal RF lens at different N_e. Panel a is adapted with permission from Ref. [119].

method (ML-FMM) calculations designed to preserve the stochastic scattering effect in the beam dynamics simulations, one shows that the collective phase space volume is nearly conserved once the pulse is fully extracted (Liouville's theorem) from the cathode [130]. Hence, the perceived SCE associated with the pulse lengthening caused by the internal Coulombic forces can be overcome via dynamically reshaping the phase space structure of the pulse [121, 131, 132], without leading to degradation of the throughput.

This leaves the pulse brightness, defined as (particle number)/(phase space volume), as a main figure of merit in designing the photo-emission electron sources and plays a key role for improving the UEM/UED performance. In particular, a central effort has been to avoid the uncontrolled growth of phase space due to the stochastic effect [124] that leads to the degradation of the brightness, but not necessarily the (collective) SCE. Such an issue is addressed in ML-

FMM calculation by studying the brightness figures and phase space structures as a function of F_a [119]. Prototypical SCE-led pulse evolutions under a nominal $F_a = 10$ MV/m are shown in Figure 4a, where the phase space structures at two stages (630 fs and 100 ps) along the transverse (x) and the longitudinal (z) directions are compared. The particle momenta (p_x and p_z) depicted by the arrows give a certain spreading but largely are correlated with the position (x and z) led by SCE. Accordingly, the brightness is tracked as a function of particle number $N_{e,0}$ with the extraction field (F_a) as the control parameter.

A main conclusion from ML-FMM simulations is that the transverse (x–y plane) phase space grows sub-linearly with respective to $N_{e,0}$ until the virtual cathode limit (VCL)—one when the space-charge forces associated with the positive counter ions at the emitting surface become strong enough to reduce the efficiency of the photoemission [119, 124, 133, 134]. This is seen in the left panel of Figure 4b where the yield over the drive laser power becomes sub-linear and the charge particle flows switch from laminar to turbulent. In the specific UEM arrangement, the observation is made at the detector where the peripheral hot electrons around the electron pulse have been sliced off with an aperture in the beamline such that the delivered particle number, N_e, is typical 5–10% of $N_{e,0}$ at the cathode [127]. Nonetheless, the presence of VCL is represented by an inflection point (Figure 4b). Characterization of VCL is important as only when driven above VCL, the stochastic phase space size of the pulse will significantly increase from the onset of turbulence within the charge particle flow; the particle flow is otherwise laminar in the regime below VCL [119]. This means that one can significantly gain transverse brightness by increasing $N_{e,0}$ up to the brink of VCL. The effect translates to improving the performance related to the transverse phase space, such as the spatial resolution of UEM or the **q**-resolution of UED. Meanwhile, one finds the phase space along the z direction increases nearly linearly with respect to $N_{e,0}$, and the pulse-width (Δz) grows as $N_{e,0}^{1/2}$, also confirmed by the experiment [119]. From the right panel of Figure 4b where the longitudinal phase space size is translated into the compressibility in time, one can conclude that even at VCL under just a fair $F_a \sim 2$ MV/m in a DC gun arrangement, a sub-ps resolution can easily be achieved from tuning the RF field to realign the phase space.

The left panel of Figure 5 shows the setup of the electron-optical system for conducting the UED and UEM experiments. The two approaches share a similar electron-optical system before the specimen. A feature here is the incorporation of the RF cavity system, before and after the specimen for realigning the longitudinal phase space structure. Effectively here, the RF cavity acts as the longitudinal lens in a very similar role as the magnetic lens for controlling the phase space structure in the transverse direction—a feature that is fully implemented in the conventional TEM. The two lens systems combined allow the UEM/UED apparatus to achieve an optimal pulse shape targeted by the different modalities [93, 121]. The additional optical system in UEM consists of intermediate and projection lenses and the spectrometer, intended to decode the nonequilibrium physics encoded in the phase space of the scattered particles in the modality of imaging or spectroscopy [107, 108, 121, 135–142]; whereas without such optics (or set at the diffraction mode in a UEM), the scattered electrons are focused onto the screen to form the diffraction image directly.

The right panel of Figure 5 shows schematically how the operating parameters are set based on the modality's feature-of-merit (FOM), defined by the projected phase space. For example, for coherent scattering, a key is to maximize the incident particle density projected along the transverse momentum space. This can be achieved via the condenser lens adjusted to minimize the tilt of the transverse phase space (p_x vs x in lab frame or $\Delta\alpha$ vs Δr in pulse frame) as the pulse arrives at the sample. This can be considered as a pulse compression along p_x (or $\Delta\alpha$). For ultrafast imaging where the resolution is typically dose-limited, the optics are frequently optimized to produce a better focusing along x at the expense of beam coherence. Meanwhile,

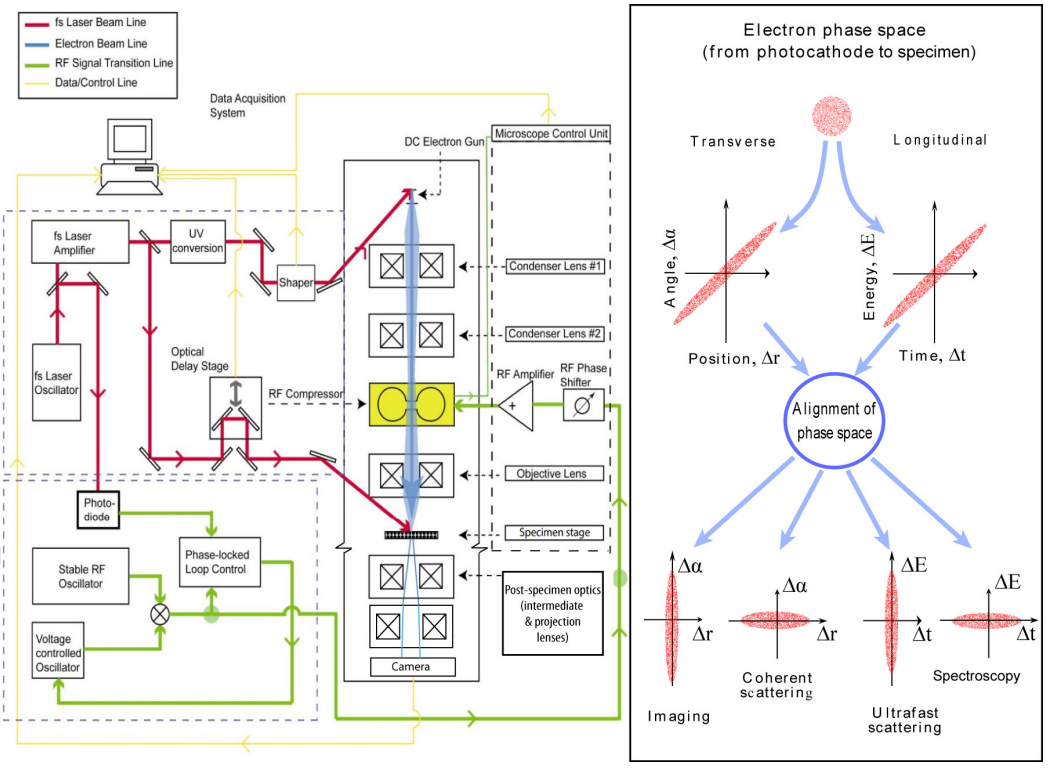

Figure 5. Configuration of an ultrafast electron microscope system. The main concept aims to incorporate the high temporal resolution into an existing transmission electron microscope with the rearrangement of the electron optical system to accommodate a high-density photo-electron source, which is driven by ultraviolet laser pulses. The electron pulse coming off from the cathode rapidly develops into a chirped pulse, influenced by the intrinsic strong Coulombic space-charge forces at the low energy stage. This collective space-charge effect manifests not in a blowout of the phase space, but instead in a highly correlated momentum-position phase space structures in both the longitudinal and transverse directions; see right panel where the two phase spaces are depicted in $(\Delta t, \Delta E)$ and $(\Delta r, \Delta \alpha)$ respectively. To remediate the resulted pulse broadening, one or more RF cavities act as the longitudinal lenses in the beamline to recompress the projected phase space along Δt or ΔE, while a similar strategy along the transverse directions is handled by the existing magnetic lenses. These two combined lead to focusing both in the longitudinal (energy and time) and transverse (crossover and coherence) dimensions. In general, different optical adjustments will allow the phase space of the incidence pulses to be realigned for the best performance of diffraction, imaging, and spectroscopy without sacrificing the electron beam dose. The successful operation of the new RF lenses relies on synchronization between the laser pulse and the cavity field, which is controlled by the phase-locked loop electronics with feedback control to counteract phase jittering within the RF cavity field for focusing; see the left panel. The physical limit of the performance is the phase space density, or brightness, of the pulse that can be delivered to the specimen. The resolution is defined in the projected sub-phase space targeted by different modalities and the relevant information encoded in the scattering process is deconvoluted by the post-specimen optics and projected onto the detector; see discussions in Refs [92, 93, 143].

for achieving ultrashort time resolution, the adjustment is made via a compression along z (Δt), whereas for spectroscopy a compression along p_z (ΔE) is needed to monochromatize the pulse. The post-specimen optics are typically tuned to project the proper phase space structure of scattered pulse onto the screen; see e.g. Refs [93, 121] for optimization and mode matching strategies. Their discussions are beyond the scope of this paper. As a result, the new approach can sidestep the conventional collective SCE from a high-density beam and leads to the possibility of multi-modal scattering and imaging experiments within a single platform [95]. This adaptive optics strategy has been recently employed in the UED [23] and prototype UEM [108, 135] experiments; some of which will be discussed in Section 6.

In Figure 6a, we give the scattering patterns from the ultrafast coherent electron pulses delivered via the pulse compression schemes. The pulse width here is ~100 fs (Figure 4b), whereas the transverse momentum compression by the condenser and objective lenses leads to a high beam coherence length (~40 nm; Ref. [23]). The combination of the two provides the resolutions to probe long-range cooperativity over an ultrafast time window for the nonequilibrium CDW phase transition. The order parameters of the CDW states are encoded in the satellite peaks as shown in Figure 6b, including the higher-order satellites present due to the domain structures of the CDW [144–148]. The satellite network from three degenerate CDW branches with momentum wavevector $\mathbf{Q_i}$ and their higher-order multi-$\mathbf{Q}$ components represents the Fourier spectra of the real-space hexagonal domain state [149, 150]—so-called near-commensurate CDW (NC-CDW) [144–148, 151], which can be converted from the scattering pattern; see Figure 6c. In addition, the scattering from fluctuation waves tied to the electronic instabilities is often more spread out in the momentum space and forms the diffuse scattering background [53, 56]. The diffuse scattering gives central information on the pre-transitional phenomena dominated by the preformed short-range orders or soft phonon modes. Given the scattering intensity from these features are significantly smaller than the intensities of the Bragg peak ($\mathbf{G}$) from the average lattice unit cells, the useable dose on the sample is a key factor for successfully probing the quantum material phase transitions [144,148,151]. Furthermore, ensuring no residual effect after the pumping of thermally isolated thin specimens requires a low repetition rate (≤1 kHz). For these reasons, the adaptive optics approach is the method of choice as it does not rely on the aperture to improve the resolution.

6. Example systems

The possibility to access long-lived states with desired unconventional properties has motivated an increasing number of ultrafast experiments exploring correlated quantum materials [1, 2, 4, 11, 12, 152]. In this section, we illustrate how the measurements of the nonequilibrium order parameters by the ultrafast scattering, when connected with the Landau–Ginzburg formalism, can be used to explore the global energy landscape of the nonequilibrium quantum materials and study the nonequilibrium physics therein. We will focus on three prototypical systems, i.e., $CeTe_3$, 1T-TaS_2, and VO_2, all of which exhibit long-range states ordered on the lattice with distinctive light-tunable and structurally coupled electronic phase transitions. The three systems have varying strengths of electron correlation as well as different natures of electron-lattice coupling, as depicted in Figure 7. The charge orderings range from purely incommensurate, to near commensurate, to commensurate or even bond-ordered density waves, making them representative systems for the comparisons. The nonequilibrium platform here focuses on the ultrafast optical pump–scattering probe settings using typically isolated sub-50 nm scale thin films or nanocrystals. The entire samples are covered within pump laser and probe electron beams. The settings facilitate a condition where the pump laser with a similar penetration depth as the film thickness introduces interference effect within the film and hence may establish a

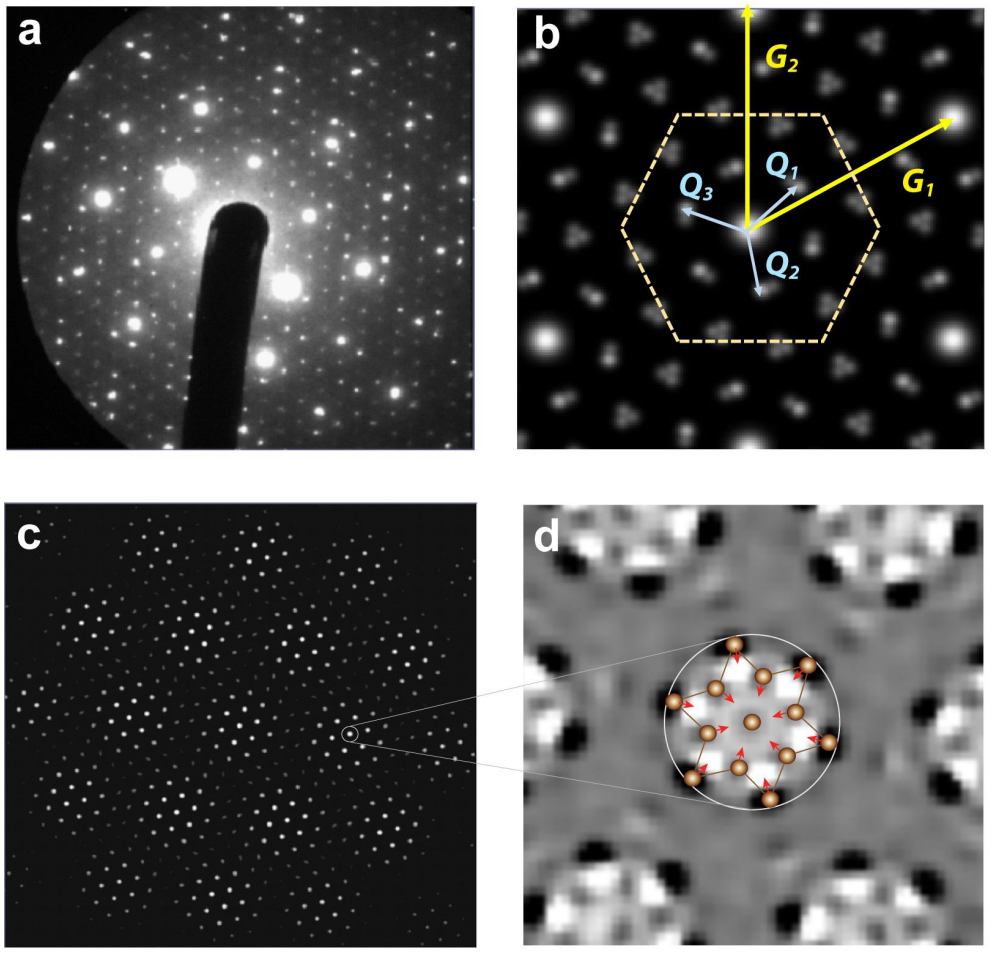

Figure 6. Diffraction of 1T-TaS_2 thin film measured with an ultrafast electron diffraction setup. (a) The diffraction pattern obtained at the beam energy of 100 keV. (b) A local diffraction pattern constructed from refining all relevant Bragg peaks (CDW and lattice) gives the distribution of satellites associated with the triply degenerate CDW branches and the associated high-order harmonics of the CDW from inter-CDW coupling; these features appear around each Bragg diffraction peak from the main lattice. The main CDW satellites are marked by the respective momentum wavevector $\mathbf{Q_i}$, whereas the main lattice peaks are marked with the reciprocal unit cell wavevectors $\mathbf{G}_1$ and $\mathbf{G}_2$. (c) The real-space representation deduced from the CDW patterns showing the long-range hexagonal domain structures. (d) The 13-atom supercell of the density wave in David-Star shape, presented in the lattice distortion map.

uniformly excited material system in which the nonequilibrium state evolves initially from a homogeneous quench. The sample is typically suspended freely over a fine grid held under the vacuum environment. Therefore, one may safely assume that absorbed energy in the pumped system is preserved to the entire probe window (over 1–2 ns). The pump–probe repetition rate is set at 0.1 to 1 kHz, adjusted to ensure that the pumped system fully relaxes on the much longer time scales. This platform allows us to discuss nonequilibrium dynamics as an internal relaxation

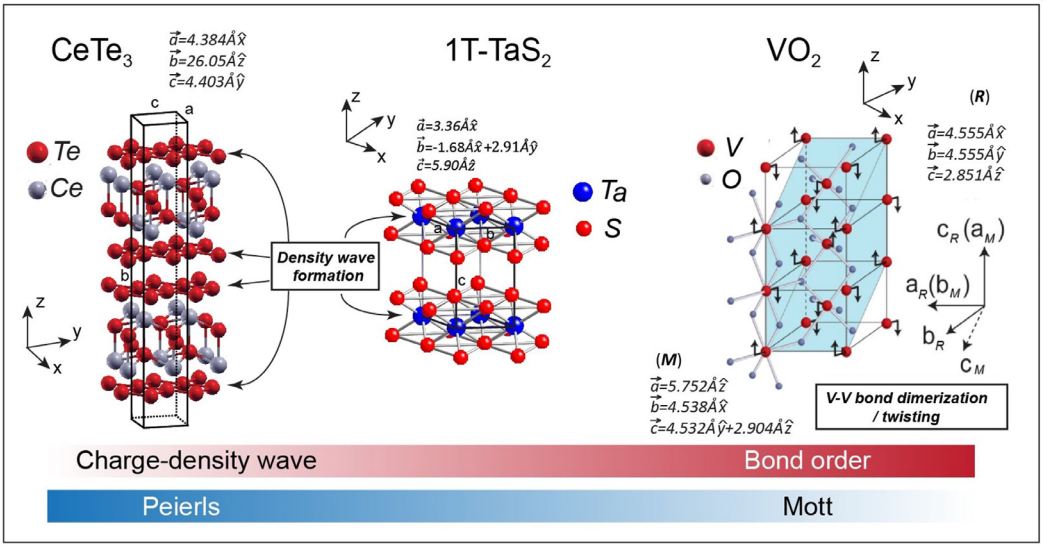

Figure 7. The crystal structures of $CeTe_3$, 1T-TaS_2, and VO_2 investigated by the ultrafast scattering techniques.

process. We will discuss implications to the interpretation of the experimental results when the conditions of pump-homogeneity are not met.

6.1. *Competing degenerate broken-symmetry orders: rare-earth tritellurides*

The rare-earth tritelluride (RTe_3) compound is one of the most systematically studied CDW systems to undergo continuous phase transition [153–155]. This system consists of square Te planes, alternating with weakly coupled RTe slabs (see Figure 7). Despite the fundamental C4 symmetry in the 2D Te sheet to host CDW formation, the stripe phases are the predominant CDW orders due to spontaneous symmetry breaking. We note, bearing on a small asymmetry owing to the coupling between the two nonequivalent square Te nets [72], the dominant ground state is the stripe phase along the c-axis. However, the recent inelastic X-ray scattering revealed pre-transitional critical fluctuations in nearly equal strengths along both c and a-axes [156, 157]—a signature of the two order parameter fields vying for the spectroscopic weight to become a static order. Nonetheless, the SSB dictates that, upon ordering along the c-axis which removes a significant amount of the potential a-CDW spectral weight [155, 158], subsequent formation of a-CDW will be excluded [159].

The surprising light-induced formation of a new broken-symmetry order in the direction orthogonal to the pre-existing state (a-CDW) was unveiled recently in the two light rare-earth RTe_3 family members of $LaTe_3$ [22] and $CeTe_3$ [23]. Given that the a-CDW does not exist in the system prior to applying a fs near-infrared pulse, this is a rare scenario where the suppressed field of a new broken-symmetry phase can be created from scratch over a relatively short timescale. Therefore, from studying the real-time ultrafast dynamics of the CDW system in RTe_3, it is possible for one to gather crucial insight into how an SSB phase transition emerges out of equilibrium beyond the mean-field description in a condensed matter system.

In the equilibrium state phase transition, there has been already a high degree of control evidenced in the significant shift of the critical temperature $T_{c,1}$ by changing the rare-earth element and applying pressure [153–155]. The effects, such as downsizing the gap size and

the CDW amplitude due to Lanthanide shrinking, are results of weakening the inter-orbital coupling strengths that shape the FS [72]. Given the two CDW order parameters are already strongly competing in the equilibrium state, it is possible to tip the balance of the competitions thus transforming the free-energy surface by shifting the orbital states occupancies [160]. The surprising introduction of a-CDW, even in a system deep inside the pre-existing order of c-CDW by applying short near-infrared pulses (here $T_b = 300\ \mathrm{K} \ll T_c = 540\ \mathrm{K}$), indeed reflects this.

The possibility of optically manipulating the free energy surface allows the RTe_3 to be the prototype system for transient control of nonequilibrium phases. The basic physics of competitively driven transformation of the free-energy landscape and, as a result, the introduction of the hidden a-CDW has been given on a phenomenological ground; see Section 3. Here, we will validate the theoretical hypotheses and focus on elaborating the more intricate microscopic dynamics and the nonequilibrium processes enabling such phenomena. At the center stage of the discussion is the ultrafast scattering-based approaches serving to capture the nonequilibrium order parameters and the associated field fluctuations. We will show how one uses such information to reconstruct a competitive global energy landscape poised to the different orderings upon quench and the nonequilibrium physics it entails.

Transient dynamics in a system with two competing orders η_c and η_a, in this case, are recorded using an RF-optics-augmented UED system with the transverse lenses tuned to optimize the **q**-resolution [23, 92]. In particular, the amplitude dynamics as described in (9) are manifested in the integrated intensity of the structure factor, $m_l(\mathbf{Q}; t)$, that one can retrieve from the dynamical diffraction patterns (27). The spatially nonuniform order parameter evolution is also detected by following the correlation lengths (ξ) of the system encoded in the width of the structure factor (25). Taken from Ref. [23], Figure 8a shows the raw diffraction pattern where the main signature of the broken-symmetry order at $t = -1$ ps is the c-CDW superlattice satellites at $\mathbf{G}_{hkl} \pm \mathbf{Q}_c$ with $\mathbf{Q}_c = 0.28\mathbf{c}^*$ around the Bragg peaks of the square lattice at $\mathbf{G}_{hkl}$. The inset shows the patterns from the $\mathbf{G}_{401}$ region before (-1 ps) and after ($+1$ ps) the laser excitation. Clearly, by $+1$ ps the system establishes a new pair of satellites at $\pm 0.30\ \mathbf{a}^*$ ($\mathbf{Q}_a$). The results inform the occurrence of a new broken-symmetry phase on $\approx$1 ps timescale. The respective order parameter dynamics are plotted in Figure 8b.

6.1.1. *Method to retrieve global free-energy surface through ultrafast scattering-detected order parameters*

To begin with, we give a pedagogical description on how the experimental protocol helps retrieve the Landau parameters based on controlled studies of transient metastable phases. The basic assumption is that the quenched free-energy landscape will decide the coordinates of the metastable states as its stationary points. Hence, by following the relative changes of the two competing order parameters at the metastable stages as the controlling laser fluence (F) is tuned the bi-dimensional free-energy surface shaped by the competitions between the two sub-systems can be evaluated. The coordinates of free energy minimum taken from the stationary points of (11) are

$$\begin{cases} |\eta_c|^2 = \dfrac{-(a'(T - T_c) + \tilde{A}|\eta_a|^2)}{A_4'} \\ |\eta_a|^2 = \dfrac{-(a(T - T_c) + \tilde{A}|\eta_c|^2)}{A_4}. \end{cases} \tag{31}$$

These coordinates, equivalent to $\hat{m}_{Q_l}(t) \equiv m_{Q_l}(t)/m_{Q_c}(t < 0)$ ($l = a$ or c), are reported as a function of F; see inset of Figure 8b. We use the two critical fluences identified in Figure 8b to set the scale of the Landau parameters. First, from the established critical energy density $E_{c,c} \approx 0.64\ \mathrm{eV/nm^3}$ (converted from the applied fluence $F_{c,c} \approx 2.0\ \mathrm{mJ/cm^2}$ needed to suppress $|\eta_c|$ to 0), one derives the c-CDW-associated parameters: $a = 4|E_{c,c}|/(T_c - T_b) = 1.05 \times 10^{-2}\ \mathrm{eV{\cdot}nm^{-3}{\cdot}K^{-1}}$,

and $A_4 = a(T_c - T_b) = 2.54$ eV·nm^{-3}. In addition, the successfully identified nonthermal critical fluence $F_{c,a} = 0.59$ mJ/cm^2 gives the critical condition over which a nonzero static $|\eta_a|$ will be created according to (31). From $|\eta_{c,\mathrm{th}}| \approx 0.87$ at $F_{c,a}$, one gets $\tilde{A} = 4.10$ eV·nm^{-3}, $a' = 1.29 \times 10^{-2}$ eV·nm^{-3}·K^{-1}, and $A_4' = 22.0$ eV·nm^{-3} by fitting the results with (31).

6.1.2. *Impulse-adiabatic phenomenology*

We point to the fact that with the above-the-gap excitation, the pump does not couple to the order parameter directly; rather it heats up the carriers first and that suppresses the CDW spectroscopic gap on a shorter timescale than the long-wave response associated with the lattice order parameter. This is consistent with the observation of a carrier spectral weight transfer and the adjustment of the FS topology within 100 fs by photoemission [160, 161]; whereas the overdamped suppression of the associated order parameter amplitude appears on a slower (~300 fs) timescale, observed by the scattering techniques (Figure 8b) [22, 23, 162]. These hierarchic temporal responses reflect the basic impulse-adiabatic phenomenology for the description of the light-induced phase transition on the free-energy landscape.

The new bidimensional free-energy landscape is now plotted using the refined Landau parameters; see Figure 8c. We then seek to understand the dynamics of the subsequent order parameter amplitude evolution following the quench presented in Figure 8b as a potential-driven process on the free energy. Based on the local curvature of the potential surface, the initial dynamics shall appear on a downward trajectory (see arrowed line in red in Figure 8c) along which the existing order-parameter amplitude is significantly suppressed, manifesting in a nonthermal melting as witnessed in the initial *c*-CDW state evolution. We note during this period there is no detectable change in **Q** (top panel, Figure 8e). This means the order parameter is temporarily trapped at the saddle point following the local steepest descent. Next, for the nonequilibrium system to establish the broken-symmetry phase with bi-directional components at the new global minimum, the order-parameter dynamics must switch direction. This occurs in the next ≈1 ps based on the **Q**-shift and the rise of *a*-CDW intensity ($\hat{m}_a$). However, in the evolution toward the new global minimum the order-parameter field is incoherent driven by fluctuation waves. Since the amplitude mode is gapped, the rate-limiting step is the alignment of the local phase and hence the phase rigidity controls the buildup time. Experimentally, this manifests in the expansion of the static correlation length along with the order parameter amplitude (Figure 8b). The long-wave modes order the field on increasingly larger scales at the bottom of the free energy surface—a scenario described by coarsening as discussed in Section 2 and Figure 1c. Hence, the simple phenomenological free-energy model explains the stepwise manner in which the hidden state is introduced into the system as observed by the UED experiment.

6.1.3. *Connections between field instabilities and soft modes*

Now we utilize further UED results to look into the microscopic details of the nonequilibrium processes. Of particular interest here is to understand how the rise of the microscopic soft modes is connected to the order-parameter field fluctuations in a nonequilibrium SSB driven by the quench. Here, the nonadiabicity plays a role because of separation of scales. Along the $|\eta_a|$ direction, the order parameter field is initially disordered. Mathematically, a long-wave AM is formed by coherently joining two counter-propagating soft modes. However, initially the order-parameter field is unstable because of the upturned parabolic free energy at initial times [61,163]. Only the longest fluctuation wave ($|\mathbf{k}| \to 0$, $\omega \to 0$) will be relevant to the formation of a single-wavevector incommensurate CDW. The phase transition cannot be said to have happened if the ensemble averaging is taken over a fluctuating order parameter field, where $\langle|\eta_\alpha|(\mathbf{r}, t)\rangle$ amounts to zero. The rectification to form a static order from the dynamical modes here requires a parametric growth of phase-coherent AM modes.

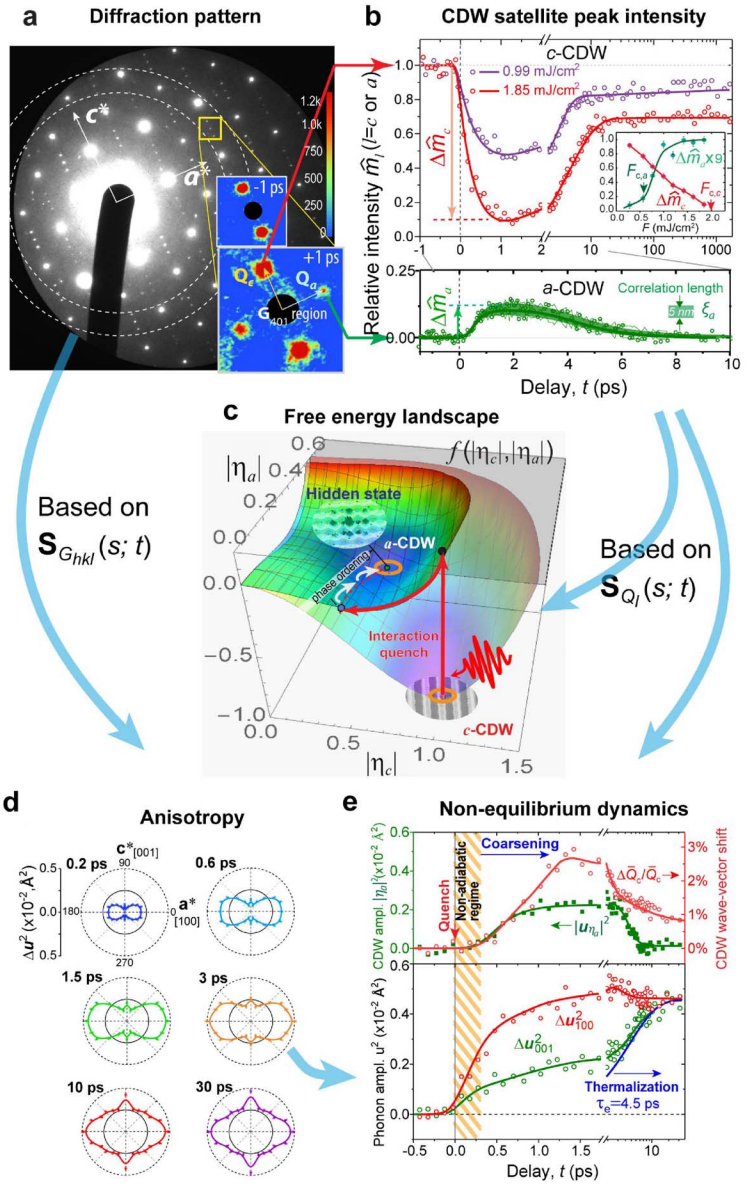

Figure 8. Nonequilibrium dynamics into a hidden checkerboard order in $CeTe_3$. (a) Diffraction pattern of $CeTe_3$ thin film. The inset shows the scale-up view of the patterns near $\mathbf{G}_{401}$ before (−1 ps) and after (+1 ps) applying pump pulses. (b) The evolution presented in terms of the diffraction integrated intensity for the order parameters. The inset shows the respective changes obtained at the metastable period (~1.5 ps) as a function of fluence. (c) The Landau–Ginzburg free-energy surface obtained for the $F = 1.85$ mJ/cm^2 case. (d) Lattice phonon responses deduced by the momentum-dependent Debye–Waller analyses. (e) (Top) The order parameter field evolution examined via $|u_{0,\eta_a}|^2$ and $\Delta\bar{Q}_c/\bar{Q}_c$ respectively for a- and c-CDWs. Here, $\bar{Q}_c$ is the mean wavevector of the c-CDW. (Bottom) The vibrational *ms* phonon amplitude changes projected along [001] and [100] were obtained from the Debye–Waller analysis. Panels a, b, d, e are adapted with permission from Ref. [23].

To understand the initial nonadiabicity pertaining to SSB driven by a quench, we track the scattering weight transfer between $S_{\mathbf{G}}$ and $S_{\mathbf{Q}}$. For evaluating **q**-dependent phonon dynamics, one obtains the differential-mean-square lattice fluctuations Δu^2_{hkl} by taking the logarithm of the normalized $\hat{m}_{\mathbf{G}}$ (after excluding the contributions from the quasi-static CDW-related Bessel function terms; see (27)–(30). This results in a differential DWF, i.e., $l_{hkl}(t) = \mathrm{e}^{-2M_{hkl}(t)}/\mathrm{e}^{-2M_{hkl}(t<0)} = \mathrm{e}^{-2\Delta M_{hkl}(t)}$, which can be taken at different $\mathbf{G}_{hkl}$ to determine the differential fluctuations $\Delta u^2_{hkl} = 2\Delta M_{hkl}$ projected in the direction of $\mathbf{G}_{hkl}$; see (20). The results of this analysis taken from an array of $\mathbf{G}_{hkl}$ along different directions are shown in Figure 8d. The strong anisotropy in Δu^2 reflects the underpinning energy landscape, or **q**-dependent electron–phonon coupling that shapes the phonon dispersion curves of the lattice modes upon phase transitions. The large amplitudes of motion reflected in the Δu^2_{hkl} along the [100] and [001] directions indeed reveal the predominance of the soft modes directly driven by the landscape changes. Their excitation, within the first 500 fs (see Figure 7e), is clearly much faster than the generic laser-induced heating (over a few ps).

Now, we turn our attention to the correspondingly determined long-wave parameters, specifically the order parameter amplitude $|u_{0,\eta_a}|^2$ and the momentum wavevector shift (see Figure 8e). It is quite evident that the build-up of the long-wave modes appears mainly after the soft mode amplitudes have peaked. The results obtained here highlight the essential different dynamics due to separation of scales, and the close relationship between the fluctuation waves (both in the symmetry-breaking and recovery processes) and the respective order-parameter evolution. The empirical results also show nonergodicity between soft modes pertaining to the two CDW systems. A period, where the soft mode amplitudes characterized by the $\Delta u^2_{100}(t)$ and $\Delta u^2_{001}(t)$ along the two perpendicular CDW fields diverge, is witnessed (Figure 8e, bottom panel). One can easily correlate this period with the timescale where the metastable a-CDW phase is created and then destroyed. This reaffirms the out-of-equilibrium phonon dynamics have a key role in sustaining the hidden state. Accordingly, the system thermalization timescale t_{th} is determined to be ~4.5 ps.

6.1.4. *Nonthermal critical point*

Finally, we address how conceptually one can unite the interaction quench with the temperature quench to understand nonthermal SSB as a condensation process on a new free-energy landscape. As is the case under the equilibrium condition, the local temperature of the CDW state is a co-control parameter for the transient free-energy landscape when it is influenced to undergo SSB by the laser interaction quench. Accordingly, we can introduce the concept of the nonthermal critical point T^*_c, which is defined by rearranging the Landau–Ginzburg equation:

$$T^*_{c,a} = T_{c,1} - \frac{\tilde{A}}{a'}|\eta_c|^2. \tag{32}$$

First, one can see how this concept applies to suppress the formation of a-CDW under a competitive SSB at equilibrium. Given the degenerate critical point $T_{c,1} = 540$ K [154, 159], with the c-CDW chosen as the equilibrium ground state ($|\eta_c| = 1$ at $T_b = 300$ K), the experimentally identified $\tilde{A}$ and a' shift $T^*_{c,a}$ to a lower temperature (222 K) than T_b. Furthermore, following the BCS behavior, the $|\eta_c|$ is expected to rise as T_b is lowered [154]. This means further cooling the system in the broken-symmetry phase will continue to push the $T^*_{c,a}$ even lower. This explains why under the equilibrium condition the a-CDW is suppressed once c-CDW becomes the dominant ground state. However, the scenario will change entirely under a nonequilibrium condition where $|\eta_c|$ is driven to an amplitude below the critical threshold ($|\eta_{c,\mathrm{th}}| \approx 0.87$ from (12)) by an interaction quench. In the case described in Figure 8b, the $|\eta_c|$ is reduced down to 0.32 at the laser fluence of 1.85 mJ/cm^2, where the corresponding $T^*_{c,a}$ (508 K) is now well above T_b. Therefore, from the

perspective of a-CDW, the system is now in a scenario akin to a deep temperature quench and will undergo condensation to form a new broken-symmetry order in much the same way.

6.2. *Metamorphosis in vestigial density-wave system: tantalum disulfide*

Here we will approach a different type of light-induced hidden phases involving competitions but not in the same vein as the RTe_3 system. The system is 1T-TaS_2, which belongs to a broad class of layered transition metal dichalcogenide (TMDC) compounds [164]. Similar to RTe_3, these TMDC compounds have isolated 2D metallic layers; see Figure 7. However, the in-layer atomic structure is triangular rather than square lattices within which the triply degenerate CDWs emerge [164]. Of particular interest here is 1T-TaS_2, which hosts nontrivial charge-density wave orders driven by several factors: the instabilities at the Fermi surface, the large lattice distortion possible, and the localized orbital that leads to a Mott–Hubbard gap at the low temperature [151, 164–166]. The hidden CDW state formation in 1T-TaS_2 [18] was among the first that was demonstrated in TMDC and since cross-examined by optical [167], resistivity [168], scan tunneling microscopy (STM) [169–171], X-ray [172] and electron scattering [19, 173] techniques. Besides1T-TaS_2 [18, 19, 168, 169, 172], light-induced hidden states have also been found in 1T-$TaSe_2$ [174], 3R-$Ta_{1+x}Se_2$ [175, 176], and 1T-$TaS_{1-x}Se_x$ [173].

Within the Ta layer, the low-temperature ground state forms 13-site clusters in which 12 out of 13 Ta^{4+} ions are distorted towards the central Ta atom to a David-Star shape; see Figure 6d. It is understood that the unpaired electron in a 13-site cluster with a large spin-orbital coupling gives enough correlation to form a Mott insulator. The $\sqrt{13} \times \sqrt{13}$ superlattice clustering forces the density-wave state to lock-in to the atomic lattice, forming the long-range commensurate charge density order (C-CDW) under ambient pressure. Upon warming, the increasing electronic instabilities deviate the CDW from its perfect commensuration with the lattice, driving a series of discommensurate (DC) state. Upon warming from C-CDW, the ordering first changes to a triclinic state (T-CDW) state at $T_{\text{C-CDW}} \sim 220$ K, then to a hexagonal nearly commensurate density wave (NC-CDW) state at $T_{\text{H-NC}} \sim 280$ K, and finally to an incommensurate CDW (IC-CDW) state at $T_{\text{IC}} \sim 350$ K. The material eventually loses the density-wave order and becomes metallic at $T_{\text{M}} \sim 540$ K [146–148, 177].

The delicate density-wave ordering is also subject to tuning by chemical doping or applying pressure and can generally lock into a certain type of nearly commensurate ordering before the system entirely loses the David-Star clustering feature. Eventually, melting of the David-Star clusters allows the system to adopt a purely sinusoidal form of single-wave vector IC-CDW [178]. The multi-**Q** effect (Figure 6b) is pronounced in all forms of NC-CDW [144], in which the CDW deforms from the sinusoidal shape by developing periodic phase slip at distance ξ_D [179], forming the domain walls or discommensurate (DC) region. Within the domain, the CDW maintains the commensurate ordering, whereas on average the NC-CDW state has an incommensurate wavevector to avoid the penalty of raising the elastic energy as a whole [151, 178, 180]. This new self-organizing scheme as pointed out by McMillan [178] creates long-range periodic DC textures. In principle, this discreteness effect from the longer-range lock-in scenario will lead to stabilization at every possible topologically compatible DC network, so-called Devil's staircase [181]. In practice, only a few DC structures will develop out of balance between the commensuration energy and instabilities driven by thermal excitations. The triclinic [182] and hexagonal NC [53, 177] states identified in the equilibrium phase transitions belong to these DC states [145, 178].

In these intermediate phases, the C-CDW characteristics are only partially lost by the increase in itinerant instabilities. Therefore, they may be considered as a type of vestigial order [67,68,183]. Here, unlike the case for RTe_3, the CDW transformation may be modelled on a single order

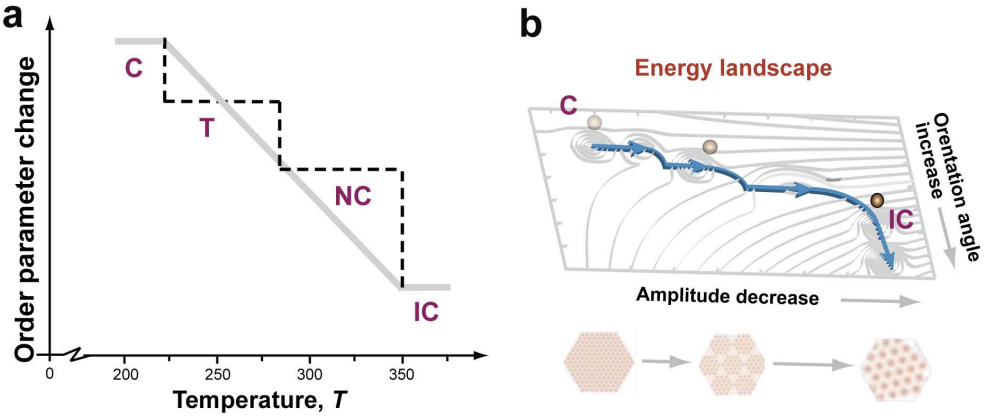

Figure 9. Theoretical depiction of the CDW order parameter evolution in TaS_2. (a) The temperature dependence of various order parameters. (b) The two-dimensional landscape hosting the various CDW orders. Panel b is adapted with permission from Ref. [19].

parameter $\eta = |\eta|e^{i\phi}$, where the deviation from $\phi(r) = \mathbf{Q}_c \cdot \mathbf{r}$ locally produces additional free energy gain [178–180]. With McMillan's DC network additional terms in the Landau's free-energy equation are introduced where the CDW phase plays an explicit role in the lock-in energy. The essence of McMillan's model has been shown to describe CDW systems with different types of commensurate orderings; see e.g. Refs [145, 180].

Taking the essence of McMillan theory and the chief experimental observables from the UED experiments, one can give a similar phenomenological model [113, 184] to capture the essential features in TaS_2 CDW phase transition in which the free-energy density is given by

$$f = f_0 + C|\eta|^2(\nabla\phi - \mathbf{Q}_{\mathrm{IC}})^2 - D|\eta|^2\cos(\phi - \mathbf{Q}_{\mathrm{C}} \cdot \mathbf{r}) + \mathrm{H.O.} \tag{33}$$

The first term $f_0 = A|\eta|^2 + B|\eta|^4$, where $A = \alpha/2(T - T_M)$ has the expression like (1) and is the leading order in the Landau–Ginzburg equation that defines a continuous phase transition. The second term comes from the energy cost of distorting the CDW structure from its ideal IC state set by the susceptibility. The third term reflects the lock-in effect, which favors the commensurate order. The last term contains the additional higher-order CDW interactions and the multi-**Q** effects [179]. It is easy to see from (33) that the most important factor setting the energy scale is the CDW amplitude $|\eta|$, whereas the lock-in condition set by topology will determine the stable **Q** that the vestigial order could settle (discreteness conditions). Here, the coefficients A, B, C, and D are all positive, which allows (33) to capture the generic trend of IC-to-C transition [148, 180]. First, let us assume the system is homogeneous. Driven by the lock-in energy gain by the amplitude increases upon lowering the temperature from T_M, the **Q** evolves continuously and creates a jump in both **Q** at $T_{\text{C-CDW}}$; see solid line Figure 9a that is the case for the 2H-$TaSe_2$ phase transition [47]. Now considering the inhomogeneity created by the DC network, relevant to the 1T-polymorph, the CDW system gains additional stabilities by deformation under the discreteness conditions. Here, deviating from the purely sinusoidal form by developing $\Delta\phi(\mathbf{r})$ in the associated DC network, additional jumps by the new vestigial orders are created; see dash line in Figure 9a. Given that the magnitude of the **Q** does not change significantly, the free-energy landscape can be cast in two effective parameters [19]: the amplitude ($|\eta|$) and the orientation angle of **Q** (φ) with respect to $\mathbf{Q}_c$ [148] measured in UED. Such a 2D free-energy landscape is schematically depicted in Figure 9b.

More exact models considering the multi-**Q** and high-harmonic effects will be required to precisely determine the experimentally observed vestigial triclinic and hexagonal NC-CDW states [145, 179]. We note, the delicate discommensuration model extended by Shiba and coworkers to include all essential high-harmonics and multi-**Q** interactions based on diffraction [144, 145, 179] can accurately predict the structure of the triclinic and hexagonal NC-CDW states, which have been confirmed by STM experiment [185]. Nonetheless, the phenomenological model given here, while ignoring the multi-**Q** and high-harmonic effects, is sufficient to capture the essential physics of DC phase transitions.

With the phenomenological equation, we are now in a position to understand the basic physics of photoinduced CDW transformation. While not a direct competitive scenario [23], driving down the $|\eta|$ via a laser quench can tip the balance between the commensuration energy gain and the elastic energy cost, triggering the reorganization of the density waves as discussed above. The narrow half-filled band is crucial for the low-temperature Mott phase and the associated cluster-type structure distortions. Therefore, the optical interband excitation from this localized band can lead to the effect of doping poised to shift the energy landscape before carrier thermalization [186]. The experimental phenomenology relevant to the impulse-adiabatic picture of unfolding the order-parameter free-energy landscape [18, 19, 167] is given by recent experiments: trARPES shows the collapse of the Mott–Hubbard gap within 50 fs [186, 187], while the carrier thermalization appears in ∼200 fs to reduce the Peierls gap [187]; the carrier-lattice equilibrium proceeds on an even longer timescale (ps) which are probed by UED [19, 188–191].

Taking the lead from the interaction quench scenario in $CeTe_3$ problem [23], we can identify the critical thresholds into different DC states as identified by the equilibrium free energy equation. In principle, there is a direct mapping between the equilibrium phase transition and photoinduced phase transition in this manner. By rearranging (33), we obtain

$$f = \frac{\alpha}{2}(T - T^*_{c,l})|\eta|^2 + B|\eta|^4 + \text{H.O.},$$

with a new critical threshold $T^*_{c,l}$ shifted by the interaction quench:

$$T^*_{c,l} = T_{c,l} - \frac{2}{V\alpha}\int \mathrm{d}\mathbf{r}[C(\nabla\phi - \mathbf{Q}_{\mathrm{IC}})^2 - D\cos(\phi - \mathbf{Q}_{\mathrm{C}}\cdot\mathbf{r})], \tag{34}$$

where V is the volume of the specimen excited by the laser and l denotes different thermal states. However, the balance between the lock-in energy and the energy cost in deviation from the natural $\mathbf{Q}_{\mathrm{IC}}$ is expected to be different in the temperature and interaction-mediated (doping and applying pressure) pathways. Therefore, the intermediate vestigial ordering will likely be different. For example, a stable triclinic phase has not been known under pressure tuning [151, 192] or chemical doping [193, 194].

Nonetheless, this simple picture allows us to better understand the phase diagrams of nonequilibrium phase transition reported by Han *et al.* [19] and Ravnik *et al.* [167]. In these studies, different metastable phases emerge on the ps or longer timescales. The thresholds for creating these states were found to be dependent on the absorbed photon density, rather than the excitation energy. The UED experiments (Ref. [19]) gave the results on the CDW amplitude and orientation angle for these states, which can be mapped into the Landau–Ginzburg free-energy landscape assuming they are the stationary conditions. In the spectroscopic investigation (Ref. [167]), the time-domain amplitude mode was employed as an indicator for the shifting of the rigidity associated with the free-energy basin supporting the emergence of a new type of CDW orders. These two different views are complementary to each other.

To understand the role of photo-doping, two different pump laser wavelengths, 800 and 2500 nm, were employed. While in both cases, interband excitation (hence photo-doping) is possible, the excess heat deposited per creation of an electron–hole pair is quite different in

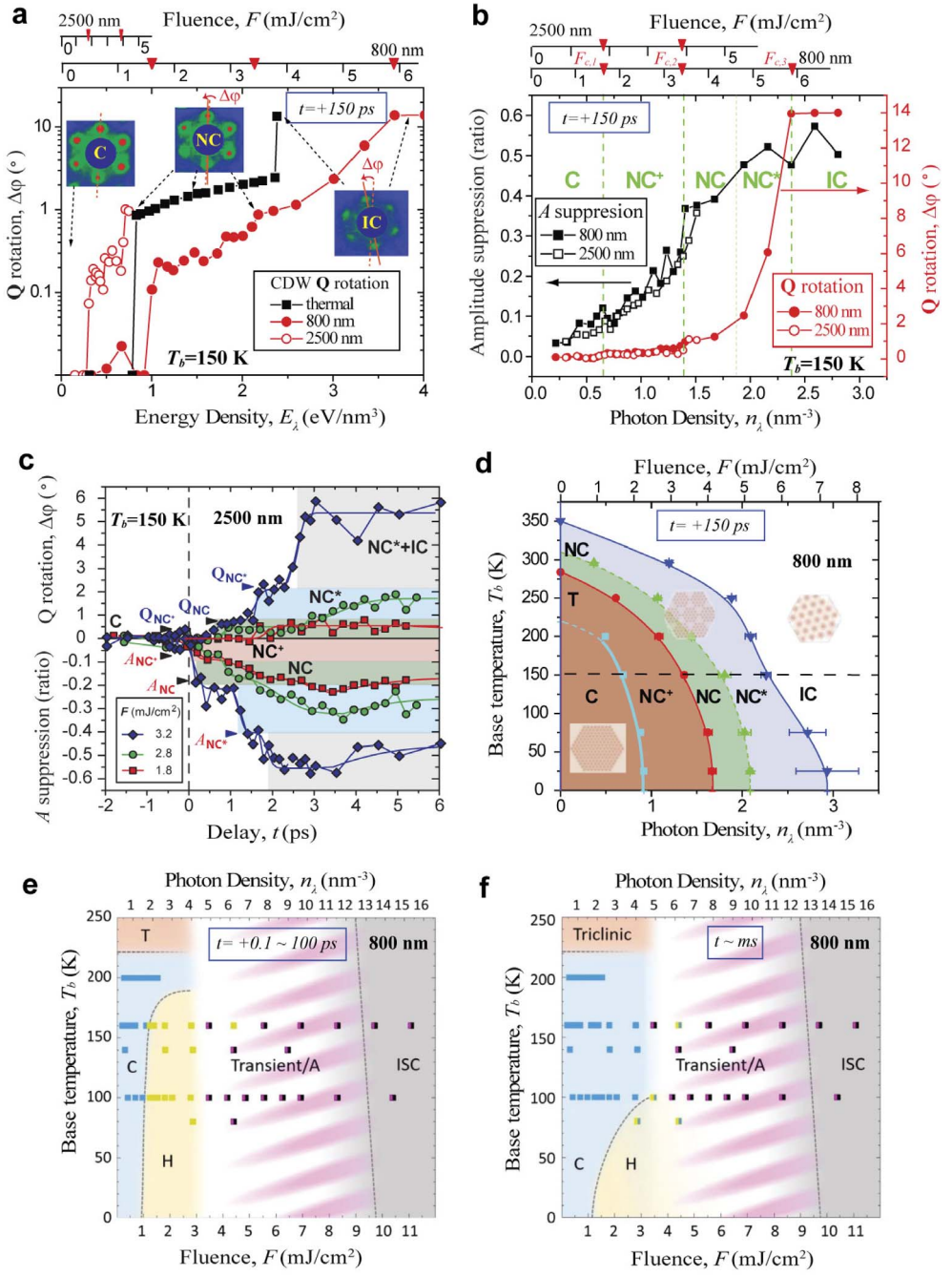

Figure 10. Photoinduced CDW re-ordering dynamics in 1T-TaS_2. (a) Energy-density evolution of the CDW wavevector in thermal and photoinduced phase transitions. (b) Absorbed photo density evolution of the CDW wavevector and the amplitude pumped by 800 and 2500 nm photons. (c) The short-time evolution of the CDW order parameters obtained at 2500 nm. (d) The temperature–photon-density phase diagram obtained at 150 ps pumped by 800 nm photons. (e, f) Temperature-fluence phase diagrams obtained for the ultrashort (0.1–100 ps) and ~1 ms timescales pumped by 800 nm photons. Panels a–d are adapted with permission from Ref. [19]; panels e–f are adapted with permission from Ref. [167].

the two cases—differs by a factor of 3. In Figures 10a and b, the respective CDW amplitude and orientation angle changes are recorded at delay $t = 150$ ps. The distinct shift in the orientation angle gives a handle to compare phases driven by the two different excitation wavelengths. The relevant changes obtained under the tuning by temperature are included for comparing results based on the applied energy density into the system with the initial state temperature (base temperature, T_b) set at 150 K well below the $T_{\text{C-CDW}} \approx 280$ K.

We note that from the diffraction results the eventually achieved IC structure (by 800 nm laser) is consistent with that of a thermal state. However, the intermediate phases, identified by the steps in the angular shift, appear to deviate slightly from the known triclinic and near commensurate phases [148, 182]. We also note that in the results obtained from the two different laser excitations the correlation between the amplitude and orientation angle changes is excellent. This allows Han *et al.* [19] to rescale the applied fluence into a common scale based on the absorbed photon density within the experimental uncertainties, taking into account the difference in the absorption cross-sections from the two laser wavelengths. These results thus are in support of distinct pathways from the non-thermal transitions, irrespective of the applied photon wavelengths. A notable difference is, while the 800 nm laser pulse can bring the system entirely to the eventual IC phase, the 2500 nm excitation fails to reach the same level without causing irreversible change to the CDW system. This observation suggests that thermal energy plays a more important role to fully establish IC-CDW than in the transitions into other vestigial orders.

The phase diagram reported by UED portrays the metastable phases that can persist up to 150 ps (Figure 10d) [19]. The time-resolved measurements using 2500 nm laser pulses however confirm that the multi-stability nature of the light-induced free-energy landscape already appears on a relatively short timescale [25]. Three different fluences were applied targeting different eventual phases based on the phase diagram established using the data at 150 ps; see Figure 10c. The phase progression was tracked through $|\eta|$ and $\Delta\varphi$ of the CDW. Without any exception, the phase evolutions progress in a stepwise fashion [19]. First, at a higher photodoping level where one may assume a greater number of free-energy basins will become accessible; see Figure 9b. However, the steepest descent is only defined by the accessible pathway to the nearest energy basin, and those different basins are separated physically by the length scales set by discreteness conditions (orientation angles)—along which the slope of the free energy is significantly smaller. This explains the stepwise behavior in which the transformation is taken place as the free-energy landscape does not allow a straight path from the initial to the eventual state.

As shown by Figure 10c the metastable states that could be accessed over a shorter time period are slightly different as the free-energy landscape will continue to evolve over time due to thermalization with the baths. Nonetheless, the key characteristics of these states, as characterized by $|\eta|$ and φ, do not change significantly. This indicates that the reported vestigial orders are distinct. Furthermore, from the width of the corresponding satellite scattering structure factors, these orders generally possess a long correlation length. As the appearance of the metastable state is relaxational (9), the stronger initial quench due to carrier doping naturally leads to a deeper level of the energy basin to be exposed before the system has time to thermalize. This is an important point to raise because it shows that the impulsive unfolding of the energy landscape is key to set the stage for the order parameter evolution as a relaxational dynamic.

The remarkable ability for the vestigial system to self-organize into different long-range phases in a relatively short timescale shows the evolution is driven largely by the potential effect than the stochastic dynamics. Should the excitation be by a longer pulse, as so demonstrated with a pulse longer than 4 ps in the experiment by Stojchevska *et al.* [18] and during which the slowly doped system has a sufficient time to interact with the bath, the order parameter evolution would be more thermal-like, namely one would not be able to observe the reported HCDW (Refs [18, 167]) in this case.

There is a growing body of evidences [167, 169, 172] suggesting that the first vestigial order (labelled initially as "T" phase in Ref. [19]) following the laser quench to be one that is identified as HCDW. The key signature to identify a vestigial order is by its deviation from the commensurate ordering ($\mathbf{Q}_c - \boldsymbol{\delta}$) ~ $\mathbf{Q}_c \Delta\varphi$, thereby defining a characteristic domain size, $\xi_D = 0.69a/\Delta\varphi$ (nm), related by the Fourier analysis [179]. The change in φ at the first critical point identified in Figures 10a, b is ~0.2°, which is much smaller than that of the triclinic phase at equilibrium (~1°). This signifies a much longer-range domain/discomemnsuration structure [179]. Interestingly, this relevant length scale matches the characteristic length scale of the HCDW structure revealed by STM [169], which also suggests the structure as chiral. A recent X-ray diffraction investigation of HCDW also indicated a φ-shift and correlated the change with the loss of interlayer dimerization [172]—which the authors attribute as a defining factor introducing the insulating behavior in the C-CDW phase [195], although the relative roles of interlayer stacking and the Mott physics for the insulator-metal transition in TaS_2 are still debated [165, 171, 196–199]. The three independent measurements give a similar laser threshold ~1 mJ/cm^2, for the light-induced phase transition. Therefore, it is very likely the first vestigial order identified here to be the same as HCDW first reported by Stojchevska *et al.* [18].

All the vestigial states identified by the UED experiments are demonstrated to reverse back to the C-CDW after the pump–probe cycles of 1–10 ms. While the initial discovery of the persistent HCDW is obtained at the lower temperature than studied by UED, with a higher base temperature as investigated by Ravnik *et al.* the HCDW is shown to be less stable. This may explain why the system is reversible over a ms repetition rate, making it subject to the pump–probe optical measurements. To this end, the time-domain phase diagram established by Ravnik *et al.* (Ref. [167]) also gives a second threshold for transitioning into other types of ordering upon a higher level of excitations—see Figure 10f. This second fluence threshold is ~3 mJ/cm^2, which again is consistent with what reported by UED for transition into the second NC vestigial order via 800 nm laser pulses (Figure 10a) [19]. However, we wish to point out a key difference between the two studies that the irreversibility or disordered states tend to emerge under a higher level of excitation in the STM experiments; whereas in UED studies the system can be driven all the way to the IC state while maintaining the long-range correlation in the photo-doping regime. This notable difference may be explained on the basis of distinction in the sample settings in the two experimental approaches. In the UED investigations, the specimens are typically exfoliated to the thickness less than 50 nm and studied at a higher base temperature. This is in contrast to the STM experiments where the nonequilibrium dynamics are induced at the surface of a bulk sample and typically required a lower temperature to induced a long-live HCDW [167]. Below, we investigate this initial state sensitivity relevant to controlling the evolution of the vestigial orders.

6.3. *Pump-inhomogeneity-driven dynamics*

Recently from careful analyses of the order parameter responses through time-resolved optical techniques [200] and X-ray diffraction [201], transient stabilization of inverse order parameters [202–205] have been suggested. This possibility is explained on the basis that the broken-symmetry state with local lattice distortion opposite to that of the ground date can be transiently trapped due to the formation of domain walls [200, 206] between the two extrema phases. This scenario was thought to originate from the short penetration depth of the laser pulse relative to the sample thickness. The inhomogeneous excitation could lead to distinctly different phases at different depths within the sample in systems with multiple stable alternative ground states. The externally applied pressure or the strain induced due to sample-substrate mismatch has been used to create a metastable state [168, 207]. It is possible that the light-induced inhomogeneity

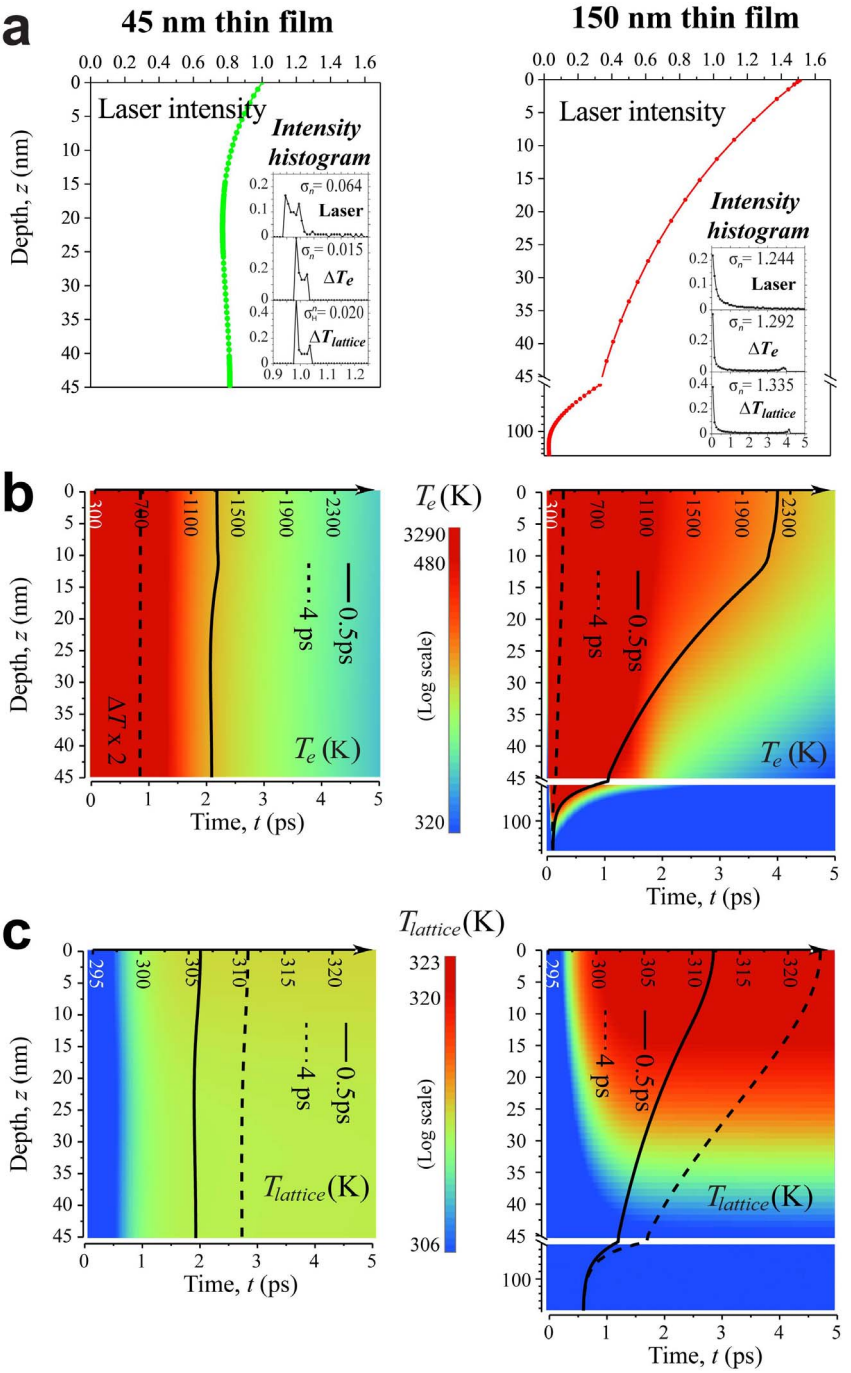

Figure 11. Quasi-particle (electrons and phonons) temperature evolutions in photoexcited TaS_2 thin films by the three-temperature diffusion model. (a) The laser excitation (800 nm, 50 fs) profile within the 45 and 150 nm thin films. The inset shows the histograms of the intensity and temperature distributions along z taken at 4 ps. (b) The time (t)-depth (z) evolution of the electronic temperature, $T_e(z,t)$. (c) The time (t)-depth (z) evolution of the lattice temperature, $T_{\text{lattice}}(z,t)$.

may be yet another control parameter that plays a role in creating the metastable energy landscape.

We look into this issue by considering near-infrared laser excitations in samples with slab thickness used in the UED experiment (45 nm) and one that is much larger (150 nm) representing the bulk limit. A focus is to consider how different sample thickness settings will alter the excitations and hence influence the interpretation of the results obtained from the different types of pump–probe experiments. In Figure 11a we show that by simply changing the sample thickness by a factor of ≈3, the excitation of the materials can be altered drastically. The differences are most apparent by comparing the laser absorption intensity profile $I(z)$, calculated for the 1T-TaS_2 [208] by solving the Maxwell's equations [209,210]. In the same sub-surface region (0–45 nm) from the top excited surface ($z = 0$), the 150 nm system shows an exponential-like decay profile with an effective penetration depth of just ≈25 nm, which is expected as if the film is a bulk sample. On the other hand, for the 45 nm film, the profile becomes nearly homogeneous. This striking difference reflects the effect of the interferences active in the thinner film where a finite optical penetration leaves a sizeable, reflected component for the waves to interfere internally. This Fabry–Perot effect can sufficiently build up before the ≈50 fs pulse leaves the slab. It can even create an inverted effect as shown in the 45 nm slab where the intensity from the back surface is slightly higher than the one in the middle; see the left panel in Figure 11b.

To characterize the effect of interferometric modification, we calculate the normalized intensity distribution given in a histogram (see inset of Figure 11a). The differential RMS value evaluating the dispersion effect is calculated as:

$$\sigma_n = \sqrt{\frac{1}{N}\sum_i \left(\frac{I(z_i)}{\langle I(z)\rangle} - 1\right)^2}.$$

We obtain a σ_n of 0.064 for the 45 nm film, whereas for the 150 nm film it is 1.244. It is intriguing to observe how this initial laser intensity profile will drive the diffusion of the carriers and phonons in the systems. The exchange of kinetic energies between the carriers and phonons, which defines respective effective temperatures for electrons, SCP, and WCP subsystems, is described by the three-temperature model (3TM) (Section 5 and the Appendix of this paper). We note the typical 3TM [13, 109–112] is conceived mainly for a homogeneous system. To consider diffusions by the hot carriers and phonons excited more significantly at the top surface, we set up the diffusion equations [211] coupling to 3TM and establish the three-temperature diffusion model (3TDM) [212] to allow us capturing the spatial temperature profile evolution. Here, we report on the temperature profiles $T_e(z,t)$ and $T_{\text{lattice}}(z,t)$ for the electron and lattice subsystems that will be relevant to addressing the complementary perspectives of the microscopic dynamics probed by the ultrafast scattering, trARPES, THz spectroscopy, and optical reflectivity techniques.

We set up the problem by considering the ultrafast dynamics of electron temperature, $T_e(t)$, made available recently for 1T-$TaSe_2$ by trAPRES experiments [174]. We apply the 3TDM with the 3TM coupling parameters determined based on fitting the experimental $T_e(t)$ data. These parameters are used as the generic coupling constants and applied to the 1T-TaS_2 dynamics. We note that from the fitting of the coupling constants between the electron subsystem, SCP and WCP, we derive three characteristic timescales for "electron–phonon" coupling: 0.5, 1.8 and 40 ps, which lead to a general ps heating dynamics of the lattice consistent with many recent experiments [189–191, 213]. We then report in Figures 11b, c the transient temperature maps $T_e(z,t)$ and $T_{\text{lattice}}(z,t)$ with the mean lattice temperature calculated according to $T_{\text{lattice}} = \alpha T_{\text{SCP}} + (1-\alpha) T_{\text{WCP}}$, where $\alpha = 0.1$ as the fraction for SCP is determined also from the fitting. The details of the modeling and the parameters used are listed in the Appendix.

The full results for the first 5 ps are depicted in Figures 11b, c in the dynamical temperature maps of $T_e(t,z)$ and $T_{\text{lattice}}(t,z)$. To see the effects of diffusion, one can compare the temperature

profile at a given time (the results from 500 fs and 4 ps are highlighted) with the initial $I(z)$. Notably, for the 150 nm film, diffusion strongly modifies the temperature profile already in the sub-ps timescale in the top surface region, which is probed by trARPES and X-ray diffraction. From the results obtained at 500 fs for the 150 nm film, the diffusion effect creates a nearly homogeneously excited top region ($\approx$10 nm) and a sub-surface region where a sharp decay occurs; see the right panel in Figure 11b. However, over the entire period of observation, the strong inhomogeneous profile over the 150 nm film has not been lifted in the temperature evolutions. Meanwhile, for the 45 nm film the diffusion effects have improved the uniformness of the temperature profile further, as indicated in the σ_n calculated for $T_e(t,z)$ and $T_{\text{lattice}}(t,z)$ going from 0.064 of $I(z)$ to 0.015 and 0.020 respectively. The high degree of uniformness starting even at the short timescales is expected to be an important aspect in characterizing the critical dynamics associated with the nonequilibrium phase transitions.

We examine how this pump-associated inhomogeneity affects the experimental results. Locally applying the impulse-adiabatic scenario for introducing the free-energy landscape, the strong inhomogeneity scenario is expected to have a direct consequence on the order parameter competitions in the key length scales. This effect has been recently reported for $SmTe_3$ system [201], but the phenomenon has been discussed earlier for $TbTe_3$ [200]. The authors posited that the excitation intensity gradient may lead to phase separation along the slab making the domain wall formation between the highly excited region and below. The domain wall formation is said to have helped stabilize the formation of inverse order parameters which were recently hinted also in other TMDC systems [202–205].

We now discuss how the pump-inhomogeneity-driven dynamics affect the dynamical order parameter measurements. It may be now apparent that employing a reasonably thin or small volume specimen will present a better chance to investigate the delicate nonequilibrium critical dynamics. The homogeneous initial condition in the pump profile allows the volume- integrated scattering intensity profile to reveal the true statistics of the nonequilibrium phases in the transient evolution of the state. In contrast, while the surface sensitive probe also samples a relatively homogeneous region, the dispersion effect is less well-defined with the diffusion effects present in nearly all the time. This energy dissipation from the surfaces however might help reduce the bath temperatures in the region that couples to the light-induced state. The study of $CeTe_3$ suggests this may lead to a slower decay of the transiently induced hidden phase [23]. In general, σ_n sets a limit on the ability to characterize the width of the phase transition curves and the critical thresholds which are crucial for modeling the nonequilibrium phase transitions as discussed earlier. In addition, the 3TDM investigation here shows that to cross-correlate the results from the different types of measurements, the empirically derived critical thresholds will need to be adjusted to consider the excitation profile differences. Such differences are likely to play a role in properly assigning the optical doping concentration in Figures 10d–f.

Two different possibilities of additional phase control might result from the pump-induced inhomogeneity. Forming domain walls between competing broken-symmetry phases is one of them. The second control could be the strain effect introduced by the dynamical inhomogeneity, which will be most dominant in a system where different morphologies or lattice structures are created during the phase transition. Such effect could be mediated by the interlayer couplings in layered quantum materials.

6.4. *UEM experiments*

The ultrafast electron microscopy provides a unified setting to probe the order parameter dynamics in both the real space and momentum space. This can potentially address the questions concerning inhomogeneities both in terms of the sample as well as the pump setting as

discussed earlier. Central to the multi-messenger approach is to cross-correlate the information obtained about the same illuminated materials in spectral, imaging, and diffraction modalities. Thus far, the discussion of nonequilibrium phase transition presumes a homogeneous dynamical system—one that does not always occur as discussed earlier.

Transmission electron microscope (TEM) provides information of the microscopic features in greater detail than optical approaches. Such information is highly valuable in cross-examining the results provided through spectroscopic or diffraction approaches that typically integrate signals across the region of the entire probe. Unpacking site-specific information requires adjusting only the post-specimen imaging optics of the TEM [143, 214], which, when switched from the diffraction setting to imaging, offers a direct view of the dynamical system in exactly the same pump and probe conditions at the sample plane.

There are multiple ways with which the imaging contrast can be created under a TEM. In Figure 12a we present the typical exfoliated sample images of TaS_2 obtained using the ultrafast electron microscope. The image is obtained in the so-called bright-field mode in which an aperture at the back focal plane of the objective lens (the diffraction plane) passing only the unscattered beam to form the image [215]. In this geometry, the mass-thickness determines the baseline of the intensity level—e.g. see the thinner film at the edge and the small debris left on top of the film are respectively lighter and darker than the general area of the 40 nm film. But even with the same film thickness, the diffraction effect produces fringes, so-called bend contour, from the sample curvature [215].

The diffraction-mediated contrast is sensitive to the inclination of the sample relative to the beam. At the regions of the bright or dark fringes, selected by a tilt angle, the diffraction contrast is enhanced drastically [215]. This is utilized to measure the acoustic waves created as a side product of the laser excitation. The waves traveling back and forth between the front and the back surfaces form a standing wave pattern modulating the sample thickness [216–223]. At the level of exciting density-wave phase transition (~1 mJ/cm^2 in fluence), the lattice acoustic wave amplitude is expected to be less than 1% of the lattice constant based on heating [146, 224, 225]. However, the intensity modulation from the bend fringes can achieve resolution better than 0.01%, serving as a powerful way to resolve the out-of-plane dynamics.

The dynamical contrast based on the oscillation frequency can offer a measurement of sample thickness to the precision of mono-stacking layer [217, 222]. This is shown in comparing the results from different regions, marked in A, B, C, and D in Figure 12c; here in the region B the film oscillates in the direction opposite to that of the regions A, C, D. Taking the oscillation out to 400 ps, the oscillation from region D is slightly out of sync with the rest. From the phase difference, one can determine the delay of 6 ps being developed and gives a local film thickness of 0.59 nm (one Ta layer; Figure 7) higher than the other areas.

Of particular interest is to compare the out-of-plane crystal oscillation with the photoinduced CDW order parameter dynamics, which one obtains by switching to the diffraction mode, as shown in Figure 12b. Both experiments are conducted under the same sample pump conditions (the ~1 mJ/cm^2, 50 fs near-infrared pulse illumination in nearly normal incidence at the repetition rate of 1 kHz). It is interesting to see the two dynamics decouple from each other. The CDW order parameter responds to the laser quench within the first 500 fs, and yet it takes more than 5 ps for the acoustic wave amplitude to start building up. The results here show there is no impulsively driven strain wave created over the first few ps, which is anticipated due to the fact that the in-plane heating, which is much more effective here, is largely homogeneous across the layer as predicted for the 45 nm film (Figure 11). Furthermore, the slow onset and the persistent oscillation of the out-of-plane mode and the absence of such signatures from the CDW order parameter dynamics indicates that the light-induced phase transition behavior is largely a 2D

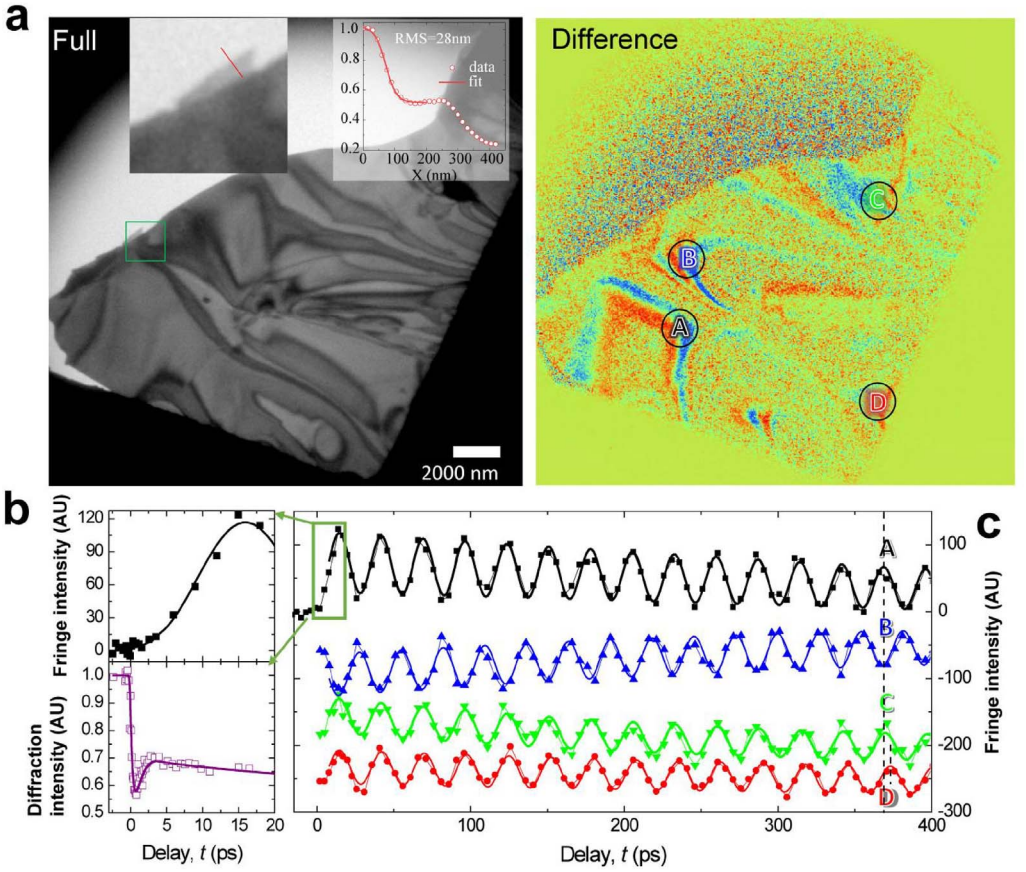

Figure 12. Ultrafast electron microscopy investigation of 1T-TaS_2 thin film. (a) The bright-field image (BFI) of the TaS_2 thin film taken under the UEM in full and difference images. The full image is taken at $t = -20$ ps; while the difference image is taken by subtracting the negative-time full image with one obtained at $t = 15.5$ ps. (b) The BFI intensity oscillation versus the CDW satellite intensity evolution in the first 20 ps upon applying 1.5 mJ/cm^2 near-infrared laser pulse. (c) BFI intensity oscillations at selected regions of the image (see (a)). Region A, B and C have the same time period (T) of 27.20 ± 0.05 ps. A and B are out of phase. Area D has a slightly different time period 27.60 ± 0.08 ps, which is 1.5% higher than the other areas. After 14 cycles of oscillation, we can see a clear offset from area D. The longitudinal speed of sound along the c-axis is $v \approx 3$ nm/ps [54, 227]. The sample thickness can be estimated by $d = vT/2 \approx 40$ nm. The 1.5% difference in the time periods gives ~0.59 nm difference in thickness, which is almost exactly 1 van der Walls layer of TaS_2.

phenomenon—although one fully expects the 3D structural relaxation [225, 226] will take place when the new 2D structure motif is established and the system thermalizes eventually.

6.5. *Light-induced states in strained vanadium dioxide nanocrystals*

Vanadium dioxide is a prototypical phase change material in which a strong metal-to-insulator transition (MIT) occurs near room temperature ($T_M = 68$ °C) [228, 229], making it a subject of strong interests in applied fields [230, 231]. In MIT, distinct changes in the lattice symmetry

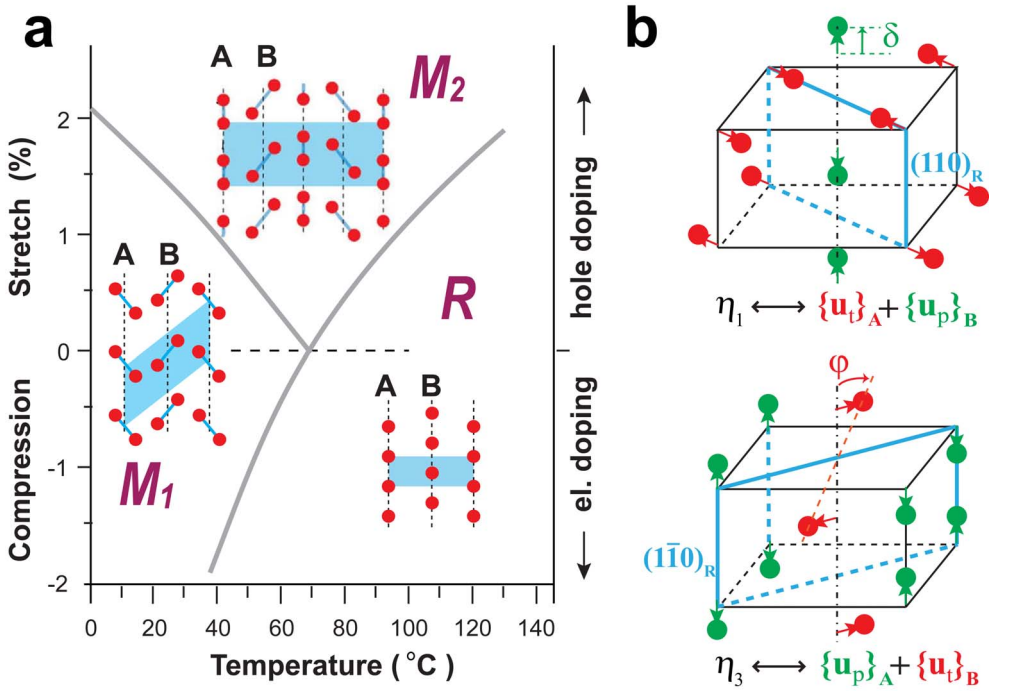

Figure 13. VO_2 structure phase diagram. (a) The schematic phase diagram of VO_2. The layout of the structures highlights the vanadium atom distortions in the A and B sublattice chains (oxygen atoms are omitted). The shaded areas represent the unit cell. (b) The two types of structural distortions $\mathbf{u}_p$ and $\mathbf{u}_t$ along sublattice chains couple to form the structural order parameters η_1 and η_3 for describing phase transitions between R to different broken-symmetry phases [229, 249].

from rutile to monoclinic are involved. The equilibrium temperature-stress/temperature-doping phase diagram involving a triple critical point [232–234] between the rutile (R) and the two monoclinic phases (M_1 and M_2) is depicted in Figure 13a. However, decoupling phenomena between MIT and structure phase transition (SPT) have also been reported in scenarios with additional stimulation by light [235, 236], or applications of external field or current [237], as well as under strain [238, 239] or driven by the interfacial carrier doping [240, 241]. These unexpected complex phase change behaviors casted in doubt the conventional wisdom of MIT based on a simple extension of the Peierls [242] or Mott [243] physics, but rather a picture where both Peierls and Mott physics are involved, referred to as Peierls–Mott or Mott–Peierls mechanism [244–248].

The VO_2 SPT, which intimately couples to different types of MIT, can be described over the two types of antiferroic structural distortion along $\mathbf{c}_R$ [251]: $\mathbf{u}_p$, longitudinal V shift (~0.14 Å) forming V–V pairs and $\mathbf{u}_t$, transverse V shift (~0.18 Å) twisting the V–V chain away from $\mathbf{c}_R$ [229]; see Figure 13b separately in red and green dots representing the movements. Empirical data have suggested that these two types of distortions are not independent. Two degenerate representations involving the coupled $\mathbf{u}_p$ and $\mathbf{u}_t$ distortion occurring separately in two sub-lattice chains (A and B) are outlined in Figure 14b as η_1 and η_3 (following the convention used in Ref. [249]) where $\mathbf{u}_p$ and $\mathbf{u}_t$ are located in the orthogonal $(110)_R$ and $(1\bar{1}0)_R$ planes of the rutile structure. Alternatively, one may also consider η_2 and η_4 where the sequence of $\mathbf{u}_p$ and $\mathbf{u}_t$ in the orthogonal $(110)_R$ and $(1\bar{1}0)_R$ planes are switched. However, only one such a pair is required to construct the

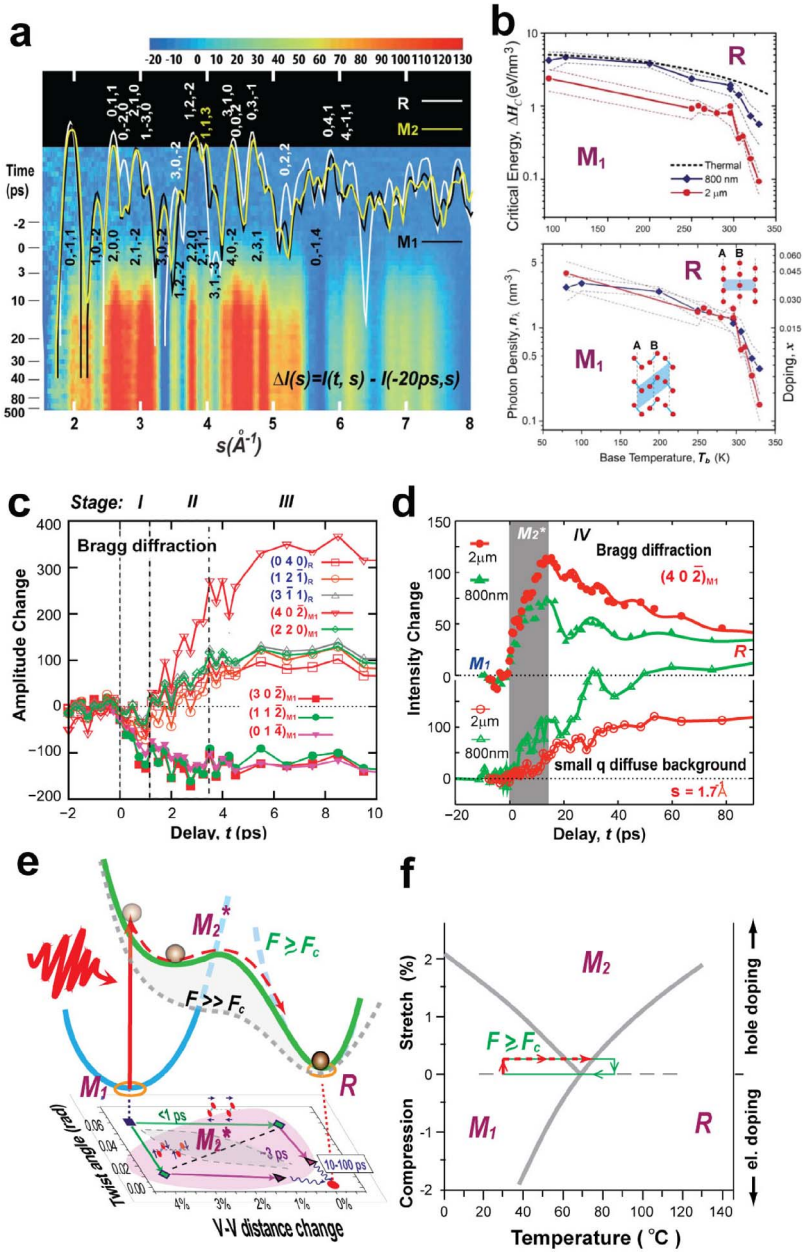

Figure 14. VO_2 structure phase diagram. (a) The diffraction curves modelled after different VO_2 phases and the corresponding diffraction difference map highlighting the change in intensities relative to the unpumped M_1 phase ($t < 0$). (b) The empirical energy density (ΔH)—temperature (T_b) and photon density (n_λ)—temperature (T_b) phase diagrams for VO_2 phase transitions obtained under two different pumping wavelengths. (c) Selected diffraction evolution at the short time. (d) The $(40\bar{2})_M$ diffraction evolution at a longer time showing a cross-over behavior. (e) Schematic free-energy changes that drive a non-straightforward path from M_1 to R state. The intermediate structure domain is that of the M_2, but not exact; hence noted as M_2^*. (f) The structure pathway under the hole doping, involving M_2. Panels a–e are adapted with permission from Ref. [250].

Landau–Ginzburg free-energy density functional for VO_2 written as [249]:

$$f = \frac{a}{2}(T - T_M)\sum_i \eta_i^2 + \frac{1}{4}\sum_{i,j} b_{ij}\eta_i^2\eta_j^2 + \frac{1}{6}\sum_{i,j} d_{ij}\eta_i^2\eta_j^4 \tag{35}$$

where the 4 known stable phases can be identified as the local minimum states with the coordinates of the free-energy basins at $(0,0)$ for R, (η,η) for M_1, $(\eta,0)$ for M_2, and (η,η') for T (triclinic phase) [249]. In this representation, M_2 state, considered as an intermediate between R and M_1 [234, 252] under hole doping or tensile stress (Figure 14a) can transform continuously to M_1 or R—by simply a progressive η_3 or η_1 distortion, respectively [229, 249].

These structural distortions may be linked to the electronic changes at the MIT. The $\mathbf{u}_t$ shift destabilizes the π^* state and provokes an interband charge transfer from π^* to the quasi-1D $d_{//}$ band, which becomes half-filled and can then trigger the Peierls instability to open up an insulating gap through the V–V pairing ($\mathbf{u}_p$) in the M_1 state [228]. However, electron–electron correlations may not be ignored in this scenario [243, 252]. The NMR studies have found that the electron gas in the metallic rutile state is weakly correlated, while the electrons are localized in the dimerized V–V chains in M_1 [234].

Given that VO_2 also exhibits key characteristics of electron-lattice-coupled competitions found in RTe_3 and TaS_2, it is intriguing to ask if there will be a light-induced metastable state whose properties are unlike any known thermodynamic phase of VO_2? Before addressing this, we first note that recent advances from ultrafast measurements have provided rich literature to cast light on the microscopic mechanism of phase transition induced by light excitations. The ultrafast transient electron dynamics investigated by optical [253–255], THz [256–258] and, trARPES [259, 260] generally suggested a more rapid collapse of the band gap when compared to the structure transformations, which were investigated by the diffraction techniques [235, 250, 261–263]. In addition, the transition thresholds as identified by various spectroscopy techniques were found to be smaller than those of the diffraction approaches [250]. These results were taken as indicators that IMT and SPT are decoupled in light-induced phase transitions. However, a recent re-examination of relevant ultrafast spectroscopic measurements has called into question some of the early claims, citing the differences in the pump–probe repetition rates and sample settings as the causes for discrepancies [120]. These issues remain unsettled and remind us of the challenging topics related to the cross-examinations. At the heart of the debates are not simply the nonequilibrium physics from the Peierls distortions versus the electron correlations [228, 229] but also the issues pertaining to the sample conditions [231, 264], such as the strain, disorder, and interfaces that all play a role in the photoinduced phase transitions.

Here, we give a simple phenomenological nonequilibrium model that might unify the understanding of different recent results from UED, trARPES, and optical measurements. It is based on the impulse-adiabatic free-energy evolution picture as one gives to understand the phase transition of the density wave systems. Upon ultrafast laser excitation, a transient free-energy surface is created in which the M_1 structure is no longer the lowest energy basin [249]. Here, the monoclinic phase of VO_2 is characterized by two effective distortive parameters: the twisting angle φ and pairing displacement δ (Figure 13b), which can be directly deduced by analyzing the powder diffraction of VO_2 in the UED experiments. The trajectory of the two distortive parameters which are linked to η_1 and η_3 (Figure 13b) can map the phase transition over the new landscape. Because the eventual R phase has an energy basin where both η_1 and η_3 are zero [234, 249], the relative dynamics of the transient state can be described on the new free-energy surface as symmetry-recovery by melting the two order parameters—simultaneously or sequentially.

The impulse-driven new energy landscape mediating the phase evolution is justified from the initial rapid suppression of the distortive symmetry-breaking parameters. The events have been recorded by the UED experiments [235, 250, 261], which show the static amplitude of

the pairing disappears within the first 300 fs of applying laser pulses beyond a threshold E_{th}. Meanwhile, trARPES has reported the Mott–Hubbard gap collapses on an even shorter timescale (<100 fs) [255, 259, 265], which is understood as driven by the photocarrier doping [255, 265] to both the localized bonding and nonbonding orbitals [265]. Below the threshold dose, the laser excitation typically leads to coherent gap dynamics at 6 THz, observed by the transient THz conductivity [256–258] and optical reflectivity measurements [254, 255]. This coherent phonon signature is effectively the amplitude mode and has been successfully employed as a marker for monitoring the presence of the M_1 order [254, 255]. The density functional theory (DFT) calculation [265] puts an optical doping density at 10^{21} e–h pairs/cm^3 that is needed to entirely soften the landscape supporting the experimental findings.

The DFT found that the characteristic pretransition 6 THz coherent phonon generation upon optical excitation is tied to the perturbative change of the free energy of the monoclinic phase, induced by hole carrier doping of the Mott phase. The V-shift associated with this displacive mode is in the monoclinic $\mathbf{b}_{\text{M}}$–$\mathbf{c}_{\text{M}}$ plane, which is the $(0\bar{1}1)_R$ plane of the rutile structure [265]. Therefore, there is no obvious route to continuously change the M_1 phase to the R phase through rectifying the coherent distortive mode excited by hole-doping. Additional (transverse) modes have to be involved as well due to the nonzero contributions from the distortive components, i.e., $\mathbf{u}_{\text{p}}$ and $\mathbf{u}_{\text{t}}$, of the order parameters out of the $(0\bar{1}1)_R$ plane.

We now consider the role of sample settings. The hidden 1D characteristics of VO_2 phases give a very prominent lattice constant changes along the crystalline $\mathbf{c}_{\text{R}}$ direction during the symmetry-breaking phase transition. End-clamping the VO_2 nanobeams, grown along $\mathbf{c}_{\text{R}}$, upon cooling from the R phase is equivalent to applying tensile stress, which is known to induce the intermediate M_2 phase [234, 249, 252]. This occurs because applying tensile stress or hole doping tips the balance of the cooperative symmetry-breaking between η_1 and η_3, which is maintained during the thermal R–M_1 transition under ambient pressure. On the other hand, in studying ultrafast VO_2 phase transition the stress is transiently induced by the rapid heating across T_M where the lattice expands disruptively. Stress relief is a key step involved in the transition between M_1 and R phases [263]. This calls into consideration of the feedback effect from the internal pressure created during phase evolution on the external control parameter. Crystal cracking upon rapid heating has also been a well-known problem [266] in studying bulk or epitaxially grown materials in the pump–probe studies [25]. To remediate these effects, employing free-standing nanobeams or microbeams [267, 268] or small-volume [269] VO_2 crystals can not only preserve the intrinsic first-order transition characteristics but also maintain the integrity over repeated experimental cycles without causing the sample to crack.

Taking the transient stress into account, Tao *et al.* conducted the UED experiments using 31 nm VO_2 crystalline grains deposited on the non-epitaxial Si membrane (9 nm) [250]. The sample excitation involves both 800 nm and 2000 nm laser pulses—a setting similar to the study of the TaS_2 system to verify the photodoping effect driving the nonequilibrium phase transitions. The powder diffraction patterns of VO_2 phase transitions are presented in Figure 14a. The inhomogeneous crystalline grain size distribution leads to a dispersion effect manifested in the line-broadening in the diffraction, which can be attributed to the surface-strain size effect. Given the high sensitivity of VO_2 phase transition to the strain, the size dispersion also leads to a broadening of T_M in the transition curves. The broadening effect is naturally extended to the pump-induced state under both pump wavelengths; see Figure 14b for the transition curves taken based on the diminishments of the monoclinic reflections, such as $(30\bar{2})_M$.

It was shown that a stable R phase can be introduced at the +150 ps time period by ultrafast pulses of 800 nm and 2000 nm wavelengths, respectively. The transient phase transitions occur despite that the calculated absorbed energy density is much lower than what is typically required for thermodynamically heating up the crystal lattices from the base temperature (T_b) to T_M; see

Figure 14b top panel. Similar to the case of TaS_2 this nonthermal scenario is reconciled by joining the scales for phase transition using the absorbed phonon density n_λ rather than the deposited energy ΔH for comparison; see Figure 14b bottom panel. Incidentally, the threshold behavior set by the disappearance of the monoclinic features is at the level of 4×10^{21} e–h pairs/cm^3 at low temperatures. This is in the range of what was presented for the carrier-doping-induced collapse of the Mott–Hubbard gap—a proof that the applied photon dose would be sufficient to transform the monoclinic free-energy surface despite of being sub-thermal, paving the way for photoinduced phase transitions.

However, from the free-energy perspective the heating effect must also be considered, especially in this cooperative system where a strong shift in T_M is known from applying pressure or doping (Figure 13a). Hence, similar to the case of TaS_2, the effective critical temperature T_M^* for the phase transition (34) could be downshifted by the photo-doping effect. This explains why a lower laser dose is needed for the transition into R; whereas by the same reasoning, increasing T_b shall also decrease the required laser dose—an effect observed in Figure 14b closer to T_M.

For a sufficiently small crystalline specimen, one may argue that the system may self-manage the elastic stress and favors a homogenous state to reduce the free-energy cost as the microbeam experiments have repeatedly confirmed [231]. This makes the experiments by Tao *et al.* [250] interesting with regard to the dynamics of stress relief [263] and its implication for the photoinduced phase transition. There is a better chance of seeing a more stable free-energy basin or saddle point from the order parameter dynamics if the pump fluence is placed just above the critical threshold. This allows the relaxation dynamics to map the intermediate landscape with less heating-related blurring induced by coupling to the stochastic bath set up by laser pumping. The chosen fluences in the comparative experiments are set at 20% above the mean threshold, corresponding to the two sigmas of the transition window (Figures 14a, c, d) for two wavelengths.

The line-scan data of the raw diffraction images with the pre-pumped state pattern subtracted (diffraction difference image) to show the pump-induced state evolution are depicted in Figure 14a as the color map. The general trend of ultrafast evolution of the multi-step changes in the representative group of symmetry-breaking and recovery Bragg peaks are shown (see the downward moving and up-warding moving raw peak intensities respectively in Figure 14c where an initial sub-ps decrease of diffuse background offsets the scale), which, in a broad stroke, are quite similar to the other UED investigations of systems with larger grain sizes [236] or single crystals [261]. Here, the universal collapse in intensities of pairing-related peaks and a slower increase in intensities of the higher symmetry peaks of the rutile state are quite pronounced. We take these signals as an evidence showing the route from the initial state of M_1 to the eventual state of R is not direct. This reminds us of the same phenomenology in the previous two systems where we also see the interaction quench leads to a different order-parameter basin or saddle point before turning toward that of the eventual state.

The gentler quench (here for 800 nm it is at ~8.5 mJ/cm^2, which is 2–5 times smaller than the deep quench investigations [236,259,270]) does give more details of the trajectory reflecting order parameter evolution immediately following the intensity drop of the low-symmetry peaks; here a slower second decay in intensities appears on a similar time scale to the rise of the high-symmetry Bragg peaks after their delayed onset. However, the high-symmetry groups will continue to evolve. On this longer evolution (Figure 14d), the behaviors from the two different excitations will diverge after 10 ps where the higher photon energy pulse leads to a quicker turning over in the $(40\bar{2})_M$ (a high-low symmetry mixed peak; see Figure 14d) dynamics to settle on a more even level characteristic of the R phase than the trajectory taken by the 2000 nm case.

An acoustic modulation of the peak intensity characteristic of the breathing mode of the nanoparticles was also identified driven by impulsive heating on the ps timescale (Figure 15d).

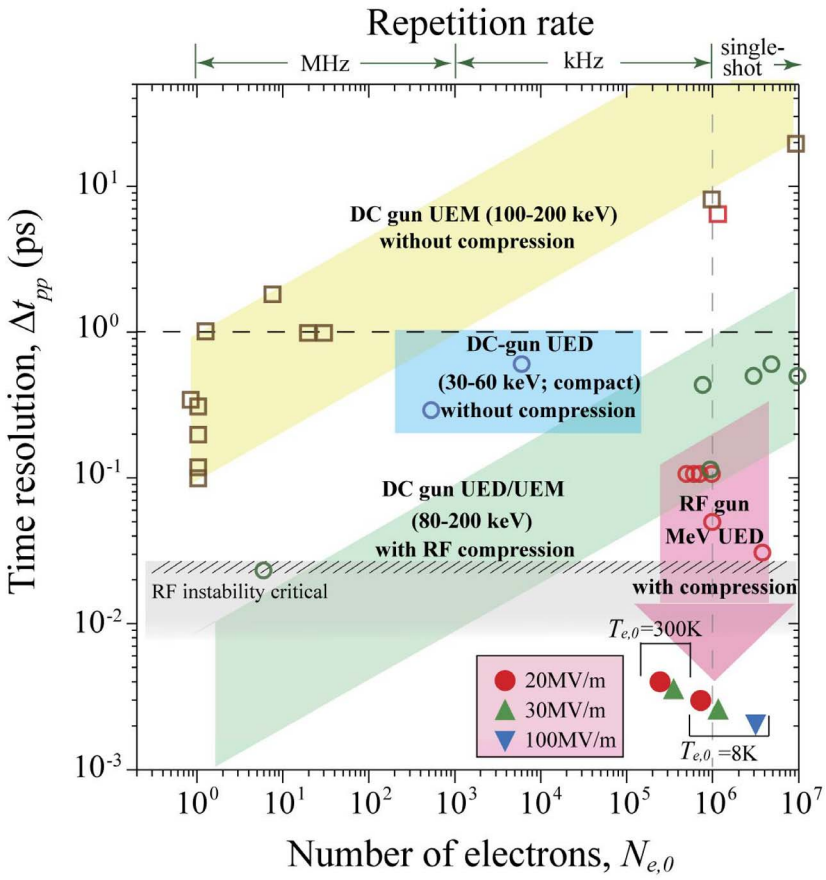

Figure 15. Performance of UED/UEM instrumentation. The data are extracted from the recent literatures of the photoemission keV DC gun UED and UEM with [87, 88, 91, 92] and without [83, 92, 95–97, 99, 100, 102–104, 107] pulse compression and the MeV RF gun UED systems [81, 82, 85, 86, 90, 98, 205]. The $T_{e,0}$ represents the source effective temperature, a property of the energy spread in the cathode region.

The frequency changes evidence a shift in the elastic speed of sound from one characteristic of the monoclinic phase to the slower one of the rutile phase, occurring interestingly on roughly the same timescale as the $(40\bar{2})_M$ intensity changes. These results seem to indicate that the acoustic potential of the broken-symmetry state only changes into that of the melted phase after the transient stress is released, as unveiled by acoustic modulations. The less distinct turning over behavior under the 800 nm excitation leads one to believe the transient state characteristics would be even less distinct if a higher excitation fluence were applied. An increase in the diffuse background observed here is consistent with more heat being generated by the 800 nm pulses. The transient heating, while largely impacting the system after the impulse period, will modify the adiabatic free-energy surface with an increased base temperature along the path that makes the trajectory more like the thermodynamic one with a larger stochastic blurring effect; see the deep quench scenario ($F \gg F_c$) in Figure 14e. The recent ultrafast thermal diffuse scattering studies of VO_2 phase transition under a deep quench have shown the transition pathway to be largely stochastically driven [270].

As the photo-doping effect is involved, it is intriguing to consider the role of the M_2 known to be introduced under a moderate level of hole doping. However, more excessive hole doping will drive the system eventually to the R phase where the M_2 state may pose as a saddle point. A simple structural model based on the homogeneous system evolution suggests this is a more likely scenario. The structural model applies a continuous change in (φ, δ) to fit the experimental results with the coordinates of the M_1 phase as the starting point, as presented in Figure 14e. Unsurprisingly, the data cannot be reconciled with a direct path from M_1 to R [250]. The best fit to the results requires the two sub-lattice to act differently as is the case of the M_1–M_2 transition where only one order parameter (η_3) is to be melted. The short period of metastability and limited gains in strength signifies that the lattice instabilities normally associated with the M_2 symmetry are gaining, but it is unlikely to be consolidated into a long-range order. The digression into the M_2 structural domain is simply because, when induced, the M_2 basin/saddle point is closer to the initial ground state than the R basin on the free-energy surface. To further transition into R, the additional order parameter (η_1) needs to be melted. This situation occurs, as indicated by the findings, as an energetically more favorable path after the system has entered the domain of M_2 but not before.

One cannot rule out yet other vestigial orders, as predicted by the free-energy equation with all four independent order parameters considered [249] may be involved. However, the gateway picture proposed here based on a non-straightforward order parameter trajectory is different from an isostructural solution identified as a monoclinic metallic phase [236,262]. Some modification of the structure distortion prototypical to M_1 might still contribute to the difference map (Figure 15a) as the low-frequency background. Future more precise experiments allowing a better momentum resolution to distill out different symmetry-breaking contributions shall help address this topic.

7. Summary and future perspectives

In this topical review, we discussed a set of results that provide important insights into ultrafast nonthermal control of quantum materials, in particular, the photoinduced phase transitions to thermodynamically inaccessible states by ultrashort optical excitation in RTe_3, TaS_2 and VO_2. Here, one utilizes light to shift the electronic interactions, break or restore the crystal symmetries to change the balance between competing phases to stabilize novel quantum phases out of equilibrium. Their nonequilibrium behaviors as probed by ultrafast electron scattering have revealed the interplays between the co-control parameters introduced by the pump responsible for the free energy: the local effective temperature and the interaction quench. Useful concepts in conjunction with the Landau–Ginzburg paradigm of description, such as the nonthermal critical point and the local effective temperatures, are introduced to facilitate the understanding of both the heating and interaction effects necessarily to account for the observed evolution of the order-parameter dynamics. In order to realize robust ultrafast control of nonthermal states, the studies here show it is desirable to minimize energy absorption while promoting a controlled modification of the free-energy landscape through different frequency optical quench. The studies also unveil the need for understanding the role of dissipation and properly considering pump inhomogeneity to reach a cross-platform understanding of ultrafast nonthermal controls reported using different pump–probe experimental settings.

As the present paper focuses on the quench dynamics and the relevant nonequilibrium landscape for their description, we intentionally leave out key fields of photoinduced phase transitions mediated by different pump schemes; other nonequilibrium routes to stabilize novel phases of matter include nonlinear phononics and Floquet control under periodic driving; e.g.,

see recent reviews [271, 272]. In these studies, instead of driving the system through above-the-gap carrier excitations by applying brief high-frequency photons, lower-energy or off-resonance laser fields are preferred to avoid excessive absorption. Furthermore, exploring nonequilibrium universities under a soft quench to the proximities of the nonthermal critical point shall reveal the salient features of the transient energy landscape inaccessible at equilibrium. These topics are ripe for future investigations.

The experiments discussed above demonstrate how the advance of ultrashort electron pulses into brighter and more coherent territories will have a far-reaching impact on nonequilibrium quantum material sciences. While the FEL-based X-ray sources, including the latest development of seeded FEL, will remain the ultimate powerhouse for achieving high resolutions, the ultrafast high-brightness electron sources will revolutionize the research on mesoscopic sciences with integrated multi-messenger approaches. Given the high-brightness electron source and FEL ultrafast instrumentation share many core technologies, such as the precise synchronization between the source and the pump optical fields, the RF accelerator and optical controls, and the detector technologies, the two fields will likely advance together. Indeed, the transformation from integrating the RF accelerator technologies into the UED and the next-generation UEM instrumentation has been tremendous. From the source brightness perspective, the utilities of the electron sources, while still technically challenging to implement to the fullest, remain largely under-explored. This is evident in comparing the performances of UED and UEM plotted in terms of time resolution (Δt_{pp}) and particle numbers in Figure 15, summarized from the recent literatures. Here the comparisons are hard to be precise given the broad varieties of system configurations. Nonetheless, for a given type of instrument the trends that Δt_{pp} largely follows the $N_{e,0}^{1/2}$ as discussed in ML-FMM are quite clear. This gives some confidence in giving projections on the future faces of the technologies with the knowledge from the ML-FMM simulations.

With the mesoscopic material applications in mind, the future of ultrafast electron sciences shall lie in the high-flux regime with potentially the ability to conduct single-shot experiments. This is because the intrinsic high electron scattering cross-section sets a relatively low bar of the required $N_{e,0}$ of 10^6–10^8 (based on applications), which are accessible by both the photoemission DC and RF guns at their respective virtual cathode limit of emission. The implementation of pulse compression schemes easily boosted the temporal resolution into sub-ps regimes at such high-flux limits; see Figure 15. However, we want to emphasize that in both types of instrumentation, the current levels of performance are strongly influenced by the RF system and the beamline (both optical and electron) stabilities that affect the arrival time and the precision of the time and energy focusing at the samples. The performance can be further improved by a factor of 10 before reaching the physical limits set by the beam brightness. With complete control of the electron pulse parameters under advanced compression and streaking schemes, it is possible to obtain pulses with few femtosecond durations with MeV RF UED system and few tens of fs for the keV DC gun systems, operating near the virtual cathode limit. Clearly, the facility-based MeV UED systems will ultimately be the prime options for most dose-hungry and high-temporal-resolution-prone experiments, and likely rival many FEL-type experiments in these directions in the years to come. Putting the ultimate temporal resolution and dose aside, the keV DC gun system, however, will excel in the momentum and energy resolutions. Armed with the matured technologies developed for the current electron microscopes at the familiar beam energy scale, we envision in the decade ahead, a major push will be in obtaining robust resolutions for a true multi-messenger approach that combines diffraction, imaging, and spectroscopy under a single platform. To reach the resolution limits set by the source brightness of the DC-gun designs ($\lesssim$50 fs, $\lesssim$1 nm, and $\lesssim$100 meV levels close to the virtual cathode limit respectively), the development of ingenious schemes to integrate beam stabilization, pump–

probe synchronization and implementing suitable electron optics/detector technologies will be the main focus.

Acknowledgements

The authors acknowledge the many helpful discussions with M. Berz, K. Chang, P.M. Duxbury, M. Eckstein, I.R. Fisher, J. Freericks, Y.A. Gerasimenko, R.H. Haglund, T.R.T. Han, M.G. Kanatzidis, R. Kandle, A.F. Kemper, S. Lund, M. Maghrebi, S.D. Mahanti, K. Makino, C.D. Malliakas, D. Mihailovic, R. Murdick, K. Nasu, J. Portman, N. Sepulveda, T. Sun, Z. Tao, S. Wall, J. Williams, B. Zerbe, H. Zhang, M. Zhang, F. Zhou. The work was funded by the U.S. Department of Energy, Grant DE-FG0206ER46309. The experimental facility was supported by U.S. National Science Foundation, Grant DMR 1625181.

Appendix A. Three-temperature diffusion model (3TDM) calculation

The 3TDM considers the microscopic energy relaxations following the electronic laser quench in the quantum materials. This model extends on the conventional three-temperature model (3TM) [13, 109–112], where one typically assumes the absorbed photon energy is deposited into the electronic sub-system and internally thermalizes instantaneously. The subsequent relaxation involves energy transfer from the electrons to a subset of phonons strongly coupled to the initial electronic excitation, referred to as strongly coupled phonons (SCP), and also to the rest of the lattice modes that are less efficiently coupled, referred to as weakly coupled phonons (WCP). The dynamics of energy relaxation are described by a set of coupled differential equations with the local temperature T_i and specific heat C_i prescribed to each subsystem. In the simplest form of 3TM without considering the diffusion effects, one may write the coupled rate equation $C_i\partial_t T_i = -G_{i-j}(T_i - T_j) - G_{i-k}(T_i - T_k)$, where G_{i-j} is the coupling constant between the subsystems i and j. In this picture, the characteristic timescale for energy transfer ($i \rightarrow j$) is given by: $\tau_{ij}^{-1} = G_{i-j}/C_i$. Hence, a larger specific heat typically slows down the dynamics of energy transfer from the subsystem. This schematic three-temperature model is given in Figure A16 where the extent of partition of specific heat between the SCP and WCP is given by the fraction α.

However, such a model is not complete for an inhomogeneous system driven also by the diffusion effects. This is exemplified in the trARPES and the grazing incidence X-ray diffraction experiments conducted predominantly over the surface regions where the energy dissipation into the bulk interior is important for considering the nonequilibrium phase transition. To this end, the 3TDM considers the non-Fourier thermal diffusion of carriers and phonons [211]. The full description of the 3TDM is given in Ref. [212]. Here, we apply the 3DTM to give key predictions about the dynamical behaviors involving different sample thickness settings typical for the UED and trARPES experiments. The calculation is based on a near-infrared (800 nm) pump pulse with a duration of 50 fs at 45° incidence and S-polarization.

The goal here is to illustrate how varying the excitations in the materials (based on solving the Maxwell equation; see Section 6.3) may lead to drastically different nonequilibrium temperature relaxation profile in two different thin films (45 and 150 nm). The results will impact the evolution of the developed nonequilibrium phases therein, which are probed by UED and trARPES. For establishing a common baseline, the detailed $T_e(t)$ dataset made available recently by trARPES on 1T-$TaSe_2$ is employed as the target for refining the 3TDM model. The key parameters that reproduce the dynamics are given in Table A1. Here, the model considers 150 nm and the $T_e(t; z = 0)$ is calculated to reproduce the data; see Figure A16. Given the three-way dynamical couplings, it is generally difficult to directly isolate the relaxation times from the data, but based on the refined 3TDM parameters and $\tau_{ij}^{-1} = G_{i-j}/C_i$, we may give nominal values of

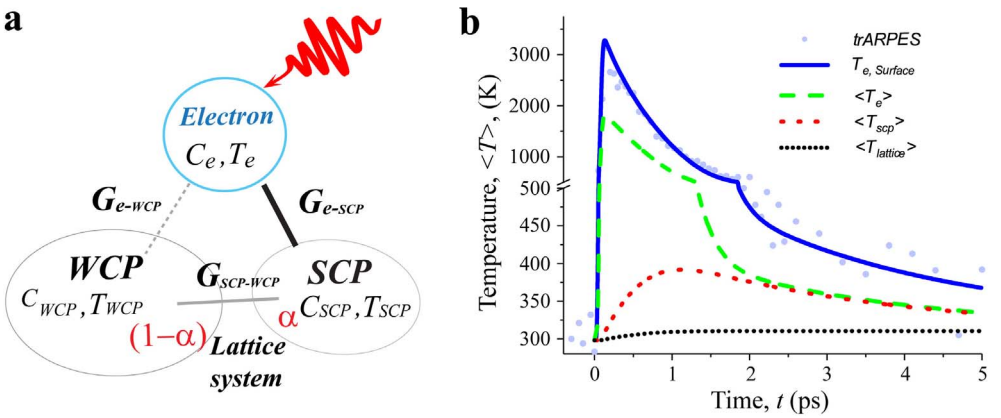

Figure A16. The effective temperature calculations based on the three-temperature diffusion model. (a) The schematic picture of the three-temperature model with the initial excitation energy from laser first stored in the electronic subsystem, then transferred to the lattice subsystem which is sub-divided into two types of phonon manifolds (SCP and WCP) due to the coupling hierarchy. (b) The temperatures obtained for different subsystems using the three-temperature diffusion model (3TDM) in thin film geometry [212]. The 3TDM calculates the surface electronic temperature evolution, $T_e(t)$ in solid blue line, for 1T-$TaSe_2$ at 0.69 mJ/cm^2 and compared with the data (light blue dots) taken from the trARPES (see Supplementary Materials from Ref. [174]). The parameters used in the calculations are listed in Table A1. Alternatively, under the same pump condition, $\langle T_i(t)\rangle$ are obtained for a 45 nm 1T-TaS_2 thin film with the bracket denoting averaging, relevant to the study by the ultrafast scattering techniques; see text for discussion.

$\tau_{\text{el-SCP}} = 0.5$ ps, $\tau_{\text{el-WCP}} = 1.8$ ps, and $\tau_{\text{SCP–WCP}} = 40$ ps, which are in general agreements with the reports of electron-phonon coupling times of 0.5–4 ps for these systems [18, 19, 187–191]. The same calculation is then conducted for the 45 nm film, whereas discussed in Section 6.3, and a significantly more homogenous profile can be obtained due to the interference effect. With the UED experiments in mind, here we give the temperatures (noted in bracket) averaged over the entire slab. The lattice temperature is calculated as $T_{\text{lattice}} = \alpha T_{\text{SCP}} + (1-\alpha) T_{\text{WCP}}$, where $\alpha = 0.1$ is determined from fitting. The time and depth-dependent temperature profiles for the two different films are given in Figures 11b and c.

To consider the temperature profile away from surface regions, the out-of-plane electron thermal conductivity K_e plays an important role. The nominal value used in the simulation is derived from the out-of-plane resistivity $\rho_\perp = 1.0 \times 10^{-5}$ Ω·m but the reported value for $\rho_\perp$ differed by an order of magnitude in different measurement geometries; see Refs [274] and [275]. The impact of different $\rho_\perp$ on the excited material temperature profile is evaluated for the 150 nm film. Increasing K_e by 10 ($\rho_\perp = 1.0 \times 10^{-6}$ Ω·m), the σ_n calculated for T_e decreases by 40% whereas decreasing K_e by 10 ($\rho_\perp = 1.0 \times 10^{-4}$ Ω·m), σ for T_{lattice} increases by 20%. The impacts on the lattice temperature track generally with T_e changes. These calculations are taken at 4 ps when T_e and T_{lattice} reach a fair level of thermalization. The calculation here shows that the different $\rho_\perp$ values reported in the literature have some effects on the pump inhomogeneity profile. In general, reducing $\rho_\perp$ will lead to a higher homogeneity in the temperature profiles. This is relevant as one generally expects that $\rho_\perp$ will be smaller in the pumped state—a phenomenon that should be resolvable by studying long-time relaxation dynamics with the help of 3TDM modeling.

Table A1. Parameters for three-temperature diffusion model

Name	Meaning	Parameters used for 1T-TaS_2
$C_e = \gamma T_e$	Electron heat capacity	$\gamma = 12.96\ \mathrm{J{\cdot}m^{-3}{\cdot}K^{-2}}$ (Ref. [273])
τ_e	Electron relaxation time	0.2 ps (Ref. [213])
$K_e = \frac{\mathrm{Lrtz}T_e}{\rho_\perp}$ [a]	Out-of-plane electron thermal conductivity	$\rho_\perp = 1.0\times10^{-5}\ \Omega$m (Refs [274] and [275])
K_l [b]	Out-of-plane lattice thermal conductivity	0.5 ($\mathrm{W{\cdot}m^{-1}{\cdot}K^{-1}}$) (Refs [274] and [276])
C_{tot}	Total nuclear heat capacity	1.85×10^6 ($\mathrm{J{\cdot}m^{-3}{\cdot}K^{-1}}$) (Ref. [189])
α	Strongly coupled phonon fraction	0.1 (Ref. [212])
$G_{\text{el-SCP}}$	Coupling constant between electron and strongly coupled phonons	$2.5\times10^{16}\ \mathrm{W{\cdot}m^{-3}{\cdot}K^{-1}}$
$G_{\text{el-WCP}}$	Coupling constant between electron and weakly coupled phonons	$1.0\times10^{14}\ \mathrm{W{\cdot}m^{-3}{\cdot}K^{-1}}$
$G_{\text{SCP–WCP}}$	Coupling constant between strongly coupled phonons and weakly coupled phonons	$6.0\times10^{16}\ \mathrm{W{\cdot}m^{-3}{\cdot}K^{-1}}$

[a] The calculation of electronic thermal conductivity follows the Wiedemann-Franz law. Lrtz is the Lorentz number, and Lrtz = $2.44\times10^{-8}\ \mathrm{W{\cdot}K^{-2}}$.
[b] The out-of-plane lattice thermal conductivity is taken to be 1/10 of the in-plane value reported in Ref. [276], based on the understanding that the two typically differs by an order of magnitude [274].

References

[1] D. N. Basov, R. D. Averitt, D. Hsieh, "Towards properties on demand in quantum materials", *Nat. Mater.* **16** (2017), p. 1077-1088.
[2] Y. Tokura, M. Kawasaki, N. Nagaosa, "Emergent functions of quantum materials", *Nat. Phys.* **13** (2017), p. 1056-1068.
[3] National Academies of Sciences, Engineering Medicine, *Frontiers of Materials Research: A Decadal Survey*, The National Academies, Washington, DC, 2019.
[4] B. Keimer, J. E. Moore, "The physics of quantum materials", *Nat. Phys.* **13** (2017), p. 1045-1055.
[5] P. W. Anderson, "More is different", *Science* **177** (1972), p. 393-396.
[6] L. D. Landau, "On the theory of phase transitions", *Zh. Eksp. Teor. Fiz* **7** (1937), p. 19-32.
[7] L. D. Landau, "On the theory of phase transitions. II", *Zh. Eksp. Teor. Fiz.* **7** (1937), p. 627-632.
[8] P. W. Anderson, *Basic Notions of Condensed Matter Physics*, The Benjamin-Cummings publishing company, Inc., Menlo park, CA, 1984.
[9] P. C. Hohenberg, A. P. Krekhov, "An introduction to the Ginzburg–Landau theory of phase transitions and nonequilibrium patterns", *Phys. Rep.* **572** (2015), p. 1-42.
[10] W. H. Zurek, "Cosmological experiments in condensed matter systems", *Phys. Rep.* **276** (1996), p. 177-221.
[11] J. Orenstein, "Ultrafast spectroscopy of quantum materials", *Phys. Today* **65** (2012), p. 44-60.
[12] M. Buzzi, M. Först, R. Mankowsky, A. Cavalleri, "Probing dynamics in quantum materials with femtosecond X-rays", *Nat. Rev. Mater.* **3** (2018), p. 299-311.
[13] C. Giannetti, M. Capone, D. Fausti, M. Fabrizio, F. Parmigiani, D. Mihailovic, "Ultrafast optical spectroscopy of strongly correlated materials and high-temperature superconductors: a non-equilibrium approach", *Adv. Phys.* **65** (2016), p. 58-238.
[14] J. Zhang, R. D. Averitt, "Dynamics and control in complex transition metal oxides", *Annu. Rev. Mater. Res.* **44** (2014), p. 19-43.
[15] T. F. Nova, A. S. Disa, M. Fechner, A. Cavalleri, "Metastable ferroelectricity in optically strained $SrTiO_3$", *Science* **364** (2019), p. 1075-1079.
[16] X. Li, T. Qiu, J. Zhang, E. Baldini, J. Lu, A. M. Rappe, K. A. Nelson, "Terahertz field-induced ferroelectricity in quantum paraelectric $SrTiO_3$", *Science* **364** (2019), p. 1079-1082.
[17] H. Ichikawa, S. Nozawa, T. Sato, A. Tomita, K. Ichiyanagi, M. Chollet, L. Guerin, N. Dean, A. Cavalleri, S.-i. Adachi,

T.-h. Arima, H. Sawa, Y. Ogimoto, M. Nakamura, R. Tamaki, K. Miyano, S.-y. Koshihara, "Transient photoinduced "hidden" phase in a manganite", *Nat. Mater.* **10** (2011), p. 101-105.
[18] L. Stojchevska, I. Vaskivskyi, T. Mertelj, P. Kusar, D. Svetin, S. Brazovskii, D. Mihailovic, "Ultrafast switching to a stable hidden quantum state in an electronic crystal", *Science* **344** (2014), p. 177-180.
[19] T.-R. T. Han, F. Zhou, C. D. Malliakas, P. M. Duxbury, S. D. Mahanti, M. G. Kanatzidis, C.-Y. Ruan, "Exploration of metastability and hidden phases in correlated electron crystals visualized by femtosecond optical doping and electron crystallography", *Sci. Adv.* **1** (2015), article no. e1400173.
[20] D. Fausti, R. I. Tobey, N. Dean, S. Kaiser, A. Dienst, M. C. Hoffmann, S. Pyon, T. Takayama, H. Takagi, A. Cavalleri, "Light-induced superconductivity in a stripe-ordered cuprate", *Science* **331** (2011), p. 189-191.
[21] A. Cantaluppi, M. Buzzi, G. Jotzu, D. Nicoletti, M. Mitrano, D. Pontiroli, M. Riccò, A. Perucchi, P. Di Pietro, A. Cavalleri, "Pressure tuning of light-induced superconductivity in K_3C_{60}", *Nat. Phys.* **14** (2018), p. 837-841.
[22] A. Kogar, A. Zong, P. E. Dolgirev, X. Shen, J. Straquadine, Y.-Q. Bie, X. Wang, T. Rohwer, I. C. Tung, Y. Yang, R. Li, J. Yang, S. Weathersby, S. Park, M. E. Kozina, E. J. Sie, H. Wen, P. Jarillo-Herrero, I. R. Fisher, X. Wang, N. Gedik, "Light-induced charge density wave in $LaTe_3$", *Nat. Phys.* **16** (2020), p. 159-163.
[23] F. Zhou, J. Williams, S. Sun, C. D. Malliakas, M. G. Kanatzidis, A. F. Kemper, C.-Y. Ruan, "Nonequilibrium dynamics of spontaneous symmetry breaking into a hidden state of charge-density wave", *Nat. Commun.* **12** (2021), article no. 566.
[24] "Quantum phases on demand", *Nat. Phys.* **16** (2020), p. 1.
[25] K. Nasu, *Photoinduced Phase Transitions*, World Scientific, Singapore, 2004.
[26] J. Eisert, M. Friesdorf, C. Gogolin, "Quantum many-body systems out of equilibrium", *Nat. Phys.* **11** (2015), p. 124-130.
[27] U. C. Tauber, *Critical Dynamics: A Field Theory Approach to Equilibrium and Non-equilibrium Scaling Behavior*, Cambridge University Press, Cambridge, 2014.
[28] G. Ódor, "Universality classes in nonequilibrium lattice systems", *Rev. Mod. Phys.* **76** (2004), p. 663-724.
[29] A. Polkovnikov, K. Sengupta, A. Silva, M. Vengalattore, "Colloquium: nonequilibrium dynamics of closed interacting quantum systems", *Rev. Mod. Phys.* **83** (2011), p. 863-883.
[30] H. Aoki, N. Tsuji, M. Eckstein, M. Kollar, T. Oka, P. Werner, "Nonequilibrium dynamical mean-field theory and its applications", *Rev. Mod. Phys.* **86** (2014), p. 779-837.
[31] Z. Sun, A. J. Millis, "Transient trapping into metastable states in systems with competing orders", *Phys. Rev. X* **10** (2020), article no. 021028.
[32] W. Fu, L.-Y. Hung, S. Sachdev, "Quantum quenches and competing orders", *Phys. Rev. B* **90** (2014), article no. 024506.
[33] B. Damski, W. H. Zurek, "Adiabatic-impulse approximation for avoided level crossings: from phase-transition dynamics to Landau–Zener evolutions and back again", *Phys. Rev. A* **73** (2006), article no. 063405.
[34] J. Berges, A. Rothkopf, J. Schmidt, "Nonthermal fixed points: effective weak coupling for strongly correlated systems far from equilibrium", *Phys. Rev. Lett.* **101** (2008), article no. 041603.
[35] T. W. B. Kibble, "Topology of cosmic domains and strings", *J. Phys. A: Math. Gen.* **9** (1976), p. 1387-1398.
[36] T. W. B. Kibble, "Symmetry breaking and defects", in *Patterns of Symmetry Breaking* (H. Arodz, J. Dziarmaga, W. H. Zurek, eds.), Springer, Dordrecht, Netherlands, 2003, p. 3-36.
[37] M. Gring, M. Kuhnert, T. Langen, T. Kitagawa, B. Rauer, M. Schreitl, I. Mazets, D. A. Smith, E. Demler, J. Schmiedmayer, "Relaxation and prethermalization in an isolated quantum system", *Science* **337** (2012), p. 1318-1322.
[38] T. Kinoshita, T. Wenger, D. S. Weiss, "A quantum Newton's cradle", *Nature* **440** (2006), p. 900-903.
[39] Y. Tang, W. Kao, K.-Y. Li, S. Seo, K. Mallayya, M. Rigol, S. Gopalakrishnan, B. L. Lev, "Thermalization near Integrability in a dipolar quantum Newton's cradle", *Phys. Rev. X* **8** (2018), article no. 021030.
[40] M. Prüfer, P. Kunkel, H. Strobel, S. Lannig, D. Linnemann, C.-M. Schmied, J. Berges, T. Gasenzer, M. K. Oberthaler, "Observation of universal dynamics in a spinor Bose gas far from equilibrium", *Nature* **563** (2018), p. 217-220.
[41] S. Erne, R. Bücker, T. Gasenzer, J. Berges, J. Schmiedmayer, "Universal dynamics in an isolated one-dimensional Bose gas far from equilibrium", *Nature* **563** (2018), p. 225-229.
[42] C. Eigen, J. A. P. Glidden, R. Lopes, E. A. Cornell, R. P. Smith, Z. Hadzibabic, "Universal prethermal dynamics of Bose gases quenched to unitarity", *Nature* **563** (2018), p. 221-224.
[43] P. Calabrese, J. Cardy, "Time dependence of correlation functions following a quantum quench", *Phys. Rev. Lett.* **96** (2006), article no. 136801.
[44] A. Mitra, "Quantum quench dynamics", *Annu. Rev. Condens. Matter Phys.* **9** (2018), p. 245-259.
[45] M. Eckstein, M. Kollar, P. Werner, "Thermalization after an interaction quench in the Hubbard model", *Phys. Rev. Lett.* **103** (2009), article no. 056403.
[46] A. H. Zewail, "Femtochemistry: Atomic-scale dynamics of the chemical bond", *J. Phys. Chem. A* **104** (2000), p. 5660-5694.
[47] W. L. McMillan, "Microscopic model of charge-density waves in 2H–$TaSe_2$", *Phys. Rev. B* **16** (1977), p. 643-650.
[48] L. D. Landau, "Scattering of X-rays by crystals near the Curie point", *Zh. Eksp. Teor. Fiz.* **7** (1937), p. 1232-1241.
[49] P. A. Lee, T. M. Rice, P. W. Anderson, "Fluctuation effects at a Peierls transition", *Phys. Rev. Lett.* **31** (1973), p. 462-465.

[50] A. W. Overhauser, "Observability of charge-density waves by neutron diffraction", *Phys. Rev. B* **3** (1971), p. 3173-3182.
[51] G. Gruner, "The dynamics of charge-density waves", *Rev. Mod. Phys.* **60** (1988), p. 1129-1182.
[52] M. A. Krivoglaz, *Diffuse Scattering of X-ray and Neutrons by Fluctuations*, Springer-Verlag, Berlin, Heidelberg, 1996.
[53] P. M. Williams, G. S. Parry, C. B. Scrub, "Diffraction evidence for the Kohn anomaly in 1T-TaS_2", *Philos. Mag.: A J. Theor. Exp. Appl. Phys.* **29** (1974), p. 695-699.
[54] K. R. A. Ziebeck, B. Dorner, W. G. Stirling, R. Schollhorn, "Kohn anomaly in the $1T_2$ phase of TaS_2", *J. Phys. F: Met. Phys.* **7** (1977), p. 1139-1143.
[55] W. Minor, L. D. Chapman, S. N. Ehrlich, R. Colella, "Phason velocities in TaS_2 by X-ray diffuse scattering", *Phys. Rev. B* **39** (1989), p. 1360-1362.
[56] Y. Machida, T. Hanashima, K. Ohkubo, K. Yamawaki, M. Tanaka, S. Sasaki, "Observation of soft phonon modes in 1T-TaS_2 by means of X-ray thermal diffuse scattering", *J. Phys. Soc. Jpn.* **73** (2004), p. 3064-3069.
[57] M. Trigo, M. Fuchs, J. Chen, M. P. Jiang, M. Cammarata, S. Fahy, D. M. Fritz, K. Gaffney, S. Ghimire, A. Higginbotham, S. L. Johnson, M. E. Kozina, J. Larsson, H. Lemke, A. M. Lindenberg, G. Ndabashimiye, F. Quirin, K. Sokolowski-Tinten, C. Uher, G. Wang, J. S. Wark, D. Zhu, D. A. Reis, "Fourier-transform inelastic X-ray scattering from time-and momentum-dependent phonon–phonon correlations", *Nat. Phys.* **9** (2013), p. 790-794.
[58] T. Chase, M. Trigo, A. H. Reid, R. Li, T. Vecchione, X. Shen, S. Weathersby, R. Coffee, N. Hartmann, D. A. Reis, X. J. Wang, H. A. Dürr, "Ultrafast electron diffraction from non-equilibrium phonons in femtosecond laser heated Au films", *Appl. Phys. Lett.* **108** (2016), article no. 041909.
[59] L. P. René de Cotret, J.-H. Pöhls, M. J. Stern, M. R. Otto, M. Sutton, B. J. Siwick, "Time-and momentum-resolved phonon population dynamics with ultrafast electron diffuse scattering", *Phys. Rev. B* **100** (2019), article no. 214115.
[60] W. L. McMillan, "Collective modes of a charge-density wave near the lock-in transition", *Phys. Rev. B* **16** (1977), p. 4655-4658.
[61] D. Forster, *Hydrodynamic Fluctuations, Broken Symmetry, and Correlation Functions*, CRC Press, Boca Raton, 1975.
[62] A. W. Overhauser, "Spin density waves in an electron gas", *Phys. Rev.* **128** (1962), p. 1437-1452.
[63] A. D. Bruce, R. A. Cowley, "The theory of structurally incommensurate systems. III. The fluctuation spectrum of incommensurate phases", *J. Phys. C: Solid State Phys.* **11** (1978), p. 3609-3630.
[64] U. C. Täuber, "Field-theory approaches to nonequilibrium dynamics", in *Ageing and the Glass Transition* (M. Henkel, M. Pleimling, R. Sanctuary, eds.), Springer, Berlin, Heidelberg, 2007, p. 295-348.
[65] P. M. Chaikin, T. C. Lubensky, *Principles of Condensed Matter Physics*, Cambridge University Press, Cambridge, 1995.
[66] A. J. Bray, "Theory of phase-ordering kinetics", *Adv. Phys.* **43** (1994), p. 357-459.
[67] R. M. Fernandes, P. P. Orth, J. Schmalian, "Intertwined vestigial order in quantum materials: Nematicity and beyond", *Annu. Rev. Condens. Matter Phys.* **10** (2019), p. 133-154.
[68] E. Fradkin, S. A. Kivelson, J. M. Tranquada, "Colloquium: Theory of intertwined orders in high temperature superconductors", *Rev. Mod. Phys.* **87** (2015), p. 457-482.
[69] E. Dagotto, "Complexity in strongly correlated electronic systems", *Science* **309** (2005), p. 257-262.
[70] E. Fradkin, S. A. Kivelson, "High-temperature superconductivity: Ineluctable complexity", *Nat. Phys.* **8** (2012), p. 864-866.
[71] L. Balents, L. Bartosch, A. Burkov, S. Sachdev, K. Sengupta, "Putting competing orders in their place near the Mott transition", *Phys. Rev. B* **71** (2005), article no. 144508.
[72] H. Yao, J. A. Robertson, E.-A. Kim, S. A. Kivelson, "Theory of stripes in quasi-two-dimensional rare-earth tellurides", *Phys. Rev. B* **74** (2006), article no. 245126.
[73] A. Guinier, *X-ray Diffraction in Crystals, Imperfect Crystals, and Amorphous Bodies*, Dover, New York, 1994.
[74] B. T. M. Willis, "Thermal diffuse scattering of X-rays and neutrons", in *International Tables for Crystallography Volume B: Reciprocal Space* (U. Shmueli, ed.), Springer, Dordrecht, Netherlands, 2001, p. 400-406.
[75] G. F. Giuliani, A. W. Overhauser, "Structure factor of a charge-density wave", *Phys. Rev. B* **23** (1981), p. 3737-3743.
[76] C.-Y. Ruan, V. A. Lobastov, R. Srinivasan, B. M. Goodson, H. Ihee, A. H. Zewail, "Ultrafast diffraction and structural dynamics: The nature of complex molecules far from equilibrium", *Proc. Natl Acad. Sci. USA* **98** (2001), p. 7117-7122.
[77] A. del Campo, W. H. Zurek, "Universality of phase transition dynamics: Topological defects from symmetry breaking", *Int. J. Mod. Phys. A* **29** (2014), article no. 1430018.
[78] L. W. Clark, L. Feng, C. Chin, "Universal space–time scaling symmetry in the dynamics of bosons across a quantum phase transition", *Science* **354** (2016), p. 606-610.
[79] W. H. Zurek, "Causality in condensates: gray solitons as relics of BEC formation", *Phys. Rev. Lett.* **102** (2009), article no. 105702.
[80] W. Kohn, "Image of the Fermi surface in the vibration spectrum of a metal", *Phys. Rev. Lett.* **2** (1959), p. 393-394.
[81] R. Li, C. Tang, Y. Du, W. Huang, Q. Du, J. Shi, L. Yan, X. Wang, "Experimental demonstration of high quality MeV ultrafast electron diffraction", *Rev. Sci. Instrum.* **80** (2009), article no. 083303.

[82] Y. Murooka, N. Naruse, S. Sakakihara, M. Ishimaru, J. Yang, K. Tanimura, "Transmission-electron diffraction by MeV electron pulses", *Appl. Phys. Lett.* **98** (2011), article no. 251903.
[83] B. J. Siwick, J. R. Dwyer, R. E. Jordan, R. J. D. Miller, "An atomic-level view of melting using femtosecond electron diffraction", *Science* **302** (2003), p. 1382-1385.
[84] C.-Y. Ruan, Y. Murooka, R. K. Raman, R. A. Murdick, R. Worhatch, A. Pell, "Developemnt and applications for ultrafast electron nanocrystallography", *Microsc. Microanal.* **15** (2009), p. 323-337.
[85] S. P. Weathersby, G. Brown, M. Centurion, T. F. Chase, R. Coffee, J. Corbett, J. P. Eichner, J. C. Frisch, A. R. Fry, M. Gühr, N. Hartmann, C. Hast, R. Hettel, R. K. Jobe, E. N. Jongewaard, J. R. Lewandowski, R. K. Li, A. M. Lindenberg, I. Makasyuk, J. E. May, D. McCormick, M. N. Nguyen, A. H. Reid, X. Shen, K. Sokolowski-Tinten, T. Vecchione, S. L. Vetter, J. Wu, J. Yang, H. A. Dürr, X. J. Wang, "Mega-electron-volt ultrafast electron diffraction at SLAC national accelerator laboratory", *Rev. Sci. Instrum.* **86** (2015), article no. 073702.
[86] F. Fu, S. Liu, P. Zhu, D. Xiang, J. Zhang, J. Cao, "High quality single shot ultrafast MeV electron diffraction from a photocathode radio-frequency gun", *Rev. Sci. Instrum.* **85** (2014), article no. 083701.
[87] O. Zandi, K. J. Wilkin, Y. Xiong, M. Centurion, "High current table-top setup for femtosecond gas electron diffraction", *Struct. Dyn.* **4** (2017), article no. 044022.
[88] R. P. Chatelain, V. R. Morrison, C. Godbout, B. J. Siwick, "Ultrafast electron diffraction with radio-frequency compressed electron pulses", *Appl. Phys. Lett.* **101** (2012), article no. 081901.
[89] F. Ji, D. B. Durham, A. M. Minor, P. Musumeci, J. G. Navarro, D. Filippetto, "Ultrafast relativistic electron nanoprobes", *Commun. Phys.* **2** (2019), article no. 54.
[90] H. W. Kim, N. A. Vinokurov, I. H. Baek, K. Y. Oang, M. H. Kim, Y. C. Kim, K.-H. Jang, K. Lee, S. H. Park, S. Park, J. Shin, J. Kim, F. Rotermund, S. Cho, T. Feurer, Y. U. Jeong, "Towards jitter-free ultrafast electron diffraction technology", *Nat. Photonics* **14** (2020), p. 245-249.
[91] K. J. Mohler, D. Ehberger, I. Gronwald, C. Lange, R. Huber, P. Baum, "Ultrafast electron diffraction from nanophotonic waveforms via dynamical Aharonov–Bohm phases", *Sci. Adv.* **6** (2020), article no. eabc8804.
[92] J. Williams, F. Zhou, T. Sun, Z. Tao, K. Chang, K. Makino, M. Berz, P. M. Duxbury, C.-Y. Ruan, "Active control of bright electron beams with RF optics for femtosecond microscopy", *Struct. Dyn.* **4** (2017), article no. 044035.
[93] B. W. Reed, M. R. Armstrong, N. D. Browning, G. H. Campbell, J. E. Evans, T. LaGrange, D. J. Masiel, "The evolution of ultrafast electron microscope instrumentation", *Microsc. Microanal.* **15** (2009), p. 272-281.
[94] W. E. King, G. H. Campbell, A. Frank, B. Reed, J. F. Schmerge, B. J. Siwick, B. C. Stuart, P. M. Weber, "Ultrafast electron microscopy in materials science, biology, and chemistry", *J. Appl. Phys.* **97** (2005), article no. 111101.
[95] A. H. Zewail, "4D ultrafast electron diffraction, crystallography, and microscopy", *Annu. Rev. Phys. Chem.* **57** (2006), p. 65-103.
[96] C. Zhu, D. Zheng, H. Wang, M. Zhang, Z. Li, S. Sun, P. Xu, H. Tian, Z. Li, H. Yang, J. Li, "Development of analytical ultrafast transmission electron microscopy based on laser-driven Schottky field emission", *Ultramicroscopy* **209** (2020), article no. 112887.
[97] P. K. Olshin, M. Drabbels, U. J. Lorenz, "Characterization of a time-resolved electron microscope with a Schottky field emission gun", *Struct. Dyn.* **7** (2020), article no. 054304.
[98] C. Lu, T. Jiang, S. Liu, R. Wang, L. Zhao, P. Zhu, Y. Liu, J. Xu, D. Yu, W. Wan, Y. Zhu, D. Xiang, J. Zhang, "Imaging nanoscale spatial modulation of a relativistic electron beam with a MeV ultrafast electron microscope", *Appl. Phys. Lett.* **112** (2018), article no. 113102.
[99] A. Feist, N. Bach, N. Rubiano da Silva, T. Danz, M. Möller, K. E. Priebe, T. Domröse, J. G. Gatzmann, S. Rost, J. Schauss, S. Strauch, R. Bormann, M. Sivis, S. Schäfer, C. Ropers, "Ultrafast transmission electron microscopy using a laser-driven field emitter: Femtosecond resolution with a high coherence electron beam", *Ultramicroscopy* **176** (2017), p. 63-73.
[100] Y. M. Lee, Y. J. Kim, Y.-J. Kim, O.-H. Kwon, "Ultrafast electron microscopy integrated with a direct electron detection camera", *Struct. Dyn.* **4** (2017), article no. 044023.
[101] F. Houdellier, G. M. Caruso, S. Weber, M. Kociak, A. Arbouet, "Development of a high brightness ultrafast transmission electron microscope based on a laser-driven cold field emission source", *Ultramicroscopy* **186** (2018), p. 128-138.
[102] K. Bücker, M. Picher, O. Crégut, T. LaGrange, B. W. Reed, S. T. Park, D. J. Masiel, F. Banhart, "Electron beam dynamics in an ultrafast transmission electron microscope with Wehnelt electrode", *Ultramicroscopy* **171** (2016), p. 8-18.
[103] S. Ji, L. Piazza, G. Cao, S. T. Park, B. W. Reed, D. J. Masiel, J. Weissenrieder, "Influence of cathode geometry on electron dynamics in an ultrafast electron microscope", *Struct. Dyn.* **4** (2017), article no. 054303.
[104] Y. Kurman, R. Dahan, H. H. Sheinfux, K. Wang, M. Yannai, Y. Adiv, O. Reinhardt, L. H. G. Tizei, S. Y. Woo, J. Li, J. H. Edgar, M. Kociak, F. H. L. Koppens, I. Kaminer, "Spatiotemporal imaging of 2D polariton wave packet dynamics using free electrons", *Science* **372** (2021), p. 1181-1186.
[105] X. Fu, E. Wang, Y. Zhao, A. Liu, E. Montgomery, V. J. Gokhale, J. J. Gorman, C. Jing, J. W. Lau, Y. Zhu, "Direct visualization of electromagnetic wave dynamics by laser-free ultrafast electron microscopy", *Sci. Adv.* **6** (2020), article no. eabc3456.

[106] I. Madan, G. M. Vanacore, E. Pomarico, G. Berruto, R. J. Lamb, D. McGrouther, T. T. A. Lummen, T. Latychevskaia, F. J. García de Abajo, F. Carbone, "Holographic imaging of electromagnetic fields via electron-light quantum interference", *Sci. Adv.* **5** (2019), article no. eaav8358.
[107] A. H. Zewail, "Four-dimensional electron microscopy", *Science* **328** (2010), p. 187-193.
[108] S. Sun, X. Sun, D. Bartles, E. Wozniak, J. Williams, P. Zhang, C.-Y. Ruan, "Direct imaging of plasma waves using ultrafast electron microscopy", *Struct. Dyn.* **7** (2020), article no. 064301.
[109] P. E. Dolgirev, A. V. Rozhkov, A. Zong, A. Kogar, N. Gedik, B. V. Fine, "Amplitude dynamics of the charge density wave in $LaTe_3$: Theoretical description of pump-probe experiments", *Phys. Rev. B* **101** (2020), article no. 054203.
[110] L. Perfetti, P. A. Loukakos, M. Lisowski, U. Bovensiepen, H. Eisaki, M. Wolf, "Ultrafast electron relaxation in superconducting $Bi_2Sr_2CaCu_2O_{8+\delta}$ by time-resolved photoelectron spectroscopy", *Phys. Rev. Lett.* **99** (2007), article no. 197001.
[111] B. Mansart, D. Boschetto, A. Savoia, F. Rullier-Albenque, F. Bouquet, E. Papalazarou, A. Forget, D. Colson, A. Rousse, M. Marsi, "Ultrafast transient response and electron–phonon coupling in the iron-pnictide superconductor $Ba(Fe_{1-x}Co_x)_2As_2$", *Phys. Rev. B* **82** (2010), article no. 024513.
[112] S. L. Johnson, M. Savoini, P. Beaud, G. Ingold, U. Staub, F. Carbone, L. Castiglioni, M. Hengsberger, J. Osterwalder, "Watching ultrafast responses of structure and magnetism in condensed matter with momentum-resolved probes", *Struct. Dyn.* **4** (2017), article no. 061506.
[113] Y. J. Feng, J. Y. Wang, R. Jaramillo, J. van Wezel, S. Haravifard, G. Srajer, Y. Liu, Z. A. Xu, P. B. Littlewood, T. F. Rosenbaum, "Order parameter fluctuations at a buried quantum critical point", *Proc. Natl Acad. Sci. USA* **109** (2012), p. 7224-7229.
[114] R. A. Cowley, "Acoustic phonon instabilities and structural phase transitions", *Phys. Rev. B* **13** (1976), p. 4877-4885.
[115] S. Sachdev, *Quantum Phase Transitions*, 2nd ed., Cambridge University Press, Cambridge, 2011.
[116] M. Heyl, "Dynamical quantum phase transitions: a review", *Rep. Prog. Phys.* **81** (2018), article no. 054001.
[117] O. Geza, *Universality In Nonequilibrium Lattice Systems: Theoretical Foundations*, World Scientific, Singapore, SG, 2008.
[118] U. C. Täuber, "Phase transitions and scaling in systems far from equilibrium", *Annu. Rev. Condens. Matter Phys.* **8** (2017), p. 185-210.
[119] J. Portman, H. Zhang, Z. Tao, K. Makino, M. Berz, P. M. Duxbury, C. Y. Ruan, "Computational and experimental characterization of high-brightness beams for femtosecond electron imaging and spectroscopy", *Appl. Phys. Lett.* **103** (2013), article no. 253115.
[120] L. Vidas, D. Schick, E. Martínez, D. Perez-Salinas, A. Ramos-Álvarez, S. Cichy, S. Batlle-Porro, A. S. Johnson, K. A. Hallman, R. F. Haglund, S. Wall, "Does VO_2 host a transient monoclinic metallic phase?", *Phys. Rev. X* **10** (2020), article no. 031047.
[121] F. Zhou, J. Williams, C.-Y. Ruan, "Femtosecond electron spectroscopy in an electron microscope with high brightness beams", *Chem. Phys. Lett.* **683** (2017), p. 488-494.
[122] R. Srinivasan, V. A. Lobastov, C. Y. Ruan, A. H. Zewail, "Ultrafast electron diffraction (UED)—A new development for the 4D determination of transient molecular structures", *Helv. Chim. Acta* **86** (2003), p. 1763-1838.
[123] A. Gahlmann, S. Tae Park, A. H. Zewail, "Ultrashort electron pulses for diffraction, crystallography and microscopy: theoretical and experimental resolutions", *Phys. Chem. Chem. Phys.* **10** (2008), p. 2894-2909.
[124] Z. S. Tao, H. Zhang, P. M. Duxbury, M. Berz, C. Y. Ruan, "Space charge effects in ultrafast electron diffraction and imaging", *J. Appl. Phys.* **111** (2012), article no. 044316.
[125] B. J. Siwick, J. R. Dwyer, R. E. Jordan, R. J. D. Miller, "Ultrafast electron optics: Propagation dynamics of femtosecond electron packets", *J. Appl. Phys.* **92** (2002), p. 1643-1648.
[126] B. W. Reed, "Femtosecond electron pulse propagation for ultrafast electron diffraction", *J. Appl. Phys.* **100** (2006), article no. 034916.
[127] B. S. Zerbe, X. Xiang, C. Y. Ruan, S. M. Lund, P. M. Duxbury, "Dynamical bunching and density peaks in expanding Coulomb clouds", *Phys. Rev. Accel. Beams* **21** (2018), article no. 064201.
[128] N. Bach, T. Domröse, A. Feist, T. Rittmann, S. Strauch, C. Ropers, S. Schäfer, "Coulomb interactions in high-coherence femtosecond electron pulses from tip emitters", *Struct. Dyn.* **6** (2019), article no. 014301.
[129] B. L. Qian, H. E. Elsayed-Ali, "Electron pulse broadening due to space charge effects in a photoelectron gun for electron diffraction and streak camera systems", *J. Appl. Phys.* **91** (2002), p. 462-468.
[130] H. Zhang, M. Berz, "The fast multipole method in the differential algebra framework", *Nucl. Instrum. Methods Phys. Res. A: Accel. Spectrom. Detect. Assoc. Equip.* **645** (2011), p. 338-344.
[131] T. van Oudheusden, P. L. E. M. Pasmans, S. B. van der Geer, M. J. de Loos, M. J. van der Wiel, O. J. Luiten, "Compression of subrelativistic space-charge-dominated electron bunches for single-shot femtosecond electron diffraction", *Phys. Rev. Lett.* **105** (2010), article no. 264801.
[132] M. Gao, Y. Jiang, G. H. Kassier, R. J. Dwayne Miller, "Single shot time stamping of ultrabright radio frequency compressed electron pulses", *Appl. Phys. Lett.* **103** (2013), article no. 033503.

[133] A. Valfells, D. W. Feldman, M. Virgo, P. G. O'Shea, Y. Y. Lau, "Effects of pulse-length and emitter area on virtual cathode formation in electron guns", *Phys. Plasmas* **9** (2002), p. 2377-2382.
[134] P. Zhang, A. Valfells, L. K. Ang, J. W. Luginsland, Y. Y. Lau, "100 years of the physics of diodes", *Appl. Phys. Rev.* **4** (2017), article no. 011304.
[135] S. Sun, X. Sun, J. Williams, C.-Y. Ruan, "Development of RF-compressed high-throughput femtosecond electron microscope", *Microsc. Microanal.* **26** (2020), p. 1-4.
[136] B. Barwick, A. H. Zewail, "Photonics and plasmonics in 4D Ultrafast electron microscopy", *ACS Photonics* **2** (2015), p. 1391-1402.
[137] M. T. Hassan, J. S. Baskin, B. Liao, A. H. Zewail, "High-temporal-resolution electron microscopy for imaging ultrafast electron dynamics", *Nat. Photonics* **11** (2017), p. 425-430.
[138] D. J. Flannigan, B. Barwick, A. H. Zewail, "Biological imaging with 4D ultrafast electron microscopy", *Proc. Natl Acad. Sci. USA* **107** (2010), p. 9933-9937.
[139] A. Yurtsever, R. M. van der Veen, A. H. Zewail, "Subparticle ultrafast spectrum imaging in 4D electron microscopy", *Science* **335** (2012), p. 59-64.
[140] A. Feist, K. E. Echternkamp, J. Schauss, S. V. Yalunin, S. Schafer, C. Ropers, "Quantum coherent optical phase modulation in an ultrafast transmission electron microscope", *Nature* **521** (2015), p. 200-203.
[141] R. M. van der Veen, T. J. Penfold, A. H. Zewail, "Ultrafast core-loss spectroscopy in four-dimensional electron microscopy", *Struct. Dyn.* **2** (2015), article no. 024302.
[142] Z. Su, J. S. Baskin, W. Zhou, J. M. Thomas, A. H. Zewail, "Ultrafast elemental and oxidation-state mapping of hematite by 4D electron microscopy", *J. Am. Chem. Soc.* **139** (2017), p. 4916-4922.
[143] P. W. Hawkes, J. C. H. Spence, *Science of Microscopy*, Springer, New York, 2007.
[144] K. Nakanishi, H. Takatera, H. Yamada, H. Shiba, "The near commensurate phase and effect of Harmonics on the successive phase transition in 1T-TaS_2", *J. Phys. Soc. Jpn.* **43** (1977), p. 1509-1517.
[145] K. Nakanishi, H. Shiba, "Theory of 3-dimensional orderings of charge-density waves in 1T-TaS_2, IT–$TaSe_2$", *J. Phys. Soc. Jpn.* **53** (1984), p. 1103-1113.
[146] A. Suzuki, M. Koizumi, M. Doyama, "Thermal evidences for successive CDW phase transitions in 1T-TaS_2", *Solid State Commun.* **53** (1985), p. 201-203.
[147] A. Spijkerman, J. L. de Boer, A. Meetsma, G. A. Wiegers, S. van Smaalen, "X-ray crystal-structure refinement of the nearly commensurate phase of 1T-TaS_2 in (3 + 2)-dimensional superspace", *Phys. Rev. B* **56** (1997), p. 13757-13767.
[148] T. Ishiguro, H. Sato, "Electron microscopy of phase transformations in 1T-TaS_2", *Phys. Rev. B* **44** (1991), p. 2046-2060.
[149] R. E. Thomson, U. Walter, E. Ganz, J. Clarke, A. Zettl, P. Rauch, F. J. DiSalvo, "Local charge-density-wave structure in 1T-TaS_2 determined by scanning tunneling microscopy", *Phys. Rev. B* **38** (1988), p. 10734-10743.
[150] R. E. Thomson, B. Burk, A. Zettl, J. Clarke, "Scanning tunneling microscopy of the charge-density-wave structure in 1T-TaS_2", *Phys. Rev. B* **49** (1994), p. 16899-16916.
[151] B. Sipos, A. F. Kusmartseva, A. Akrap, H. Berger, L. Forro, E. Tutis, "From Mott state to superconductivity in 1T-TaS_2", *Nat. Mater.* **7** (2008), p. 960-965.
[152] L. J. Li, E. C. T. O'Farrell, K. P. Loh, G. Eda, B. Ozyilmaz, A. H. C. Neto, "Controlling many-body states by the electric-field effect in a two-dimensional material", *Nature* **529** (2016), p. 185-189.
[153] C. D. Malliakas, M. G. Kanatzidis, "Divergence in the behavior of the charge density wave in RETe3 (RE = rare-earth element) with temperature and RE element", *J. Am. Chem. Soc.* **128** (2006), p. 12612-12613.
[154] N. Ru, C. L. Condron, G. Y. Margulis, K. Y. Shin, J. Laverock, S. B. Dugdale, M. F. Toney, I. R. Fisher, "Effect of chemical pressure on the charge density wave transition in rare-earth tritellurides RTe_3", *Phys. Rev. B* **77** (2008), article no. 035114.
[155] V. Brouet, W. L. Yang, X. J. Zhou, Z. Hussain, R. G. Moore, R. He, D. H. Lu, Z. X. Shen, J. Laverock, S. B. Dugdale, N. Ru, I. R. Fisher, "Angle-resolved photoemission study of the evolution of band structure and charge density wave properties in RTe_3 (R = Y, La, Ce, Sm, Gd, Tb, and Dy)", *Phys. Rev. B* **77** (2008), article no. 235104.
[156] M. Maschek, D. A. Zocco, S. Rosenkranz, R. Heid, A. H. Said, A. Alatas, P. Walmsley, I. R. Fisher, F. Weber, "Competing soft phonon modes at the charge-density-wave transitions in $DyTe_3$", *Phys. Rev. B* **98** (2018), article no. 094304.
[157] H.-M. Eiter, M. Lavagnini, R. Hackl, E. A. Nowadnick, A. F. Kemper, T. P. Devereaux, J.-H. Chu, J. G. Analytis, I. R. Fisher, L. Degiorgi, "Alternative route to charge density wave formation in multiband systems", *Proc. Natl Acad. Sci. USA* **110** (2013), p. 64-69.
[158] D. Leuenberger, J. A. Sobota, S. L. Yang, A. F. Kemper, P. Giraldo-Gallo, R. G. Moore, I. R. Fisher, P. S. Kirchmann, T. P. Devereaux, Z. X. Shen, "Classification of collective modes in a charge density wave by momentum-dependent modulation of the electronic band structure", *Phys. Rev. B* **91** (2015), article no. 201106.
[159] A. Banerjee, Y. Feng, D. M. Silevitch, J. Wang, J. C. Lang, H. H. Kuo, I. R. Fisher, T. F. Rosenbaum, "Charge transfer and multiple density waves in the rare earth tellurides", *Phys. Rev. B* **87** (2013), article no. 155131.
[160] L. Rettig, R. Cortés, J. H. Chu, I. R. Fisher, F. Schmitt, R. G. Moore, Z. X. Shen, P. S. Kirchmann, M. Wolf, U. Bovensiepen, "Persistent order due to transiently enhanced nesting in an electronically excited charge density wave", *Nat. Commun.* **7** (2016), article no. 10459.

[161] F. Schmitt, P. S. Kirchmann, U. Bovensiepen, R. G. Moore, L. Rettig, M. Krenz, J. H. Chu, N. Ru, L. Perfetti, D. H. Lu, M. Wolf, I. R. Fisher, Z. X. Shen, "Transient electronic structure and melting of a charge density wave in $TbTe_3$", *Science* **321** (2008), p. 1649-1652.

[162] W. S. Lee, P. S. Kirchman, Y. D. Chuang, A. F. Kemper, M. Trigo, L. Patthey, D. H. Lu, O. Krupin, M. Yi, D. A. Reis, D. Doering, P. Denes, W. F. Schlotter, J. J. Turner, G. Hays, P. Hering, T. Benson, J. H. Chu, T. P. Devereaux, I. R. Fisher, Z. Hussain, Z. X. Shen, "Ultrafast resonant soft X-ray diffraction dynamics of the charge density wave in $TbTe_3$", *Phys. Rev. B* **93** (2016), article no. 024304.

[163] R. J. Rivers, "Zurek–Kibble causality bounds in time-dependent Ginzburg–Landau theory and quantum field theory", *J. Low Temp. Phys.* **124** (2001), p. 41-83.

[164] J. A. Wilson, F. J. Di Salvo, S. Mahajan, "Charge-density waves and superlattices in the metallic layered transition metal dichalcogenides", *Adv. Phys.* **24** (1975), p. 117-201.

[165] K. T. Law, P. A. Lee, "1T-TaS_2 as a quantum spin liquid", *Proc. Natl Acad. Sci. USA* **114** (2017), p. 6996-7000.

[166] K. Rossnagel, "On the origin of charge-density waves in select layered transition-metal dichalcogenides,", *J. Phys. Condens. Matter* **23** (2011), article no. 213001.

[167] J. Ravnik, M. Diego, Y. Gerasimenko, Y. Vaskivskyi, I. Vaskivskyi, T. Mertelj, J. Vodeb, D. Mihailovic, "A time-domain phase diagram of metastable states in a charge ordered quantum material", *Nat. Commun.* **12** (2021), article no. 2323.

[168] I. Vaskivskyi, J. Gospodaric, S. Brazovskii, D. Svetin, P. Sutar, E. Goreshnik, I. A. Mihailovic, T. Mertelj, D. Mihailovic, "Controlling the metal-to-insulator relaxation of the metastable hidden quantum state in 1T-TaS_2", *Sci. Adv.* **1** (2015), article no. e1500168.

[169] Y. A. Gerasimenko, P. Karpov, I. Vaskivskyi, S. Brazovskii, D. Mihailovic, "Intertwined chiral charge orders and topological stabilization of the light-induced state of a prototypical transition metal dichalcogenide", *npj Quantum Mater.* **4** (2019), article no. 32.

[170] L. Ma, C. Ye, Y. Yu, X. F. Lu, X. Niu, S. Kim, D. Feng, D. Tomanek, Y.-W. Son, X. H. Chen, Y. Zhang, "A metallic mosaic phase and the origin of Mott-insulating state in 1T-TaS_2", *Nat. Commun.* **7** (2016), article no. 10956.

[171] D. Cho, S. Cheon, K.-S. Kim, S.-H. Lee, Y.-H. Cho, S.-W. Cheong, H. W. Yeom, "Nanoscale manipulation of the Mott insulating state coupled to charge order in 1T-TaS_2", *Nat. Commun.* **7** (2016), article no. 10453.

[172] Q. Stahl, M. Kusch, F. Heinsch, G. Garbarino, N. Kretzschmar, K. Hanff, K. Rossnagel, J. Geck, T. Ritschel, "Collapse of layer dimerization in the photo-induced hidden state of 1T-TaS_2", *Nat. Commun.* **11** (2020), article no. 1247.

[173] K. Sun, S. Sun, C. Zhu, H. Tian, H. Yang, J. Li, "Hidden CDW states and insulator-to-metal transition after a pulsed femtosecond laser excitation in layered chalcogenide 1T-$TaS_{2-x}Se_x$", *Sci. Adv.* **4** (2018), article no. eaas9660.

[174] X. Shi, W. You, Y. Zhang, Z. Tao, P. M. Oppeneer, X. Wu, R. Thomale, K. Rossnagel, M. Bauer, H. Kapteyn, M. Murnane, "Ultrafast electron calorimetry uncovers a new long-lived metastable state in 1T-$TaSe_2$ mediated by mode-selective electron–phonon coupling", *Sci. Adv.* **5** (2019), article no. eaav4449.

[175] N. Yoshikawa, H. Suganuma, H. Matsuoka, Y. Tanaka, P. Hemme, M. Cazayous, Y. Gallais, M. Nakano, Y. Iwasa, R. Shimano, "Ultrafast switching to an insulating-like metastable state by amplitudon excitation of a charge density wave", *Nat. Phys.* **17** (2021), p. 909-914.

[176] C.-Y. Ruan, "Hidden in plain light", *Nat. Phys.* **17** (2021), p. 884-885.

[177] C. B. Scruby, P. M. Williams, G. S. Parry, "The role of charge density waves in structural transformations of 1T TaS_2", *Philos. Mag.: A J. Theor. Exp. Appl. Phys.* **31** (1975), p. 255-274.

[178] W. L. McMillan, "Theory of discommensurations and the commensurate-incommensurate charge-density-wave phase transition", *Phys. Rev. B* **14** (1976), p. 1496-1502.

[179] K. Nakanishi, H. Shiba, "Domain-like incommensurate charge-density-wave states and the first-order incommensurate–commensurate transitions in layered tantalum dichalcogenides. I. 1T-Polytype", *J. Phys. Soc. Jpn.* **43** (1977), p. 1839-1847.

[180] Y. J. Feng, J. van Wezel, J. Y. Wang, F. Flicker, D. M. Silevitch, P. B. Littlewood, T. F. Rosenbaum, "Itinerant density wave instabilities at classical and quantum critical points", *Nat. Phys.* **11** (2015), p. 865-871.

[181] P. Bak, J. von Boehm, "Ising model with solitons, phasons, and "the devil's staircase"", *Phys. Rev. B* **21** (1980), p. 5297-5308.

[182] S. Tanda, T. Sambongi, T. Tani, S. Tanaka, "X-ray study of charge density wave structure in 1T-TaS_2", *J. Phys. Soc. Jpn.* **53** (1984), p. 476-479.

[183] J. C. S. Davis, D.-H. Lee, "Concepts relating magnetic interactions, intertwined electronic orders, and strongly correlated superconductivity", *Proc. Natl Acad. Sci. USA* **110** (2013), p. 17623-17630.

[184] R. Jaramillo, Y. Feng, J. C. Lang, Z. Islam, G. Srajer, P. B. Littlewood, D. B. McWhan, T. F. Rosenbaum, "Breakdown of the Bardeen–Cooper–Schrieffer ground state at a quantum phase transition", *Nature* **459** (2009), p. 405-409.

[185] X. L. Wu, C. M. Lieber, "Hexagonal domain-like charge density wave phase of TaS_2 determined by scanning tunneling microscopy", *Science* **243** (1989), p. 1703-1705.

[186] L. Perfetti, P. A. Loukakos, M. Lisowski, U. Bovensiepen, H. Berger, S. Biermann, P. S. Cornaglia, A. Georges, M. Wolf,

"Time evolution of the electronic structure of 1T-TaS_2 through the insulator–metal transition", *Phys. Rev. Lett.* **97** (2006), article no. 067402.

[187] S. Hellmann, T. Rohwer, M. Kallane, K. Hanff, C. Sohrt, A. Stange, A. Carr, M. M. Murnane, H. C. Kapteyn, L. Kipp, M. Bauer, K. Rossnagel, "Time-domain classification of charge-density-wave insulators", *Nat. Commun.* **3** (2012), article no. 2078.

[188] S. Hellmann, M. Beye, C. Sohrt, T. Rohwer, F. Sorgenfrei, H. Redlin, M. Kallaene, M. Marczynski-Buehlow, F. Hennies, M. Bauer, A. Foehlisch, L. Kipp, W. Wurth, K. Rossnagel, "Ultrafast melting of a charge-density wave in the Mott insulator 1T-TaS_2", *Phys. Rev. Lett.* **105** (2010), article no. 187401.

[189] M. Eichberger, H. Schaefer, M. Krumova, M. Beyer, J. Demsar, H. Berger, G. Moriena, G. Sciaini, R. J. D. Miller, "Snapshots of cooperative atomic motions in the optical suppression of charge density waves", *Nature* **468** (2010), p. 799-802.

[190] C. Laulhé, T. Huber, G. Lantz, A. Ferrer, S. O. Mariager, S. Grübel, J. Rittmann, J. A. Johnson, V. Esposito, A. Lübcke, L. Huber, M. Kubli, M. Savoini, V. L. R. Jacques, L. Cario, B. Corraze, E. Janod, G. Ingold, P. Beaud, S. L. Johnson, S. Ravy, "Ultrafast formation of a charge density wave state in 1T-TaS_2 observation at nanometer scales using time-resolved X-ray diffraction", *Phys. Rev. Lett.* **118** (2017), article no. 247401.

[191] K. Haupt, M. Eichberger, N. Erasmus, A. Rohwer, J. Demsar, K. Rossnagel, H. Schwoerer, "Ultrafast metamorphosis of a complex charge-density wave", *Phys. Rev. Lett.* **116** (2016), article no. 016402.

[192] T. Ritschel, J. Trinckauf, G. Garbarino, M. Hanfland, M. V. von Zimmermann, H. Berger, B. Buchner, J. Geck, "Pressure dependence of the charge density wave in 1T-TaS_2 and its relation to superconductivity", *Phys. Rev. B* **87** (2013), article no. 125135.

[193] R. Ang, Y. Tanaka, E. Ieki, K. Nakayama, T. Sato, L. J. Li, W. J. Lu, Y. P. Sun, T. Takahashi, "Real-space coexistence of the melted mott state and superconductivity in Fe-substituted 1T-TaS_2", *Phys. Rev. Lett.* **109** (2012), article no. 176403.

[194] L. J. Li, W. J. Lu, X. D. Zhu, L. S. Ling, Z. Qu, Y. P. Sun, "Fe-doping-induced superconductivity in the charge-density-wave system 1T-TaS_2", *Eur. Phys. Lett.* **97** (2012), article no. 67005.

[195] T. Ritschel, J. Trinckauf, K. Koepernik, B. Buchner, M. v. Zimmermann, H. Berger, Y. I. Joe, P. Abbamonte, J. Geck, "Orbital textures and charge density waves in transition metal dichalcogenides", *Nat. Phys.* **11** (2015), p. 328-331.

[196] C. J. Butler, M. Yoshida, T. Hanaguri, Y. Iwasa, "Mottness versus unit-cell doubling as the driver of the insulating state in 1T-TaS_2", *Nat. Commun.* **11** (2020), article no. 2477.

[197] Y. D. Wang, W. L. Yao, Z. M. Xin, T. T. Han, Z. G. Wang, L. Chen, C. Cai, Y. Li, Y. Zhang, "Band insulator to Mott insulator transition in 1T-TaS_2", *Nat. Commun.* **11** (2020), article no. 4215.

[198] J. Lee, K.-H. Jin, H. W. Yeom, "Distinguishing a mott insulator from a trivial insulator with atomic adsorbates", *Phys. Rev. Lett.* **126** (2021), article no. 196405.

[199] P. Darancet, A. J. Millis, C. A. Marianetti, "Three-dimensional metallic and two-dimensional insulating behavior in octahedral tantalum dichalcogenides", *Phys. Rev. B* **90** (2014), article no. 045134.

[200] R. Yusupov, T. Mertelj, V. V. Kabanov, S. Brazovskii, P. Kusar, J. H. Chu, I. R. Fisher, D. Mihailovic, "Coherent dynamics of macroscopic electronic order through a symmetry breaking transition", *Nat. Phys.* **6** (2010), p. 681-684.

[201] M. Trigo, P. Giraldo-Gallo, J. N. Clark, M. E. Kozina, T. Henighan, M. P. Jiang, M. Chollet, I. R. Fisher, J. M. Glownia, T. Katayama, P. S. Kirchmann, D. Leuenberger, H. Liu, D. A. Reis, Z. X. Shen, D. Zhu, "Ultrafast formation of domain walls of a charge density wave in $SmTe_3$", *Phys. Rev. B* **103** (2021), article no. 054109.

[202] M. J. Wei, W. J. Lu, R. C. Xiao, H. Y. Lv, P. Tong, W. H. Song, Y. P. Sun, "Manipulating charge density wave order in monolayer 1T-$TiSe_2$ by strain and charge doping: A first-principles investigation", *Phys. Rev. B* **96** (2017), article no. 165404.

[203] J. Zhang, C. Lian, M. Guan, W. Ma, H. Fu, H. Guo, S. Meng, "Photoexcitation induced quantum dynamics of charge density wave and emergence of a collective mode in 1T-TaS_2", *Nano Lett.* **19** (2019), p. 6027-6034.

[204] Y. Zhang, X. Shi, M. Guan, W. You, Y. Zhong, T. R. Kafle, Y. Huang, H. Ding, M. Bauer, K. Rossnagel, S. Meng, H. C. Kapteyn, M. M. Murnane, "Creation of a novel inverted charge density wave state", https://arxiv.org/abs/2011.07623, 2020.

[205] S. Duan, Y. Cheng, W. Xia, Y. Yang, F. Qi, T. Tang, Y. Guo, D. Qian, D. Xiang, J. Zhang, W. Zhang, "Optical manipulation of electronic dimensionality in a quantum material", https://arxiv.org/abs/2101.08507v1, 2021.

[206] M. Trigo, P. Giraldo-Gallo, M. E. Kozina, T. Henighan, M. P. Jiang, H. Liu, J. N. Clark, M. Chollet, J. M. Glownia, D. Zhu, T. Katayama, D. Leuenberger, P. S. Kirchmann, I. R. Fisher, Z. X. Shen, D. A. Reis, "Coherent order parameter dynamics in $SmTe_3$", *Phys. Rev. B* **99** (2019), article no. 104111.

[207] J. Zhang, X. Tan, M. Liu, S. W. Teitelbaum, K. W. Post, F. Jin, K. A. Nelson, D. N. Basov, W. Wu, R. D. Averitt, "Cooperative photoinduced metastable phase control in strained manganite films", *Nat. Mater.* **15** (2016), p. 956-960.

[208] A. R. Beal, W. Y. Liang, H. P. Hughes, "Kramers–Kronig analysis of the reflectivity spectra of 3R–WS_2 and 2H–WSe_2", *J. Phys. C: Solid State Phys.* **9** (1976), p. 2449-2457.

[209] S. W. King, M. Milosevic, "A method to extract absorption coefficient of thin films from transmission spectra of the films on thick substrates", *J. Appl. Phys.* **111** (2012), article no. 073109.

[210] M. Milosevic, S. L. Berets, "Applications of the theory of optical spectroscopy to numerical simulations", *Appl. Spectrosc.* **47** (1993), p. 566-574.
[211] R. A. Murdick, "Investigations on interfacial dynamics with ultrafast electron diffraction", PhD Thesis, Michigan State University, USA, 2009.
[212] Z. S. Tao, T. R. T. Han, C. Y. Ruan, "Anisotropic electron–phonon coupling investigated by ultrafast electron crystallography: Three-temperature model", *Phys. Rev. B* **87** (2013), article no. 235124.
[213] L. Perfetti, P. A. Loukakos, M. Lisowski, U. Bovensiepen, M. Wolf, H. Berger, S. Biermann, A. Georges, "Femtosecond dynamics of electronic states in the Mott insulator 1T-TaS_2 by time resolved photoelectron spectroscopy", *New J. Phys.* **10** (2008), article no. 053019.
[214] R. F. Egerton, *ProQuest, Physical Principles of Electron Microscopy: An Introduction to TEM, SEM, and AEM*, Springer, New York, 2005.
[215] D. B. Williams, C. B. Carter, *Transmission Electron Microscopy: A Textbook for Materials Science*, Springer, New York, 2009.
[216] H. Park, X. Wang, S. Nie, R. Clinite, J. Cao, "Mechanism of coherent acoustic phonon generation under nonequilibrium conditions", *Phys. Rev. B,* **72** (2005), article no. 100301.
[217] H. S. Park, J. S. Baskin, B. Barwick, O. H. Kwon, A. H. Zewail, "4D ultrafast electron microscopy: imaging of atomic motions, acoustic resonances, and moiré fringe dynamics", *Ultramicroscopy* **110** (2009), p. 7-19.
[218] R. P. Chatelain, V. R. Morrison, B. L. M. Klarenaar, B. J. Siwick, "Coherent and incoherent electron–phonon coupling in graphite observed with radio-frequency compressed ultrafast electron diffraction", *Phys. Rev. Lett.* **113** (2014), article no. 235502.
[219] L. Wei, S. Sun, C. Guo, Z. Li, K. Sun, Y. Liu, W. Lu, Y. Sun, H. Tian, H. Yang, J. Li, "Dynamic diffraction effects and coherent breathing oscillations in ultrafast electron diffraction in layered 1T-TaSeTe", *Struct. Dyn.* **4** (2017), article no. 044012.
[220] A. Feist, N. Rubiano da Silva, W. Liang, C. Ropers, S. Schäfer, "Nanoscale diffractive probing of strain dynamics in ultrafast transmission electron microscopy", *Struct. Dyn.* **5** (2018), article no. 014302.
[221] T. E. Karam, J. Hu, G. A. Blake, "Strongly coupled electron–phonon dynamics in few-layer $TiSe_2$ exfoliates", *ACS Photonics* **5** (2018), p. 1228-1234.
[222] Y. Zhang, D. J. Flannigan, "Observation of anisotropic strain-wave dynamics and few-layer dephasing in MoS_2 with ultrafast electron microscopy", *Nano Lett.* **19** (2019), p. 8216-8224.
[223] A. Nakamura, T. Shimojima, Y. Chiashi, M. Kamitani, H. Sakai, S. Ishiwata, H. Li, K. Ishizaka, "Nanoscale imaging of unusual photoacoustic waves in thin flake VTe_2", *Nano Lett.* **20** (2020), p. 4932-4938.
[224] A. R. Beal, H. Hughes, W. Y. Liang, "The reflectivity spectra of some group VA transition metal dichalcogenides", *J. Phys. C Solid State Phys.* **8** (1975), p. 4236.
[225] O. Sezerman, A. M. Simpson, M. H. Jericho, "Thermal expansion of 1T-TaS_2 and 2H–$NbSe_2$", *Solid State Commun.* **36** (1980), p. 737-740.
[226] F. L. Givens, G. E. Fredericks, "Thermal expansion of $NbSe_2$ and TaS_2", *J. Phys. Chem. Solids* **38** (1977), p. 1363-1365.
[227] M. H. Jericho, A. M. Simpson, R. F. Frindt, "Velocity of ultrasonic waves in 2H–$NbSe_2$, 2H–TaS_2, and 1T-TaS_2", *Phys. Rev. B* **22** (1980), p. 4907-4914.
[228] V. Eyert, "The metal–insulator transitions of VO_2: a band theoretical approach", *Ann. Phys.* **11** (2002), p. 650-702.
[229] J. P. Pouget, "Basic aspects of the metal–insulator transition in vanadium dioxide VO_2: a critical review", *C. R. Phys.* **22** (2021), p. 37-87.
[230] Y. Zhou, S. Ramanathan, "Correlated electron materials and field effect transistors for logic: a review", *Crit. Rev. Solid State Mater. Sci.* **38** (2013), p. 286-317.
[231] K. Liu, S. Lee, S. Yang, O. Delaire, J. Wu, "Recent progresses on physics and applications of vanadium dioxide", *Mater. Today* **21** (2018), p. 875-896.
[232] J. Cao, Y. Gu, W. Fan, L. Q. Chen, D. F. Ogletree, K. Chen, N. Tamura, M. Kunz, C. Barrett, J. Seidel, J. Wu, "Extended mapping and exploration of the vanadium dioxide stress–temperature phase diagram", *Nano Lett.* **10** (2010), p. 2667-2673.
[233] J. H. Park, J. M. Coy, T. S. Kasirga, C. Huang, Z. Fei, S. Hunter, D. H. Cobden, "Measurement of a solid-state triple point at the metal–insulator transition in VO_2", *Nature* **500** (2013), p. 431-434.
[234] J. P. Pouget, H. Launois, "Metal–insulator phase transition in VO_2", *J. Phys. Colloq.* **37** (1976), p. C4-49-C4-57.
[235] W.-P. Hsieh, M. Trigo, D. A. Reis, G. Andrea Artioli, L. Malavasi, W. L. Mao, "Evidence for photo-induced monoclinic metallic VO_2 under high pressure", *Appl. Phys. Lett.* **104** (2014), article no. 021917.
[236] V. R. Morrison, R. P. Chatelain, K. L. Tiwari, A. Hendaoui, A. Bruhács, M. Chaker, B. J. Siwick, "A photoinduced metal-like phase of monoclinic VO_2 revealed by ultrafast electron diffraction", *Science* **346** (2014), p. 445-448.
[237] H. T. Kim, B. G. Chae, D. H. Youn, S. L. Maeng, G. Kim, K. Y. Kang, Y. S. Lim, "Mechanism and observation of Mott transition in VO_2-based two- and three-terminal devices", *New J. Phys.* **6** (2004), article no. 52.
[238] J. Laverock, S. Kittiwatanakul, A. A. Zakharov, Y. R. Niu, B. Chen, S. A. Wolf, J. W. Lu, K. E. Smith, "Direct observation

of decoupled structural and electronic transitions and an ambient pressure monoclinic-like metallic phase of VO_2", *Phys. Rev. Lett.* **113** (2014), article no. 216402.

[239] M. Yang, Y. Yang, H. Bin, L. Wang, K. Hu, Y. Dong, H. Xu, H. Huang, J. Zhao, H. Chen, L. Song, H. Ju, J. Zhu, J. Bao, X. Li, Y. Gu, T. Yang, X. Gao, Z. Luo, C. Gao, "Suppression of structural phase transition in VO_2 by epitaxial strain in vicinity of metal–insulator transition", *Sci. Rep.* **6** (2016), article no. 23119.

[240] Z. S. Tao, T. R. T. Han, S. D. Mahanti, P. M. Duxbury, F. Yuan, C. Y. Ruan, K. Wang, J. Q. Wu, "Decoupling of structural and electronic phase transitions in VO_2", *Phys. Rev. Lett.* **109** (2012), article no. 166406.

[241] D. Lee, B. Chung, Y. Shi, G.-Y. Kim, N. Campbell, F. Xue, K. Song, S.-Y. Choi, J. P. Podkaminer, T. H. Kim, P. J. Ryan, J.-W. Kim, T. R. Paudel, J.-H. Kang, J. W. Spinuzzi, D. A. Tenne, E. Y. Tsymbal, M. S. Rzchowski, L. Q. Chen, J. Lee, C. B. Eom, "Isostructural metal–insulator transition in VO_2", *Science* **362** (2018), p. 1037-1040.

[242] J. B. Goodenough, "The two components of the crystallographic transition in VO_2", *J. Solid State Chem.* **3** (1971), p. 490-500.

[243] N. F. Mott, *Metal–Insulator Transitions*, 2nd ed., Taylor & Francis, London, New York, 1990.

[244] S. Biermann, A. Poteryaev, A. I. Lichtenstein, A. Georges, "Dynamical singlets and correlation-assisted Peierls transition in VO_2", *Phys. Rev. Lett.* **94** (2005), article no. 026404.

[245] M. W. Haverkort, Z. Hu, A. Tanaka, W. Reichelt, S. V. Streltsov, M. A. Korotin, V. I. Anisimov, H. H. Hsieh, H. J. Lin, C. T. Chen, D. I. Khomskii, L. H. Tjeng, "Orbital-assisted metal–insulator transition in VO_2", *Phys. Rev. Lett.* **95** (2005), article no. 196404.

[246] T. C. Koethe, Z. Hu, M. W. Haverkort, C. Schüßler-Langeheine, F. Venturini, N. B. Brookes, O. Tjernberg, W. Reichelt, H. H. Hsieh, H. J. Lin, C. T. Chen, L. H. Tjeng, "Transfer of spectral weight and symmetry across the metal–insulator transition in VO_2", *Phys. Rev. Lett.* **97** (2006), article no. 116402.

[247] W. H. Brito, M. C. O. Aguiar, K. Haule, G. Kotliar, "Metal–Insulator transition in VO_2: A DFT+DMFT perspective", *Phys. Rev. Lett.* **117** (2016), article no. 056402.

[248] C. Weber, D. D. O'Regan, N. D. Hine, M. C. Payne, G. Kotliar, P. B. Littlewood, "Vanadium dioxide: a Peierls–Mott insulator stable against disorder", *Phys. Rev. Lett.* **108** (2012), article no. 256402.

[249] A. Tselev, I. A. Luk'yanchuk, I. N. Ivanov, J. D. Budai, J. Z. Tischler, E. Strelcov, A. Kolmakov, S. V. Kalinin, "Symmetry relationship and strain-induced transitions between insulating M_1 and M_2 and Metallic R phases of vanadium dioxide", *Nano Lett.* **10** (2010), p. 4409-4416.

[250] Z. Tao, F. Zhou, T.-R. T. Han, D. Torres, T. Wang, N. Sepulveda, K. Chang, M. Young, R. R. Lunt, C.-Y. Ruan, "The nature of photoinduced phase transition and metastable states in vanadium dioxide", *Sci. Rep.* **6** (2016), article no. 38514.

[251] A. Zylbersztejn, N. F. Mott, "Metal–insulator transition in vanadium dioxide", *Phys. Rev. B* **11** (1975), p. 4383-4395.

[252] T. M. Rice, H. Launois, J. P. Pouget, "Comment on VO_2: peierls or Mott–Hubbard? A view from band theory", *Phys. Rev. Lett.* **73** (1994), p. 3042-3042.

[253] A. Cavalleri, T. Dekorsy, H. H. W. Chong, J. C. Kieffer, R. W. Schoenlein, "Evidence for a structurally-driven insulator-to-metal transition in VO_2: A view from the ultrafast timescale", *Phys. Rev. B* **70** (2004), article no. 161102.

[254] S. Wall, D. Wegkamp, L. Foglia, K. Appavoo, J. Nag, R. F. Haglund, J. Stähler, M. Wolf, "Ultrafast changes in lattice symmetry probed by coherent phonons", *Nat. Commun.* **3** (2012), article no. 721.

[255] K. Appavoo, J. Nag, B. Wang, W. Luo, G. Duscher, E. A. Payzant, M. Y. Sfeir, S. T. Pantelides, R. F. Haglund, "Doping-driven electronic and lattice dynamics in the phase-change material vanadium dioxide", *Phys. Rev. B* **102** (2020), article no. 115148.

[256] C. Kubler, H. Ehrke, R. Huber, R. Lopez, A. Halabica, R. F. Haglund, A. Leitenstorfer, "Coherent structural dynamics and electronic correlations during an ultrafast insulator-to-metal phase transition in VO_2", *Phys. Rev. Lett.* **99** (2007), article no. 116401.

[257] T. L. Cocker, L. V. Titova, S. Fourmaux, G. Holloway, H. C. Bandulet, D. Brassard, J. C. Kieffer, M. A. El Khakani, F. A. Hegmann, "Phase diagram of the ultrafast photoinduced insulator–metal transition in vanadium dioxide", *Phys. Rev. B* **85** (2012), article no. 155120.

[258] A. Pashkin, C. Kubler, H. Ehrke, R. Lopez, A. Halabica, R. F. Haglund, R. Huber, A. Leitenstorfer, "Ultrafast insulator–metal phase transition in VO_2 studied by multiterahertz spectroscopy", *Phys. Rev. B* **83** (2011), article no. 195120.

[259] D. Wegkamp, M. Herzog, L. Xian, M. Gatti, P. Cudazzo, C. L. McGahan, R. E. Marvel, R. F. Haglund, A. Rubio, M. Wolf, J. Stähler, "Instantaneous band gap collapse in photoexcited monoclinic VO_2 due to photocarrier doping", *Phys. Rev. Lett.* **113** (2014), article no. 216401.

[260] D. Wegkamp, J. Stahler, "Ultrafast dynamics during the photoinduced phase transition in VO_2", *Progr. Surf. Sci.* **90** (2015), p. 464-502.

[261] P. Baum, D.-S. Yang, A. H. Zewail, "4D visualization of transitional structures in phase transformations by electron diffraction", *Science* **318** (2007), p. 788-792.

[262] M. R. Otto, L. P. René de Cotret, D. A. Valverde-Chavez, K. L. Tiwari, N. Émond, M. Chaker, D. G. Cooke, B. J. Siwick, "How optical excitation controls the structure and properties of vanadium dioxide", *Proc. Natl Acad. Sci. USA* **116** (2019), p. 450-455.

[263] X. He, N. Punpongjareorn, W. Liang, Y. Lin, C. Chen, A. J. Jacobson, D.-S. Yang, "Photoinduced strain release and phase transition dynamics of solid-supported ultrathin vanadium dioxide", *Sci. Rep.* **7** (2017), article no. 10045.

[264] B. T. O'Callahan, A. C. Jones, J. Hyung Park, D. H. Cobden, J. M. Atkin, M. B. Raschke, "Inhomogeneity of the ultrafast insulator-to-metal transition dynamics of VO_2", *Nat. Commun.* **6** (2015), article no. 6849.

[265] K. Appavoo, B. Wang, N. F. Brady, M. Seo, J. Nag, R. P. Prasankumar, D. J. Hilton, S. T. Pantelides, R. F. Haglund, "Ultrafast phase transition via catastrophic phonon collapse driven by plasmonic hot-electron injection", *Nano Lett.* **14** (2014), p. 1127-1133.

[266] M. Liu, A. J. Sternbach, M. Wagner, T. V. Slusar, T. Kong, S. L. Bud'ko, S. Kittiwatanakul, M. M. Qazilbash, A. McLeod, Z. Fei, E. Abreu, J. Zhang, M. Goldflam, S. Dai, G.-X. Ni, J. Lu, H. A. Bechtel, M. C. Martin, M. B. Raschke, R. D. Averitt, S. A. Wolf, H.-T. Kim, P. C. Canfield, D. N. Basov, "Phase transition in bulk single crystals and thin films of VO_2 by nanoscale infrared spectroscopy and imaging", *Phys. Rev. B* **91** (2015), article no. 245155.

[267] J. Cao, E. Ertekin, V. Srinivasan, W. Fan, S. Huang, H. Zheng, J. W. L. Yim, D. R. Khanal, D. F. Ogletree, J. C. Grossmanan, J. Wu, "Strain engineering and one-dimensional organization of metal–insulator domains in single-crystal vanadium dioxide beams", *Nat. Nanotechnol.* **4** (2009), p. 732-737.

[268] J. Wei, Z. H. Wang, W. Chen, D. H. Cobden, "New aspects of the metal–insulator transition in single-domain vanadium dioxide nanobeams", *Nat. Nanotechnol.* **4** (2009), p. 420-424.

[269] K. A. Hallman, K. J. Miller, A. Baydin, S. M. Weiss, R. F. Haglund, "Sub-picosecond response time of a hybrid VO_2: silicon waveguide at 1550 nm", *Adv. Opt. Mater.* **9** (2021), article no. 2001721.

[270] S. Wall, S. Yang, L. Vidas, M. Chollet, J. M. Glownia, M. Kozina, T. Katayama, T. Henighan, M. Jiang, T. A. Miller, D. A. Reis, L. A. Boatner, O. Delaire, M. Trigo, "Ultrafast disordering of vanadium dimers in photoexcited VO_2", *Science* **362** (2018), p. 572-576.

[271] R. Mankowsky, M. Först, A. Cavalleri, "Non-equilibrium control of complex solids by nonlinear phononics", *Rep. Progr. Phys.* **79** (2016), article no. 064503.

[272] T. Oka, S. Kitamura, "Floquet engineering of quantum materials", *Annu. Rev. Condens. Matter Phys.* **10** (2019), p. 387-408.

[273] H. Murayama, Y. Sato, T. Taniguchi, R. Kurihara, X. Z. Xing, W. Huang, S. Kasahara, Y. Kasahara, I. Kimchi, M. Yoshida, Y. Iwasa, Y. Mizukami, T. Shibauchi, M. Konczykowski, Y. Matsuda, "Effect of quenched disorder on the quantum spin liquid state of the triangular-lattice antiferromagnet 1T-TaS_2", *Phys. Rev. Res.* **2** (2020), article no. 013099.

[274] E. Martino, A. Pisoni, L. Ćirić, A. Arakcheeva, H. Berger, A. Akrap, C. Putzke, P. J. W. Moll, I. Batistić, E. Tutiš, L. Forró, K. Semeniuk, "Preferential out-of-plane conduction and quasi-one-dimensional electronic states in layered 1T-TaS_2", *npj 2D Mater. Appl.* **4** (2020), article no. 7.

[275] K. Okajima, S. Tanaka, "Electronic conduction in the commensurate charge density wave state of 1T-TaS_2", *J. Phys. Soc. Jpn.* **53** (1984), p. 2332-2341.

[276] M. D. Núñez-Regueiro, J. M. Lopez-Castillo, C. Ayache, "Thermal conductivity of 1T-TaS_2 and 2H–$TaSe_2$", *Phys. Rev. Lett.* **55** (1985), p. 1931-1934.

Comptes Rendus
Physique
2021, 22, nº S2, p. 75-94
https://doi.org/10.5802/crphys.85

Physics of ultra-fast phenomena / *Physique des phénomènes ultra-rapides*

Structural dynamics probed by X-ray pulses from synchrotrons and XFELs

Matteo Levantino [a], Qingyu Kong [b], Marco Cammarata [a], Dmitry Khakhulin [c], Friedrich Schotte [d], Philip Anfinrud [d], Victoria Kabanova [e], Hyotcherl Ihee [f], Anton Plech [g], Savo Bratos [h] and Michael Wulff [*, a]

[a] ESRF — The European Synchrotron, 71 Avenue des Martyrs, 30043 Grenoble Cedex, France

[b] Soleil Synchrotron, L'Orme des Merisiers, 91190 Saint-Aubin, France

[c] European XFEL, 22869 Schenefeld, Germany

[d] National Institute of Health, Bethesda, MD 20892, USA

[e] PSI, SwissFEL, 5232 Villigen, Switzerland

[f] Department of Chemistry, KAIST, Daejeon, South Korea

[g] Karlsruhe Institute of Technology, 76021 Karlsruhe, Germany

[h] Université Pierre et Marie Curie, Paris 75252, France

E-mails: matteo.levantino@esrf.fr (M. Levantino), qingyu.kong@synchrotron-soleil.fr (Q. Kong), marco.cammarata@esrf.eu (M. Cammarata), dmitry.khakhulin@xfel.eu (D. Khakhulin), FriedrichS@intra.niddk.nih.gov (F. Schotte), PhilipA@intra.niddk.nih.gov (P. Anfinrud), victoria.kabanova@gmail.com (V. Kabanova), hyotcherl.ihee@kaist.ac.kr (H. Ihee), anton.plech@kit.edu (A. Plech), bratossavo@gmail.com (S. Bratos), wulff@esrf.fr (M. Wulff)

Abstract. This review focuses on how short X-ray pulses from synchrotrons and XFELs can be used to track light-induced structural changes in molecular complexes and proteins via the pump–probe method. The upgrade of the European Synchrotron Radiation Facility to a diffraction-limited storage ring, based on the seven-bend achromat lattice, and how it might boost future pump–probe experiments are described. We discuss some of the first X-ray experiments to achieve 100 ps time resolution, including the dissociation and in-cage recombination of diatomic molecules, as probed by wide-angle X-ray scattering, and the 3D filming of ligand transport in myoglobin, as probed by Laue diffraction. Finally, the use of femtosecond XFEL pulses to investigate primary chemical reactions, bond breakage and bond formation, isomerisation and electron transfer are discussed.

Keywords. Structural dynamics, Synchroton radiation, Pump and probe, Single shot X-ray experiment, Photolysis, Dissociation dynamics.

Available online 13th September 2021

[*] Corresponding author.

1. Introduction

In order to gain a deeper understanding into how physical, chemical and biological processes work at the atomic level, it is important to know how the structure evolves as a function of time. Whereas static structures can often be determined with laboratory X-ray sources, structural characterization of short-lived intermediates requires short, high-intensity X-ray pulses from synchrotrons or Free Electron Lasers (XFEL). Examples of the time and length scales that have been studied with short X-ray and laser pulses are shown in Figure 1. These processes span 18 orders of magnitude in time, from attoseconds to seconds. The time scale of a given process is intimately linked to the length scale. For example, conformational changes in proteins evolve on the microsecond to millisecond time scale whereas structural changes in small molecules, bond breakage/formation, isomerisation and electron transfer, span from femtoseconds to nanoseconds. The primary time scale in chemistry is governed by the vibrational period of bonded atoms, with higher Z atoms having longer vibrational periods [1]. For example, the oscillation period in the ground states of H_2 and I_2 are 10 fs and 156 fs, respectively. Structural changes in molecules propagate at the speed of sound, typically 1000 m/s, which corresponds to 100 fs/Å.

The femtosecond time scale became accessible with the advent of ultrafast lasers in the 1980s and spawned the field of femtochemistry. For filming molecular reactions by optical absorption spectroscopy and electron diffraction, the Nobel Prize in Chemistry was awarded to Zewail in 1999 [2, 3]. This work was made possible by the development of chirped-pulse amplification, in which a weak femtosecond optical pulse is stretched before amplification to high energy levels, and then recompressed back to its original pulse duration. Prior to this innovation, for which Gerard Mourou from Ecole Polytechnique in France was awarded the Nobel Prize in Physics in 2019, the pulse energy achievable with ultrashort pulses was severely limited by nonlinear optical processes that would otherwise destroy the gain medium. The ability to amplify femtosecond pulses to high energy levels is critically important for laser/X-ray experiments that often require high pulse energies at specific wavelengths to produce a detectable signal [4].

The time resolution at synchrotrons and XFELs is ultimately limited by the X-ray pulse length, which is 100 ps for synchrotrons and 10–100 fs for XFELs. The longer duration of synchrotron pulses is a consequence of the spread in energy in the electron bunch that arises from random emission of radiation in the bending magnets of the ring. In linear accelerators, the electrons are accelerated without emission and the electron bunch can therefore be very small in space and short in time.

The signal from short pulses is usually not resolved by detectors and the fastest time resolution can only be obtained by the pump–probe method. In a laser/X-ray pump–probe experiment, the system is initiated rapidly and uniformly by a short laser pulse, which triggers a structural or electronic change and a delayed X-ray pulse probes the evolution. By varying the delay, the process is probed or filmed by a series of snapshots that can be stitched together into a movie. The instrumental time resolution is the convolution of the X-ray and laser pulse lengths and their relative jitter. The pump–probe principle is shown in Figure 2.

The present manuscript is organised as follows. First, we briefly describe the European Synchrotron Radiation Facility (ESRF) in Grenoble, where the first picosecond X-ray experiments were performed in 1994. This is followed by a short presentation of the Extremely Bright Source (EBS) upgrade of the ESRF to a nearly diffraction limited source that was completed in January 2020. The pulse intensity and spectral bandwidth of the EBS beam and the potential for new experiments will also be discussed. Then we'll present some unpublished work from early pump probe experiments at ESRF examining the dissociation and recombination dynamics of I_2 in liquid CCl_4 and the dissociation of CO from Myoglobin studied by Laue diffraction that was the first 3D movie of a protein at work. The manuscript will finally mention a few XFEL experiments with femtosecond resolution.

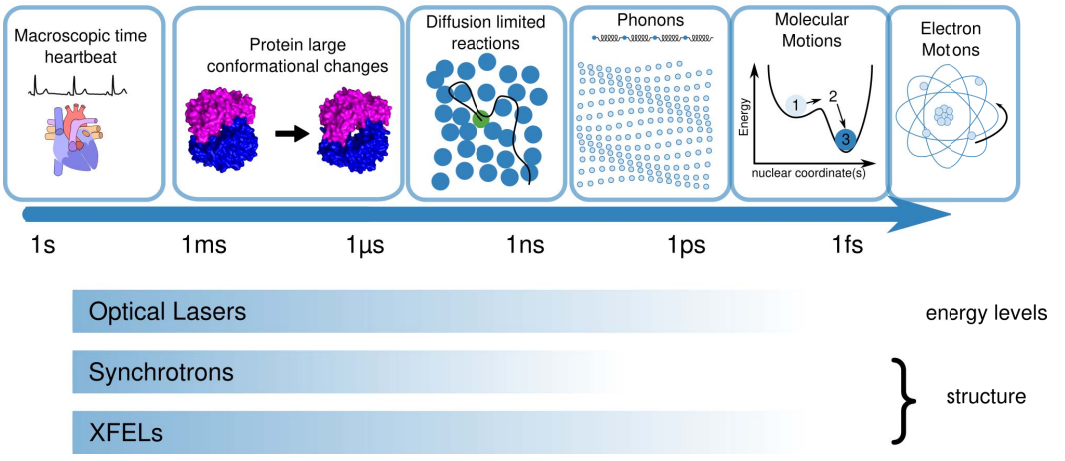

Figure 1. Dynamic process and techniques. On time scales below 1 ms, the time resolution is obtained by pump–probe with optical reaction initiation.

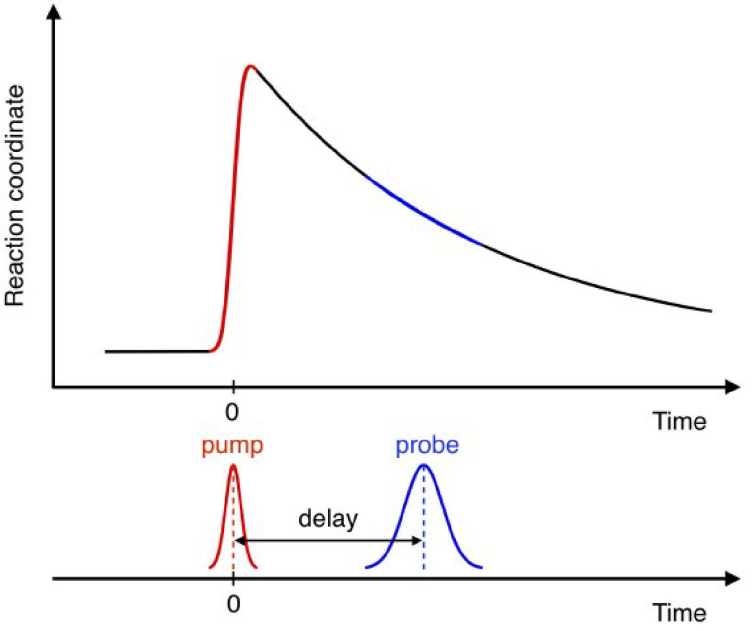

Figure 2. Pump and probe principle. The pump pulse (red) triggers a structural change that is probed by a delayed X-ray pulse (blue). When the sample is refreshed between pulses, the diffraction pattern arising from single pump–probe pairs can be accumulated on an area detector to improve the signal to noise ratio. In femtosecond serial crystallography, the flux is so high that diffraction patterns from single probe pulses can be indexed. The technique is freed from radiation damage since diffraction is faster than radiation damage.

2. Pump probe experiments at ESRF

The European Synchrotron Radiation Facility (ESRF) was the first large synchrotron to produce hard X-rays from undulators. It is a 6.0 GeV ring with a circumference of 844 m. With its sister

Figure 3. European Synchrotron Radiation Facility (ESRF) in Grenoble (2020). The facility is funded by 22 countries, employs 705 people (2021), and has 47 beamlines including collaborating research group beamlines (CRG). The seven-bend-achromat lattice was installed during a 12-month shutdown in 2019 and opened for users in August 2020.

facilities in the USA and Japan, the APS at Argonne and SPring8 near Kyoto, these third-generation synchrotrons have revolutionised X-ray science in fields from nuclear physics to cultural heritage. This is due to the wide energy range, high radiation intensity, coherence and short pulses. The ESRF has 47 beamlines, where 750 experiments are conducted with users per year. Beam time is allocated in peer review competition. The ESRF is shown in Figure 3. The beamlines are highly specialised with unique optics, sample environments and detectors. The facility was upgraded in 2014 with 6 long beamlines with nanometre focusing. The extended experimental hall for these beamlines appears in the photo with the reddish roof.

In spite of the success of third-generation synchrotrons, the large horizontal emittance is an obstacle for making smaller and more coherent beams. The ESRF storage ring was upgraded in 2019 to become a diffraction-limited storage ring, the Extremely Bright Source (EBS). In the EBS design, the maximum curvature in the bending sections in the ring is reduced by the use of 7 closely spaced bending magnets rather than by two strongly deflecting electromagnets in classical designs. The extended bend of the orbit reduces the energy loss to synchrotron radiation making the electron beam more monochromatic, which reduces the spatial dispersion everywhere in the ring. The current of the electron beam is kept constant at 200 mA by frequent top-ups, typically every 10 min at present. The cross section of the electron beam is $76 \times 16\ \mu m^2$ (H × V) in the insertion device sections (FWHM). The brilliance of the photon source has increased by 30–100 depending on the photon energy. The EBS principle is shown in Figure 4 together with the U17 undulator spectra. The EBS pulse length is unchanged, for the time being at least, at 100 ps (FWHM). For more details the reader is referred to the articles by Pantaleo Raimondi, the ESRF accelerator director, who designed the lattice with his colleagues [5, 6].

As for the technology for pump–probe experiments at synchrotrons, the first issue to consider is that the repetition rate of wavelength tuneable lasers is much lower that the X-ray pulse frequency. The present picosecond laser on beamline ID09 runs at 1 kHz compared to the synchrotron producing 5.7 MHz pulses in the 16-bunch mode. In practice, the X-ray frequency is

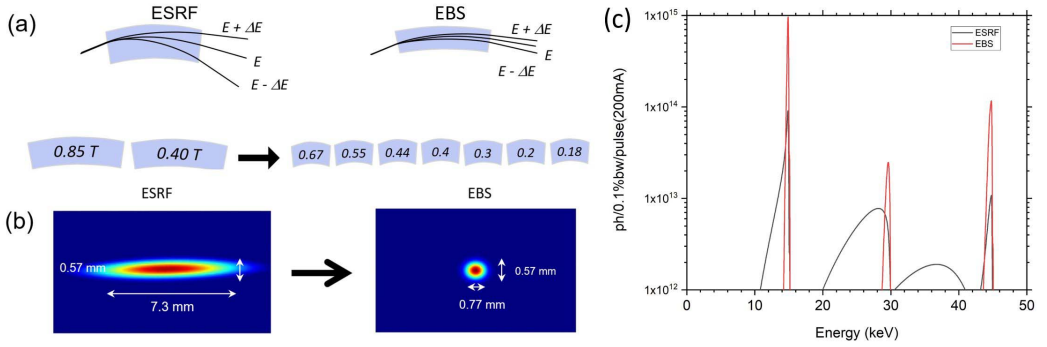

Figure 4. Comparison of the original ESRF and upgraded EBS synchrotron. (a) Dispersion of the electron beam passing through a bending magnet sector. The dispersion is reduced by employing 7 bending magnets rather than by 2 strong ones used in the old design, which results in a 30-fold reduction in horizontal emittance. (b) Beam profile of the EBS and ESRF beam 27 m from the source (U17 undulator @ 15 keV). (c) Spectral intensity of the U17 undulator for the ESRF and EBS. The intensity is measured in a 0.5×0.5 mm^2 slits 27 m from the source to show the gain in intensity in the centre of the beam. Many experiments can be performed without a monochromator, which affords a very significant gain in flux.

lowered by mechanical choppers, which allow to isolate single pulses from special diluted filling modes of the ring. The ID09 choppers reduce the average intensity (ph/s) on the sample by a factor 5700. As a result, it is important to use the intense pink beam (~100 W) whenever possible. The intensity of the radiation increases with the magnetic field acting on the electrons and to maximise the field, the magnets in the U17 undulator are inside the vacuum of the storage ring. The bunch current is limited to 10 mA/bunch in 4-bunch mode due to the reduction in lifetime at higher currents. The maximum flux from the U17 undulator is 1×10^{10} ph at 15 keV for a 10 mA bunch with fully opened slits. At this setting the relative bandwidth $\delta E/E$ is 4.0% which can be used in small angle scattering experiments. If the slits are set to accept the central cone only, the bandwidth is reduced to 2.0% with 1×10^9 ph/pulse.

One advantage of reducing the pulse frequency to 1 kHz is that a liquid sample can be exchanged between pulses in a flow cell so that irreversible processes can be studied [7]. The lower frequency also protects the sample from the damage of the full beam. In practice, the white beam at ID09 is first chopped by a pre-chopper, the so called heatload chopper, into 36 μs pulses at 1 kHz. These macro pulses are then chopped by a high-speed chopper (HSC) in front of the sample. The rotor in the HSC is a flat triangle with two slits at the tips of one of the three edges. The HSC opens for 265 ns, short enough for isolating a single pulse from the 4-bunch, 16-bunch and hybrid mode. The isolation of a single pulse from the 16-bunch mode is shown in Figure 5. The details of the chopper system are described by Cammarata *et al.* [8].

A typical sample environment for pump–probe liquid experiments is shown in Figure 6. The 1.2 ps laser pulse impinges on the sample 15° above the collimator pipe and the delayed 100 ps X-ray pulse is guided to the sample inside a pipe to reduce air scattering. The diffracted signal is recorded by a CCD detector (Rayonix MX170-HS). As mentioned, the pump-pulse frequency for liquid experiments is 1 kHz, whereas experiments with solid samples run at lower frequencies due to the heatload from the laser. In liquid experiments, the detector is exposed for 1–10 s before readout, accumulating 1000–10000 X-ray pulses in the image. To extract the laser induced change, the experiment is first done without laser or, better, at a negative delay, to keep the average sample temperature constant. After azimuthal integration and scaling of the resulting 1D curves

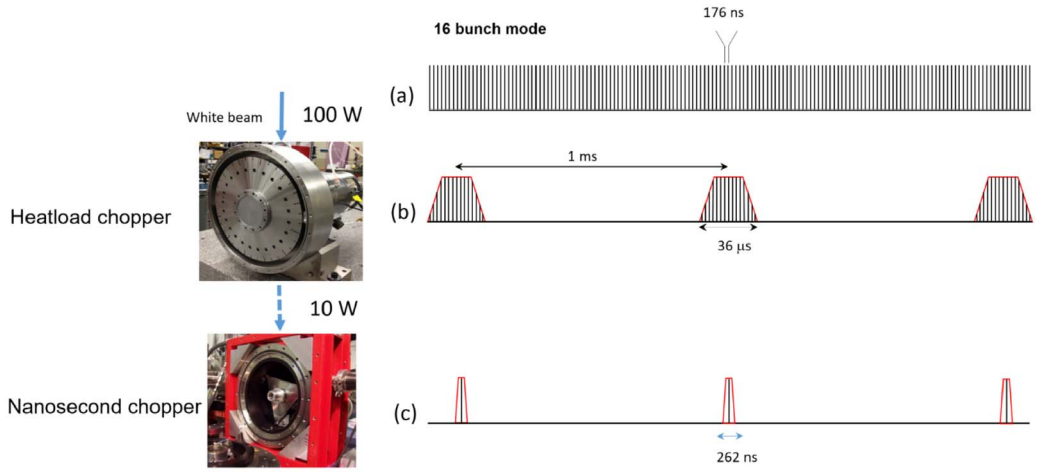

Figure 5. Chopper system on beamline ID09/ESRF. (a) The 16-bunch mode has 176 ns between pulses. (b) To reduce the heat load on the optics, the beam is pre-chopped into 37 µs bursts of pulses at 1 kHz. (c) Single bunches from each burst are isolated by a nanosecond chopper, which transmits a 1 kHz pulse train of ~100 ps pulses.

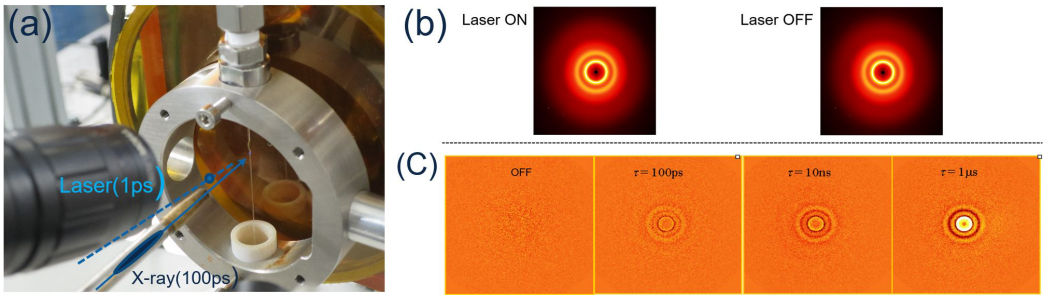

Figure 6. (a) Flow cell used for wide-angle scattering on ID09/ESRF. The liquid solution is injected in a capillary. It is then exposed to a 1.2 ps laser pulse followed by a delayed 100 ps X-ray pulse (illustrated as a 30 mm long needle in the collimator). (b) Scattering patterns from non-excited and excited solutions. The signal from the solute is superimposed on a large solvent background in a ratio of ~1:1000 in most cases. (c) Difference patterns for 3-time delays in the iodine experiment in liquid CCl_4 that is described below.

at high q near the edge of the detector, the difference curves are calculated. Only a fraction of the solutes (or unit cells in a crystal) is excited due to the limited laser penetration or the finite pulse energy that the liquid can tolerate. The shape of the difference curve $dS(q)$ is independent of the degree of excitation since the contribution from non-excited solutes (unit cells) cancels out in the difference. This approximation, however, breaks down in the case of multiphoton absorption or sequential absorption, in which case the laser fluence has to be reduced.

The spectra from ESRF and EBS are compared in Figure 4b. The spectra are measured through a small primary slit 0.5×0.5 mm^2 slit 27 m from the source. The gain in intensity from the EBS is a factor 10. Additionally, the horizontal source size is 60 µmH, a 50% reduction compared with the old synchrotron. The total intensity with fully opened slits is the same for the new and old lattice. The line shape of the EBS fundamental is freed from the low-energy pedestal,

a characteristic synchrotron feature caused by off-axis radiation from the more divergent electron beam. The beam is focused by a Pd coated toroidal mirror to Ø25 μm. The incidence angle is 2.48 mrad and the mirror cut-off 24 keV. Synchrotron beams are very stable unlike XFEL beams for which the position, intensity and spectrum have to be measured pulse-by-pulse and sorted later.

3. Photolysis of small molecules in solution

Historically, the first ultrafast photo triggered reaction was a study of the dissociation & recombination dynamics of I_2 in liquid CCl_4 by *K*. Eisenthal and his colleagues at Bell Labs in 1974 [9]. They found that most of the dissociated I atoms are captured by the liquid cage and that these atoms recombine in 120 ps while heating the solvent. 15% of the dissociated atoms were found to escape the cage and recombine in microseconds via bimolecular diffusion. The potential energy curve for I_2 is shown in Figure 7 for the ground and lower energy states of interest. At large atom–atom separations, the force in the *X* potential is attractive and drives the atoms closer together towards the potential minimum. At shorter distances, the potential is repulsive. The minimum is the equilibrium bond length of the molecule. A classical and quantum description of diatomic molecules is given by Slater [1]. The paper details the parameters of the Morse potential, the oscillation frequency and amplitude as a function of energy. The energy of the molecule is quantized in discrete vibrational levels, but at ambient temperature, the ground state is essentially 100% occupied. For gas phase I_2, the bond length is 2.666 Å in the ground state. The oscillation frequency is 6.2×10^{12} Hz and the vibrational amplitude 0.05 Å [10]. In Figure 7b, the vibrational relaxation from the dissociation energy to the ground state is simulated assuming a time constant of 100 ps. The amplitude of the oscillation becomes smaller as I_2^* returns to the ground state. The solvent, through collisions, dissipates the excess heat. The Eisenthal experiment was repeated with X-rays at ESRF by Plech *et al.* in [11]. In the I_2:CCl_4 experiment, the heavy solvent molecules slow down the recombination to 140 ps, which can be resolved with 100 ps X-ray pulses from a synchrotron. The first experiment did not resolve the contraction of I_2^* versus time; rather the recombination was inferred from the heat deposition in the solvent from the cooling of $I_2^*(X)$. In a follow-up experiment by Lee and his colleagues in 2013, laser slicing was used to push the time resolution below 100 ps [12]. Slicing takes advantage of the short 1.2 ps laser pulse and the low timing jitter between the pump and probe. By collecting time delays in steps of 10 ps, from −150 to 150 ps, the shape of the $dS(q,t)$ curves could be fitted against a model of the recombination process. The shape of the $dS(q,t)$ curves are consistent with the exponential cooling decay in a Morse Potential.

One important observation from the first iodine studies with X-rays is that the difference curves $dS(q,t)$ have two principal components: the signal from the changes in solute/cage structure, the goal of the experiment, and a thermal signal from the change in temperature, pressure and density of the solvent. The excitation produces molecules in high energy states and the return to the ground state is accompanied by heat dissipation in the solvent. The effect has a unique X-ray signature $dS_s(q)$, which is solvent specific. Since it is impossible to determine two signals from one measurement, the solvent signal has to be measured separately. That can be done by diluting dye molecules that absorb at the wavelength of the experiment. Alternatively, the heat can be generated by exciting the solvent molecules with near infrared light (1000–2000 nm) whereby heat is transferred into vibrational modes, usually via overtones of vibrational modes. Most of the common solvents have been characterised thermally by the dye method by Kjaer and his colleagues in 2013 [13] and the near infrared method was applied by Cammarata and his colleagues [14].

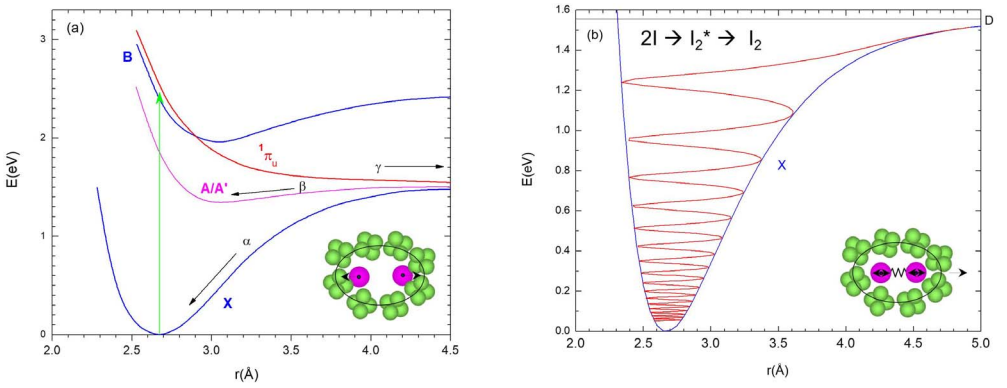

Figure 7. (a) Potential energy of a diatomic molecule illustrated by I_2. Excitation by an ultrashort 530 nm laser pulse excites the molecule vertically into the repulsive B and π states. The dissociated atoms collide with the solvent cage in ~300 fs. Recombination in the cage is the dominant process in CCl_4 with 85% of molecules recombining geminately and 15% escaping the cage. Three pathways have been identified, α and β, and γ corresponding to direct vibrational cooling along the X potential to the ground state, the formation of the A/A' triplet state ($S = 1$) and cage escape. (b) Schematic presentation of X state vibrational cooling. The bond is re-formed at the dissociation energy at 1.52 eV in a large amplitude vibrational state. It relaxes to the ground state while losing energy to the solvent via cage collisions.

When solvent hydrodynamics is included in the analysis, the time dependence of the temperature and density can be determined independently from the low q part of $\mathrm{d}S(q)$ which serves as a check of the overall consistency of the model. The temperature and pressure versus time for I_2 in CCl_4 are shown in Figure 8 as an example. The temperature jump at 1 ps is from the first collisions of I atoms with the cage. The temperature is not defined in the early out-of-equilibrium states; it is calculated here from the average energy uptake of the solvent. After 1 ps, the temperature rises from the cooling of $I_2^*(X)$ as illustrated in Figure 7b. After 200 ps, the slope change is due to the recombination of the 2.7 ns A/A' state. After 10 ns, the solvent expands accompanied by a drop in temperature. The expansion proceeds at the speed of sound until the pressure return to ambient in about 1 μs. The pressure versus time profile is shown in Figure 8b. The theory of heat dissipation is described in more detail in the work by Wulff *et al.* [15]. Thus, time-resolved X-ray scattering adds information on the reaction mechanism by being sensitive to all the constituents in the sample.

The structural sensitivity of X-rays to atom–atom distances in molecules is illustrated in Figure 9. The diatomic molecule is exposed to a monochromatic plane wave. The scattering from the two atoms produces spherical secondary waves that interfere. From the intensity profile on the detector, the change in the atom–atom distance can be deduced, even for a random ensemble of molecules. The principle is the same as in Young's two-slit experiment. The averaging over all orientations produces the soft modulated pattern shown in Figure 9b.

Calculating the scattering from isolated gas molecules is the first step in understanding the scattering curves during a chemical transformation. The gas scattering is given by the Debye Function [16]:

$$S(q) = \sum_{i,j} f_i(q) f_j(q) \frac{\sin(q r_{ij})}{q r_{ij}}.$$

Here $f_i(q)$ and $f_j(q)$ are the atomic form factors of atoms i and j and r_{ij} is the distance. The form factors are the sine-Fourier transform of the electron density of the respective atoms. $f(q)$ is

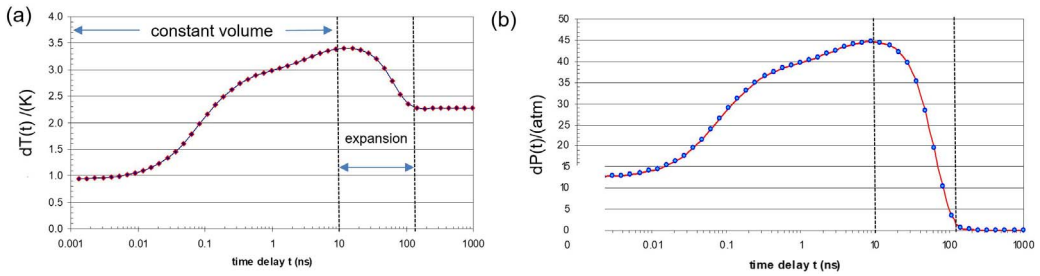

Figure 8. CCl_4 hydrodynamics caused by I_2^* recombination. (a) The solvent temperature versus time. In the time range 0.001 to 0.01 ns, the rise is from the first collisions of trapped I atoms prior to bond formation. From 0.01 to 10 ns, the temperature rises further from the vibrational cooling in the X and A/A' states. The volume is constant and the system adiabatic. In the following time range 10–100 ns, the sample expands due to the pressure gradient caused by the spatial profile of the laser beam. (b) Pressure versus time during recombination.

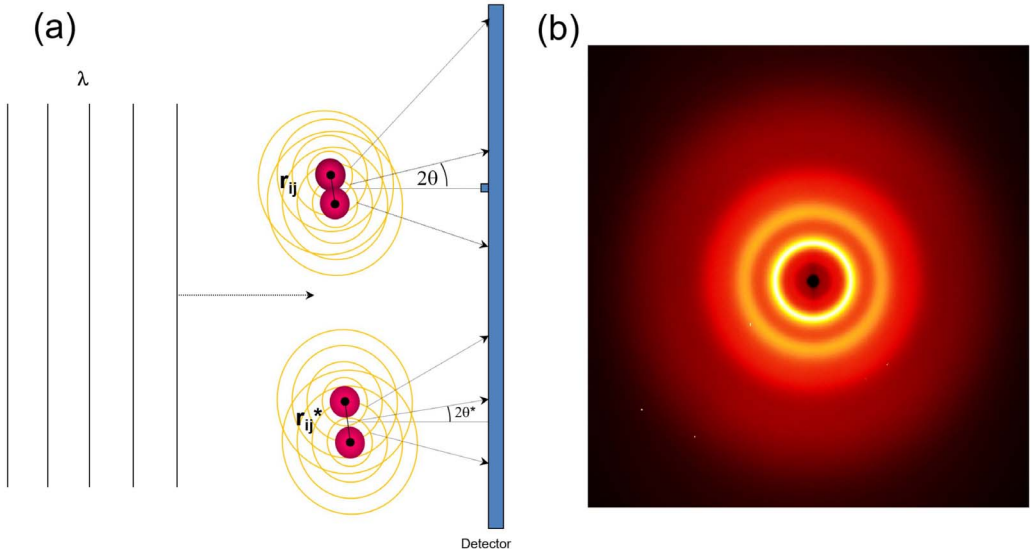

Figure 9. (a) Interference from a diatomic molecule in an X-ray beam. The atoms scatter the radiation isotopically and the interference pattern probes the atom–atom distance. (b) The radiation from randomly oriented molecules produce interference cones on a CCD detector. The dark spot in the centre is the beam stop.

approximately a Gaussian function with a half-width of $2\pi/r$, where r is the atomic radius. The expression applies to an ensemble of gas molecules randomly oriented in space. It should be noted that when X-rays are used to measure positions in a molecule, it is the position of the full electron density that is probed unlike with neutrons that probe the nuclear positions. The Fourier inversion of the X-ray scattering to real space produces peaks and valleys of finite width from the *size* of the atoms. The Debye functions $S(q)$ and $\mathrm{d}S(q)$ from structural changes in I_2 are shown in Figure 10 and the experimental curve $\mathrm{d}S$ (q, 460 ps) for I_2 in CCl_4 is shown in Figure 11. The solvent background is ~1000 times greater than the solute signal due to the low solute concentration (mM). It is particularly important to measure $S(q, t)$ well in the high q range

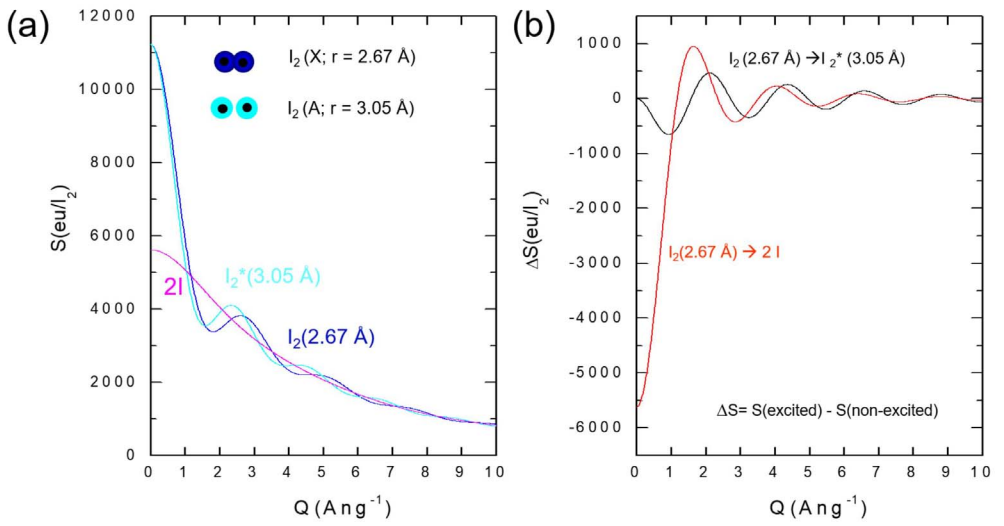

Figure 10. (a) Gas phase scattering from I_2 and I. The forward scattering is proportional to Z^2_{mol}, where Z is the number of electrons in the molecule. In the expanded triplet state I_2^*, the scattering function contracts. (b) Finger printing structural changes. Dissociation has a large negative forward scattering due to the smaller coherent scattering from 2 separated atoms.

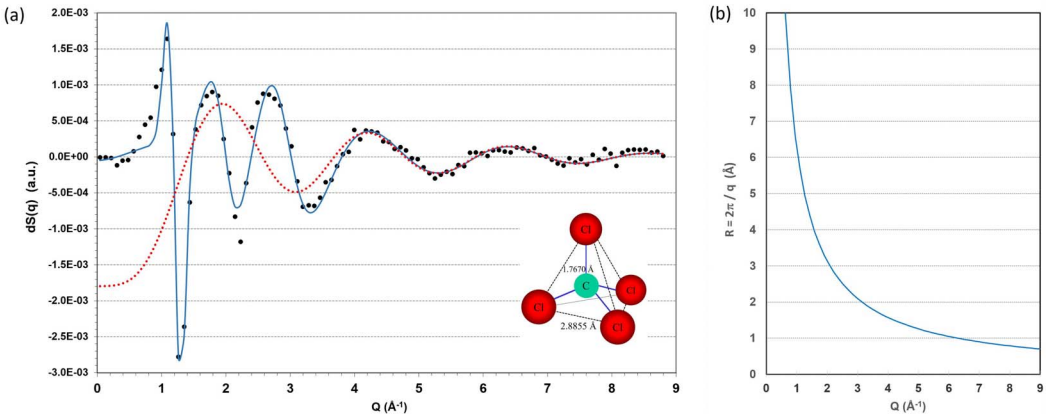

Figure 11. (a) Difference scattering for I_2 in CCl_4 460 ps after laser excitation. The gas component shown in red provides a good fit above 4 $Å^{-1}$. The experimental difference $dS(q,t)$ has two components: the iodine/cage scattering and the thermal solvent contribution from the change in temperature. (b) Resolution versus Q. Intra molecular changes in iodine dominate the signal for $q > 4$ $Å^{-1}$.

8–10 $Å^{-1}$ for the scaling of laser ON and laser OFF images. The scaling is based on the fact that in that range $S(q,t)$ can be calculated by the Debye function for the excited solutes and solvent. Expressed differently, the liquid appears as a collection of gas molecules at high q. In the dS (q, 460 ps) curve for the I_2:CCl_4 solution, the red curve is the gas phase part as explained in Figure 10b.

In the generalisation of the Debye Equation to a solution, the structure of the liquid solute/solvent mixture is expressed by statistical atom–atom distribution functions $g_{ij}(r)$ that represent the fluctuating structure in a liquid. The $g_{ij}(r)$ functions have two parts: the sharp and well-defined intra molecular part and a broad extra molecular part at larger r that describes the bulk solvent and the solute cage. The scattering is calculated from the $g_{ij}(r)$ functions from MD via:

$$S(q) = \sum_{i,j}^{N,N} f_i(q) f_j(q) \left(N_i N_j \delta_{i,j} + \frac{N_i N_j}{V} \int g_{i,j}(r) \mathrm{e}^{\mathrm{i}qr} \, \mathrm{d}V \right).$$

The expression is a generalisation of the Zernike–Prins formula for monoatomic liquids [17] and molecular liquids as described in the book by Hansen and McDonald [18]. N_i is the number of atoms of kind i, V the volume and $\delta_{ij}(r)$ the Kronecker delta function $\delta_{ii} = 1$, and $\delta_{ij} = 0$ for $i \neq j$. For a time-resolved experiment, the starting solute structures are calculated by density functional theory (DFT) including point charges on the atoms that are important for the solvent interaction. The next step is to perform a MD simulation with the DFT candidate structures for the ground and excited states structures. MD calculations assume thermal equilibrium so only quasi stationary structures can be approximated in this way. MD provides the $g_{ij}(r)$ functions including the cage. The Zernike–Prins equation is then used to calculate the change in scattering $\mathrm{d}S(q)$.

A more intuitive presentation of the structural changes is obtained by the sine-Fourier transform:

$$\Delta S[r,t] = \frac{1}{2\pi^2 r} \int_0^\infty \mathrm{d}q \frac{1}{\sum_{i \neq j} f_i(q) f_j(q)} q \Delta S(q,t) \sin(qr).$$

The denominator in the integral is the sharpening function which partially corrects for the broadening from atomic form factors that, as mentioned, probe the size of the atoms unlike the g_{ij} functions that measure the positions of the nuclei. The notation $\Delta S[r]$, i.e. with square brackets is to distinguish it from the sister $\Delta S(q)$ from which it is derived. $\Delta S[r]$ is an X-ray biased measure of the change in the radial electron density of an average excited atom. High-Z atoms are amplified in X-ray scattering unlike for neutrons.

The $g_{ij}(r)$ functions for the I_2/CCl_4 solution were calculated by the MD software Moldy using 512 rigid CCl_4 and one I_2 molecule. The $g_{ij}(r)$ functions that probe the cage for $I_2(X)$ are shown in Figure 12(a). The cage radius is given by g(I–Cl) since I is surrounded by Cl atoms in CCl_4. The first peak in g(I–Cl) is at 3.93 Å. The first coordination shell is at 5.10 Å as defined by the first peak in g(I–C).

The change in the cage structure of the reaction products are examined in Figure 11b. The g(I–Cl) distributions for X and A are nearly identical, in position and amplitude, as expected from the bond elongation of ~0.38 Å in the A/A's state. In contrast, the $I_2(X) \rightarrow 2I$ and $I_2(A/A') \rightarrow 2I$ transitions lead to a 27% increase in Cl population around I. The number of I–Cl pairs increases after dissociation as Cl fills the space vacated by I.

The real space change $\Delta S[r]$ is shown in Figure 13 for the gas and solution phase transitions. In the simple gas phase transition $I_2(X) \rightarrow I_2(A/A')$, the bond expands from 2.67 to 3.05 Å. That gives a negative peak for the depletion of the ground state and a positive creation peak. The change in cage structure follows that trend, i.e. the cage radius is slightly larger for A/A'. The gas phase reaction $I_2 \rightarrow 2I$ with I atoms infinitely apart, has a single depletion peak at the $I_2(X)$ bond length. In solution, the entering Cl atom produces a positive peak at 3.9 Å. In summary, time-resolved wide angle scattering with synchrotron and XFEL radiation is a powerful method for structural studies of molecular reactions in solution. The X-rays probe all pairs of atoms and that provides precious information about the structural dynamic. When the X-ray data is taken over a wide q range, the excited solute structures and the hydrodynamics parameters of the solvent medium can be determined from models combining DFT and MD.

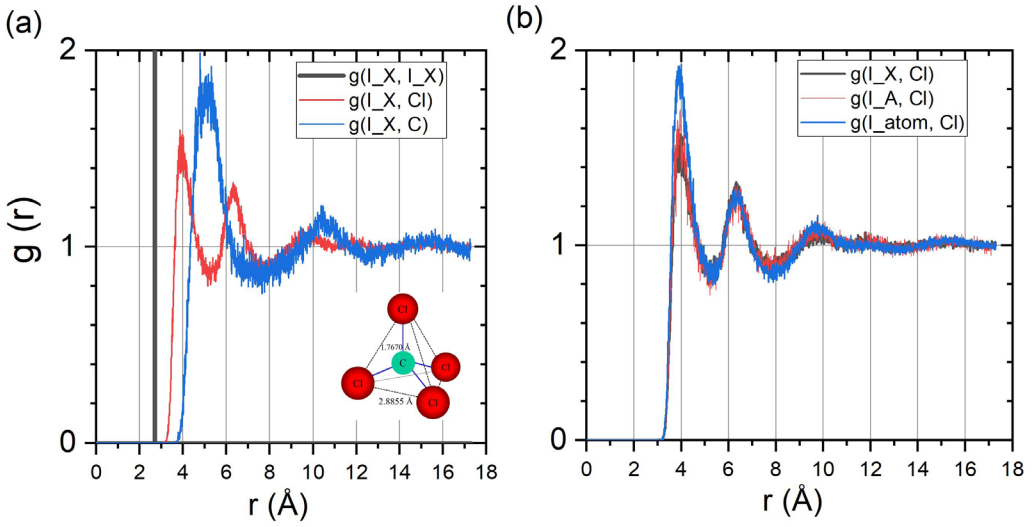

Figure 12. Molecular dynamics of I_2 in CCl_4 with g functions for I_2 and I in the X, A and atomic state. (a) I_2 is in the ground state X. The cage radius is the first peak in g(I–Cl) at 3.93 Å. The first peak in g(I, C) is at 5.10 Å, the distance to the centre of CCl_4. (b) Cage functions for the three states of iodine. For free I atoms, Cl fills the space vacated in the dissociation expressed by the increase of the blue curve at 3.93 Å.

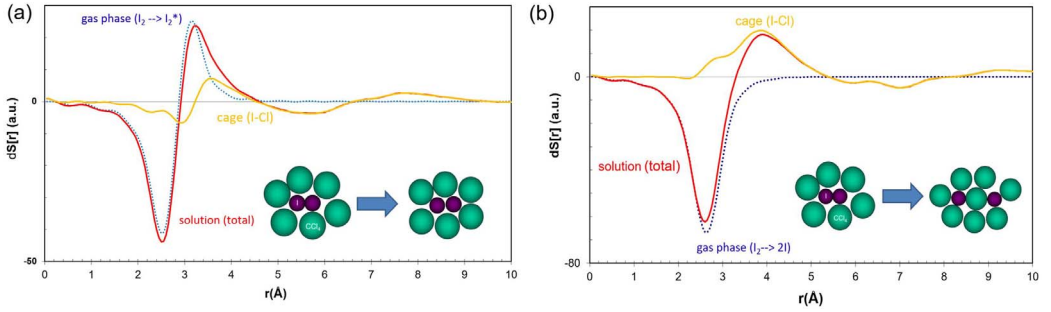

Figure 13. Change in radial distribution function d$S[r]$ probed by X-ray scattering. (a) Signature of bond elongation in the $I_2(X)$ to $I_2(A/A')$ transition. The red curve shows the total difference signal from the A/A' state formation calculated from the MD simulation. The negative peak at ~2.7 Å shows the depletion of ground state I_2 and the positive peak at 3.2 Å, the creation of the A/A' state. The cage component is shown in yellow. (b) Signature of cage escape of I atoms. In this process, the missing I neighbour in I_2 is replaced by Cl.

4. Protein dynamics in solution

Many proteins cannot be crystallised and time-resolved wide-angle scattering in solution offers a way to study large amplitude conformational changes. The low protein concentration (few mM or less) is a challenge and the large size, about a thousand times larger than a small molecule, complicates the analysis. Recent TR-WAXS data from proteins have demonstrated that medium and large-scale changes in some photo sensitive proteins are to be checked against model predicted scattering patterns. The TR-WAXS method for proteins was pioneered by Marco Cammarata and his colleagues on human haemoglobin (Hb), a tetrameric protein with two

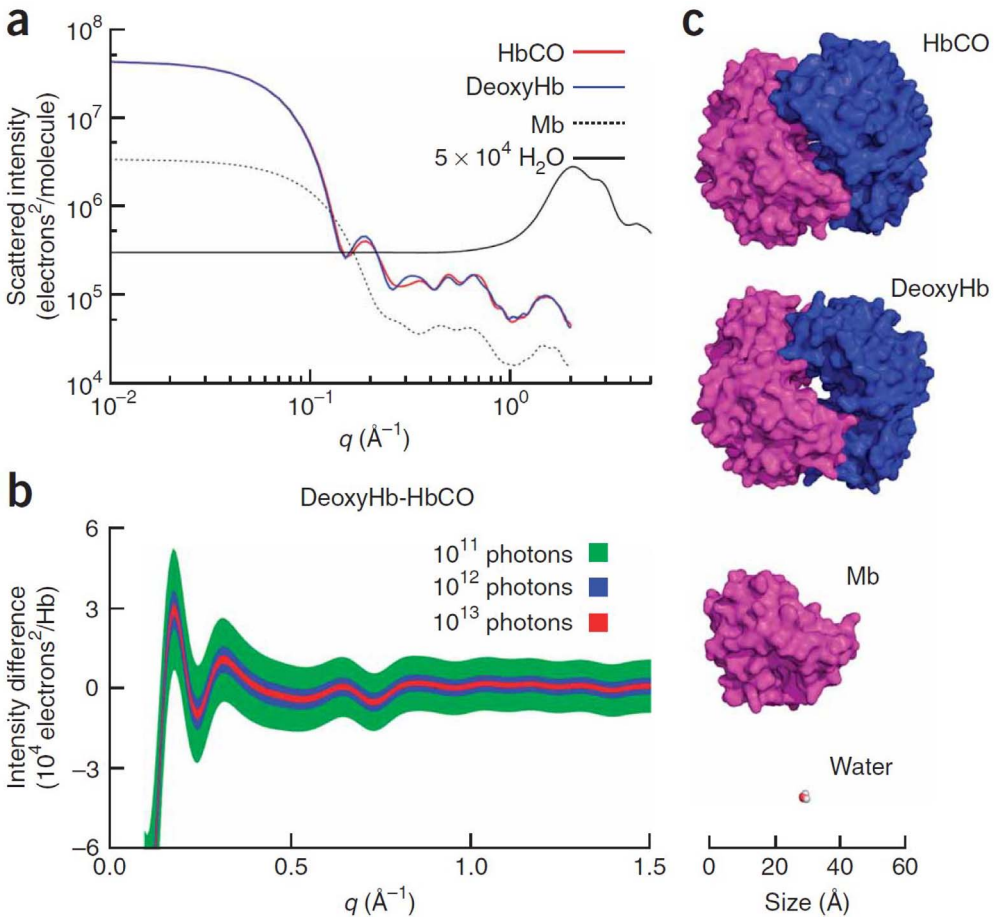

Figure 14. Calculated Debye scattering for haemoglobin (HbCO and Hb), myoglobin (Mb) and water. The calculations were performed with CRYOSOL using the crystal structures adapted to the solution phase. The protein signal is much stronger than the water background in the low q limit. (b) Relative change of the protein signal to the water background for the R-to-T transition (HbCO → Hb) for an excited-state concentration of 1 mm. (c) Snapshots of the molecular structures used in the simulations [18].

identical $\alpha\beta$ dimers [19]. HbCO in solution is known to have two quaternary structures, a ligated stable R (relaxed) state and an unligated stable T (tense) state. The tertiary and quaternary changes of HbCO, initiated by a ns green laser pulse, were probed by TR-WAXS [20, 21]. The analysis was using the allosteric kinetic model for Hb. It was found that the R–T transition takes 1–3 µs which is shorter than observed by optical spectroscopy. In Figure 14a the gas-phase scattering from the crystal structures of HbCO and Hb (deoxyHb) is shown together with a myoglobin and water molecule. In Figure 14b, the relative change from the transition HbCO → Hb is calculated for a 1 mM concentration. Note the good signal-to-background ratio between 0.1–1 $Å^{-1}$ due to the weak water scattering in that q range. The structure of the proteins and water is shown in Figure 14c. The optically induced tertiary relaxation of myoglobin and the refolding of cytochrome c were also studied with TR-SAXS/WAXS. The advantage of TR-SAXS/WAXS over time-resolved X-ray protein crystallography is that it can probe irreversible reactions and large-scale conformational changes that cannot take place within a crystal [22–24].

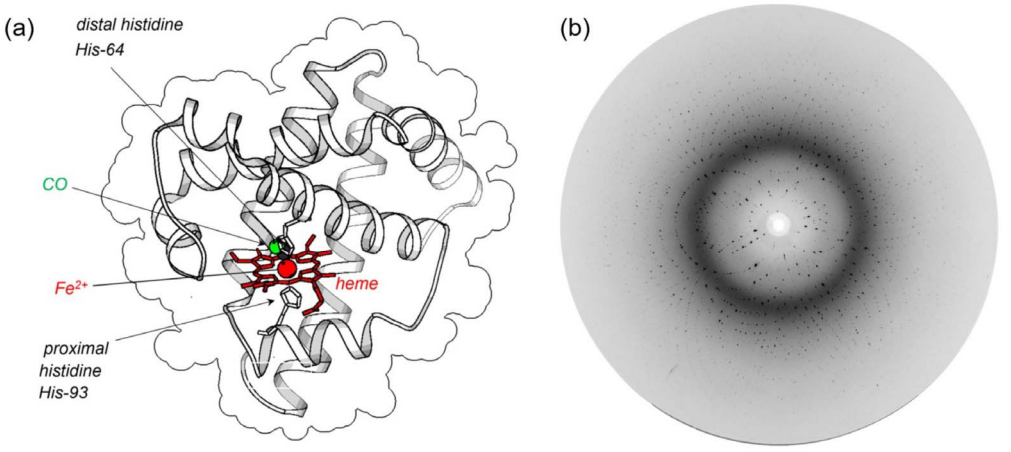

Figure 15. (a) Myoglobin is composed of a single polypeptide chain of 153 amino acids. There are 1270 atoms without hydrogen ($C_{823}N_{222}O_{221}S_3Fe$). MbCO retains its ligand binding functionality in crystals. (b) Laue pattern from a pink beam (0.775 Å, 4% bw, 2×10^9 ph/pulse). 32 pulses are accumulated on the detector (MARCCD 130). The dark ring is from water scattering. The data was analysed to 1.9 Å resolution.

Although the scattering patterns from proteins in solution contain structural information, the information is insufficient to reconstruct the structure in atomic detail. In this respect the use of structures from X-ray crystallography and NMR as a starting point is promising and the development of a more advanced analysis is in progress. For more information on these techniques the reader is referred to the recent articles by Bjorling *et al.* [25] and Ravishankar *et al.* [26].

5. Filming a protein at work by Laue diffraction

Myoglobin (Mb) is a ligand-binding heme protein whose structure was the first to be solved by X-rays in 1958 [27, 28]. Its Fe atom reversibly binds small ligands such as O_2, CO and NO, which is readily photo dissociated from the heme. The structural changes triggered by ligand photolysis was first filmed with near-atomic resolution at the ESRF in 1996 via time-resolved Laue diffraction by Keith Moffat, University of Chicago and Michael Wulff, ESRF and their co-workers [29].

Diffraction images were generated by single, 100 ps X-ray pulses photolysis of MbCO. The structure of MbCO is shown in Figure 15a. A Laue pattern from a monoclinic crystal (P21) with a linear size of 100–200 µm shown in Figure 15b.

The work was done using monoclinic crystals (P21) with a linear size of 100–200 µm as shown in Figure 16a. The packing of the unit cells is shown in Figure 16b for the hexagonal lattice. The latter shows the arrangement of the unit cells and the important space between them that is filled with water. The suspension in water allows the crystalline state to undergo smaller structural changes freed from lattice constraints.

The photolysis of a protein crystal is delicate and should be done without damaging the crystal, while still exciting enough unit cells to give a detectable signal. For example, the absorption gradient of the laser beam in the crystal has to be small to avoid thermal bending and thus broadening of the diffraction spots. The unit cell concentration is high in the monoclinic structure, (49.3 mM), so the laser wavelength has to be chosen judiciously to penetrate the crystal. The MbCO absorption spectrum has three features, the Soret band at 420 nm and two weaker bands

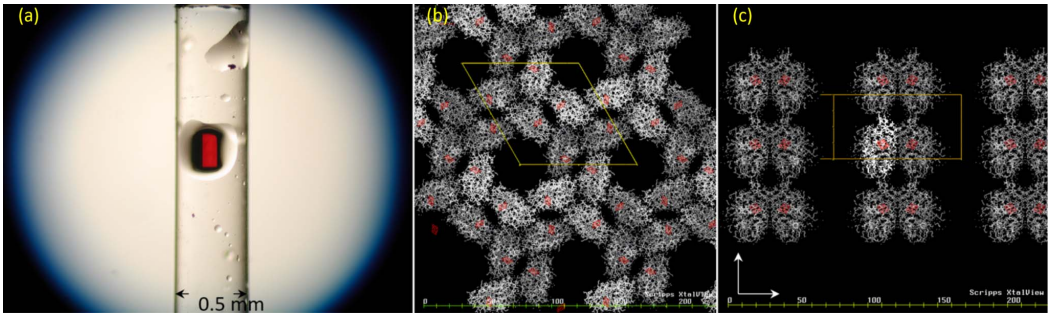

Figure 16. (a) MbCO in the P6 hexagonal lattice (a = b = 91.20 Å, c = 45.87 Å, $\alpha = \beta = 90°$, $\gamma = 120°$). (b) Structure along the c axis. The heme is shown in red. The black areas are water channels. (c) Structure along the a axis.

at 550 and 585 nm, the *Q* bands α and β. The penetration depth is 1.5 μm on the Soret band and 15 μm on α and β. However, by exciting on the shoulder of the β band at 625 nm, where dissociation still works, the absorption length is 420 μm, a good match to the crystal dimensions in the experiment [30,31]. The fraction of unit cells photolyzed by a 1 mJ pulse of 0.5 mm diameter was ~20–30%.

The crystals were mounted in capillaries in a CO atmosphere and 16–32 images from single pulses were accumulated on the detector before readout. The crystals were rotated in steps of 3°, from 0–180° to fully sample reciprocal space. In some cases, the crystals would be damaged after some time, then replaced and the data merged later.

The diffraction pattern is sensitive to changes inside the unit cells. When the non-excited starting structure is known from the PDB data base, the measured intensity changes d$I(hkl)$ allow to determine the change in electron density via the Fourier Difference Method [31]. The first experiment used the spectrum from a wiggler (W70) covering 7–28 keV. The wiggler was replaced in 2000 by the narrow-band undulator U17 which increased the SNR due to a much lower diffuse background from water in the protein. A second spin off of the narrow band is the lower number of spatial overlaps in the images from the well-defined relation between the scattering angle and the d-spacing (Bragg's law) provided by the narrow 5% bandwidth spectrum at 15 keV.

From the measurements of 50,000 intensity changes $\Delta I(hkl)$, the Fourier difference maps were derived as shown in Figure 17. The difference density is superimposed on the CO ligated initial structure in white: red volumes are due to loss of density, blue is from a gain. CO is seen to move to the solvent via 2 interstitial cavities. Initially, it is trapped in a small cavity next to Fe for 5 ns. The CO hole is partially filled by a shift in position of the distant His-64 that blocks geminate recombination. The new CO position is also pushing the Ile-107 residue slightly. Note the tilt of the heme plane and the Fe motion out of the plane. The doming is from the change in coordination from 6 to 5 of Fe after dissociation. Note that red and blue volumes are side-by-side consistent with small rigid translocations. In the 30 ns map, the first cavity is empty and CO is not resolved. In the 300 ns map, CO reappears on the proximal side in a cavity, which is known from studies of Xe gas pockets in myoglobin under pressure. The Fe heme doming persists in the absence of the Fe–CO bond. CO diffuses to the solvent and returns to Fe via random diffusive motion on the ms time scale.

The first Laue work on sperm whale myoglobin was followed by studies of on mutants lead by Anfinrud [32] and Brunori [33]. As the CO is on the distal side of the heme at early time delays, the protein function is strongly influenced by the amino acid side chains around that site. The L29F mutant of MbCO, where leucine Leu29 is substituted by phenylalanine, exhibits 1000 time faster dynamics [32].

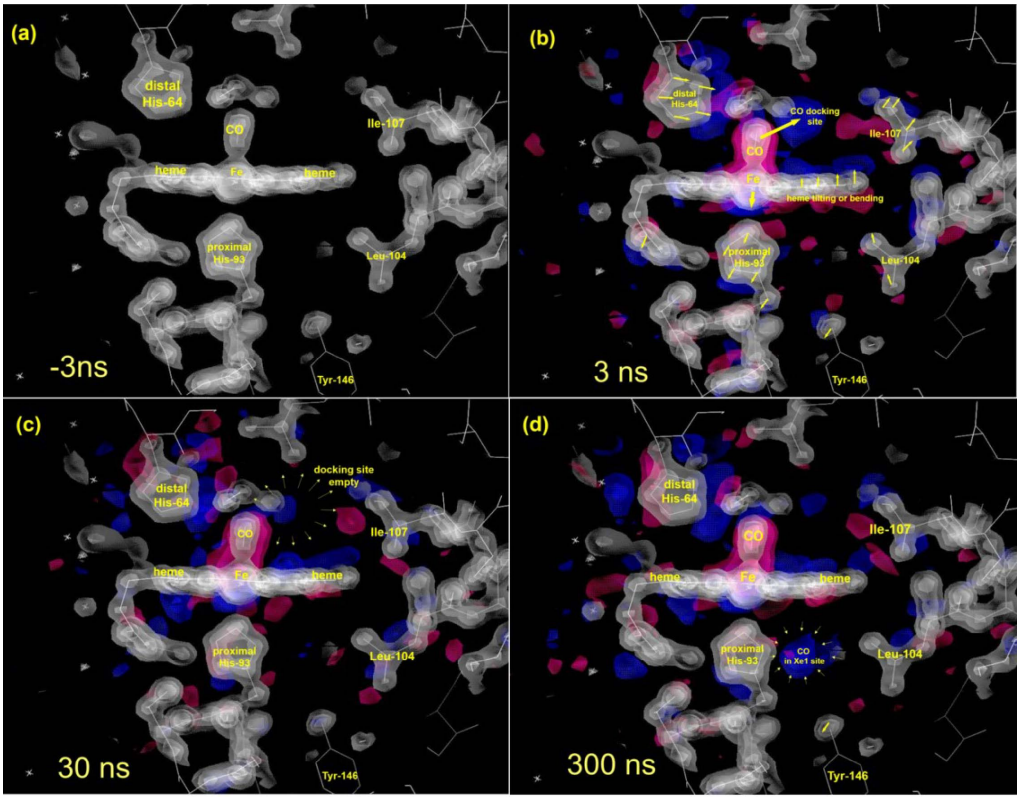

Figure 17. 3D maps of the dissociation of CO from the Fe binding site in sperm whale Myoglobin MbCO. The dissociation is triggered by a 2.3 ns laser pulse at 620 nm. (a) Initial electron density of MbCO near the heme. The electron density is contoured in white at 3, 5 and 7σ. The map is the 2MGK model of sperm whale MbCO at 1.7 Å resolution. (b) Fourier difference maps taken 3 ns after dissociation by single pulse Laue diffraction. The difference is superimposed on the initial state. Red represent loss of density, blue gain in density. CO is captured in the "docking site" on the distal side of the heme. Fe has moved 0.2 Å out of the heme plane in response to the change in coordination from 6 to 5. Note how the distal and proximal histidine move in response to the new CO position. That structural change blocks CO geminate recombination to Fe. (c) At 30 ns the docking site population is decreasing. (d) After 300 ns, CO is accumulating in a pocket on the proximal side from where it diffuses into the solvent. After 1 ms, CO returns to the binding site. That pathway is not observed due the loss of synchronization in the reverse reaction. The maps are rendered with the software O7.0 (Alwen Jones, Uppsala University).

6. XFEL experiments

The Linear Coherent Light Source (LCLS) at SLAC in Stanford was the first hard X-ray FEL facility to open in 2009. The LCLS was followed by SACLA at SPring8 in Japan in 2011, SwissFEL in Villigen (CH) in 2016 and the European EuXFEL in Schenefeld (D) in 2017. In XFELs bunches of electrons are accelerated to 5–15 GeV in a linear accelerator and injected into long undulators. After a certain point in the undulator, the X-ray field induces a density modulation in the bunch, the SASE effect, which amplifies the intensity by orders of magnitude. The electrons in a micro

bunch emit in phase as super electrons. The intensity is then proportional to N_e^2 (micro bunch electrons) × N_p^2 (periods). The energy range is currently limited to 1–16 keV but higher energies will become available at the EuXFEL in the near future. For a review of the SASE principle, the reader is referred to the article by Margaritondo *et al.* [34]. XFEL pulses are 10^3 to 10^4 times shorter than synchrotron pulses, i.e. 10–100 fs, and the intensity can reach 1×10^{12} photons/pulse in a 0.1% BW at 12 keV. The beam is less stable due to the stochastic nature of SASE and it is important to record the beam parameters, the timing jitter in particular, for every pulse. To exploit the short XFEL pulses, the laser/X-ray delay has to be sorted and averaged after the experiment.

Femtosecond pulses are perfect for filming bond breakage and bond formation in chemical reactions, isomerization, electron transfer reactions and coherent wave packet motion etc. Diffraction patterns from micro and nano-sized proteins can be acquired with single XFEL pulses. The number of diffraction spots is large enough for indexing, i.e. determining the orientation of randomly oriented crystals, and the pulse is so short that the diffraction can be recorded before the crystal is destroyed by the Coulomb explosion as described by Neutze *et al.* [35]. The term "diffraction before destruction" is the principle behind Serial Femtosecond Crystallography (SFX). The crystals are injected in the XFEL beam from a jet and thousands to millions of crystals are exposed randomly. By merging the scaled intensity data from thousands of images, the structure can be determined. There are two major advantages of SFX: very small crystals are easier to produce and the structure can be determined at room temperature rather than at cryogenic temperature, where the mobility of the protein is greatly reduced. The reader is referred to the review by Chapman *et al.* for more details [36]. The SFX technique is applicable to pump–probe work on light sensitive proteins as well. Schlichting and her co-workers studied the helix dynamic following photo dissociation of CO from myoglobin MbCO at the LCLS using SFX at 6.8 keV with a resolution of 1.8 Å [37]. The study revealed that the C, F and H helices move away from the heme whereas the E and A helices move towards it in less than 500 fs, confirming the results previously obtained with TR-WAXS measurements at the LCLS on MbCO [38].

One of the first scattering experiments probing a femtosecond chemical reaction in solution was performed by Hyotcherl Ihee from KAIST in Korea in collaboration with Shin-ichi Adachi, KEK, using the SACLA XFEL at SPring8 [39]. They studied the formation of a gold trimer $[Au(CN)_2^-]_3$. In the ground state, the Au atoms in three molecules are weakly bonded by van der Waals interactions. Upon photo activation, an Au electron is excited to a bonding orbital producing a covalent Au–Au bond with a linear geometry with a lifetime of 500 fs. The Au bonds shorten in a second 1.6 ps step. Finally this linear conformation combines with a free $Au(CN)_2^-$ in 3 ns to form a tetramer. The reaction is shown in Figure 18.

The first X-ray spectroscopy experiment from an XFEL was reported by Henrik Lemke and Marco Cammarata and their co-workers in 2013 [40]. They performed a XANES study of the spin-cross-over complex $[Fe(bpy)_3]Cl_2$ in a 50 mM aqueous solution using 100 fs pulses from the LCLS. The position of the Fe absorption edge depends on the Fe–N distance from which they deduce that the switch from the low-spin (LS) to the high-spin (HS) state takes 160 fs. The HS state subsequently decays to the LS state in 650 ps. The experiment was done with fluorescence detection and the XFEL white beam was monochromatized with a diamond monochromator. The K-edge was scanned over 45 eV, the spectral width of the white beam. The main challenge was timing drifts, which could be up to 100 fs per hour. That problem was later solved by time stamping the X-ray pulse followed by sorting the actual delay [41], which allows to exploit the full potential of the short XFEL pulses.

In spite of the high intensity and short pulse from XFELs, synchrotrons will remain important for slower dynamics, from 100 ps to seconds, due to the higher beam stability, wider energy range and easier accessibility. It is also important that users have enough time to get to know the beamline and optimise the experimental parameters.

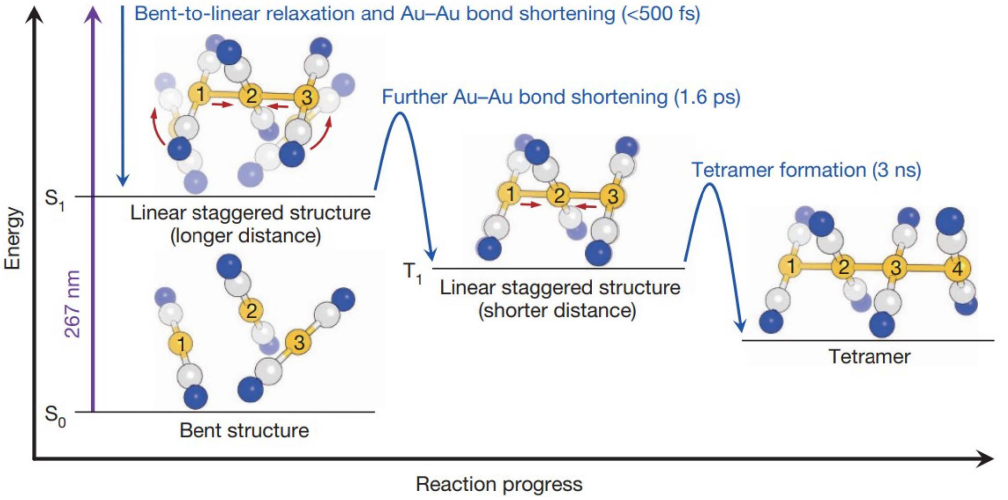

Figure 18. Pioneering solution phase TR-WAXS experiment from an XFEL by the Ihee and Adachi groups. The formation of a covalent bond between the three Au atoms in $[Au(CN)_2^-]_3$ is monitored by time-resolved solution scattering with 100 fs pulses at 15 keV with 1×10^{12} ph/pulse in a 0.6% BW [32].

Table 1. Beam parameters for a synchrotron and XFEL beamline (ID09/ESRF versus FXE/EuXFEL)

Parameter	ID09/EBS	FXE/EuXFEL
Pulse length (ps)	100	0.05
Pulse intensity (ph)	1×10^9	1×10^{12}
Pulses per second	1000	10 (27000)
Energy range (keV)	7–24 keV	6–18 keV
Focus (μm)	25	10
Intensity per second	1×10^{12}	1×10^{13}

The beam parameters for a synchrotron and XFEL beam are shown in Table 1 for ID09 at ESRF and FXE at EuXFEL. The pulse structure at EuXFEL is a 10 Hz macro pulse with each macro pulse having up to 2700 sub pulses that are separated by 220 ns. The large Pixel Detector at EuXFEL and the excitation laser can synchronise to this time structure. It is challenging however, to exchange the samples in the 220 ns dark period between pulses in the macro-pulse train which is often needed since the sample might be destroyed by the pulses.

Acknowledgements

The authors wish to thank Keith Moffat, Vukica Šrajer, Dominique Bourgeois, Thomas Ursby, Simone Techert, Maciej Lorenc, Richard Neutze, Rodolphe Vuilleumier, Fabien Mirloup and the many users, students and postdocs that have worked on beamline ID09/ESRF over many years for their dedication and friendship. Finally HI was supported by the Institute of Basic Science (IBS-R004).

References

[1] N. B. Slater, "Classical motion under a morse potential", *Nature* **180** (1957), p. 1352-1353.
[2] A. H. Zewail, "The birth of molecules", *Sci. Am.* **263** (1990), p. 76-82.
[3] A. H. Zewail, "Filming the invisible in 4-D", *Sci. Am.* **303** (2010), p. 75-81.
[4] G. A. Mourou, D. Umstadter, "Extreme light", *Sci. Am.* **286** (2002), p. 80-86.
[5] P. Raimondi, "The ESRF low emittance upgrade", in *IPAC 2016 – Proc. 7th Int. Part. Accel. Conf.*, CERN, Geneva, 2016, https://accelconf.web.cern.ch/IPAC2016/papers/wexa01.pdf, p. 2023-2027.
[6] P. Raimondi, "ESRF-EBS: The extremely brilliant source project", *Synchrotron Radiat. News* **29** (2016), p. 8-15.
[7] A. Plech, V. Kotaidis, M. Lorenc, J. Boneberg, "Femtosecond laser near-field ablation from gold nanoparticles", *Nat. Phys.* **2** (2006), p. 44-47.
[8] M. Cammarata, L. Eybert, F. Ewald, W. Reichenbach, M. Wulff, P. Anfinrud, F. Schotte, A. Plech, Q. Kong, M. Lorenc, B. Lindenau, J. Räbiger, S. Polachowski, "Chopper system for time resolved experiments with synchrotron radiation", *Rev. Sci. Instrum.* **80** (2009), article no. 015101.
[9] T. J. Chuang, G. W. Hoffman, K. B. Eisenthal, "Picosecond studies of the cage effect and collision induced predissociation of iodine in liquids", *Chem. Phys. Lett.* **25** (1974), p. 201-205.
[10] E. J. Baran, "Mean amplitudes of vibration of the halogen molecules", *Z. Naturforsch. A* **58** (2003), p. 36-38.
[11] A. Plech, M. Wulff, S. Bratos, F. Mirloup, R. Vuilleumier, F. Schotte, P. A. Anfinrud, "Visualizing chemical reactions in solution by picosecond X-ray diffraction", *Phys. Rev. Lett.* **92** (2004), article no. 125505.
[12] J. H. Lee, M. Wulff, S. Bratos, J. Petersen, L. Guerin, J. C. Leicknam, M. Cammarata, Q. Kong, J. Kim, K. B. Møller, H. Ihee, "Filming the birth of molecules and accompanying solvent rearrangement", *J. Am. Chem. Soc.* **135** (2013), p. 3255-3261.
[13] K. S. Kjær, T. B. Van Driel, J. Kehres, K. Haldrup, D. Khakhulin, K. Bechgaard, M. Cammarata, M. Wulff, T. J. Sørensen, M. M. Nielsen, "Introducing a standard method for experimental determination of the solvent response in laser pump, X-ray probe time-resolved wide-angle X-ray scattering experiments on systems in solution", *Phys. Chem. Chem. Phys.* **15** (2013), p. 15003-15016.
[14] M. Cammarata, M. Lorenc, T. K. Kim, J. H. Lee, Q. Y. Kong, E. Pontecorvo, M. Lo Russo, G. Schiró, A. Cupane, M. Wulff, H. Ihee, "Impulsive solvent heating probed by picosecond X-ray diffraction", *J. Chem. Phys.* **124** (2006), article no. 124504.
[15] M. Wulff, S. Bratos, A. Plech, R. Vuilleumier, F. Mirloup, M. Lorenc, Q. Kong, H. Ihee, "Recombination of photodissociated iodine: A time-resolved X-ray-diffraction study", *J. Chem. Phys.* **124** (2006), article no. 034501.
[16] B. E. Warren, *X-ray Diffraction*, Dover Publications, New York, 1990.
[17] F. Zernike, J. A. Prins, "Die Beugung von Röntgenstrahlen in Flüssigkeiten als Effekt der Molekülanordnung", *Z. Phys.* **41** (1927), p. 184-194.
[18] J.-P. Hansen, I. R. McDonald, *Theory of Simple Liquids: with Applications to Soft Matter*, Academic Press, 2013.
[19] M. Cammarata, M. Levantino, F. Schotte, P. A. Anfinrud, F. Ewald, J. Choi, A. Cupane, M. Wulff, H. Ihee, "Tracking the structural dynamics of proteins in solution using time-resolved wide-angle X-ray scattering", *Nat. Methods* **5** (2008), p. 881-886.
[20] M. Cammarata, M. Levantino, M. Wulff, A. Cupane, "Unveiling the timescale of the R-T transition in human hemoglobin", *J. Mol. Biol.* **400** (2010), p. 951-962.
[21] M. Levantino, A. Spilotros, M. Cammarata, G. Schiro, C. Ardiccioni, B. Vallone, M. Brunori, A. Cupane, "The Monod–Wyman–Changeux allosteric model accounts for the quaternary transition dynamics in wild type and a recombinant mutant human hemoglobin", *Proc. Natl. Acad. Sci. USA* **109** (2012), p. 14894-14899.
[22] M. Levantino, B. A. Yorke, D. C. F. Monteiro, M. Cammarata, A. R. Pearson, "Using synchrotrons and XFELs for time-resolved X-ray crystallography and solution scattering experiments on biomolecules", *Curr. Opin. Struct. Biol.* **35** (2015), p. 41-48.
[23] I. Josts, S. Niebling, Y. Gao, M. Levantino, H. Tidow, D. Monteiro, "Photocage-initiated time-resolved solution X-ray scattering investigation of protein dimerization", *IUCrJ* **5** (2018), p. 667-672.
[24] T. W. Kim, S. J. Lee, J. Jo, J. G. Kim, H. Ki, C. W. Kim, K. H. Cho, J. Choi, J. H. Lee, M. Wulff, Y. M. Rhee, H. Ihee, "Protein folding from heterogeneous unfolded state revealed by time-resolved X-ray solution scattering", *Proc. Natl. Acad. Sci. USA* **117** (2020), p. 14996-15005.
[25] A. Björling, O. Berntsson, H. Lehtivuori, H. Takala, A. J. Hughes, M. Panman, M. Hoernke, S. Niebling, L. Henry, R. Henning, I. Kosheleva, V. Chukharev, N. V. Tkachenko, A. Menzel, G. Newby, D. Khakhulin, M. Wulff, J. A. Ihalainen, S. Westenhoff, "Structural photoactivation of a full-length bacterial phytochrome", *Sci. Adv.* **2** (2016), article no. e1600920.
[26] H. Ravishankar, M. N. Pedersen, M. Eklund, A. Sitsel, C. Li, A. Duelli, M. Levantino, M. Wulff, A. Barth, C. Olesen, P. Nissen, M. Andersson, "Tracking Ca 2+ ATPase intermediates in real time by X-ray solution scattering", *Sci. Adv.* **6** (2020), article no. eaaz0981.

[27] J. C. Kendrew, G. Bodo, H. M. Dintzis, R. G. Parrish, H. Wyckoff, D. C. Phillips, "A three-dimensional model of the myoglobin molecule obtained by X-ray analysis", *Nature* **181** (1958), p. 662-666.
[28] J. C. Brooks-Bartlett, E. F. Garman, "The nobel science: One hundred years of crystallography", *Interdiscip. Sci. Rev.* **40** (2015), p. 244-264.
[29] V. Srajer, T.-Y. Teng, T. Ursby, C. Pradervand, Z. Ren, S.-I. Adachi, W. Schildkamp, D. Bourgeois, M. Wulff, K. Moffat, "Photolysis of the carbon monoxide complex of myoglobin: Nanosecond time-resolved crystallography", *Science* **274** (1996), p. 1726-1729.
[30] E. Antonini, M. Brunori, *Hemoglobin and Myoglobin in their Reactions with Ligands*, North-Holl. Publ. Co., Amsterdam, Netherlands, 1972.
[31] J. R. Helliwell, *Macromolecular Crystallography with Synchrotron Radiation*, Cambridge University Press, Cambridge, 1992.
[32] F. Schotte, M. Lim, T. A. Jackson, A. V. Smirnov, J. Soman, J. S. Olson, G. N. Phillips, M. Wulff, P. A. Anfinrud, "Watching a protein as it functions with 150-ps time-resolved X-ray crystallography", *Science* **300** (2003), p. 1944-1947.
[33] D. Bourgeois, B. Vallone, F. Schotte, A. Arcovito, A. E. Miele, G. Sciara, M. Wulff, P. Anfinrud, M. Brunori, "Complex landscape of protein structural dynamics unveiled by nanosecond Laue crystallography", *Proc. Natl. Acad. Sci. USA* **100** (2003), p. 8704-8709.
[34] G. Margaritondo, P. Rebernik Ribic, "A simplified description of X-ray free-electron lasers", *J. Synchrotron Radiat.* **18** (2011), p. 101-108.
[35] R. Neutzo, R. Wouts, D. Van Der Spoel, E. Weckert, J. Hajdu, "Potential for biomolecular imaging with femtosecond X-ray pulses", *Nature* **406** (2000), p. 752-757.
[36] H. N. Chapman, P. Fromme, A. Barty, T. A. White, R. A. Kirian, A. Aquila, M. S. Hunter, J. Schulz, D. P. DePonte, U. Weierstall, R. B. Doak, F. R. N. C. Maia, A. V. Martin, I. Schlichting, L. Lomb, N. Coppola, R. L. Shoeman, S. W. Epp, R. Hartmann, D. Rolles, A. Rudenko, L. Foucar, N. Kimmel, G. Weidenspointner, P. Holl, M. Liang, M. Barthelmess, C. Caleman, S. Boutet, M. J. Bogan, J. Krzywinski, C. Bostedt, S. Bajt, L. Gumprecht, B. Rudek, B. Erk, C. Schmidt, A. Hömke, C. Reich, D. Pietschner, L. Strüder, G. Hauser, H. Gorke, J. Ullrich, S. Herrmann, G. Schaller, F. Schopper, H. Soltau, K.-U. Kühnel, M. Messerschmidt, J. D. Bozek, S. P. Hau-Riege, M. Frank, C. Y. Hampton, R. G. Sierra, D. Starodub, G. J. Williams, J. Hajdu, N. Timneanu, M. M. Seibert, J. Andreasson, A. Rocker, O. Jönsson, M. Svenda, S. Stern, K. Nass, R. Andritschke, C.-D. Schröter, F. Krasniqi, M. Bott, K. E. Schmidt, X. Wang, I. Grotjohann, J. M. Holton, T. R. M. Barends, R. Neutze, S. Marchesini, R. Fromme, S. Schorb, D. Rupp, M. Adolph, T. Gorkhover, I. Andersson, H. Hirsemann, G. Potdevin, H. Graafsma, B. Nilsson, J. C. H. Spence, "Femtosecond X-ray protein nanocrystallography", *Nature* **470** (2011), p. 73-77.
[37] T. R. M. Barends, L. Foucar, A. Ardevol, K. Nass, A. Aquila, S. Botha, R. B. Doak, K. Falahati, E. Hartmann, M. Hilpert, M. Heinz, M. C. Hoffmann, J. Kofinger, J. E. Koglin, G. Kovacsova, M. Liang, D. Milathianaki, H. T. Lemke, J. Reinstein, C. M. Roome, R. L. Shoeman, G. J. Williams, I. Burghardt, G. Hummer, S. Boutet, I. Schlichting, "Direct observation of ultrafast collective motions in CO myoglobin upon ligand dissociation", *Science* **350** (2015), p. 445-450.
[38] M. Levantino, G. Schirò, H. T. Lemke, G. Cottone, J. M. Glownia, D. Zhu, M. Chollet, H. Ihee, A. Cupane, M. Cammarata, "Ultrafast myoglobin structural dynamics observed with an X-ray free-electron laser", *Nat. Commun.* **6** (2015), article no. 6772.
[39] K. H. Kim, J. G. Kim, S. Nozawa, T. Sato, K. Y. Oang, T. W. Kim, H. Ki, J. Jo, S. Park, C. Song, T. Sato, K. Ogawa, T. Togashi, K. Tono, M. Yabashi, T. Ishikawa, J. Kim, R. Ryoo, J. Kim, H. Ihee, S. I. Adachi, "Direct observation of bond formation in solution with femtosecond X-ray scattering", *Nature* **518** (2015), p. 385-389.
[40] H. T. Lemke, C. Bressler, L. X. Chen, D. M. Fritz, K. J. Gaffney, A. Galler, W. Gawelda, K. Haldrup, R. W. Hartsock, H. Ihee, J. Kim, K. H. Kim, J. H. Lee, M. M. Nielsen, A. B. Stickrath, W. Zhang, D. Zhu, M. Cammarata, "Femtosecond X-ray absorption spectroscopy at a hard X-ray free electron laser: Application to spin crossover dynamics", *J. Phys. Chem. A* **117** (2013), p. 735-740.
[41] M. Harmand, R. Coffee, M. R. Bionta, M. Chollet, D. French, D. Zhu, D. M. Fritz, H. T. Lemke, N. Medvedev, B. Ziaja, S. Toleikis, M. Cammarata, "Achieving few-femtosecond time-sorting at hard X-ray free-electron lasers", *Nat. Photonics* **7** (2013), p. 215-218.

Comptes Rendus
Physique
2021, 22, nº S2, p. 95-102
https://doi.org/10.5802/crphys.35

Physics of ultra-fast phenomena / *Physique des phénomènes ultra-rapides*

Picosecond dynamics in layered cobalt perovskites studied by time-resolved Raman spectroscopy

Ryo Fukaya [a], Nao Yamaya [a], Tadahiko Ishikawa [a], Shin-ya Koshihara [a], Yoichi Okimoto [*, a], Ken Onda [b], Akira Isayama [c], Takao Sasagawa [c] and Kazumasa Horigane [d]

[a] Department of Chemistry, Tokyo Institute of Technology, 2-12-1, Ookayama, Tokyo, 152-8551, Japan

[b] Department of Chemistry, Kyushu University, 744 Motooka, Nishi, Fukuoka 819-0395, Japan

[c] Laboratory for Materials and Structures, Tokyo Institute of Technology, 4259 Nagatsuta, Yokohama, 226-8503, Japan

[d] Research Institute for Interdisciplinary Science, Okayama University, 3-1-1, Tsushimanaka, Okayama, 700-8530, Japan

Current address: Institute of Materials Structure Science, High Energy Accelerator Research Organization, 1-1 Oho, Tsukuba, Ibaraki 305-0801, Japan (R. Fukaya)

E-mails: ryo.fukaya@kek.jp (R. Fukaya), tishi@chem.titech.ac.jp (T. Ishikawa), skoshi@chem.titech.ac.jp (S.-y. Koshihara), okimoto.y.aa@m.titech.ac.jp (Y. Okimoto), konda@chem.kyushu-univ.jp (K. Onda), sasagawa.t.aa@m.titech.ac.jp (T. Sasagawa), k-horigane@okayama-u.ac.jp (K. Horigane)

Abstract. Picosecond dynamics of the photoexcited charge-ordered perovskite-type cobalt oxides $La_{1.5}Ca_{0.5}CoO_4$ and $La_{1.5}Sr_{0.5}CoO_4$ were investigated based on time-resolved Raman and reflection spectroscopy. These cobalt oxides show strong Raman scattering at around 700 cm^{-1}, originating from the breathing vibration mode of the CoO_6 octahedron coupled with the checkerboard-type charge ordering of Co^{2+} and Co^{3+}. We performed time-resolved Raman and reflection spectroscopy by photoirradiating with picosecond pulses at 400 nm, exciting the charge transfer (CT) transition from the O 2*p* site to the Co 3*d* site. As a result of the excitation, the Raman intensity of the breathing mode was suppressed by 10% on a similar time scale in the reflectance change without changing the frequency of the mode, directly indicating ultrafast suppression of the order parameter of the charge-ordered state by CT transition.

Keywords. Spin crossover cobaltite, Perovskite-type oxide, Time-resolved spectroscopy, Raman spectroscopy, Femtosecond technology.

Available online 7th January 2021

* Corresponding author.

1. Introduction

The spin crossover (SC) phenomenon is a variation of the spin state in a strong ligand field, and is especially observed in materials containing divalent Fe^{2+} or trivalent Co^{3+} ions. These transition metal cations have six d electrons, and when the crystal field is greater than Hund coupling energy, the low spin (LS) state appears in which all the spins occupy t_{2g} levels (t_{2g}^6). By contrast, when the crystal field is weak, a high spin (HS, $t_{2g}^4 e_g^2$) or an intermediate spin (IS, $t_{2g}^5 e_g^1$) state is realized. An interesting point of the SC material is that the external perturbation such as temperature variation, applying pressure, and light illumination can cause the spin state change [1]. Hence, SC systems have attracted much interest as an example of exotic phase control with external stimuli.

As one of the SC materials, perovskite-type cobalt oxides with Co^{3+} ions have been investigated during the past quarter century [2]. A typical SC cobalt example is $LaCoO_3$ (LCO). The LCO crystal shows the SC transition with changing temperature at around 100 K [3–5]. Although it remains to be seen whether the excited state is an HS or IS state, a lot of experiments to understand the mechanism of the SC phenomena in the LCO system have been reported [2–5].

In addition to LCO, it is known that layered perovskite-type cobalt oxides such as $La_{1.5}Ca_{0.5}CoO_4$ (LCCO) and $La_{1.5}Sr_{0.5}CoO_4$ (LSCO) also show the SC transition. The crystal structure is the so-called K_2NiF_4 type [6, 7], which is identified with that of the high-T_c cuprate. In LCCO and LSCO, the nominal valence of the cobalt ion is 2.5+ and $Co^{2+} : Co^{3+} = 1 : 1$. Note that in the layered cobaltite there is real-space ordering of Co^{2+} and Co^{3+} as shown in the inset of Figure 1(a), and the charge order makes the cobaltites insulating [8]. X-ray diffraction measurement suggests that the two types of cobalt ions show a checkerboard-type ordering in the ab-plane of the K_2NiF_4 structure below $T_{co} = 800$ K [9]. Thus, both LCCO and LSCO are highly insulating with the charge ordering at room temperature. In LSCO, some experimental [10, 11] and theoretical works [12] revealed that the electronic states of Co^{2+} and Co^{3+} were HS and LS at room temperature, respectively. A magnetic study [13] suggests that an SC transition occurs in Co^{3+} between the LS and HS state at T_{co}. These results indicate that the layered cobaltites can also be viewed as an SC system like LCO.

Besides the viewpoint of the exotic spin state change, we noticed such SC cobalt oxides as a target of photoactive materials. Some SC materials, especially Fe^{2+} complexes are known to show the perpetual photoinduced spin state transition between the HS and LS state in several iron complexes [1], and furthermore, the detailed dynamics of SC has also recently been investigated using a femtosecond (fs) laser and/or X-ray pulses [14, 15]. From this respect, we have conducted ultrafast spectroscopy on several cobalt perovskites and so far demonstrated some works concerning the photoinduced electronic change involved in the SC phenomena [16–18]. One example is the LSCO system [19], on which we conducted time-resolved fs reflection spectroscopy and revealed that photoirradiation with 400 nm laser pulses could realize an exotic photoexcited state that is different from the thermally induced HS state. By comparing the observed transient absorption spectrum with the theoretically suggested one by using theoretical [20] and experimental reports [21], it is reasonable to consider that the local (polaronic) HS domains appear in response to light, although further experiments other than those on the reflection change on the ultrafast time scale would be needed.

In this paper, we report on the photonic change of Raman scattering in the layered cobaltites, LCCO and LSCO, using picosecond (ps) laser pulses. The layered perovskites show strong breathing Raman mode as depicted in the inset of Figure 1(b) [19, 22]. The symmetry of the mode is A_{1g} in the tetragonal setting ($I4mmm$) and is inactive without the checkerboard-type charge ordering in the ab-plane [22]. Thus, the intensity of the Raman peak reflects the degree of the charge order. We investigate the transient change of the breathing mode after photoirradiating with 400 nm ps

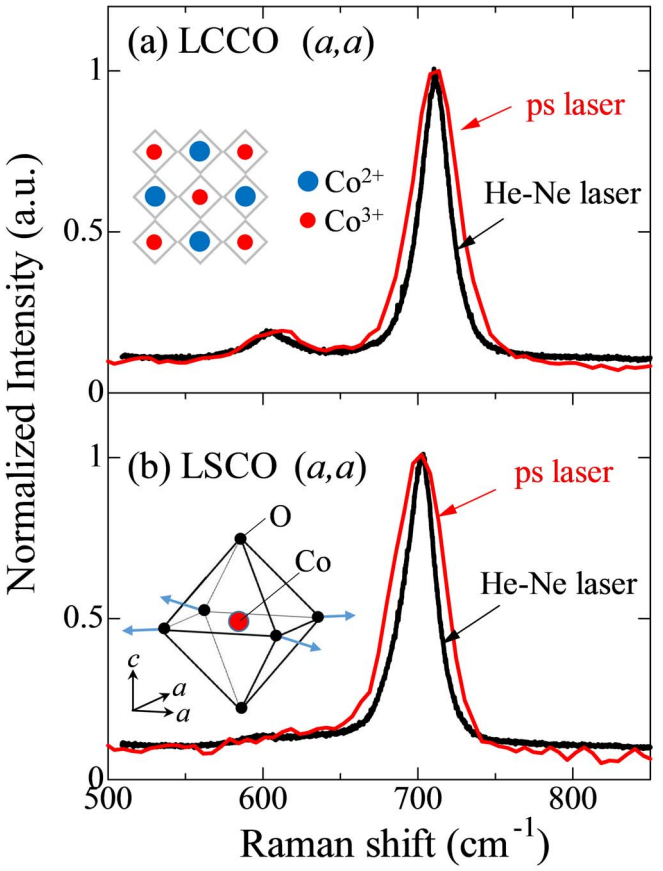

Figure 1. Static Raman spectra in (a) LCCO and (b) LSCO obtained by CW He–Ne laser light (black lines) and the ps laser pulse (red lines). The Raman intensities are normalized with the maximum value. The inset in (a) shows schematics for the ordering of Co^{2+} and Co^{3+} and in (b) for the breathing mode of the CoO_6 octahedron.

laser pulses and discuss the ps dynamics of the photoexcited state in the charge-ordered system, introducing the simultaneous measurement system used for the pump–probe reflection and Raman spectroscopy.

2. Experiment

Single crystal rods of LCCO and LSCO were grown by the floating zone method [6, 7, 19]. The crystal orientation of the grown crystal rods was examined by X-ray diffraction. The *ab*-plane of the crystal was precisely cut from the crystal rods, and the surfaces were polished with alumina powder.

Figure 2(a) shows the schematics of simultaneous measurement system with the pump–probe reflection and Raman spectroscopy. We used a mode-locked Ti-Sapphire laser powered by the regenerative and multipass amplifier (Quantronix Titan-I-3p) with the wavelength of ≈800 nm and the pulse width of ≈1.5 ps as a light source for probing the reflection and Raman scattering signals, and photoexcitation of the samples. The output beam was divided into pump and probe beams by the beam splitter (BS). By using fundamental beam, we obtained reflection signal and

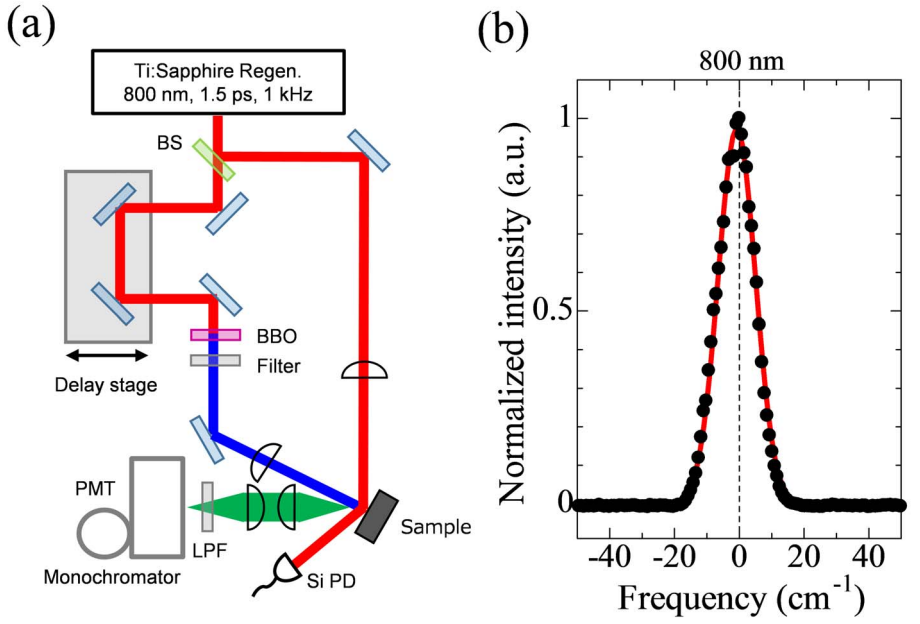

Figure 2. (a) Schematics of the experimental system for the time-resolved reflection and Raman spectroscopy. (b) A spectrum of ps laser pulse used for the time-resolved Raman spectroscopy (black circle). The red line indicates the fitted result based on the Gaussian function.

Raman scattering spectra in the configuration of quasi-backscattering geometry. The reflection signal was detected by silicon photodiode (Si PD). The scattering light through appropriate low-pass filter (LPF) with the edge wavelength at 813.7 nm (≈210.5 cm^{-1}) was dispersed by a single grating monochromator (JASCO CT-25, $f = 250$ mm), and then detected with a photomultiplier (PMT, Hamamatsu R2658). The polarization directions of the incident and scattered light were both along the a-axis of the crystal.

To photonically excite the crystals, we used a second harmonic beam (400 nm) generated by β-BaB_2O_4 (BBO) crystal, which excites the charge transfer transition from the O $2p$ band to the empty Co $3d$ band [23]. After the photoexcitation, we measured the transient change of the reflection at 800 nm and the Raman signal scarcely changing the optical configuration, as depicted in Figure 2(a).

First, let us clarify the type of ps laser pulse we used for Raman spectroscopy. Figure 2(b) shows the spectrum of the ps laser pulse used in this work that was obtained by the monochromator shown in Figure 2(a). The peak intensity is normalized with the maximum value. Reflecting the ps pulse width, the spectrum has a finite bandwidth. The red curve shows a fitted result based on the Gaussian function, indicating that the spectral resolution of the time-resolved measurement system is about 13.6 cm^{-1} full width at half maximum (FWHM).

In general, Raman spectroscopy is measured using continuous wave (CW) laser light whose wavelength is well determined. Therefore, it seems that it is difficult to get an exact Raman spectrum by ps laser pulse with a wider bandwidth. In Figures 1(a) and (b), to respond to this problem, we show Raman spectra for LCCO and LSCO obtained by ps laser pulse with the system depicted in Figure 2(a) by the red curves and ones obtained by CW He–Ne laser light and a commercially purchased Raman spectrometer (Jobin Yvon T64000) by the black lines.

As mentioned above, the conspicuous peaks were observed at around 714 cm^{-1} (LCCO) and 700 cm^{-1} (LSCO), which are assigned as the breathing mode of the CoO_6 octahedron [19]. The Raman shift in LCCO is 14 cm^{-1} greater than that in LSCO, indicating that the ionic crystal is more robust in the former than in the latter, partly because the ionic radius of Ca^{2+} is smaller than that of Sr^{2+}. An important parameter is the FWHM of the Raman peak. The values of the FWHM measured with the ps pulse are 36.7 cm^{-1} for LCCO and 39.7 cm^{-1} for LSCO, while those obtained with CW He–Ne laser light are 25.8 cm^{-1} for LCCO and 28.1 cm^{-1} for LSCO, respectively. In both the crystals, the former value with ps pulse was little greater than the latter one with He–Ne laser, but you can see that the ps laser pulse detected the Raman signal well. The breathing mode is so broad that the ps pulse can measure the Raman spectra despite the fact that the bandwidth is larger than that of the CW laser light.

3. Results and discussions

Hereafter, we discuss the ps dynamics of the layered cobaltites. In Figures 3(a) and (b), we show the time dependence of the relative change of reflectivity at 800 nm in LCCO and LSCO. In both cases, the reflectivity suddenly decreases abruptly by about 1% just after the photoirradiation and then gradually decays (the excitation fluence is ≈1.7 mJ/cm^2). To see the dynamics more quantitatively, we fit the time profile according to the following function:

$$I(t) = I_1 \exp(-t/\tau) + I_2. \tag{1}$$

The first term denotes an exponential decay (τ is the decay time) and the second a constant component relaxed from the first state. The actual fitting was performed with the convolution between $I(t)$ and the response function of the present time-resolved system. The fitted results are shown in Figures 3(a) and (b) with black lines, which well reproduce the experimental data. The estimated values of $\tau = 6.4 \pm 0.84$ ps for LCCO and 6.0 ± 1.1 ps for LSCO. Taking account of the pulse width we used (≈1.5 ps), the decaying time is comparable in the two crystals.

In Figures 3(c) and (d), we display time profiles of relative change of Raman scattering intensity at 714 cm^{-1} for LCCO and 700 cm^{-1} for LSCO by red circles, respectively. In the breathing mode depicted in the inset to Figure 2(a), when Co^{2+} and Co^{3+} can be distinguished with the charge ordering, the mode is Raman active. Hence, the cross-section of Raman intensity denotes the degree of the charge ordering in the CoO_2 layer [22]. Similar to the case of the reflection change, the time profiles of Raman intensity also suddenly decreases just after the photoexcitation in both the crystals. The magnitude of the change is more than 10%, directly indicating instant and partial melting of the charge order caused by extra injected electrons due to the CT excitation. For comparison, we plotted the time profiles of reflectivity, which seem to resemble those of Raman intensity change, implying that there are similar dynamics in the electronic change and the charge ordering. To see the photoinduced frequency change of Raman peaks, in Figures 4(a) and (b) we show the transient spectral change (ΔI) just after the photoirradiation. After the photoexcitation, ΔI shows a dip-like decrease at ≈714 cm^{-1} (LCCO) and ≈700 cm^{-1} (LSCO), which almost correspond to the Raman shift for the breathing mode before the photoexcitation (see Figures 1(a) and (b)), indicating a scarce change of the stiffness of the CoO_6 octahedron in both the crystals at least on the ps time scale.

It is interesting to compare these results with the study using ≈10 fs laser pulse performed in LSCO [19]. On the fs time scale, according to the literature, the time profile of the reflectivity of LSCO oscillates from the excitation time to ≈500 fs, originating from a coherent motion of the breathing mode. The estimated frequency and decay time of the coherent mode are ≈680 cm^{-1} and ≈410 fs, suggesting that softening of the phonon instantly occurs, and the observed softening vanishes within 1 ps. This work reveals the successive dynamics and reveals that after 1 ps, partial

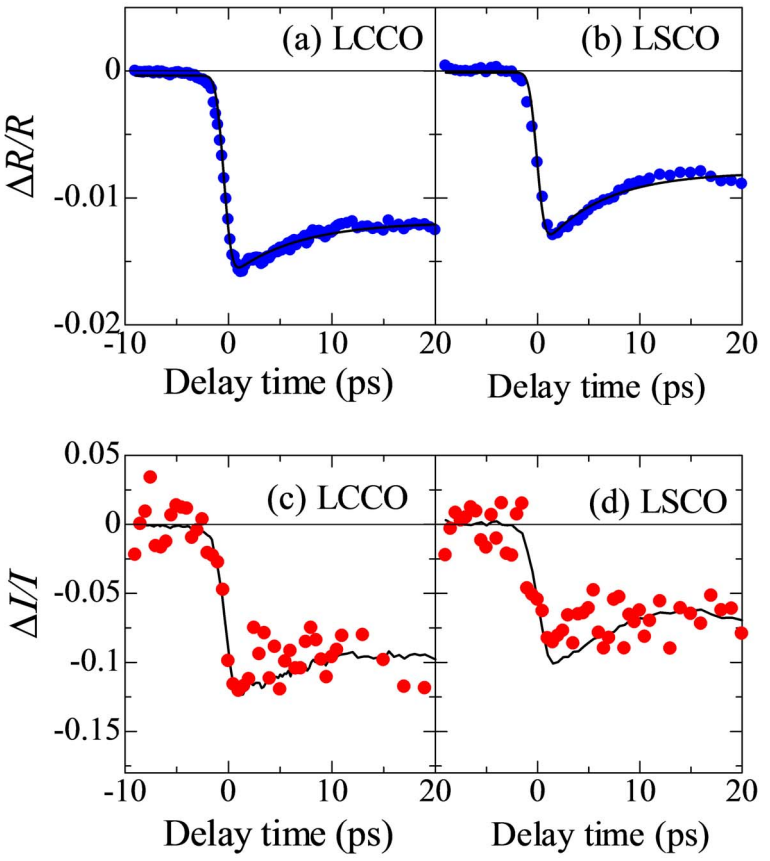

Figure 3. (a, b) Time profiles of relative change of reflectivity at 800 nm (blue circles) after the photoexcitation for LCCO and LSCO. The solid lines denote the fitting result considering the pulse width of ps laser pulse (see text). (c, d) Time profiles of relative change of Raman intensity (red circles) after the photoexcitation for LCCO at 714 cm^{-1} and LSCO at 700 cm^{-1}, respectively. The solid lines show the time profile of reflectivity.

melting of the charge ordering still persists even after the phonon softening has been recovered from the photoexcited state. This conclusion is consistent with the idea of the local formation of HS polarons by light in the layered cobaltites, and some studies such as time-resolved X-ray and/or electron diffraction measurements deserve further investigation.

4. Summary

In summary, we constructed a simultaneous time-resolved measurement system for reflection and Raman scattering using ps laser pulses and investigated the ps dynamics of the perovskite-type layered cobaltites, LCCO, and LSCO, based on pump–probe reflection and Raman spectroscopy. With the CT excitation, the Raman scattering intensity reflecting the degree of the charge ordering decreased within 1 ps by more than 10% without softening the Raman mode reflecting the stiffness of the lattice. Compared with the previous results of fs reflection spectroscopy, the lattice is relaxed on the time scale of 100 fs, while photonic melting of charge order-

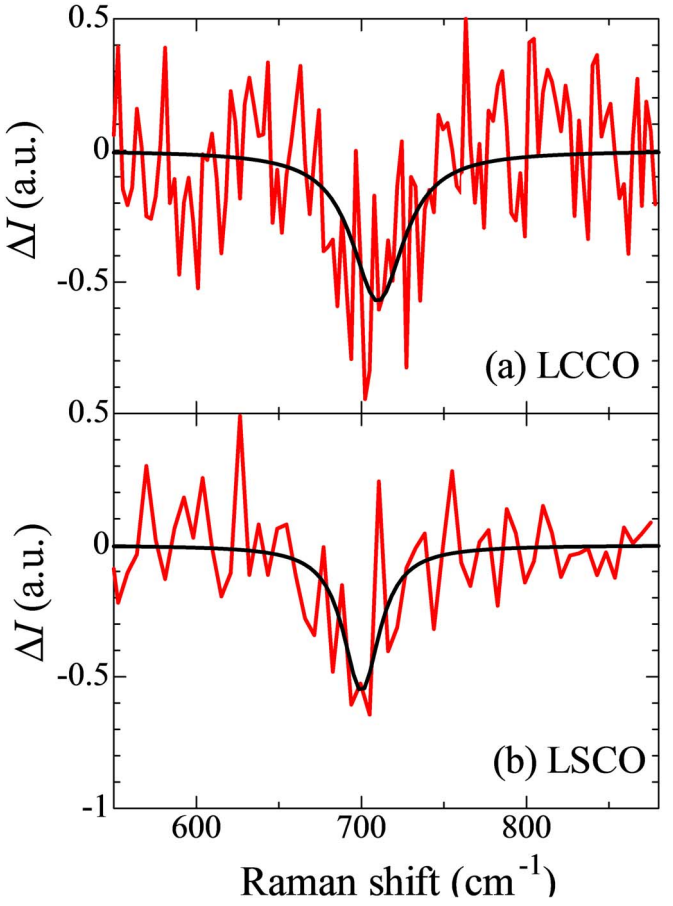

Figure 4. Change of Raman scattering spectrum (solid red line) just after the photoexcitation for (a) LCCO and (b) LSCO. The black lines denote the fitting results using Gaussian function.

ing persists with a longer life time (>1 ps), which not only implies that local spin polaronic state survives on the ps time scale but also reveals a novel aspect of photoinduced SC cobaltites.

Acknowledgments

The authors thank H. Taniguchi and M. Itoh for the early stage of this work concerning Raman spectroscopy and T. Egawa, K. Yu, H. Matsushima, and S. Tanaka for their technical assistance. This research was supported by JSPS KAKENHI Grant No. 19H01827, 18H05208, 16H04000, JP17H06375, JP18H05170.

References

[1] P. Gutlich, H. A. Goodwin (eds.), *Spin Crossover in Transition Metal Compounds I, II and III*, Springer Verlag, Berlin Heidelberg, 2004.

[2] Y. Okimoto, K. Kobayashi, T. Saitoh, S. Ishihara, "Spincrossover Cobaltites-review and Perspectives", in press, to be published by Springer.

[3] K. Asai, O. Yokokura, N. Nishimori, H. Chou, J. M. Tranquada, G. Shirane, S. Higuchi, Y. Okajima, K. Kohn, "Neutron-scattering study of the spin-state transition and magnetic correlations in $La_{1-x}Sr_xCoO_3$ (x = 0 and 0.08)", *Phys. Rev. B* **50** (1994), p. 3025-3032.

[4] T. Saitoh, T. Mizokawa, A. Fujimori, M. Abbate, Y. Takeda, M. Takano, "Electronic structure and temperature-induced paramagnetism in $LaCoO_3$", *Phys. Rev. B* **55** (1997), p. 4257-4266.

[5] S. Yamaguchi, Y. Okimoto, Y. Tokura, "Local lattice distortion during the spin-state transition in $LaCoO_3$", *Phys. Rev. B* **55** (1997), p. R8666-R8669.

[6] K. Horigane, H. Hiraka, T. Uchida, K. Yamada, J. Akimitsu, "Spin and charge orders and their hole-doping dependence in single layered cobaltate $La_{2-x}Ca_xCoO_4$ ($0.3 \le x \le 0.8$)", *J. Phys. Soc. Japan* **76** (2007), p. 114715-114722.

[7] K. Horigane, H. Nakao, Y. Kousaka, T. Murata, Y. Noda, Y. Murakami, J. Akimitsu, "Crystal structure and charge-ordering in $La_{1.5}Ca_{0.5}CoO_4$ studied by neutron and resonant X-ray scattering", *J. Phys. Soc. Japan* **77** (2008), p. 044601-044606.

[8] Y. Moritomo, K. Higashi, K. Matsuda, A. Nakamura, "Spin-state transition in layered perovskite cobalt oxides: $La_{2-x}Sr_xCoO_4$ ($0.4 \le x \le 1.0$)", *Phys. Rev. B* **55** (1997), p. R14725-R14728.

[9] I. A. Zaliznyak, J. P. Hill, J. M. Tranquada, R. Erwin, Y. Moritomo, "Independent freezing of charge and spin dynamics in $La_{1.5}Sr_{0.5}CoO_4$", *Phys. Rev. Lett.* **85** (2000), p. 4353-4356.

[10] C. F. Chang, Z. Hu, H. Wu, T. Burnus, N. Hollmann, M. Benomar, T. Lorenz, A. Tanaka, H.-J. Lin, H. H. Hsieh, C. T. Chen, L. H. Tjeng, "Spin blockade, orbital occupation, and charge ordering in $La_{1.5}Sr_{0.5}CoO_4$", *Phys. Rev. Lett.* **102** (2009), p. 116401-116404.

[11] L. M. Helme, A. T. Boothroyd, R. Coldea, D. Prabhakaran, C. D. Frost, D. A. Keen, L. P. Regnault, P. G. Freeman, M. Enderle, J. Kuld, "Magnetic order and dynamics of the charge-ordered antiferromagnet $La_{1.5}Sr_{0.5}CoO_4$", *Phys. Rev. B* **80** (2009), p. 134414-134428.

[12] H. Wu, T. Burnus, "Spin and orbital states in $La_{1.5}Sr_{0.5}CoO_4$ studied by electronic structure calculations", *Phys. Rev. B* **80** (2009), p. 081105-081108.

[13] N. Hollmann, M. W. Haverkort, M. Benomar, M. Cwik, M. Braden, T. Lorenz, "Evidence for a temperature-induced spin-state transition of Co^{3+} in $La_{2-x}Sr_xCoO_4$", *Phys. Rev. B* **83** (2011), p. 174435-174439.

[14] R. Bertoni, M. Lorenc, H. Cailleau, A. Tissot, J. Laisney, M.-L. Boillot, L. Stoleriu, A. Stancu, C. Enachescu, E. Collet, "Elastically driven cooperative response of a molecular material impacted by a laser pulse", *Nat. Mater.* **15** (2016), p. 606-610.

[15] H. T. Lemke, K. S. Kjar, R. Hartsock, T. B. van Driel, M. Chollet, J. M. Glownia, S. Song, D. Zhu, E. Pace, S. F. Matar, M. M. Nielsen, M. Benfatto, K. J. Gaffney, E. Collet, M. Cammarata, "Coherent structural trapping through wave packet dispersion during photoinduced spin state switching", *Nat. Commun.* **8** (2017), p. 15342-15349.

[16] Y. Okimoto, X. Peng, M. Tamura, T. Morita, K. Onda, T. Ishikawa, S. Koshihara, N. Todoroki, T. Kyomen, M. Itoh, "Ultrasonic propagation of a metallic domain in $Pr_{0.5}Ca_{0.5}CoO_3$ undergoing a photoinduced insulator-metal transition", *Phys. Rev. Lett.* **103** (2009), p. 027402-027405.

[17] Y. Okimoto, M. Kurashima, K. Seko, T. Ishikawa, K. Onda, S. Koshihara, T. Kyomen, M. Itoh, "Acceleration of domain wall movement by photoirradiation in perovskite-type cobaltite", *Phys. Rev. B* **83** (2011), p. 161101-161104.

[18] Y. Okimoto, S. Naruse, R. Fukaya, T. Ishikawa, S. Koshihara, K. Oka, M. Azuma, K. Tanaka, H. Hirori, "Ultrafast control of the polarity of $BiCoO_3$ by orbital excitation as investigated by femtosecond spectroscopy", *Phys. Rev. Appl.* **7** (2017), p. 064016-064020.

[19] Y. Okimoto, T. Egawa, R. Fukaya, Y. Matsubara, Y. Yamada, N. Yamada, T. Ishikawa, K. Onda, S. Koshihara, H. Taniguchi, M. Itoh, A. Isayama, T. Sasagawa, "Ultrafast real space dynamics of photoexcited state in a layered perovskite-type spin crossover oxide $La_{1.5}Sr_{0.5}CoO_4$", *J. Phys. Soc. Japan* **82** (2013), p. 074721-074728.

[20] Y. Kanamori, H. Matsueda, S. Ishihara, "Photoinduced change in the spin state of itinerant correlated electron systems", *Phys. Rev. Lett.* **107** (2011), p. 167403-167406.

[21] Y. Okimoto, T. Miyata, M. Endo, M. Kurashima, K. Onda, T. Ishikawa, S. Koshihara, M. Lorenc, E. Collet, H. Cailleau, T. Arima, "Ultrafast spectral weight transfer in $RBaCo_2O_{6-\delta}$ (R = Sm, Gd, and Tb): A role of electronic correlation in photoinduced phase transition", *Phys. Rev. B* **84** (2011), p. 121102-121106.

[22] K. Yamamoto, T. Kimura, T. Ishikawa, T. Katsufuji, Y. Tokura, "Raman spectroscopy of the charge-orbital ordering in layered manganites", *Phys. Rev. B* **61** (2000), p. 14706-14715.

[23] S. Uchida, H. Eisaki, S. Tajima, "Electron correlation and optical conductivity in high-T_c copper oxides - origin of the mid-infrared absorption band", *Physica B* **186–188** (1993), p. 975-980.

Comptes Rendus
Physique
2021, 22, nº S2, p. 103-110
https://doi.org/10.5802/crphys.57

Physics of ultra-fast phenomena / *Physique des phénomènes ultra-rapides*

Ultrafast dynamics with time-resolved ARPES: photoexcited electrons in monochalcogenide semiconductors

Zhesheng Chen [a, b, c], Jonathan Caillaux [a], Jiuxiang Zhang [a], Evangelos Papalazarou [a], Jingwei Dong [b], Jean-Pascal Rueff [c], Amina Taleb-Ibrahimi [c], Luca Perfetti [b] and Marino Marsi [*, a]

[a] Université Paris-Saclay, CNRS, Laboratoire de Physique des Solides, 91405 Orsay, France

[b] Laboratoire des Solides Irradiés, Ecole Polytechnique, CNRS, CEA, 91128 Palaiseau, France

[c] Synchrotron SOLEIL, L'Orme des Merisiers, Saint-Aubin, BP48, 91192 Gif-sur-Yvette, France

E-mails: zhesheng.chen@universite-paris-saclay.fr (Z. Chen), jonathan.caillaux@universite-paris-saclay.fr (J. Caillaux), jiuxiang.zhang@universite-paris-saclay.fr (J. Zhang), evangelos.papalazarou@universite-paris-saclay.fr (E. Papalazarou), jingwei.dong@polytechnique.edu (J. Dong), jean-pascal.rueff@synchrotron-soleil.fr (J.-P. Rueff), amina.taleb@synchrotron-soleil.fr (A. Taleb-Ibrahimi), luca.perfetti@polytechnique.edu (L. Perfetti), marino.marsi@universite-paris-saclay.fr (M. Marsi)

Abstract. Time-resolved ARPES makes it possible to directly visualize the band dispersion of photoexcited solids, as well as to study its time evolution on the femtosecond time scale. In this article, we show how this technique can be used to monitor the ultrafast hot carrier dynamics and the conduction band dispersion in two typical monochalcogenide semiconductors: direct band gap, *n*-type indium selenide and indirect band gap, *p*-type germanium selenide. With this approach, one can directly estimate the effective electron masses of these semiconductors. Moreover, the dynamics of hot electrons in the two semiconductors are analyzed and compared. Our findings provide valuable information for the use of monochalcogenide semiconductors in future optoelectronic devices.

Keywords. Time-resolved ARPES, Monochalcogenide semiconductor, Ultrafast dynamics, Effective mass, Out-of-equilibrium 2D materials.

Available online 3rd May 2021

* Corresponding author.

1. Introduction

The electronic structure is a unique characteristic of a crystalline solid and encodes crucial information that determines the material's electrical, magnetic and optical properties. Therefore, the efforts to understand the electronic structure in a solid have been one of the central themes of condensed matter physics, and angle resolved photoemission spectroscopy (ARPES) is one of the most direct experimental techniques to measure the energy band dispersion $E = E(\mathbf{k})$ [1]. From the functional point of view, not only the equilibrium electronic structure, but also its out-of-equilibrium properties play a crucial role in the response of the system to an external excitation. Time-Resolved ARPES, where photoemission spectroscopy is performed in a pump–probe configuration using ultrafast light pulses, makes it possible to extend to the excited states all the advantages of this method, providing the time evolution of the non-equilibrium system, $E = E(\mathbf{k}, t)$. Figure 1 shows a schematic diagram of the way time-resolved ARPES is implemented on the FemtoARPES setup [2].

In a semiconductor, the band gap is the main parameter determining device performance, and the dispersion of the conduction band (or valence band) is related to the electron (or hole) effective mass and consequently to the carrier mobility in a device [3–6]. For example, in indirect band gap semiconductors, the radiation recombination is far slower compared to direct band gap, as the absorption or emission of phonons need to be involved in the process, which is not suitable for light emission devices [7, 8]. In anisotropic semiconductors such as black phosphorus, the dispersions of conductions band along each high symmetric directions are significantly different, which corresponds to giant electron effective mass differences, and the mobility is highly direction dependent [9, 10].

ARPES is the most direct way to observe the electronic structure of a semiconductor with high energy and momentum resolution. For example, the electronic structure of indium selenide (InSe) has been directly observed by ARPES in a previous study, and it shows out-of-plane dispersions by changing photon energy, which indicates a quasi-two dimensional nature of the bulk material; in addition, if the electronic structure of InSe is modified with surface alkali atoms doping, the observed ∼1.3 eV band gap in bulk InSe is subsequently reduced as function of doping [11].

As mentioned above, time-resolved ARPES gives us the possibility to finely observe photoexcited empty electronic states as well as their ultrafast dynamics [12,13]. This approach has already been successfully applied to topological insulators, strongly correlated materials, and some semiconductors [14–18]. For example, in gallium arsenide (GaAs) Kanasaki *et al.* directly determined the energy-, momentum-, and time-resolved distribution of hot electrons photoinjected into the conduction band by time-resolved ARPES, and found an intervalley transition time as short as 20 fs [19]. In addition, by using the same method, we transiently occupied the conduction band of black phosphorus by an ultrafast pump pulse and measured the gap value with a subsequent probe pulse. The negligible band gap renormalization and Stark broadening have been observed and explained [10].

Van der Waals stacked monochalcogenide semiconductors such as indium selenide (InSe) and germanium selenide (GeSe) have attracted a lot of interest in recent years because of the widely tunable band gap as function of thickness and ultrahigh carrier mobility in field effect transistors (FETs). The carrier mobility in few-layer InSe is as high as 10^3 $\mathrm{cm^2 \cdot V^{-1} \cdot s^{-1}}$ and 10^4 $\mathrm{cm^2 \cdot V^{-1} \cdot s^{-1}}$ at room and low temperature, respectively [4, 7, 20–22]. This value is compatible to that found in graphene and is among the highest in 2D semiconductors. Compared to InSe, layered GeSe has a unique in-plane anisotropic crystal structure, and its optical properties also show an extremely anisotropic behavior, which open up possibilities for optoelectronic applications such as polarization-sensitive photodetectors and optical waveplates [23–26]. In this

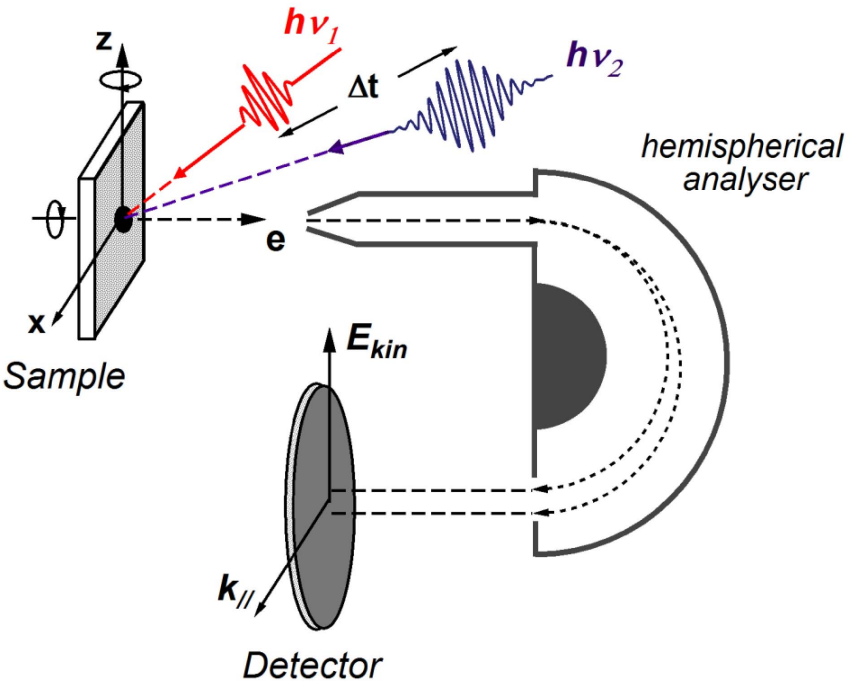

Figure 1. Schematic diagram of a time-resolved ARPES setup.

article we show how time-resolved ARPES can be used to investigate the photoexcited states in n-type InSe and p-type GeSe, and directly observe the dispersion of their conduction band and the hot carrier dynamics. The effective mass of the conduction band and hot carrier decay time are also extracted and compared. The study of the photoexcited states presented in this work provides important information for further applications of InSe and GeSe in novel optical and optoelectronic devices.

2. Experimental details

All the experiments have been performed on the FemtoARPES setup, using a Ti:sapphire laser system delivering 6 μJ pulses with a 250 kHz repetition rate [2]. Part of the laser beam (50 fs pulse, 1.57 eV) is used to pump the sample while the rest is employed to generate the 6.3 eV photons as probe pulse through cascade frequency mixing in BaB_2O_4 (BBO) crystals. The overall energy resolution of the experiment is ≅30 meV and the cross correlation between pump and probe pulses has full width at half maximum (FWHM) of 150 fs. High-quality single crystals of InSe (doped with Sn, 0.01%) we used have been grown using the Bridgmann method from a nonstoichiometric melt [11]. High-quality single crystal of GeSe was purchased from company of HQ graphene. The samples were cleaved and kept at the base pressure of 8×10^{-11} mbar. Our samples have been oriented by low energy electron diffraction and measured at the temperature of 135 K.

3. Results and discussion

The crystal structures of layered InSe and GeSe we used in this work are shown in Figure 2(a). InSe belongs to ε polytype and has hexagonal structure. The unit cell contains two parallel layers

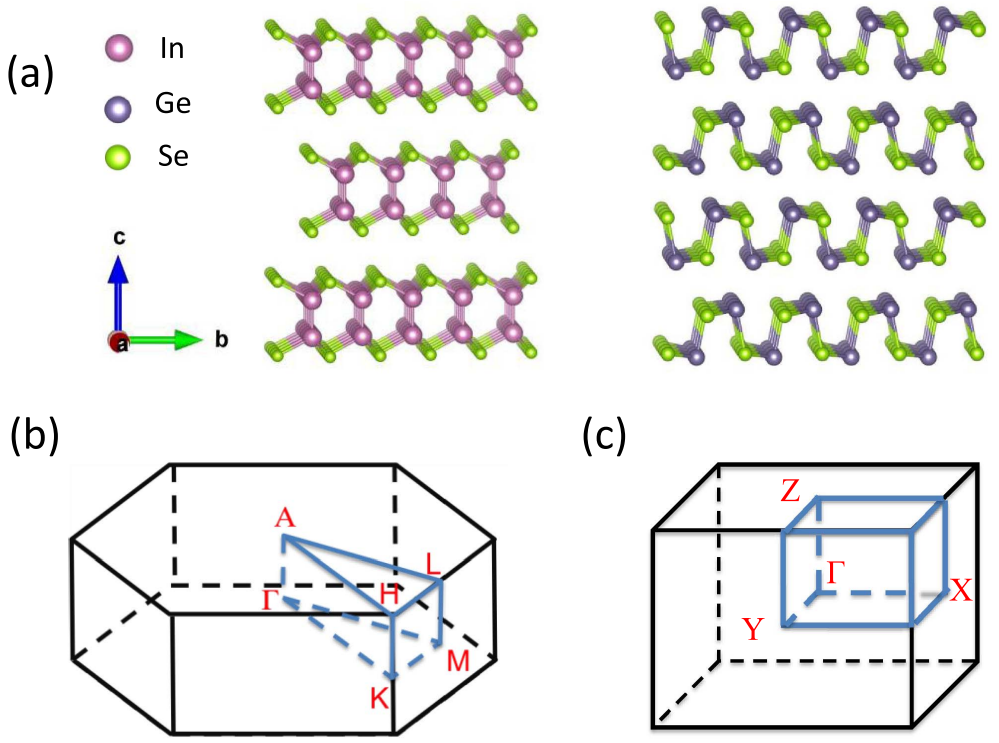

Figure 2. (a) Crystal structure of layered monochalcogenide semiconductors. Left: InSe. Right: GeSe. (b) Schematic of 3D Brillouin zone of InSe. (c) Schematic of 3D Brillouin zone of GeSe.

obtained by a translation of one layer onto another [27]. GeSe has a puckered structure similar to black phosphorus, and presents an orthorhombic crystal structure [28]. The schematics of the 3D Brillouin zones of InSe and GeSe are shown in Figure 2(b,c). Bulk InSe has a direct band gap of ~1.3 eV, with both conduction band minimum (CBM) and valence band maximum (VBM) centered in reciprocal (k) space, at the Γ point of the Brillouin zone [11, 29]. The Fermi level is inside the gap even though the sample is largely n-doped, as shown in the experimental data of Figure 3(a). After being pumped by the infrared-laser (1.57 eV), electrons in the valence band (occupied states) can be only photoexcited into the Γ valley of the conduction band (unoccupied states); other valleys cannot be reached as the maximum excess energy (E_{ex}) of electrons is ~0.27 eV (E_{ex} = 1.57 eV–1.3 eV) and the minimum energy difference between the adjacent valleys is ~0.7 eV (Γ valley to M valley). After a delay time, the photoexcited electrons are photoemitted by the ultraviolet laser probe (6.3 eV) from the conduction band to vacuum: the electron kinetic energy and momentum in k space can be thus determined by the electron energy analyzer (Figure 1). This makes it possible to observe the dispersion of the conduction band at time delay $t = 0$ and the dynamics of photoexcited electrons as a function of time delay.

Figure 3(a–d) shows the photoelectron intensity maps of InSe acquired along $\overline{\Gamma} - \overline{K}$ at different time delays between pump and probe. At negative delay of 1 ps, the system is in equilibrium conditions, and we don't observe electrons in CBM as the surface chemical potential is located below VBM, as shown in Figure 3(a). The position of the surface chemical potential depends on the doping level of the sample and also on band bending which can be slightly different for each cleaved surface. After photoexcitation, the excited electrons are transiently subject to the

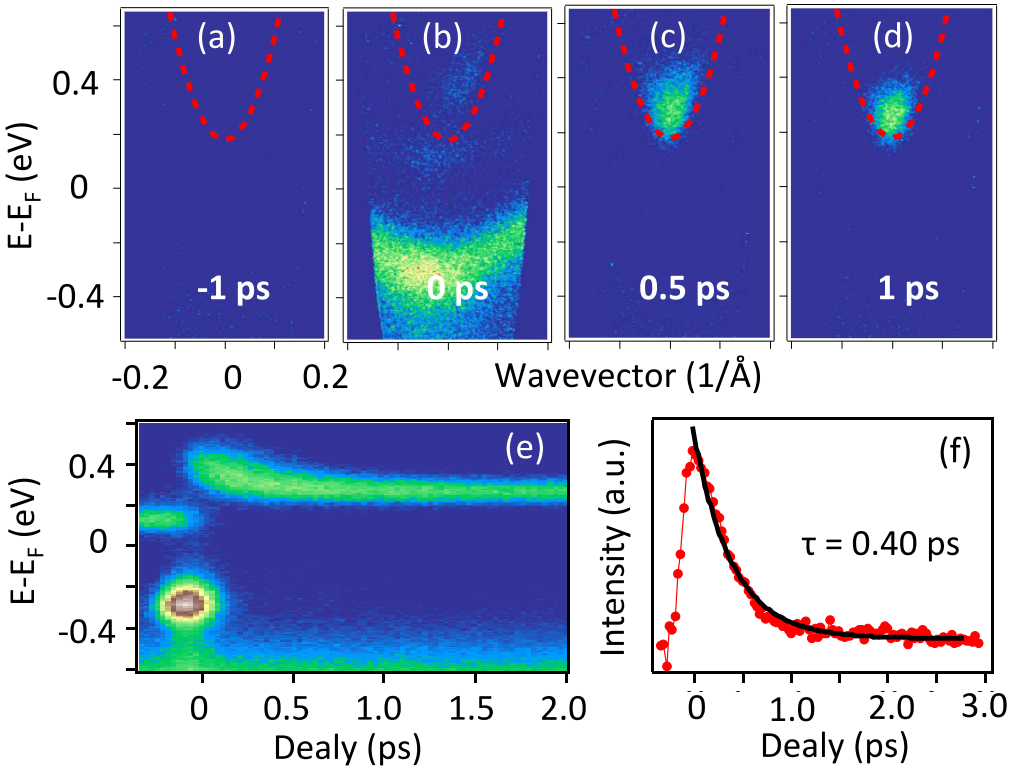

Figure 3. (a–d) Photoelectron intensity maps in InSe acquired along the $\overline{\Gamma}-\overline{K}$ direction and plotted for different delay times. The conduction band is fitted by a parabolic function and indicated by a red dashed line. (e) Dynamics of photoelectron intensity integrated in the wavevector interval $[-0.15, 0.15]$ Å^{-1}. (f) Intensity of electrons in the conduction band as a function of pump–probe delay. The black solid line is an exponential fit with decay time $\tau = 0.40$ ps.

attractive Coulomb potential from the holes as well as to the semiconductor polarization, which gives rise to two image potential states that are shown below the CBM. Image potential states are well understood on polarizable surfaces such as on bare metal surfaces, metal layers on metals, rare gas adlayers on different metallic substrates, and organic thin films on metal surfaces. To our knowledge, this is the first time that the image potential states are found on the surface of inorganic semiconductors. Moreover, we observe photoexcited electrons in the conduction band with the maximum excess energy of ~0.25 eV, as we estimated before. Such hot carrier cooling is a complex process that involves carrier–carrier, carrier–phonon, and phonon–phonon interactions. The dominant cooling process in InSe is carrier–phonon interaction, and generally there are two coupling mechanisms that drive electron–phonon scattering in inorganic semiconductors. The first one is polar Fröhlich interactions due to electron–LO phonon scattering for polar materials, that result from Coulomb interactions between the electrons and the macroscopic electric field induced by the out-of-phase displacements of oppositely charged atoms caused by the LO phonon mode. The second one is the electron-acoustic phonon scattering that is efficient at very low temperature. In InSe, the polar Fröhlich interactions via LO phonon emission is the dominant relaxation for hot carriers, allowing hot electrons to dissipate the energy in $\overline{\Gamma}$ valley and eventually cool down to CBM. In order to gain quantitative insight on the evolution of the

photoexcited states, we fit the dispersion of the $\overline{\Gamma}$ valley along $\overline{\Gamma}-\overline{K}$ by the parabolic expression $E = E_0 \pm p^2/2m_c$, where m_c is the effective mass for the conduction band. As shown by the dotted lines in Figure 3(b–d), the fitting curves reproduce with high accuracy the band dispersion with $m_c = 0.1 \pm 0.01 m_e$, where m_e is the free electron mass. The m_c of InSe extracted from the dispersion of the conduction band along $\overline{\Gamma}-\overline{K}$ in InSe is consistent in the values from other measurements such as transport and optical spectroscopy [20, 30]. Figure 3(e) shows the photoelectron intensity $I\,(E,\,t)$ integrated in the wavevector window $[-0.15, 0.15]$ Å^{-1} and plotted as a function of pump–probe delay. The total intensity of photoelectrons in the conduction band follows an exponential decay with time constant $\tau = 0.40 \pm 0.1$ ps, as shown in Figure 3(f). This timescale elucidates the main relaxation mechanism of hot carriers in the $\overline{\Gamma}$ valley, which is very similar to pristine InSe without Sn doping [29]. Therefore, we ascribe the short-time cooling process to the polar optical coupling with small momentum transfer.

Totally different from *n*-type bulk InSe with a direct band gap, pristine bulk GeSe is a *p*-doped semiconductor and has an indirect band gap. The CBM of GeSe locates at the center of Brillouin zone shown in Figure 2(c) and the gap is ~1.35 eV, which enables us to directly measure conduction band dispersion and hot carrier dynamics by time-resolved ARPES. From the photoelectron intensity maps along the zigzag direction ($\Gamma - Y$) shown in Figure 4(a–d), we observe the dispersion of photoexcited electrons in the conduction band at zero delay and positive delay. The chemical potential is ~0.7 eV below CBM, which confirms the *p*-type nature of the sample considering the indirect band gap of ~1.13 eV. Like for most semiconductors, we don't observe any image potential states, which can be explained by the different surface properties with respect to InSe. The maximum excess energy of hot electrons pumped by the infrared pulse is ~0.2 eV, which is similar to what found in InSe. However, the conduction band displays much less dispersion and one can fit it by the same parabolic function with $m_c = 1.8 \pm 0.1 m_e$. It is worth noticing that the m_c in GeSe is one order of magnitude larger than that of InSe, which might be the reason of significant mobility difference between the two materials. The photoelectron intensity $I\,(E,\,t)$ integrated in the wavevector window $[-0.2, 0.2]$ Å^{-1} and the total photoelectron intensity in the conduction band as a function of pump–probe delay are shown in Figures 4(e) and 4(f), respectively. The time constant of the hot carrier decay process is $\tau = 1.58 \pm 0.1$ ps by fitting the experimental data with exponential function, which indicates a much slower cooling process than that of InSe. Considering the similar maximum excess energy of photoexcited electrons in the conduction band of both materials, the time constant difference can be explained by the difference in energy or the phonons participating in the electron–phonon coupling process. On the other hand, the electron effective mass in GeSe is much larger than in InSe, and consequently the hot electron distribution in *k* space is very different. The distribution of hot electrons in InSe is within ± 0.1 Å^{-1} in *k* space, while their range is significantly lager (± 0.2 Å^{-1}) for GeSe. All of this can contribute to the difference between the hot carrier cooling processes in a direct band gap semiconductor like InSe and an indirect band gap semiconductor like GeSe. Further theoretical investigations will be necessary in order to clarify this issue.

4. Conclusions

In conclusion, we performed time-resolved ARPES on two different monochalcogenide semiconductors: direct band gap InSe and indirect band gap GeSe. The dispersion of the conduction band around the center of Brillouin zone and the corresponding hot electron dynamics are directly observed. The electron effective mass is extracted from the parabolic dispersion and the time constant of the decay process is obtained by exponential fittings. The electron effective mass in GeSe is much larger than that of InSe, and this is consistent with the significant large mobility in InSe found in previous studies. However, the decay process is much slower in GeSe, which might be

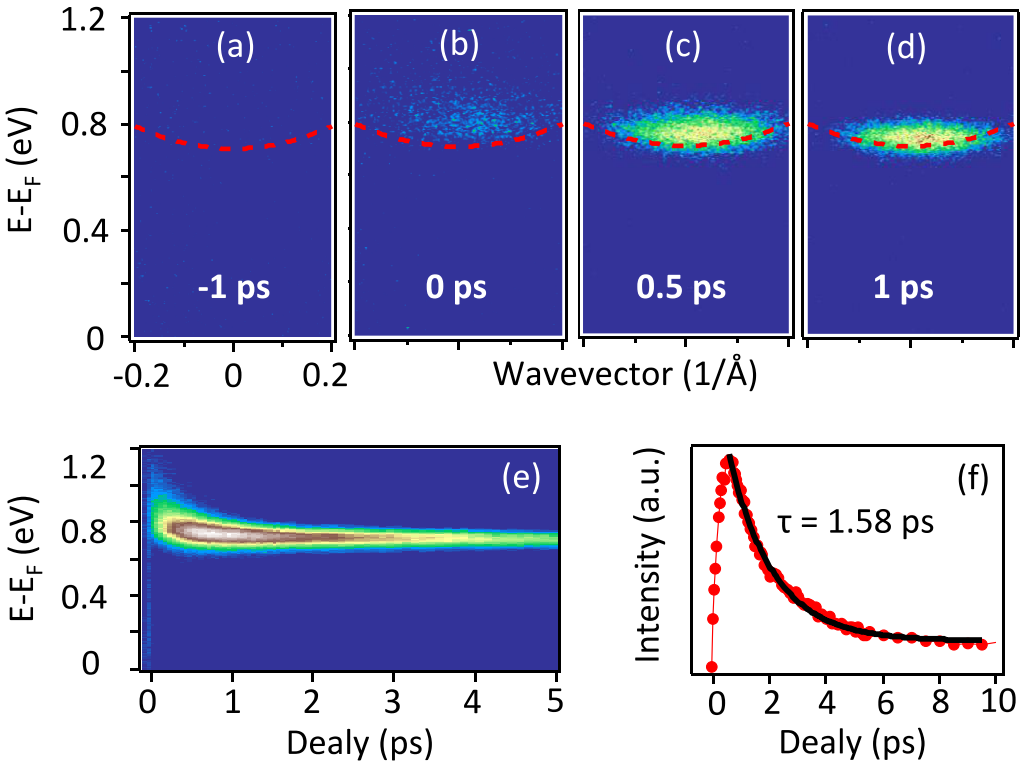

Figure 4. (a–d) Photoelectron intensity maps in GeSe acquired along the zigzag direction and plotted for different delay times. The conduction band is fitted by a parabolic function and indicated by red dashed line. (e) Dynamics of photoelectron intensity integrated in the wavevector interval $[-0.20, 0.20]$ Å^{-1}. (f) Intensity of electrons in the conduction band as a function of pump–probe delay. The black solid line is an exponential fit with decay time $\tau = 1.58$ ps.

related to the smaller matrix elements of the polar electron–phonon coupling [31]. Our observation of photoexcited states presented in this work provides useful information for further applications of InSe and GeSe in novel optical and optoelectronic devices.

Acknowledgements

We thank DIM-Oximore and the Ecole Polytechnique for funding under the project "ECO-GAN". This work was supported by the EU/FP7 under the contract Go Fast (280555) and by "Investissement d'Avenir" Labex PALM (ANR-10-LABX-0039-PALM).

References

[1] S. Hüfner, *Photoelectron Spectroscopy*, Springer, Berlin, 2003.
[2] J. Faure *et al.*, "Full characterization and optimization of a femtosecond ultraviolet laser source for time and angle-resolved photoemission on solid surfaces", *Rev. Sci. Instrum.* **83** (2012), article no. 043109.
[3] S. R. Tamalampudi *et al.*, "High performance and bendable few-layered InSe photodetectors with broad spectral response", *Nano Lett.* **14** (2014), p. 2800-2806.
[4] S. Lei *et al.*, "Evolution of the electronic band structure and efficient photo-detection in atomic layers of InSe", *ACS Nano* **8** (2014), p. 1263-1272.

[5] S. Manzeli, D. Ovchinnikov, D. Pasquier, O. V. Yazyev, A. Kis, "2D transition metal dichalcogenides", *Nat. Rev. Mater.* **2** (2017), article no. 17033.
[6] R. Roldán, A. Castellanos-Gomez, "Black phosphorus: A new bandgap tuning knob", *Nat. Photon.* **11** (2017), p. 407-409.
[7] M. J. Hamer *et al.*, "Indirect to direct gap crossover in two-dimensional InSe revealed by angle-resolved photoemission spectroscopy", *ACS Nano* **13** (2019), p. 2136-2142.
[8] N. Ubrig *et al.*, "Design of van der Waals interfaces for broad-spectrum optoelectronics", *Nat. Mater.* **19** (2020), p. 299-304.
[9] F. Xia, H. Wang, J. C. M. Hwang, A. H. C. Neto, L. Yang, "Black phosphorus and its isoelectronic materials", *Nat. Rev. Phys.* **1** (2019), p. 306-317.
[10] Z. Chen *et al.*, "Band gap renormalization, carrier multiplication, and Stark broadening in photoexcited black phosphorus", *Nano Lett.* **19** (2018), p. 488-493.
[11] Z. Zhang *et al.*, "Direct observation of band gap renormalization in layered indium selenide", *ACS Nano* **13** (2019), p. 13486-13491.
[12] T. Rohwer *et al.*, "Collapse of long-range charge order tracked by time-resolved photoemission at high momenta", *Nature* **471** (2011), p. 490-493.
[13] A. Grubišić Čabo *et al.*, "Observation of ultrafast free carrier dynamics in single layer MoS_2", *Nano Lett.* **15** (2015), p. 5883-5887.
[14] Y. Ohtsubo *et al.*, "Giant anisotropy of spin-orbit splitting at the bismuth surface", *Phys. Rev. Lett.* **109** (2012), article no. 226404.
[15] M. Caputo *et al.*, "Dynamics of out-of-equilibrium electron and hole pockets in the type-II Weyl semimetal candidate WTe_2", *Phys. Rev. B* **97** (2018), article no. 115115.
[16] G. Lantz *et al.*, "Ultrafast evolution and transient phases of a prototype out-of-equilibrium Mott–Hubbard material", *Nat. Commun.* **8** (2017), article no. 13917.
[17] C. L. Smallwood *et al.*, "Tracking Cooper pairs in a cuprate superconductor by ultrafast angle-resolved photoemission", *Science* **336** (2012), p. 1137-1139.
[18] H. Soifer *et al.*, "Band-resolved imaging of photocurrent in a topological insulator", *Phys. Rev. Lett.* **122** (2019), article no. 167401.
[19] J. Kanasaki, H. Tanimura, K. Tanimura, "Imaging energy-, momentum-, and time-resolved distributions of photoinjected hot electrons in GaAs", *Phys. Rev. Lett.* **113** (2014), article no. 237401-5.
[20] D. A. Bandurin *et al.*, "High electron mobility, quantum Hall effect and anomalous optical response in atomically thin InSe", *Nat. Nanotechnol.* **12** (2016), p. 223-227.
[21] W. Feng, W. Zheng, W. Cao, P. Hu, "Back gated multilayer InSe transistors with enhanced carrier mobilities via the suppression of carrier scattering from a dielectric interface", *Adv. Mater.* **26** (2014), p. 6587-6593.
[22] A. Gao *et al.*, "Observation of ballistic avalanche phenomena in nanoscale vertical InSe/BP heterostructures", *Nat. Nanotechnol.* **6** (2019), p. 217-222.
[23] G. Shi, E. Kioupakis, "Anisotropic spin transport and strong visible-light absorbance in few-layer SnSe and GeSe", *Nano Lett.* **15** (2015), p. 6926-6931.
[24] D.-J. Xue *et al.*, "Anisotropic photoresponse properties of single micrometer-sized GeSe nanosheet", *Adv. Mater.* **24** (2012), p. 4528-4533.
[25] H. Zhao *et al.*, "Band structure and photoelectric characterization of GeSe monolayers", *Adv. Funct. Mater.* **28** (2017), article no. 1704855-10.
[26] X. Zhou *et al.*, "Highly anisotropic GeSe nanosheets for phototransistors with ultrahigh photoresponsivity", *Adv. Sci.* **5** (2018), article no. 1800478-9.
[27] E. Doni, R. Girlanda, V. Grasso, A. Balzarotti, M. Piacentini, "Electronic properties of the III–VI layer compounds GaS, GaSe and InSe. I: Band structure", *Nuovo Cim. B* **51** (1979), p. 154-180.
[28] Y. Yang *et al.*, "In-plane optical anisotropy of low-symmetry 2D GeSe", *Adv. Opt. Mater.* **7** (2018), article no. 1801311-8.
[29] Z. Chen *et al.*, "Ultrafast electron dynamics reveal the high potential of InSe for hot-carrier optoelectronics", *Phys. Rev. B* **97** (2018), article no. 241201-5.
[30] N. Kuroda, Y. Nishina, "Anisotropies of energy-bands in GaSe and InSe", *Physica B & C* **105** (1981), p. 30-34.
[31] J. Faure *et al.*, "Direct observation of electron thermalization and electron–phonon coupling in photoexcited bismuth", *Phys. Rev. B* **88** (2013), article no. 075120.

Comptes Rendus
Physique
2021, 22, nº S2, p. 111-138
https://doi.org/10.5802/crphys.41

Physics of ultra-fast phenomena / *Physique des phénomènes ultra-rapides*

Sub-picosecond C=C bond photo-isomerization: evidence for the role of excited state mixing

Photo-isomérisation sub-picoseconde de liaisons C=C : l'importance du mélange des états excités

Damianos Agathangelou [a], Partha Pratim Roy [b], María del Carmen Marín [c], Nicolas Ferré [d], Massimo Olivucci [c, e], Tiago Buckup [b], Jérémie Léonard [a] and Stefan Haacke*, [a]

[a] Université de Strasbourg – CNRS, Institut de Physique et Chimie des Matériaux de Strasbourg, 67034 Strasbourg, France

[b] Physikalisch-Chemisches Institut, Ruprecht-Karls Universität Heidelberg, 69120 Heidelberg, Germany

[c] Biotechnology, Pharmacy and Chemistry Department, University of Siena, Siena 53100, Italy

[d] Aix-Marseille Univ. – CNRS, ICR, 13397 Marseille, France

[e] Chemistry Department, Bowling Green State University, Bowling Green, Ohio 43403, USA

Current addresses: LUMOS lab, University of Michigan, Department of Physics, USA (D. Agathangelou), University of Berkeley, Department of Chemistry, USA (P. P. Roy)

E-mails: demian22ful@gmail.com (D. Agathangelou), pproy.iitk@gmail.com (P. P. Roy), mariadelcarmen.ma@student.unisi.it (M. del Carmen Marín), nicolas.ferre@univ-amu.fr (N. Ferré), olivucci@unisi.it (M. Olivucci), tiago.buckup@pci.uni-heidelberg.de (T. Buckup), Jeremie.Leonard@ipcms.unistra.fr (J. Léonard), haacke@unistra.fr (S. Haacke)

Abstract. Sub-picosecond photo-isomerization is the major primary process of energy conversion in retinal proteins and has as such been in the focus of extensive theoretical and experimental work over the past decades. In this review article, we revisit the long-standing question as to how the protein tunes the isomerization speed and quantum yield. We focus on our recent contributions to this field, which underscore the concept of a delicate mixing of reactive and non-reactive excited states, as a result of steric properties and electrostatic interactions with the protein environment. Further avenues and new approaches are outlined

* Corresponding author.

which hold promise for advancing our understanding of these intimately coupled chromophore–protein systems.

Résumé. La photo-isomérisation sub-picoseconde est la principale réaction initiant la conversion d'énergie dans les protéines de rétinal, si bien qu'elle fait l'objet de travaux théoriques et expérimentaux approfondis depuis plus de trente ans. Dans cet article de revue, nous revisitons la question toujours ouverte de savoir comment la protéine détermine la vitesse d'isomérisation et son rendement quantique. A la lumière de nos contributions récentes en ce domaine, nous décrivons le concept d'un mélange d'états excités réactifs et non-réactifs, délicatement ajusté par les interactions stériques et électrostatiques avec l'environnement protéique. De nouvelles perspectives et approches prometteuses sont décrites qui pourront faire progresser la compréhension de ces systèmes chromophore–protéine intimement couplés.

Keywords. Photo-isomerisation, Retinal proteins, Chromophore–protein coupling, Non-adiabatic dynamics, Photo-sensory proteins, Charge transfer state.

Mots-clés. Photo-isomérisation, Protéines de rétinal, Couplage chromophore–protéines, Dynamiques non-adiabatiques, Protéines photo-senseurs, État de transfert de charge.

Available online 1st March 2021

Many organisms, from microbacteria to vertebrates, use photosensitive retinal proteins for photo-chemical energy conversion or photo-sensory functions [1–3]. Visible light-absorbing retinal proteins rely on the protonated Schiff base of retinal (rPSB) as chromophore, covalently bound to the interior of a barrel-like "opsin" protein. Their biological activity is triggered by a regioselective and stereoselective C=C double bond photoisomerization of rPSB, e.g. 11-*cis* to all-*trans* for the visual pigment rhodopsin (Rho), all-*trans* to 13-*cis* for the proton pump bacteriorhodopsin (bR), or both 13-*cis* to all-*trans* and all-trans to 13-*cis* for the bistable, photochromic Anabaena Sensory Rhodopsin (ASR). In all cases, the protein scaffold exerts electrostatic and steric interactions on the chromophore [4–7], which tune the rPSB photoreaction dynamics, e.g. the excited state lifetime (ESL) and its photoisomerization quantum yield (IQY), ultimately determined by the branching ratio between reactive and non-reactive channels. The pronounced influence of the protein interaction on rPSB photo-reactivity is evidenced by comparing with the photoreaction dynamics and IQY of rPSB in other environments, e.g. in solution [8–14] or in vacuum [15].

The photoisomerization of rPSB occurs through a conical intersection (CInt), [16, 17] which is an intersection seam between the excited (S_1) and ground (S_0) state potential energy surfaces (PES), where the molecule transiently adopts a configuration with a nearly 90° twisted reacting double bond. While it has been shown that there is no correlation between ESL and IQY [18–21], many theoretical predictions agree, that the PESs topography and the nuclear motions at the CInt decide on the branching between reactive and non-reactive pathways, hence on the overall IQY [17, 22, 23]. There is large scientific interest at investigating the photoreactions of retinal proteins in order to decipher the intra- and inter-molecular parameters which tune the photoreactivity of rPSB, as a model system for non-adiabatic dynamics through a CInt. In addition, such a fundamental understanding would be the key to define chemical design strategies to control the photoreactivity of C=C double bond isomerization in retinal chromophores or similar compounds. In particular, there is broad interest in producing rhodopsin mutants with an enhanced ESL and, as a consequence, fluorescence quantum yield (FQY) for applications in optogenetics [24, 25]. Moreover, understanding the dynamic structure-property relationships will most likely indicate new avenues for tailoring molecular devices based on ultrafast C=C double isomerization to perform photoswitching or rotary motion, at the molecular scale, with optimum efficiency [26].

Section 1 gives a brief and necessarily incomplete account of recent experimental studies on the effect of the environment of the photophysics of rPSB's, with an emphasis on the electrostatic properties, in particular the presence or protonation state of counter ions.

Sections 2–4 concentrate on both electrostatic and steric effects on the ESL and FQY of rPSB in different retinal proteins and rhodopsin-mimicking photo-switches in solution. Steric effects, in particular the distortion of the rPSB in the ground state of 11C in Rho as opposed to the more planar AT in bR is held responsible for the faster photo-isomerization reaction in Rho [27–32], as will be corroborated in these sections. In Section 2, we review the concept of $^1B_u/^2A_g$ mixing between the first two excited states (Figure 1), and how it translates both steric and electrostatic properties comprehensively. Section 3 then treats the experimental manifestation and quantitative explanation of these effects for *Anabaena Sensory Rhodopsin* and some selected mutants. Section 4 extends this combined treatment to rhodopsin-mimicking photo-switches, before Section 5 summarises the main concepts and outlines future avenues.

1. An open question studied on different systems

The protonation of the retinal Schiff base in VIS-absorbing retinal proteins makes these systems distinctively different from their UV-absorbing sisters, which function with a deprotonated chromophore [33]. The charge-transfer character of the lowest excited state [34,35], S_1, is at the heart of the high sensitivity to the presence of counter ions and dynamic electrostatic interactions, thereby controlling the excited state dynamics. This will be highlighted in the following paragraphs.

1.1. *Isolated rPSB's in solution and gas phase*

Since 11-*cis* (11C) and all-trans (AT) isomers are the ground state conformations of the visual photo-receptor and of the large majority of microbial retinal proteins, respectively, these were studied quite extensively as isolated molecules in solution and to a lesser extent in the gas phase. It was first noticed that the absorption spectra in solution are significantly blue-shifted with respect to the situation in protein cavities (referred to as the "opsin shift"). It can be quantitatively explained by a stronger polarizability of the protein environment and interaction of the rPSB with its counter ion in solution, reduced though for polar solvents, and, for AT rPSB, by an enhanced ring/chain co-planarization in proteins [36–39]. In solution, the 11-*cis* isomer photo-isomerization produces specifically the AT isomer, like in proteins. The IQY is however only about 25% in various solvents versus 67% in Rhodopsin. Conversely, the photo-isomerization of AT in solution produces a variety of product isomers, unlike in proteins where it is 100% bond-selective, and occurs with a total IQY in the range of 15% [40–42].

Femtosecond transient absorption and fluorescence spectroscopy consistently showed that the excited state lifetimes and thus the isomerization times are significantly longer than in proteins, with a dominant decay component in the 3–4 ps range, for both the 11C and AT rPSB's [8,10,12,43–45]. For AT, sub-picosecond fluorescence decay components were attributed to internal conversion and the dominant non-reactive back reaction [10,21]. The ESL increase at lower temperatures points to the existence of a small excited state barrier [12]. Conversely, in the case of 11C in solution, the sub-ps component was attributed to the minority, barrier-less reactive channel while the 4-ps component would characterize the dominant non-reactive channel [45].

In the absence of a counter ion or any polarisable environment, i.e. for rPSB's in gas phase, the absorption spectra of AT and 11C rPSB's are red-shifted with respect to the protein spectra, due to a relative destabilisation of S_0 [46,47]. The energies of the UV/VIS electronic transitions are obtained by recording the photo-fragmentation action spectra of the cationic chromophores held in an ion storage ring. Recently, this approach was extended to two-pulse experiments, which allowed to record the excited states lifetimes *in vacuo* [15]. A first pump pulse resonantly tuned onto the S_0–S_1 transition excites the molecules, and, after a delay time τ, a second pump

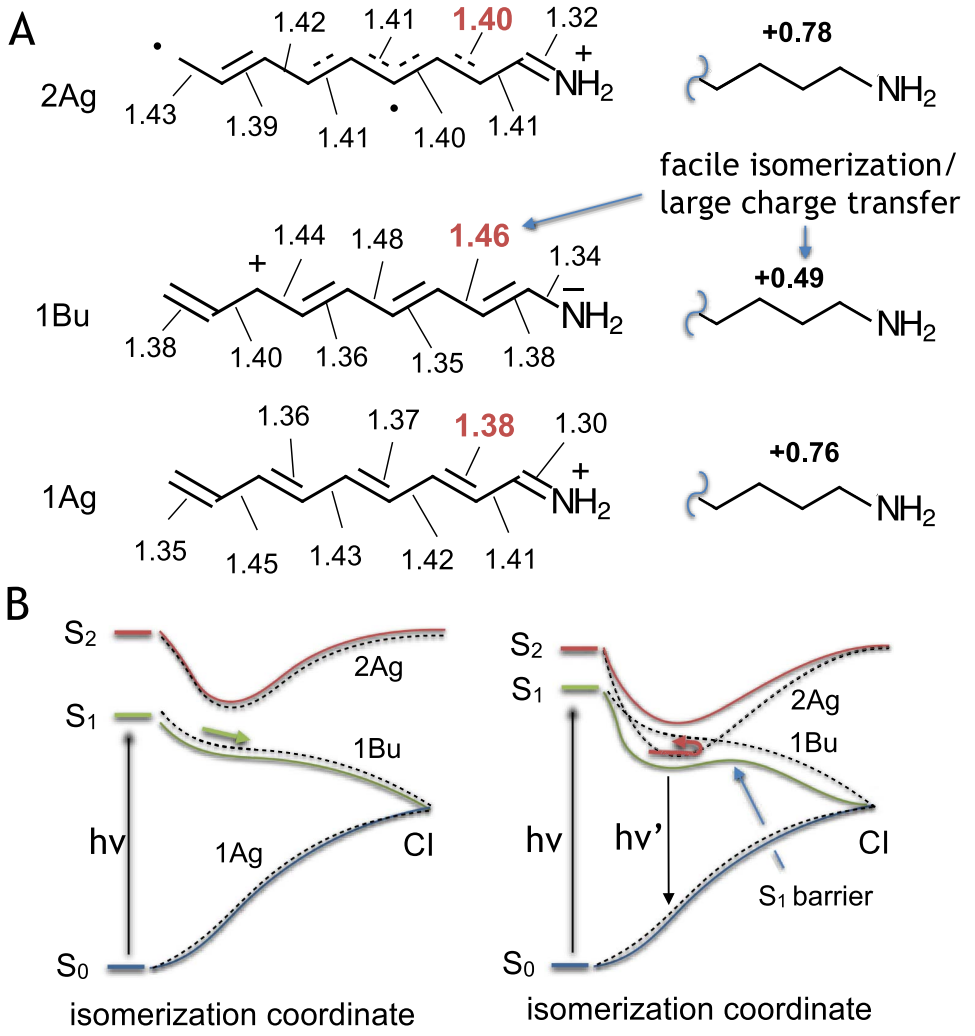

Figure 1. Schematic representation of (A) the charge transfer character and bond length alternation (BLA) of the most relevant electronic states S_0, S_1 and S_2 of rPSB in Franck–Condon geometry, and (B) two extreme cases of weak and strong mixing of the ^1B_u and ^2A_g character of the first two excited states, presented together with S_0 as a function of an effective isomerization coordinate, limited to the first 90° rotation of the reactive double bond (see also Figure 11). Note the conical intersection (CI) between S_1 and S_0. Refer to Section 2 for a more detailed discussion.

pulse at 800 nm promotes the molecules further to S_3. This additional excess energy stored in the molecule leads to enhanced photo-fragmentation, as compared to the pump pulse-only case. Due to the limited ESL, the fragmentation enhancement is dependent on τ, and the delay-dependent signal measures the time-dependent fraction of excited molecules. A series of comparative experiments, including the effect of temperature concluded that, *in vacuo*, 11C rPSB has an almost barrierless fast decay (≈0.4 ps at room temperature), while AT shows a barrier-controlled >3 ps decay.

Hence, both solution and gas phase experiments suggest, that in visual rhodopsin the ESL is inherited from the "intrinsic" properties of the 11C chromophore [15, 45], whereas in bacterial

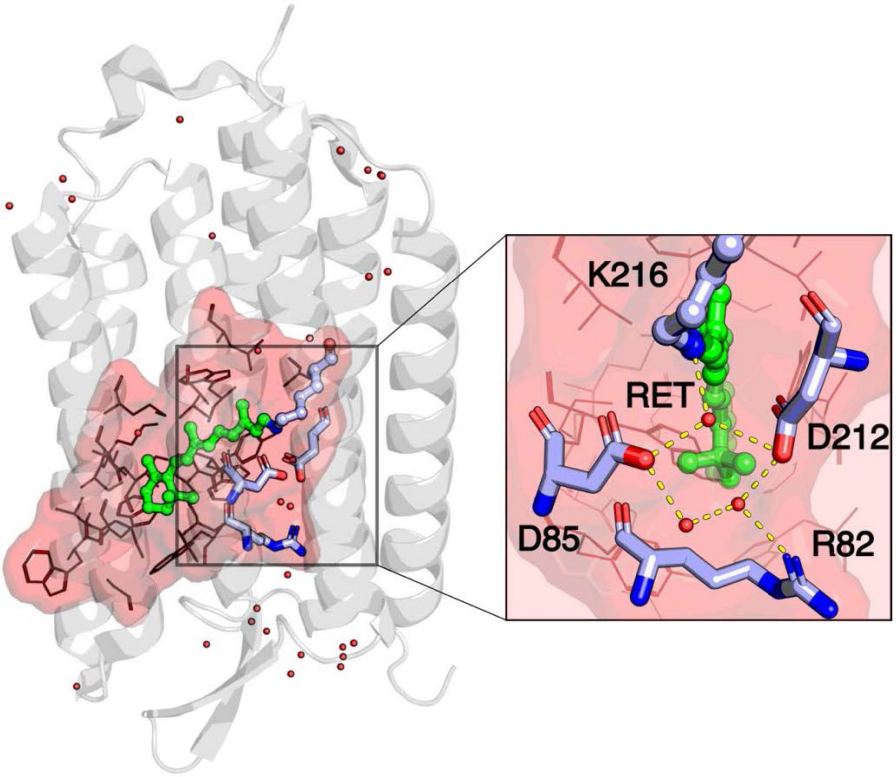

Figure 2. Crystallographic structure of bR (pdb entry 5ZIL), at pH = 7, highlighting the retinal chromophore RET (green), covalently bound to Lys216 (blue). The protonated Schiff base linking Lys216 and RET, is connected to the counter ion, the deprotonated aspartic acid D85, via a water molecule. Right: the zoom shows the H-bonding network involving three waters and key residues. Their effects on bR's ESL and IQY was studied by femtosecond spectroscopy (see text).

rhodopsins, the protein tunes the excited state potential energy surfaces (PES) of AT in terms of barrier height and bond selectivity [15, 44]. The origin of these environment-induced modifications of the PES will be discussed in detail in Section 2, on the basis of computational results involving mixing of the first two excited states. While such modelling allows rationalizing the effect of the protein environment on the ESL, the question about how the proteins tune the IQY of 11C and AT chromophores remains largely open. So far, only in the unique case of rhodopsin—showing the fastest photoisomerization reaction—a direct connection was established between the specific vibrational motions driven by the PES topography and the IQY, pointing to the central role of the relative phase between a few essential vibrational modes at the moment of decay at the CInt [23].

1.2. *Effects of mutations and pH on excited state dynamics of retinal proteins: a selection*

The most studied microbial rhodopsin is bR, a light-activated proton pump, found in *Halobacterium salinarum* [48]. In its light-adapted form, it binds the rPSB primarily in the AT form. In wild-type bR, AT → 13C photo-isomerization occurs within ≈0.5 ps [49–52], and with a quantum yield of ≈65% [53–55]. As shown in Figure 2, the crystallographic structure, at pH = 7, identifies

the deprotonated aspartic acid D85 as the main counter ion of the rPSB connected via a H-bond network with D212 and R82 via three water molecules [28]. First experimental work by El-Sayed and Lanyi [56,57] reported that the replacement of charged residues in the mutants D85N, D212N and R82Q by neutral ones increases the excited state lifetime and thus isomerization time by a factor of 5–20. Replacements of uncharged residues in mutants D115N or Y185F did not change the lifetimes significantly. The exact analysis was complicated by the fact that mutations, much like acidification [58], induce a mixture of AT and 13C isomers in the ground state. The observations were explained by a valence bond resonance model describing the excited state as a linear combination of wavefunctions, the electronic densities of which have the positive charge translocated from the Schiff base to different C atoms with odd numbers along the polyene chain. This provokes for every ground state double bond a reactive single bond character in the excited state, but depending on the fraction of local positive charge. Due to the nearby negatively charged D85 and D212, the positive charge is stabilised best on C13 in the excited state of wild-type bR, providing an intuitive explanation of the bond selectivity of the AT → 13C isomerization process. The excited state single bond character of C13=C14 allows then for a barrierless and therefore ultrafast isomerization. These effects are absent when D85 and D212 are replaced by neutral residues or if they are protonated (neutral) as in R82Q at pH = 4 [56]. The results for D85N were later confirmed and complemented by femtosecond photon echo spectroscopy, which provided evidence for a large sub-100 fs dielectric relaxation of the protein environment [59].

Another more recent example for large effects on ESL and IQY related to the chromophore environment, was recently reported for KR2, from *Krokinobacter eikastus*. In 2013, it was discovered as the first light-activated Na^+ pump [60]. Its crystallographic structure was resolved [61,62], highlighting particular motifs responsible for Na^+ binding at the protein periphery, and most importantly a transient Na+ binding site, in the vicinity of the rPSB, made up of D116, N112 and D251, and, with respect to bR, a modified H-bonding network. Comparing the crystal structures at neutral and acidic pH allowed to identify the flipping of the retinal counterion, the aspartic acid D116, as a key element for Na^+ pumping. At neutral pH, D116 is H-bonded with retinal's Schiff base (rotamer 1), but during the M intermediate of KR2's photocycle, protonation of D116 via the Schiff base (SB) occurs. This would lead to its re-orientation (rotamer 2) and disruption of the otherwise strong H-bonding network, thus enabling Na^+ translocation [61]. The overall structural changes associated with Na^+ pumping were very recently analyzed by time-resolved serial X-ray crystallography and QM/MM simulations, covering the pico- to milli-second time scales [63]. However, the changes in the SB-D116 distance were observed to be much smaller than expected, and no clear evidence for the existence of two rotameric states was found in the photocycle at pH = 8.0.

Regarding ultrafast events, Hontani *et al.* reported a spectroscopic investigation of the full photo-cycle, and in particular the primary AT → 13C isomerization to occur in KR2 within ≈200 fs, at pH = 8.0 [64]. This is significantly faster than for other microbial rhodopsins bearing AT rPSB in the ground state and was attributed to steric effects, i.e. distorsion of the AT isomer [65]. Tahara *et al.* investigated the effect of pH on the primary photo-reaction by femtosecond transient absorption spectroscopy (TAS) [66], with the main objective of obtaining new insights into minority excited state species with >3 ps lifetimes observed at pH = 8.0 [65]. Protonation of D116 occurs for pH < 7, and leads to a significant red-shift of the absorption spectrum [60], due to destabilization of the protonated SB ground state (S_0). KR2 at pH < 7 and the D116N mutant show several ps excited state decay components, in addition to the 0.18 ps ESL, whose amplitudes increase for lower pH values. The opposite is observed for pH > 7. A good correlation with the pH-dependent IQY showed that only the 0.18 ps decay channel is productive in terms of isomerization. A more detailed analysis of the data suggests that, rather than the protonation state of D116N, the key parameter favoring the fast and efficient excited state pathway is the

orientation of that residue and its fraction of population able to form H-bonds with retinal's Schiff base [66]. While a similar co-existence of multiple excited state decay components was previously attributed to reactive and non-reactive excited state pathways [21, 44, 56, 67, 68], this study points to the central role of structural inhomogeneities in the *ground state*, modulated by the protonation of D116N. Similar conclusions were recently drawn by the same authors for the photo-isomerization reactivity in proteorhodopsin [69]. In conclusion, KR2 appears to be a particular retinal protein, affording a flexible and thus disordered Schiff base environment, required for the binding of Na^+, but at the cost of a relatively low isomerization IQY. Nevertheless, intensive research is under way to use KR2 as a platform for genetic modifications in view of applications in optogenetics [3, 24, 70, 71].

Last but not least, it is worth noting that the protein environment should not be considered as a rigid grid of point charges. In addition to ultrafast nuclear motion of the surrounding residues and their related charges [72, 73], several experiments performed on bR point to a dynamic electronic response, upon excitation of rPSB, in particular for the polarisable nearby Trp residues, such as Trp86 [74–76]. From a computational point of view, these effects would require a quantum mechanical treatment of the large "rPSB/polarizable residue" system [73] and are out of the scope of the present review.

2. Theoretical framework: potential energy surfaces and CInt

Since the rPSB is a special case of a linear polyene chain, the role of possible interactions of the first and second excited states (S_1 and S_2) has been frequently evoked and examined in the past [5, 77–82]. Adopting the symmetry nomenclature of polyenes, the electronic ground state is referred to ^1A_g, and the first excited states to ^1B_u and ^2A_g symmetry (cf. Figure 1), even though the chromophore is asymmetric due to the positive charge on the Schiff base end. Hence, at the FC point (i.e., at the S_0 equilibrium structure), S_0 has ^1A_g covalent character with alternating single/double bond lengths, and a positive charge located on the $C{=}NH_2$ framework end. With respect to the ground state, the ^1B_u state can be described by a bonding π to an anti-bonding π^* electronic transition, delocalized all over the retinal backbone. Such a modification triggers a substantial structural change, characterized by single and double bond inversion (cf. Figure 1), hence the bond length alternation (BLA, defined as the average single bond length—average double bond length) changes sign. Negative BLA is necessary for the isomerization to occur, i.e. ^1B_u is the *reactive* configuration. In addition, the state has a pronounced charge-transfer (CT) character, which implies that the positive charge on the $C{=}NH_2$ framework end is reduced and translocated to the polyene backbone. By contrast, the S_2 PES has ^2A_g diradical (DIR) character with a strongly reduced BLA. Compared to ^1B_u, isomerization is hindered, and the state has *non-reactive* character. Last, similar to ^1A_g, the positive charge remains located on the $C{=}NH_2$ Schiff base end [83]. The different charge distributions in these three states lead to a situation where their energy differences, $\Delta E(S_1{-}S_0)$ and $\Delta E(S_2{-}S_1)$, are very sensitive to electrostatic interactions and thus to static or dynamic modifications of the environment (see below).

From recent quantum chemical computations, it is now well recognized that the energies of the ^1B_u and ^2A_g states are strongly dependent on the isomerization coordinate, hydrogen-out-of-plane motion and C=C dihedral angles, and that they may even come into degeneracy [84–88]. In such extreme cases, the $^1B_u/^2A_g$ mixing is complete, and the system oscillates in S_1 between the CT and DIR character, with a frequency determined by BLA. Such a regime was very recently reported to occur in bR, during the first 100 fs after excitation and only if the laser pulse was tuned to shorter wavelengths in order to explore higher vibronic states in S_1 [87].

In recent years, several papers reported on QM/MM calculations, which addressed the dynamic $^1B_u/^2A_g$ coupling along the reaction coordinate, in more general cases. Blending

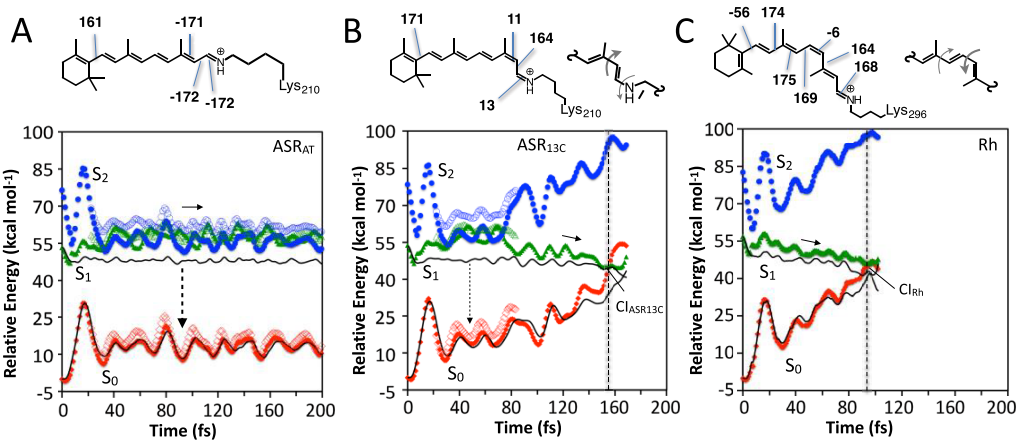

Figure 3. QM/MM trajectories of AT/ASR (A), 13C/ASR (B), and 11C/Rho (C). S_0 (red), S_1 (green), and S_2 (blue) The main out-of-plane (deviation larger than ±5°) dihedral angles of the S_0 equilibrium structure of the rPSBs are given at the top, together with the bicycle pedal motion driving the isomerization on S_1 with reversed bond order. The vertical dashed arrow represents weak fluorescence. Labels ASR_{AT}, ASR_{13C} and Rh correspond, respectively, to AT/ASR, 13C/ASR and 11C/Rho in the text. Reproduced with permission from [86].

non-reactive ^2A_g character into the S_1 state, extends the excited state lifetime. It turns out that the strength of $^1B_u/^2A_g$ interaction depends critically on the GS geometry of the rPSB (e.g. 11-*cis* versus all-trans) and on the electrostatic properties of the environment, no matter if it is a solvent or the protein cavity. The then created excited state potential energy landscape may be fully reactive or present barriers (cf. Figure 1(B)), and is thereby determining the ESL and thus the FQY and isomerization reaction speed.

Since 13-*cis* rPSB in microbial protein environments have ESL close to the ones of 11-*cis* rhodopsin, and both types of chromophores are found to be non-planar, it was concluded that a pre-twist is synonymous of a displaced excited state potential [30, 89–91] (in particular along hydrogen-out-of-plane motion (HOOP), which display larger Raman activities, cf. Section 3). This would lead to a more effective acceleration of the excited state wavepacket along the reaction coordinate [81, 92]. Recent multi-configurational QM/MM simulations go a step further and rationalise the effect of the rPSB geometry on the excited state energy landscape computing the S_1 and S_2 energies of the full chromophore within CASSCF or CASPT2 approximations, and embedded in the respective natural protein environments (bovine rhodopsin for 11-*cis*—11C/Rho; ASR for 13-*cis* (13C) and all-trans (AT), AMBER force fields) [86].

Figure 3 shows the QM/MM trajectories for the three cases in the first 200 fs or until the S_1/S_0 CInt is reached. The computed energies are found to oscillate following the BLA. For 11C/Rho, S_1 and S_2 are separated at all times and they preserve their ^1B_u and ^2A_g character, respectively until the CInt is reached, i.e. the $^1B_u/^2A_g$ coupling is negligible (panel (C)). S_1 therefore preserves a strongly reactive CT character, and Figure 4 shows that bond length inversion is complete (BLA < 0) along the C5=C6–C7=C8–C9=C10–C11=C12 fragment of the chromophore. Both effects lead in the specific protein environment to a barrierless potential and a rapid down-hill progression reaching the CInt within less than 100 fs, in agreement with experiments [31, 93–96].

In 13C/ASR, after an initial BLA displacement, S_1 and S_2 are degenerate in the 40–80 fs time interval, and the dihedral angles, along the C_{13}=C_{14} and C_{15}=N axes, remain almost planar [86]. During the same period, Figure 4 shows that BLA is positive, i.e. S_1 is dominated by a non-reactive DIR character associated with a very limited charge transfer from the –C=N moiety.

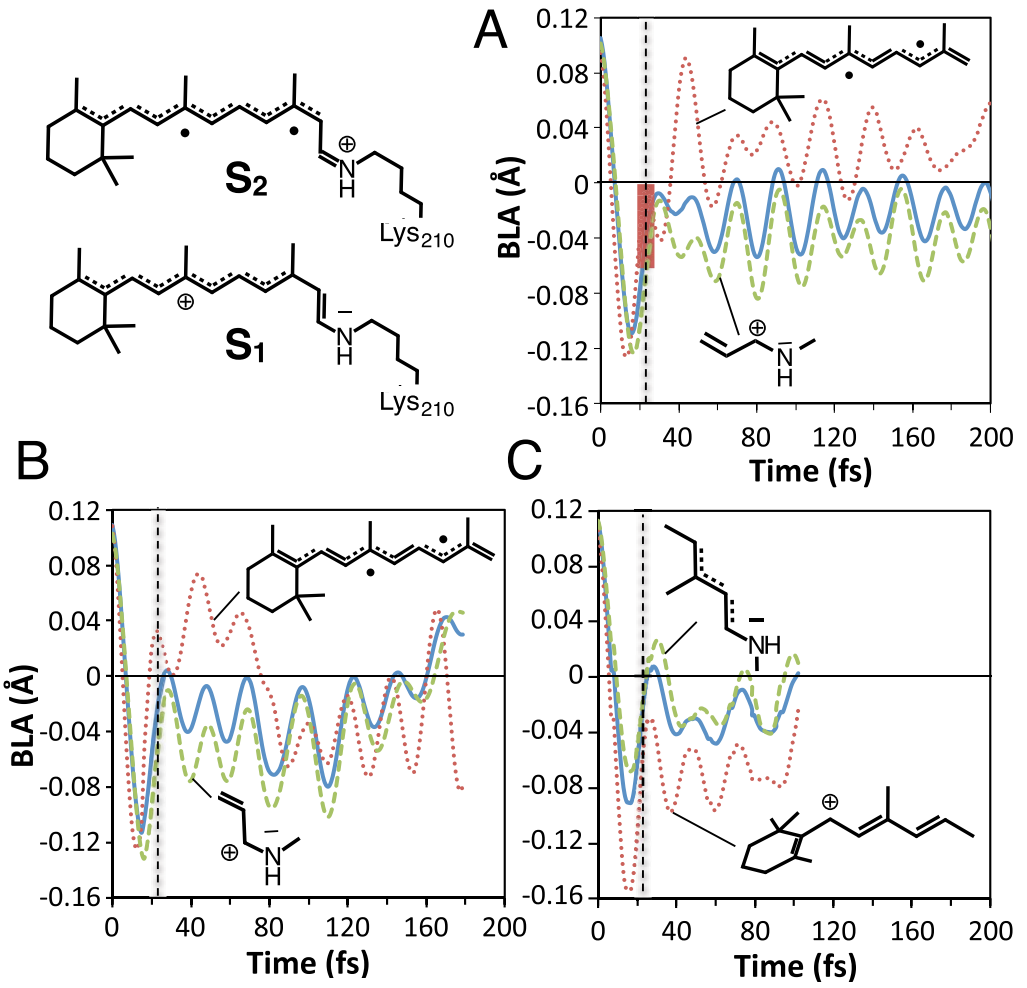

Figure 4. BLA changes in ASR and Rho. (A) BLA changes for the AT/ASR chromophore along the full conjugated chain (solid line), along the C5=C6–C7=C8–C9=C10–C11=C12–C13=C14 fragment (dotted line), and along the –C13=C14–C15=N fragment (dashed line). (B) Same data for the 13C/ASR chromophore. (C) The BLA along the full conjugated chain for the 11C/Rho (solid line), along the C5=C6–C7=C8–C9=C10–C11=C12 fragment (dotted line), and along the –C11=C12–C13=C14–C15=N fragment (dashed line). Reproduced with permission from [86].

Only after 80 fs, does S_1 display a negative BLA, a substantial charge transfer and a reactive ^1B_u character, with a down-hill progression towards the CInt by ≈150 fs, in agreement with experiments [19, 90, 97]. For AT/ASR, S_1 and S_2 are found to remain degenerate during the whole simulation interval of 200 fs (Figure 3). BLA is positive, meaning a non-reactive DIR character prevails (Figure 4(A)), explaining the longer ESL observed for AT than for the 13C rPSB in ASR [19, 90, 97].

The above empirical rule stating that the chromophore's isomeric state combined with protein-imposed deformations would control the ESL can now be explained rather intuitively, in terms of the dominant ^2A_g or ^1B_u character. In fact, AT/ASR maintains four conjugated double

bonds (C5=C6–C7=C8–C9=C10–C11=C12–) with a reduced, but still positive BLA, rather than bond length inversion (Figure 4(A)). Such a polyene-like pattern accommodates the non-reactive DIR electronic structure better than the CT structure. On the other hand, due to the pre-twisted β-ionone ring on one side and the rapidly twisting C11=C12 on the other, 11C/Rho offers a shorter fragment with two conjugated double bonds (C7=C8–C9=C10–C11) with a negative (inverted) average BLA value (Figure 4(C)). As a consequence, $\Delta E(S_2–S_1)$ will rapidly decrease towards a degeneracy along the photoisomerization coordinate in AT/ASR and 13C/ASR but not in Rho.

In subsequent publications, the concept of $^1B_u/^2A_g$ mixing was further investigated computationally for the environment-induced differences of 11-*cis* rPSB in methanol and in Rho [84], and for the effects of substitutions of the all-trans rPSB in solution with electron-donating or—withdrawing groups [84,88]. Experimental data, regarding the ESL [11,98], where consistently reproduced and explained in terms of the build-up of an excited state barrier or flat, population-stabilising regions due to an increased ^2A_g character in the S_1 state, limiting its reactivity. In summary, the concept, which emerges from these theoretical results, is that both steric and electrostatic effects act through the modifications of the S_1/S_2 energy landscape in determining the ESL of rPSB in different protein environments (exemplified in detail in Section 3), and also of rhodopsin-mimicking photo-switches in solution (Section 4).

3. Effects of point mutations: the case of Anabaena Sensory Rhodopsin

Anabaena Sensory Rhodopsin (ASR) is a membrane protein of 261 residues (26 kDa) found in the eubacterium *Anabaena* (Nostoc) sp. PCC7120 [99], and is part of the family of archeal microbial rhodopsin, as much as bR or sensory rhodopsin from *Halobacterium salinarum* [1, 100]. The main structural differences with respect to bR are the replacement of Asp212 in bR by Pro206, a non-polar residue, in the vicinity of the rPSB and a hydrogen-bonding network from Lys210 to Glu36 [101].

Regarding the ultrafast photo-isomerization, it is most notable that ASR bears a mixture of all-trans, 15-anti (AT) and 13-*cis*, 15-syn (13C) rPSB isomers, the relative content of which depends on the illumination, so-called "light-adaptation" conditions. When left in the dark, the dark-adapted (DA) form adopts 97% AT, which drops to less than 50% under illumination with orange light, at neutral pH [102]. In the context of obtaining insight into the mechanisms by which retinal proteins catalyze the rPSB photo-isomerization reaction, ASR is a model system allowing to study, within the same protein, the protein–rPSB interactions for two different rPSB conformers at the same time. Interestingly, at pH = 7, both isomers display markedly different excited state lifetimes (ESL): ≈0.7 ps for AT, and approx. 150 fs for 13C [19,90,97,103]. This was empirically related to the fact that 13C is twisted in the ground state conformation [101], but different electrostatic or dynamic interactions with the protein charge distribution may also play a role. The different excited state lifetimes were rationalized by quantum chemistry computations of the excited state potential energy surface (PES) along the minimum energy paths in ASR [22], and with excited state trajectory calculation [84, 86, 104]. As shown in Figure 3, it was found that the S_1 PES of 13C is barrierless, while that of the AT form displays a plateau or a slight barrier that could account for a short resting period of the excited state population. The precise origin of these different shapes of the S_1 PES for both isomers, and the mechanism of their fine-tuning by the protein interaction has motivated the research efforts described below. While Sections 3.1 and 3.2 summarize primarily experimental work on the electronic and vibrational dynamics of AT and 13C/ASR, as a function of mutations, Section 3.3 reviews a combined experimental/theoretical study of two cases of mutations which track the molecular origin of a 12-fold enhancement of the ESL.

3.1. *Effect of mutations on the ESL: rationalising spectral shifts and effects on excited state lifetimes*

Our first joint paper on mutation-induced effect in ASR, published in 2018, reported a combined experimental and computational study of the spectral shifts, the ground state vibrational spectra and isomerization reaction times of the AT and 13C isomers in the mutants L83Q, V112N and W76F [105].

3.1.1. *Effects of the modified protein electrostatics on the isomer-specific absorption spectra*

In L83Q and V112N, the nonpolar residues Valine and Leucine are replaced by the polar but neutral Glutamine (Q) and Asparagine (N), respectively, while the W76F mutation reduces the electron density and removes a small dipole close to the rPSB backbone (Figure 5). All mutations lead to blue-shifts of the DA and LA ground state absorption spectra with respect to wt-ASR [105]. Light-adaptation was carried out either with an orange (OA, 590 nm) or a blue (BA, 460 nm) LED, and the light-adaptation with the highest 13C isomer ratio was retained. The latter was higher than 50% in all cases, as for wt-ASR. V112N and W76F exhibit a blue-shift under LA as wt-ASR and many other mutants. The absorption spectrum of the 13C isomer of these mutants shifts by 2 nm (V112N) and 8 nm (W76F). L83Q, the blue-most shifted mutant, surprisingly shows the opposite effect, with the 13C isomer being 6 nm red-shifted with respect to AT.

From a purely computational structure of the mutated protein–chromophore complexes, obtained by the automatic retinal protein model (ARM) [106], the mutation-induced shifts were correctly reproduced, as well as the amount of LA-induced blue-shifts for W76F and V112N. For L83Q, ARM produced a wrong orientation of the dipoles of Q83, which was corrected "manually". This produced absorption maxima consistent with the observations, including the inverted LA effect. By comparing both the effects of steric and electrostatic modifications, it was concluded that the latter effects are dominant, in particular for W76F. Indeed, the mutation-induced changes of the rPSB configurations cause, with respect to the wt-ASR, rather a red-shift and not the experimentally observed blue-shifts. For both the V112N and W76F mutants, a change from Valine to Asparagine, near the β-ionone ring of the chromophore, and Tryptophan to Phenylalanine produces a destabilization of S_1 and a smaller stabilization of S_0. Hence, the observed blue-shift of the S_0–S_1 transition energy is a combined effect of S_1 up-shift and S_0 down-shift.

3.1.2. *Effects of the modified protein electrostatics on the reaction kinetics*

The excited state lifetimes and the isomerization reaction times were determined by broadband transient absorption spectroscopy in the 340–750 nm range, covering the characteristic bands of ground state bleach (GSB), excited state absorption (ESA) and stimulated emission (SE), as well the photo-product absorption in the J and K states of both AT and 13C isomers. The latter are obtained by the standard procedure subtracting the experimentally determined contribution of AT excited isomers, from the LA data. Values for ESL were extracted from ESA and SE decay times. For the AT isomers (DA), the ESA decay appeared to be bi-exponential, while it displayed mono-exponential decays for the small signal SE region probed (700–750 nm). When the SE is studied at longer wavelengths and maximum signal, all mutants display a multi-exponential excited state decay, as found for wt-ASR [90], and in agreement with the ESA decays (to be published). The fast component was found to be significantly reduced with respect to the 0.75 ps ESL of AT in wt-ASR, with L83Q showing an ESL as short as 120 fs. Whether the second slower component (in the 0.5–0.7 ps range, amplitude ≤30%) also leads to isomerization is difficult to ascertain since the rise of the photo-product (PPA) or J-state absorption naturally allows to unambiguously determine only the fastest component. A potential slower rise appears to be rather compensated by the signal decay to the J-to-K vibrational relaxation (Figure 6). We therefore quoted

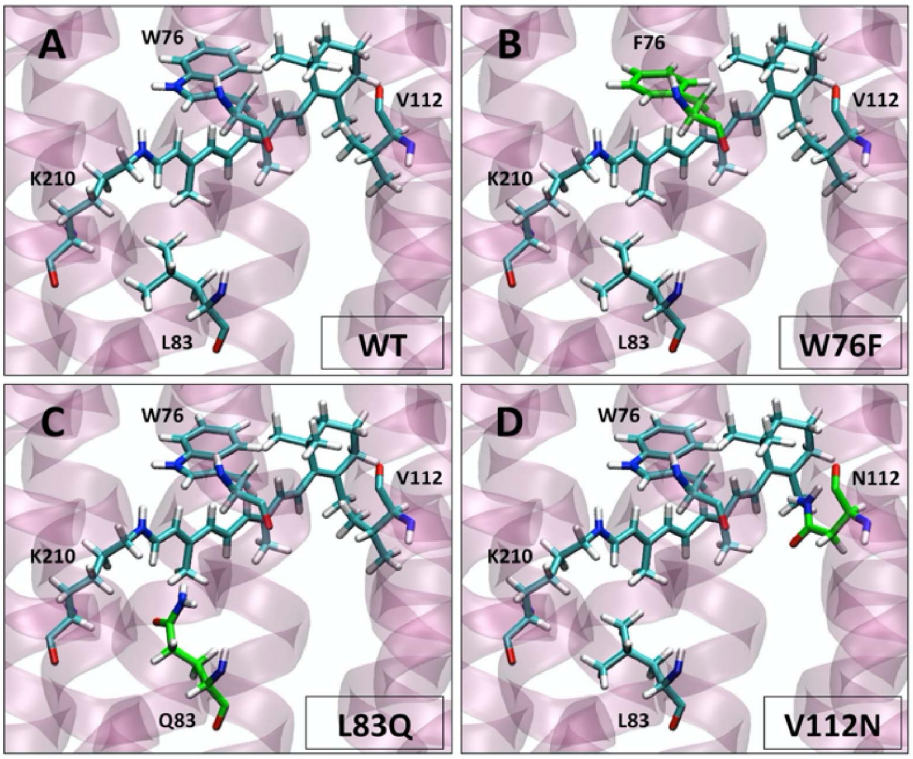

Figure 5. Calculated structures of the AT rPSB and the mutated residues L83, W76 and V112N in DA ASR (A). The replacement of Trp76 by a Phenylalanine reduces the electron density close to the AT rPSB backbone (B). Introduction of the polar Glu at position 83 and Asp at position 112 (C and D) changes the electrostatic interactions with rPSB in both S_0 and S_1.

the "isomerization reaction time" (IRT) extracted from a combined analysis of GSB, ESA, SE and PPA: L83Q—120 fs, V112N—230 fs and W76F 340 fs for the AT isomers. These values are presently reconsidered on the basis of the near-IR SE, which allow to determine ESL with higher accuracy (higher signal and zero background, Figure 6). Nevertheless, the initially reported incidental correlation is confirmed: the larger the spectral blue-shift of the GSA, the smaller the IRT.

For 13C, the mutations did not alter the IRT as much as for AT, but the values rather indicate the opposite trend: a small but significant increase of ESL and IRT. This an important result, which confirms the initial strategy of choosing ASR as a model system: the protein–chromophore interactions act differently, namely in an opposite fashion, on the two isomer conformations. The molecular basis for this observation is unclear and is the subject on ongoing work both computationally and experimentally. A central question is to figure out in as much LA changes the entire coupled protein–chromophore system in what we call the "13-*cis* isomer". i.e. both the chromophore and the protein likely undergo LA-induced structural changes.

3.2. *Details from femtosecond vibrational spectroscopy*

First vibrational spectra obtained by femtosecond non-resonant (pump-)DFWM were also reported in this paper [105] for the isomer ground states in DA and LA, as well as their photoisomerized K states (pump delay 100 ps). The procedure for extracting AT- and 13C-pure

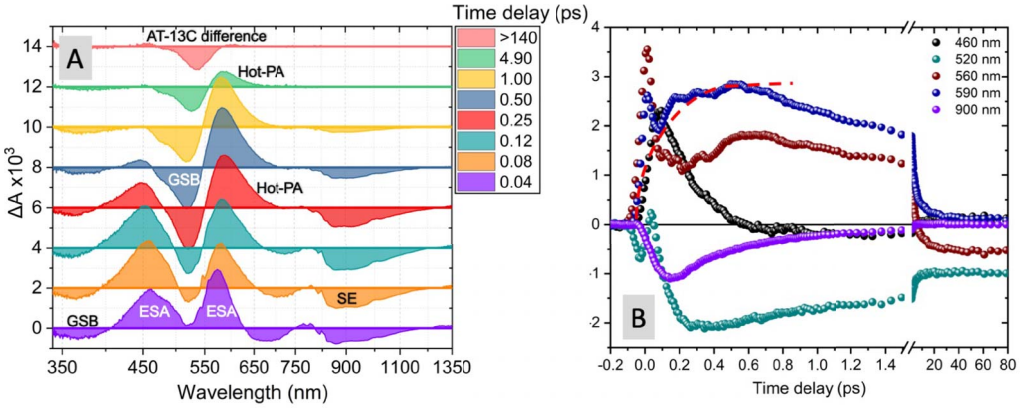

Figure 6. Transient absorption data for the ASR mutant L83Q in DA conditions (≈100% AT). (A) Combined UV–VIS and near-IR prob wavelengths, for the delay times indicated in the legend. Ground state bleach (GSB), excited state absorption (ESA), and stimulated emission (SE) highlight signal from S_1. In the 550–600 nm range ESA turns into "hot" ground state absorption by ≈200 fs. (B) Kinetics at selected wavelengths. The red dashed line is a guide to the eye with a 200 fs rise time for the "hot" ground state absorption.

vibrational spectra was explained in detail, and exploited more thoroughly in a subsequent publication [91], summarised and discussed in the following.

The vibrational spectra of both AT and 13C isomers in ASR both in the ground and excited states were analysed in detail [91]. The experimental techniques used rely on degenerate four-wave-mixing (DFWM) and impulsive vibrational spectroscopy (IVS), which can be performed also in the excited state, due to the action of an actinic pump pulse as a function of delay time [107–110].

The ground state vibrational spectra of both DA and LA forms of ASR were obtained by non-resonant DFWM and IVS, and compared to traditional spontaneous Raman spectra. Non-resonant schemes used a spectrally broad sub-15fs pulse centered at 650–660 nm, and revealed very different resonances in the high-frequency range above 1000 cm^{-1} and, most importantly, a much stronger Raman activity for 13C in the hydrogen-out-of-plane (HOOP) region around 800–900 cm^{-1}. All these observations are in-line with the differences between AT and cis rPSB conformations in other retinal proteins, like bR or channel-rhodopsin. Supported by MD simulations on the ground state, it was suggested that the larger distortion hinted on by the HOOP activity is located at the C14–C15 bond, rather than on the reactive C13=C14 bond, in agreement with X-ray data of ASR [101]. As for 11-*cis* rPSB in Rho, this pre-twist of the 13C chromophore, as opposed to the planar AT configuration, was identified as one of the reasons for the shorter ESL of 13C.

The structural changes in the excited state were followed by exciting each isomer with an actinic pump. The pure spectra of the excited state was obtained since the GS spectra of each isomer and the photo-products K_{AT} and K_{13C} could be measured separately [91]. In particular, the frequency of the C=C stretch and CH_3 rocking modes showed a transient blue-shift for both isomers, consistent with a reduced conjugation length, induced by the torsional motion. Indeed, in a 90° twisted conformation, the C14–C15–N and C5=C13 moieties are disconnected electronically. Most importantly the dynamics of the transient frequency shifts mirrors the excited state and reaction lifetimes qualitatively. The blue-shift occurs almost immediately upon excitation for 13C and decays with a half-time of 150 fs. The AT frequency shifts reach maximum only after 0.2 ps and adopt the K_{AT} values only by 0.6 ps. These studies also showed that the amplitude of these isomerization-induced changes in the CH_3 rock frequencies were different for AT as for

13C, which is taken as an indication that isomerization causes a larger rotation around the central C13=C14 bond for AT than for 13C, in agreement with previous FTIR results on the cryo-trapped K intermediates [102].

In addition, low frequency vibrations (<400 cm^{-1}), related to excited state modes, identified previously in transient absorption experiments [97], were shown to appear after a short induction time; shorter for 13C than for AT.

3.2.1. *Effects of mutations on the ground state vibrational spectra*

The mutants L83Q and V112N were studied by femtosecond DFWM and IVS in the DA and LA states [111], under exactly the same conditions as the ones used in the above TA experiments. It was found that mutations lead to an enhanced HOOP mode activity in the AT ground state of L83Q and V112N indicating a pre-distorsion of the chromophore either around the active C13=C14 bond or neighbouring C14–C15 bond of the ground state compared to the AT-isomer in the wt-ASR [111]. Additionally, the high frequency vibrations related to C–C single bond or C=C double bond stretch, as well as CH_3 rock modes change consistently with a reduced conjugation length, induced by the pre-distortion. In agreement with previous experimental and theoretical work, the pre-distortion is held responsible for the drastic reduction of the excited state lifetimes for the mutants, as compared to AT in wt-ASR. On the other hand, the mutations do not seem to enhance the pre-distortion already observed for the 13C isomer in wt-ASR, in agreement with a small increase of the ESL for 13C.

In summary, time-resolved vibrational spectroscopy, here accessed via degenerate FWM and IVS, provided new insights on structural changes during the isomerization process. For wild-type ASR and its mutants, the observations are perfectly in line with the theoretical predictions outlined in Section 2 (Figure 3), underlining here the role of a pre-twist in 13C/ASR for reducing the excited state barrier and leading to the shorter ESL.

3.3. *Towards a rational prediction of the excited state lifetime of AT rPSB in mutants*

While a detailed and comprehensive computational analysis of the mutation-induced effects on the excited state lifetimes of AT and 13C for the above mutants is still ongoing, we examined further mutations with the aim of achieving an ASR mutant with an increased excited state lifetime and thus FQY. This is of particular importance in the area of optogenetics, combined, if possible, with an increased absorption of the mutants in the red or near-IR region of the spectrum [24]. We recently reported an almost 10-fold increase of FQY in the ASR double mutant W76S/Y179F, and rationalised the observations within the context of the modified protein electrostatic environment, including the computational analysis of the excited state electronic structure and lifetimes of wt-ASR and the L83Q mutant [112]. The theoretical framework outlined in Section 2, is central to understanding the mutation-induced modifications of the $^1B_u/^2A_g$ mixing along the reaction coordinate, which, in this paper was traced down to the electrostatic interactions of the mutated residues.

The experiments were performed on the DA forms of wt-ASR and on the L83Q and W76S/Y179F mutants, together with two light-adapted forms of the latter. We focused on the mutation effects on the AT isomers, which accumulates to >95% in DA wt-ASR and L83Q, and is highest in orange-adapted form of W76S/Y179F (39%). While fluorescence of the non-canonical 7- and 9-*cis* isomers was minimised in the double mutant, by excitation with >520 nm light, contributions from 11- and 13-*cis* cannot be excluded. We found that the FQY was lowest for wt-ASR and increased by a factor of 2.2 for L83Q, and by 7.9 and 6.9 for orange- and green-adapted W76S/Y179F, respectively.

The mutation-induced shifts of the ground state absorption and steady-state emission spectra are reported and reproduced with high accuracy by the QM/MM method. The latter is

based on the ARM protocol [113], which employs the CASSCF method which is an ab initio (wavefunction-based) multi-configurational quantum chemical (MCQC) method coupled with the Amber molecular mechanics force field to obtain the S_0 QM/MM models of rhodopsins semi-automatically. Vertical excitation energies are then computed using multiconfigurational second-order perturbation theory (CASPT2) to account for the missing dynamic electron correlations. The level of agreement with the observed trends in absorption and fluorescence experiments indicate that the descriptions of the steric and electrostatic effects of the different protein environments on the S_0 and S_1 relaxed structure are trustful, and can be extended to describing the S_1 dynamics.

These were experimentally probed by measuring the decay of stimulated emission (SE) in the 850–1250 nm range, with ≈60 fs time resolution. The SE decays turned out to be almost wavelength-independent, and bi-phasic for all studied ASR variants. We thus compared the average values of ESL with the relative increase of FQY, and found that the FQY increases proportionally to ESL for W76S/Y179F with respect to wt-ASR, according to $FQY = ESL \times k_r$ with k_r the radiative rate, generally assumed to be constant. Interestingly, L83Q showed a 2.2-times larger FQY than wt-ASR, despite an almost 2-fold reduction of the ESL, indicating that L83Q has a higher radiative rate than the wild-type. This and the effects of the mutations on ESL were explained by calculations of the S_1 relaxation/reaction paths and by computing 200 fs semi-classical trajectories (Figure 7).

Indeed, relaxed scans of the S_0, S_1 and S_2 energies along the C12–C13=C14–C15 dihedral angle, computing minimised energies for fixed dihedral angles, indicate that the S_1 profile is barrierless for L83Q, while it is flatter and displays shallow barriers of ca. 3 and 6 kcal/mol for wt-ASR and the double mutant, respectively. The barriers have a maximum close to 120° torsion of the reactive C13=C12 double bond. The excited state lifetimes are best simulated by trajectories computing the time-dependent energies of the S_1 and S_2 states and their crossing with S_0 at a conical intersection (Figure 7). Here the kinetic energies in all vibrational modes of the chromophore are included, leading to different and time-dependent energy differences, in particular between S_1 and S_2. Only for L83Q do the computations predict an ultrafast S_1/S_0 crossing by ≈100 fs, consistent with the fastest 0.27 ps decay time observed in SE. On the other hand, Figure 7 shows that wt-ASR and W76S/Y179F do not reach the CI within the simulation time, consistent with the observed shortest decay times above 500 fs and with the computed S_1 barriers in the relaxed energy scans.

Interestingly, the mutations act through different mechanisms on the $^1B_u/^2A_g$ mixing. For L83Q, the reactive character of S_1 is induced through electrostatic interactions imposed by the protein environment, while in W76S/Y179F the stabilisation of emissive regions on S_1 is due to subtle changes of the chromophore structure. This was given evidence for by computing the S_1 energy profiles along the isomerization paths *in vacuo*, i.e. for the isolated rPSB taken with its protein geometry. Indeed, in the case of the L83Q chromophore structure, the energy profile appears to be very similar to the one detected for the rPSB in wt-ASR and W76S/Y179F protein environment, which would lead to a picosecond excited state lifetime and an enhanced emission. Since these are not observed, the short ESL in L83Q is a consequence of the protein environment. The computations indicate a reorientation of the π-conjugated chain along the reaction path in a way that enhances the interaction with the polar side chains of Q83. At the same time, the positive charge on the Schiff base end is further reduced upon increasing the C12–C13=C14–C15 dihedral angle (Figure 8). Both effects lead to an electrostatic stabilisation of S_1 along the reaction paths and thus to a barrierless progression on the S_1 PES.

On the other hand, the *in vacuo* analysis for wt-ASR and W76S/Y179F shows no qualitative changes in the energy profiles with respect to the respective protein environments. This indicates that the S_1 barrier is not induced but only marginally modulated by electrostatic interaction.

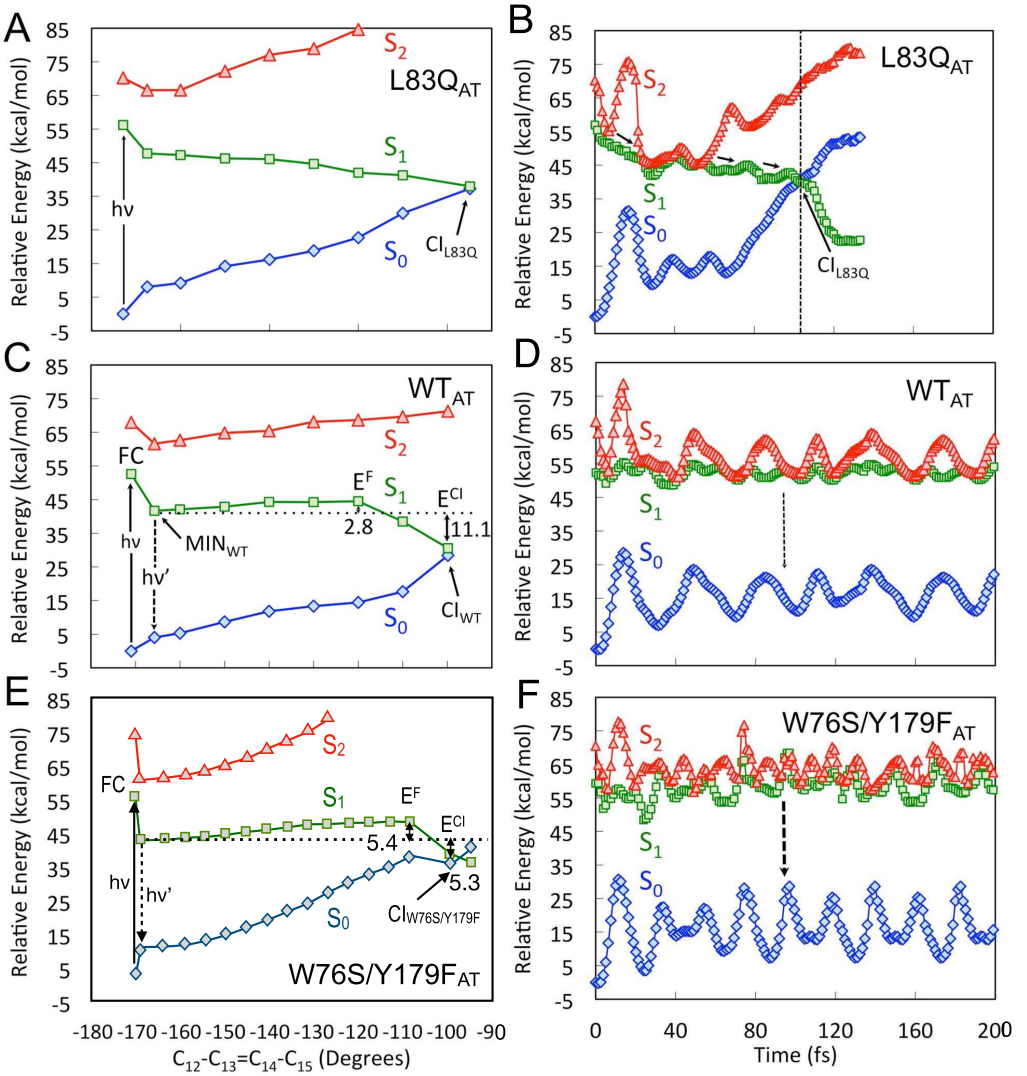

Figure 7. (A,C,E) CASPT2/CASSCF/AMBER energy profiles along the S_1 (green squares) isomerization path of L83Q, wt-ASR, and W76S/Y179F, respectively, computed in terms of a relaxed scan along the C12–C13=C14–C15 dihedral angle. Note the appearance of an excited state barrier for wt-ASR, and W76S/Y179F. Energy profiles of S_0 and S_2 are indicated by blue diamonds and red triangles, respectively. (B,D,F) Excited state QM/MM FC trajectories of L83Q, wt-ASR, and W76S/Y179F, computed at three-root state-averaged-CASSCF/AMBER level of theory and corrected at the CASPT2 level. S_0 (blue diamonds), S_1 (green squares), and S_2 (red triangles) CASPT2/CASSCF/AMBER energy profiles along the FC trajectories. The reaction path diagram in panel (E) is different from the corresponding panel in Ref. [112]. In fact, the presented path has been computed using a 3-root CASSCF level—rather than 2-root state average—to be consistent with the results presented in panels (A) and (C).

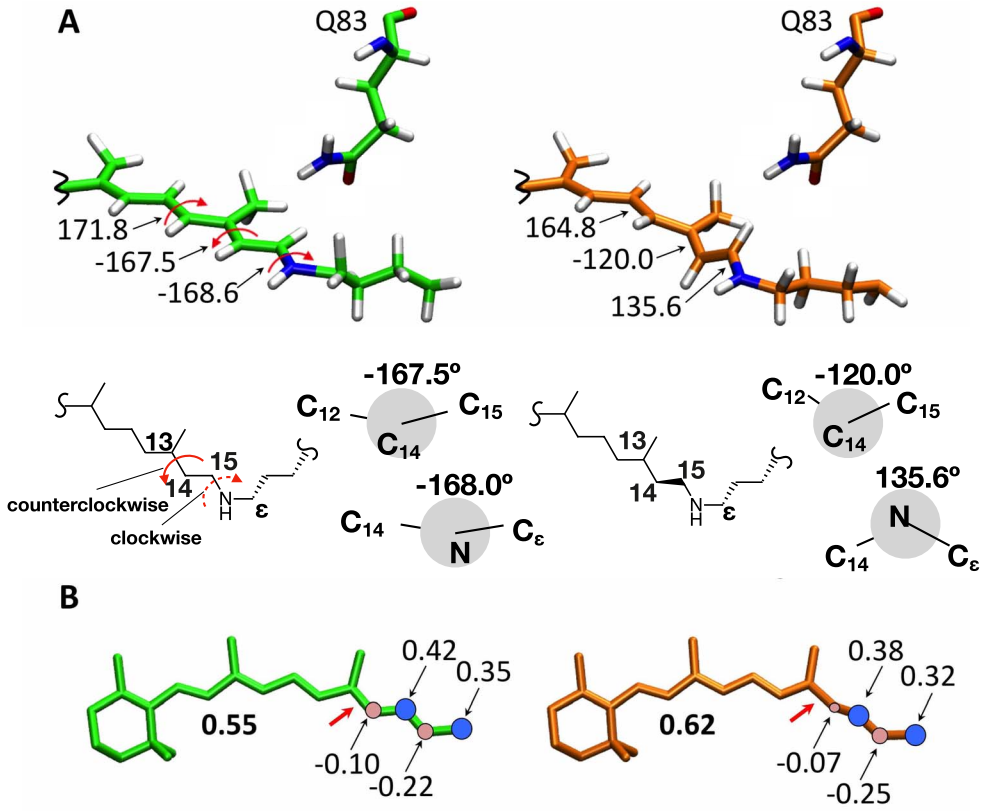

Figure 8. Evolution of the dihedral angles (A) and charges on the Schiff base end (B) along the isomerization path for L83Q. The C12–C13=C14–C15 dihedral angle is ≈−170° (left) and −120° (left). Adapted from Ref. [112].

Rather, it is an intrinsic feature of the rPSB conformation. The increased S_1 barrier in W76S/Y179F is due to subtle geometrical changes with respect to the rPSB geometry in wt-ASR. Indeed, the computations show that it is possible to transform the wt-ASR S_2, S_1, and S_0 energy profiles into W76S/Y179F-like energy profiles by simply changing the backbone dihedral angles along the wt-ASR reaction coordinate to the corresponding W76S/Y179F values. This is remarkable because those are limited changes that indicate the fluorescent tuning in rhodopsins might be achieved also through subtle geometrical (i.e. steric) effects.

In conclusion, this combined experimental and computational study outlines two pathways for a rational design of ASR mutants with enhanced ESL and FQY. It was shown that mutations can induce steric effects that induce a pronounced $^1B_u/^2A_g$ mixing, blending non-reactive character into S_1 through geometrical effects. Alternatively, it might be interesting to engineer the mutations such that the dynamic electrostatic interactions with the increasing CT character of the rPSB are of repulsive character so as to destabilise S_1 and maintain a significant $^1B_u/^2A_g$ mixing.

4. Retinal-inspired molecular switches: towards controlling photoreactivity by synthetic chemical design

An alternative, complementary strategy to decipher the tuning mechanism of the rPSB photoreactivity in rhodopsins has been to design a model chromophore that mimics—in solution—

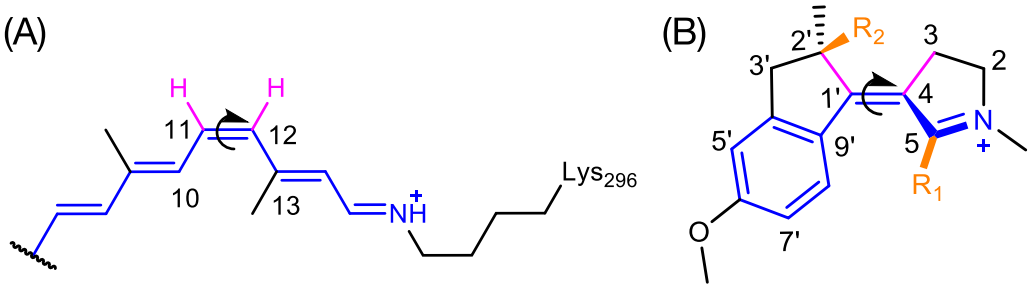

Figure 9. Chemical structure of (A) the 11-cis isomer of rPSB in Rho, and (B) the Z isomer of the IP compounds. Both IP and rPSB have a similar π-electron system (blue molecular backbones) with an S_1 state characterized by a bond length alternation and partial reduction of the protonated Schiff base through charge transfer along the carbon backbone. They also have an analogous photoreaction coordinate, which involves the torsion around the central C=C double bond (curved arrows) as well as out-of-plane motions of the purple bonds. Several IP compounds have been synthesized and studied theoretically and experimentally. They differ by the substitutions in orange: R1 = H or Me, R2 = H or Me.

the electronic structure, PES topologies and eventually photoreactivity of 11-*cis* rPSB in the visual pigment of Rhodospin (Rho) [114, 115]. In Rho, the photoisomerization is remarkably fast (<200 fs) and efficient (isomerization quantum yield, IQY = 67%) [93, 94]. Above all, this photoreaction is vibrationally coherent, a unique mechanism enabling to funnel the energy of the absorbed photon specifically into the isomerization coordinate on a time scale faster than vibrational dephasing, and held responsible for the enhanced IQY in Rho [23]. Revealing the chemical design principles underlying such an efficient light to mechanical energy transduction at the molecular scale would be of central interest in the prospect of designing efficient molecular switches and motors [116].

As discussed above in the case of ASR and due to the CT character of the S_1 state, a major parameter influencing the photophysical properties of rPSB is the protein electrostatic environment and the counterion neutralizing its positive charge [56, 117]. In the originally proposed N-alkylated IP compounds—which we name MeO-NAIP—the electron-donating MeO group on C6′ stabilizes the S_1 state by favoring its CT character, thus mimicking the stabilizing effect of the electrostatic protein environment in Rho [114]. Besides fine-tuning the S_1 CT character, another central ingredient of the biomimetic design is the intramolecular steric hindrance imposed by the two methyl groups on C2′ and the methyl group on C5. Altogether they impose the *Z* configuration of the MeO-NAIP to be the most stable S_0 isomer, in a non-planar—pre-twisted—geometry. Recently, we revealed the effect of the Me substituent on C5 on the IP photoreactivity by investigating the "demethylated" MeO-NAIP compound, named dMe-MeO-NAIP, which features no methyl on C5 (R1 = H in Figure 9). As we will illustrate below, we demonstrated that while the parent MeO-NAIP undergoes a vibrationally coherent photoreaction mimicking that of rPSB in Rho, this is not the case of dMe-MeO-NAIP. In a way similar to the case of rPSB in retinal proteins and mutants, we could conclude that this difference in photoreactivities observed within the two IP compounds is closely related to the S_1–S_2 energy gap and mixing, itself controlled by electrostatic and (intramolecular) steric properties.

UV–Vis or mid-IR transient absorption (TA) spectroscopy as well as femtosecond fluorescence spectroscopy were used to investigate the ultrafast photoisomerization reaction of a variety of IP compounds in solution [20, 115, 118–122]. While all compounds undergo a subpicosecond photoisomerization, they can be categorized within two photoisomerization

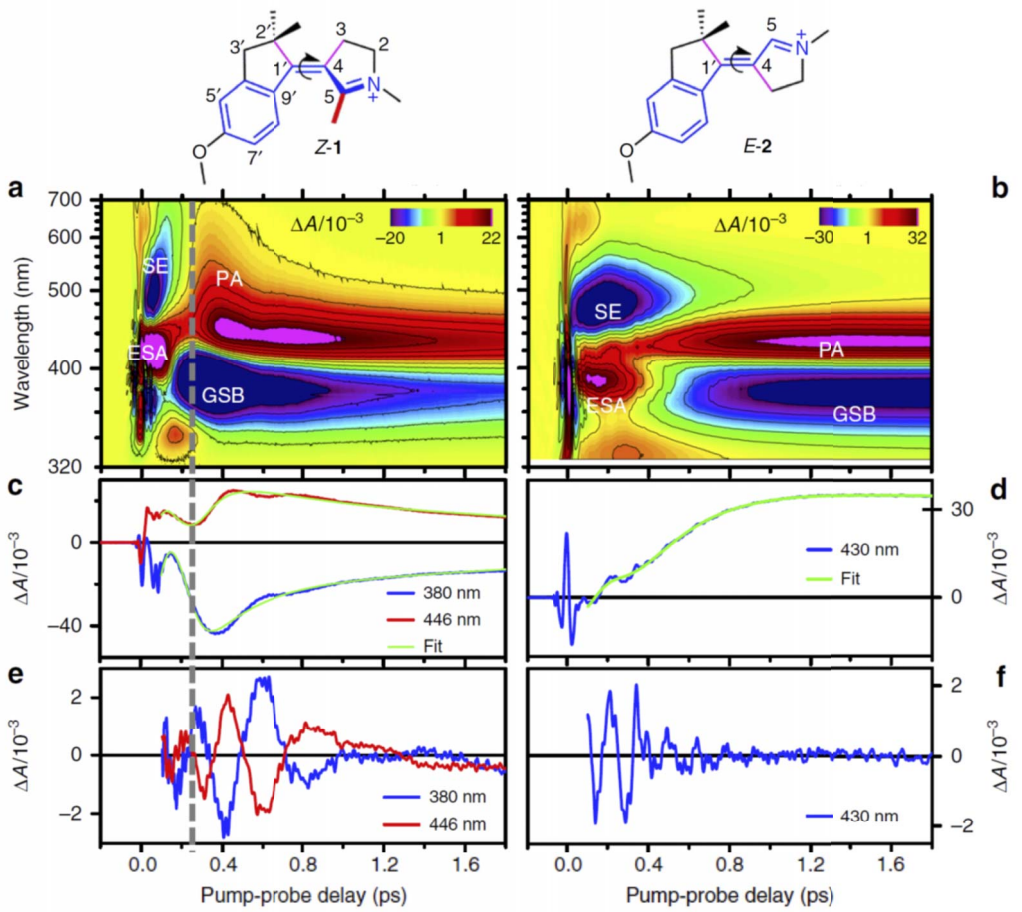

Figure 10. Transient absorption spectroscopy (TAS) of two representatives of the NAIP compounds family obtained with an 8-fs, 400-nm pump pulse. Compound Z-1 carries a methyl in C5 and its C=C double bond is pre-twisted in S_0. Its TAS signatures (a) are qualitatively different from those of the "demethylated", planar compound E-2 (b) where the methyl group on C5 is replaced by a H atom. (c,d) Selection of transient kinetics traces from the above datasets, and their fits. (e,f) The residuals of the fits are oscillatory signals revealing the vibrational dynamics accompanying the photoreaction. Abbreviations: GSB = ground state bleach; SE = stimulated emission; ESA = excited state absorption; PA = photoproduct absorption. Reproduced with permission from [118].

scenarios, corresponding to two qualitatively distinct spectroscopic signatures, as illustrated in Figure 10.

For the so-called "parent" NAIP compound [121] and its zwitterionic derivative [119], the excited state absorption (ESA) and stimulated emission (SE) from the S_1 population (Figure 10(a)) are very short-lived, they spectrally shift to the blue and to the red respectively, and they decay impulsively by 250 fs (vertical dashed line across Figure 10(a,c,e)). The ground state photoproduct absorption (PA) band immediately follows, which initially appears after the decay of the SE in the low-energy spectral range (600–700 nm), and rapidly blue shifts to ≈430 nm within ≈0.5 ps. Such dynamic spectral shifts of the S_1 and early S_0 bands have been interpreted as the signatures of

a population which evolves ballistically from the FC region to the photoproduct ground state through the CInt in the form of a vibrational wavepacket [119]. A very similar red-shifting SE impulsively followed by a blue shifting PA has been reported in Rhodopsin too and interpreted the same way [94]. Further evolution in the ground state is accompanied by a pronounced low-frequency oscillation (≈80 cm^{-1}, corresponding to ≈500 fs period, Figure 10(e)) interpreted as the signature of a vibrational wavepacket oscillating around the S_0 PES minimum along the C=C torsion coordinate [119, 121]. Importantly this vibrational wavepacket was demonstrated to be triggered by the S_1 reactive motion, meaning that this low-frequency vibrational coherence is preserved through the CInt and exponentially damped (with a ≈300 fs time constant) after the decay to S_0 [118].

Conversely, the "demethylated" NAIP compound, where C_5 carries an H atom in place of a methyl substituent, has a very similar ground state spectrum but qualitatively different TA signatures (see Figure 10(b,d,f)): the SE signature does not extent this far to the low-energy range, it is spectrally narrower and longer-lived. The SE and ESA bands decay in concert with the rise of the PA band which appears gradually at 430 nm, rather than impulsively in red part of the probing window. Hence there is no similar indication of a vibrationally coherent reactive motion that would impulsively drive the system through the CInt as discussed above. More precisely, upon light excitation with a very short (8 fs) pump pulse, a vibrationally coherent motion is detected in S_1 along (in particular 232 cm^{-1} mode, see Figure 10(f)). However, no vibrational coherence is transferred to the ground state, and in particular no vibrational activity is detected at 80 cm^{-1}.

To rationalize why these two compounds undergo such qualitatively different photoreactions, we first notice, that the most stable ground state isomer is *Z*, with a ≈15° pretwisted C=C bond, for the C5-methylated compound, but *E* in a planar conformation for the demethylated compound. These differences are controlled by the intramolecular steric hindrance introduced with the methyl substituent on C_5, which also affects the S_1 electronic structure and photoreactivity of the compounds, as rationalized by QM/MM modeling at the CASSCF/CASSPT2 level [118]. Indeed, in the planar compound, the S_1 and S_2 states are computed to be nearly degenerate, resulting in a flat S_1 PES, while in the pre-twisted compound the degeneracy is lifted and the S_1 PES slope is very steep. Consequently, in the latter case, the motion along the torsion coordinate is strongly accelerated which drives the system ballistically towards the CInt, such that the photoproduct formation occurs faster than vibrational decoherence of the 80 cm^{-1} mode, resulting in the pronounced oscillatory signal observed after the decay to S_0. In the former case, a more diffusive exploration of the S_1 PES potential would be responsible for an increased excited state lifetime and vibrational decoherence would be effective already by the time the system reaches the Cint and decays to S_0 (Figure 11).

By comparing the TA signatures and photoreaction scenarios for each isomer of half a dozen of NAIP derivatives [20], we observe that all compounds under investigation obey either the first or the second photoreaction scenario. Moreover, based on DFT modeling of the compounds S_0 equilibrium structures, we establish a perfect correlation between the C=C double pre-twist and the photoreaction scenario: all compounds featuring a significant (>10°) pre-twist obey the first photoreaction scenario, and all compounds featuring a more planar S_0 conformation (<10° pre-twist) obey the second one. This allows us to generalize the central role of the intramolecular steric effect and pre-twist at controlling the PES topography via the fine tuning of the S_1–S_2 state mixing in these retinal-inspired compounds. As reviewed in Sections 2 and 3, the same effect of a pre-twist of the chromophore is operative in 13C/ASR in reducing the excited state barrier [111].

A major outcome of our latest study [20], is that while the intramolecular steric hindrance and related S_1–S_2 state mixing controls the photoreaction dynamics, we observe no correlation between the IQY—in the range 15%–35% for all IP compounds investigated—and observables such as excited state life time, vibrational coherence, absorption wavelengths or degree of pre-twisting.

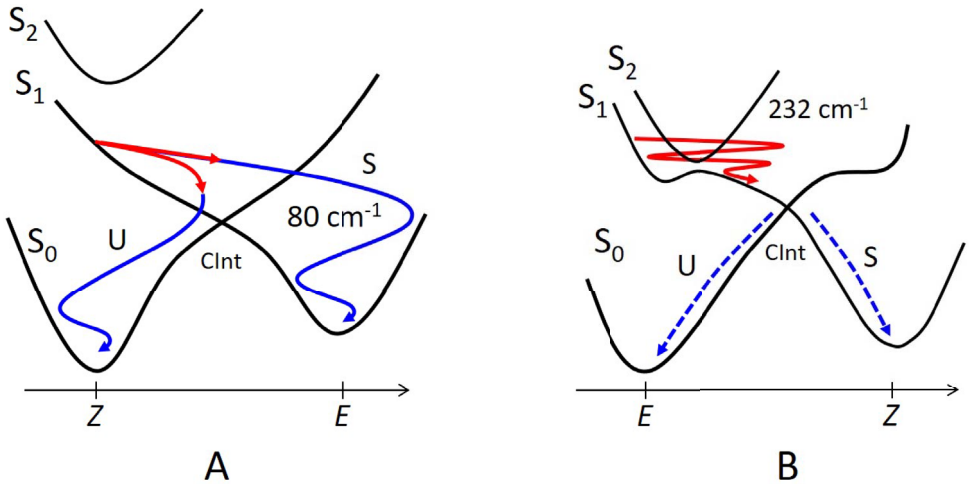

Figure 11. Schematic representations of the two distinct photoisomerization scenarios in the NAIP compounds. (A) The reactive motion of the pretwisted MeO-NAIP is governed by a steep S_1 PES driving the system ballistically towards the CInt. Upon impulsive decay to S_0, this S_1 motion coherently populates the S_0 vibrational motion along the torsion mode at 80 cm^{-1}. (B) Instead, for the planar demethylated compound, the S_1 and S_2 states are nearly degenerate, resulting in a flat PES providing a much weaker acceleration along the torsion mode, and a more diffusive motion towards the CInt. The crossing of S_1 and S_2 leads in fact to an avoided crossing. The corresponding loss of synchronization then explains the observed loss of ensemble coherence. Two decay channels ("U" = "unsuccessful", and "S" = "successful") are represented, with the evolutions on the S_1 or S_0 PES represented in red and blue, respectively. The 20–25% quantum yield indicates that channel U is dominating. Adapted from [118].

The molecular mechanism controlling the IQY in ultrafast C=C double bound isomerization thus remains an open question so far.

5. Summary and conclusions

In summary, for the sub-picosecond isomerization reactions of rPSB in a protein cavity and for the related bio-mimetic switches in solution, modifications of the ESL can be induced by steric effects (ground state pre-twist) and by changes in the electrostatic environment. The experimental and theoretical studies on the AT and 13C isomers ASR and its mutants have identified both effects, and how they are brought about by point mutations. For the photoswitches, steric [118] and electronic [20, 123] effects, brought about by substitutions of the NAIP framework were investigated experimentally. These studies showed, in addition to the change in ESL, a clear influence on the survival of vibrational coherences in the ground state. The computational framework shows that both steric and electrostatic parameters affect the excited state structure due to $^1B_u/^2A_g$ mixing, and how it determines the CT and reactive character in terms of BLA of the lowest excited state S_1. A central point is that the simulations allow to predict how this mixing changes dynamically when the chromophores evolve along the reaction coordinate. Shallow excited state barriers appear when S_1 alternates between a reactive CT and non-reactive DIR character, leading to longer ESL and higher FQY. The recent experimental observation of BLA-mediated $^1B_u/^2A_g$ oscillations demonstrates this effect clearly, within the first 100 fs of the excited state reaction in bR [87].

In order to obtain a more direct experimental insight, and a direct comparison with the simulations, measuring the time-dependent S_1–S_2 splitting would provide new insights for systems with reactive versus non-reactive excited state dynamics. The S_1–S_2 transition is expected to lie in the near- to mid-IR region (1000–8000 cm^{-1}) [84, 118], but the high time resolution required (<50 fs) makes the envisaged VIS-pump/IR-probe spectroscopy challenging.

Like mutation effects discussed in Section 3, pH is known to induce small shifts in the ASR absorption maximum wavelength [124]. A new computational protocol has been devised and successfully applied to determine the molecular origin of such a pH effect [125]. The next step, still ongoing, focuses on the pH effect on the ESL. Preliminary results point to a bi-exponential decay from S_1, modulated by its pH-dependent interaction with S_2. Further upcoming developments relate to computing the excited state vibrational spectra of the rPSB, in relation with the very informative femtosecond data [91, 111], and a possible inclusion of the dynamic polarisation of the nearest neighbour residues [15, 74, 75]. Unlike the here reported transient spectroscopies, ultrafast X-ray diffraction has the potential of revealing the detailed dynamic structural and electronic changes of the rPSB and its nearest environment, provided these experiments be carried out under single photon excitation conditions [63, 72, 73, 126].

Beyond the excited state lifetimes and vibrational coherences, another central property is the reaction quantum yield (IQY), for which we still have to understand and learn the lessons that the outstanding high values found in Rho and bR can teach us, when these are compared with the modest values obtained for the biomimetic switches in solution [20] or the low values (<2%) observed for the crowed alkenes designed as molecular rotary machine [26]. While it is generally accepted that the branching into forward and backward reaction takes place in the vicinity of the conical intersection [23], it remains to be rationalised how chemical substitutions and effects of the environment control the IQY. Femto- and attosecond photo-electron spectroscopy holds the promise to map out the wavepacket evolution across the CI in real time, and one of the main challenges for the next years will be to apply these emerging sophisticated tools for isolated chromophores in gas phase [127, 128] and solution [129].

Acknowledgements

The authors acknowledge financial support from the French-German ANR-DFG project “Femto-ASR”, (ANR-14-CE35-0015-01) and ANR support via grant no. ANR-11-JS04-010-01 “IPQCS”, and the “Investissement d’Avenir” program: Labex NIE ANR-11-LABX-0058_NIE, Labex CSC ANR-10-LABX-0026_CSC, Equipex UNION ANR-10-EQPX-52-01. Other funding came from the Université de Strasbourg for a USIAS Fellowship, from the “Alsace” region, the NSF grant no. CHE-1710191, and the Italian MIUR for grant PRIN 2015. MO acknowledges the Ohio Supercomputer Center, the Mésocentre of the Université de Strasbourg and CINECA for granted computer time. The Centre de Calcul Intensif d’Aix-Marseille is acknowledged for granting access to its high performance computing resources.

High quality samples for wild-type ASR and its mutants came from H. Kandori and K. Jung and their teams. The contributions of J. Brazard, A. Cheminal and O. Crégut are kindly acknowledged, as well as from S. Fusi, M. Paolino, L. Barneschi, E. Pieri, V. Ledentu and L. Pedraza González.

References

[1] O. P. Ernst, D. T. Lodowski, M. Elstner, P. Hegemann, L. S. Brown, H. Kandori, “Microbial and animal rhodopsins: structures, functions, and molecular mechanisms”, *Chem. Rev.* **114** (2014), p. 126-163.

[2] M. Kumauchi, T. G. Ebrey, “Visual pigments as photoreceptors”, in *Handbook of Photosensory Receptors*, John Wiley & Sons, Ltd, Hoboken (NJ), USA, 2005, p. 43-76.

[3] E. G. Govorunova, O. A. Sineshchekov, H. Li, J. L. Spudich, "Microbial rhodopsins: diversity, mechanisms, and optogenetic applications", *Annu. Rev. Biochem.* **86** (2017), p. 845-872.
[4] V. Bonačić-Koutecký, J. Köhler, J. Michl, "Prediction of structural and environmental effects on the S1-S0 energy gap and jump probability in double-bond cis—trans photoisomerization", *Chem. Phys. Lett.* **104** (1984), p. 440-443.
[5] A. Cembran, F. Bernardi, M. Olivucci, M. Garavelli, "The retinal chromophore/chloride ion pair: structure of the photo isomerization path and interplay of charge transfer and covalent states", *Proc. Natl Acad. Sci. USA* **102** (2005), p. 6255-6260.
[6] A. Wand, I. Gdor, J. Y. Zhu, M. Sheves, S. Ruhman, "Shedding new light on retinal protein photochemistry", *Annu. Rev. Phys. Chem.* **64** (2013), p. 437-458.
[7] R. Diller, "Primary reactions in retinal proteins", in *Biol. Med. Phys. Biomed. Eng.* (M. Braun, P. Gilch, W. Zinth, eds.), Springer, Berlin, Heidelberg, 2008, p. 243-273.
[8] H. Kandori, Y. Katsuta, M. Ito, H. Sasabe, "Femtosecond fluorescence study of the rhodopsin chromophore in solution", *J. Am. Chem. Soc.* **117** (1995), p. 2669-2670.
[9] P. Hamm, M. Zurek, T. Röschinger, H. Patzelt, D. Oesterhelt, W. Zinth, "Femtosecond spectroscopy of the photoisomerisation of the protonated Schiff base of all-trans retinal", *Chem. Phys. Lett.* **263** (1996), p. 613-621.
[10] G. Zgrablic, K. Voitchovsky, M. Kindermann, S. Haacke, M. Chergui, "Ultrafast excited state dynamics of the protonated Schiff base of all-trans retinal in solvents", *Biophys. J.* **88** (2005), p. 2779-2788.
[11] T. Sovdat, G. Bassolino, M. Liebel, C. Schnedermann, S. P. Fletcher, P. Kukura, "Backbone modification of retinal induces protein-like excited state dynamics in solution", *J. Am. Chem. Soc.* **134** (2012), p. 8318-8320.
[12] S. L. Logunov, L. Song, M. A. El-Sayed, "Excited-state dynamics of a protonated retinal Schiff base in solution", *J. Phys. Chem.* **100** (1996), p. 18586-18591.
[13] J. P. Kraack, T. Buckup, M. Motzkus, "Vibrational analysis of excited and ground electronic states of all-trans retinal protonated Schiff-base", *Phys. Chem. Chem. Phys.* **13** (2011), p. 21402-21410.
[14] J. P. Kraack, T. Buckup, M. Motzkus, "Coherent high-frequency vibrational dynamics in the excited electronic state of all-trans retinal derivatives", *J. Phys. Chem. Lett.* **4** (2013), p. 383-387.
[15] H. V. Kiefer, E. Gruber, J. Langeland, P. A. Kusochek, A. V. Bochenkova, L. H. Andersen, "Intrinsic photoisomerization dynamics of protonated Schiff-base retinal", *Nat. Commun.* **10** (2019), article no. 1210.
[16] M. Klessinger, "Conical intersections and the mechanism of singlet photoreactions", *Angew. Chem., Int. Ed. Engl.* **34** (1995), p. 549-551.
[17] B. G. Levine, T. J. Martínez, "Isomerization through conical intersections", *Annu. Rev. Phys. Chem.* **58** (2007), p. 613-634.
[18] T. Sovdat, G. Bassolino, M. Liebel, C. Schnedermann, S. P. Fletcher, P. Kukura, "Backbone modification of retinal induces protein-like excited state dynamics in solution", *J. Am. Chem. Soc.* **134** (2012), p. 8318-8320.
[19] A. Cheminal, J. Léonard, S.-Y. Kim, K.-H. Jung, H. Kandori, S. Haacke, "100 fs photo-isomerization with vibrational coherences but low quantum yield in Anabaena Sensory Rhodopsin", *Phys. Chem. Chem. Phys.* **17** (2015), p. 25429-25439.
[20] M. Gueye, M. Paolino, E. Gindensperger, S. Haacke, M. Olivucci, J. Léonard, "Vibrational coherence and quantum yield of retinal-chromophore-inspired molecular switches", *Faraday Discuss.* **221** (2020), p. 299-321.
[21] G. Zgrablić, A. M. Novello, F. Parmigiani, "Population branching in the conical intersection of the retinal chromophore revealed by multipulse ultrafast optical spectroscopy", *J. Am. Chem. Soc.* **134** (2012), p. 955-961.
[22] A. Valentini, D. Rivero, F. Zapata, C. García-Iriepa, M. Marazzi, R. Palmeiro, I. Fdez Galván, D. Sampedro, M. Olivucci, L. M. Frutos, "Optomechanical control of quantum yield in trans–cis ultrafast photoisomerization of a retinal chromophore model", *Angew. Chem., Int. Ed. Engl.* **56** (2017), p. 3842-3846.
[23] C. Schnedermann, X. Yang, M. Liebel, K. M. Spillane, J. Lugtenburg, I. Fernández, A. Valentini, I. Schapiro, M. Olivucci, P. Kukura, R. A. Mathies, "Evidence for a vibrational phase-dependent isotope effect on the photochemistry of vision", *Nat. Chem.* **10** (2018), p. 449-455.
[24] H. Kandori, "Retinal proteins: photochemistry and optogenetics", *Bull. Chem. Soc. Japan* **93** (2020), p. 76-85.
[25] D. Maclaurin, V. Venkatachalam, H. Lee, A. E. Cohen, "Mechanism of voltage-sensitive fluorescence in a microbial rhodopsin", *Proc. Natl Acad. Sci. USA* **110** (2013), p. 5939-5944.
[26] D. Roke, S. J. Wezenberg, B. L. Feringa, "Molecular rotary motors: unidirectional motion around double bonds", *Proc. Natl Acad. Sci. USA* **115** (2018), p. 9423-9431.
[27] T. Okada, M. Sugihara, A.-N. Bondar, M. Elstner, P. Entel, V. Buss, "The retinal conformation and its environment in Rhodopsin in light of a new 2.2 Å crystal structure", *J. Mol. Biol.* **342** (2004), p. 571-583.
[28] H. Luecke, B. Schobert, H.-T. Richter, J.-P. Cartailler, J. K. Lanyi, "Structure of bacteriorhodopsin at 1.55 Å resolution 1", *J. Mol. Biol.* **291** (1999), p. 899-911.
[29] R. Mathies, A. R. Oseroff, L. Stryer, "Rapid-flow resonance Raman spectroscopy of photolabile molecules: rhodopsin and isorhodopsin", *Proc. Natl Acad. Sci. USA* **73** (1976), p. 1-5.
[30] G. Eyring, B. Curry, A. Broek, J. Lugtenburg, R. Mathies, "Assignment and interpretation of hydrogen out-of-plane vibrations in the resonance Raman spectra of rhodopsin and bathorhodopsin", *Biochemistry* **21** (1982), p. 384-393.

[31] R. W. Schoenlein, L. A. Peteanu, R. A. Mathies, C. V. Shank, "The first step in vision: femtosecond isomerization of rhodopsin", *Science* **254** (1991), p. 412-415.
[32] J. E. Kim, R. A. Mathies, "Anti-stokes Raman study of vibrational cooling dynamics in the primary photochemistry of rhodopsin", *J. Phys. Chem.* **106** (2002), p. 8508-8515.
[33] Y. Hontani, M. Broser, M. Luck, J. Weißenborn, M. Kloz, P. Hegemann, J. T. M. Kennis, "Dual photoisomerization on distinct potential energy surfaces in a UV-absorbing rhodopsin", *J. Am. Chem. Soc.* **142** (2020), p. 11464-11473.
[34] G. I. Groma, A. Colonna, J. C. Lambry, J. W. Petrich, G. Váró, M. Joffre, M. H. Vos, J.-L. Martin, "Resonant optical rectification in bacteriorhodopsin", *Proc. Natl Acad. Sci. USA* **101** (2004), p. 7971-7975.
[35] R. Mathies, L. Stryer, "Retinal has a highly dipolar vertically excited singlet state: implications for vision", *Proc. Natl Acad. Sci. USA* **73** (1976), p. 2169-2173.
[36] H. Houjou, Y. Inoue, M. Sakurai, "Physical origin of the opsin shift of bacteriorhodopsin. Comprehensive analysis based on medium effect theory of absorption spectra", *J. Am. Chem. Soc.* **120** (1998), p. 4459-4470.
[37] R. Rajamani, J. Gao, "Combined QM/MM study of the opsin shift in bacteriorhodopsin", *J. Comput. Chem.* **23** (2002), p. 96-105.
[38] C. Punwong, J. Owens, T. J. Martínez, "Direct QM/MM excited-state dynamics of retinal protonated Schiff base in isolation and methanol solution", *J. Phys. Chem. B* **119** (2015), p. 704-714.
[39] M. Mališ, J. Novak, G. Zgrablić, F. Parmigiani, N. Došlić, "Mechanism of ultrafast non-reactive deactivation of the retinal chromophore in non-polar solvents", *Phys. Chem. Chem. Phys.* **19** (2017), p. 25970-25978.
[40] K. A. Freedman, R. S. Becker, "Comparative investigation of the photoisomerization of the protonated unprotonated n-butylamine Schiff bases of 9-cis-, 11-cis-, 13-cis-, and all-trans-retinals", *J. Am. Chem. Soc.* **108** (1986), p. 1245-1251.
[41] R. S. Becker, K. Freedman, "A comprehensive investigation of the mechanism and photophysics of isomerization of a protonated and unprotonated Schiff base of 11-cis-retinal", *J. Am. Chem. Soc.* **107** (1985), p. 1477-1485.
[42] Y. Koyama, K. Kubo, M. Komori, H. Yasuda, Y. Mukai, "Effect of protonation on the isomerization properties of n-butylamine Schiff base of isomeric retinal as revealed by direct HPLC analyses: selection of isomerization pathways by retinal proteins", *Photochem. Photobiol.* **54** (1991), p. 433-443.
[43] P. Hamm, M. Zurek, T. Röschinger, H. Patzelt, D. Oesterhelt, W. Zinth, "Femtosecond spectroscopy of the photoisomerization of the protonated Schiff base of all-trans retinal", *Chem. Phys. Lett.* **263** (1996), p. 613-621.
[44] G. Zgrablic, S. Haacke, M. Chergui, "Heterogeneity and relaxation dynamics of the photoexcited retinal Schiff base cation in solution", *J. Phys. Chem. B* **113** (2009), p. 4384-4393.
[45] G. Bassolino, T. Sovdat, A. Soares Duarte, J. M. Lim, C. Schnedermann, M. Liebel, B. Odell, T. D. W. Claridge, S. P. Fletcher, P. Kukura, "Barrierless photoisomerization of 11-cis retinal protonated Schiff base in solution", *J. Am. Chem. Soc.* **137** (2015), p. 12434-12437.
[46] L. Andersen, I. Nielsen, M. Kristensen, M. El Ghazaly, S. Haacke, M. Nielsen, M. Petersen, "Absorption of Schiff-base retinal chromophores in vacuo", *J. Am. Chem. Soc.* **127** (2005), p. 12347-12350.
[47] J. Langeland Knudsen, A. Kluge, A. V. Bochenkova, H. V. Kiefer, L. H. Andersen, "The UV-visible action-absorption spectrum of all- trans and 11-cis protonated Schiff base retinal in the gas phase", *Phys. Chem. Chem. Phys.* **20** (2018), p. 7190-7194.
[48] D. Oesterhelt, W. Stoeckenius, "Rhodopsin-like protein from the purple membrane of Halobacterium halobium", *Nature New Biol.* **233** (1971), p. 149-152.
[49] M. C. Nuss, W. Zinth, W. Kaiser, E. Kölling, D. Oesterhelt, "Femtosecond spectroscopy of the first events of the photochemical cycle in bacteriorhodopsin", *Chem. Phys. Lett.* **117** (1985), p. 1-7.
[50] H. J. Polland, M. A. Franz, W. Zinth, W. Kaiser, E. Kölling, D. Oesterhelt, "Early picosecond events in the photocycle of bacteriorhodopsin", *Biophys. J.* **49** (1986), p. 651-662.
[51] M. Du, G. R. Fleming, "Femtosecond time-resolved fluorescence spectroscopy of bacteriorhodopsin: direct observation of excited state dynamics in the primary step of the proton pump cycle", *Biophys. Chem.* **48** (1993), p. 101-111.
[52] J. Herbst, K. Heyne, R. Diller, "Femtosecond infrared spectroscopy of bacteriorhodopsin chromophore isomerization", *Science* **297** (2002), p. 822-825.
[53] J. Tittor, D. Oesterhelt, "The quantum yield of bacteriorhodopsin", *FEBS Lett.* **263** (1990), p. 269-273.
[54] R. Govindjee, S. P. Balashov, T. G. Ebrey, "Quantum efficiency of the photochemical cycle of bacteriorhodopsin", *Biophys. J.* **58** (1990), p. 597-608.
[55] G. Schneider, R. Diller, M. Stockburger, "Photochemical quantum yield of bacteriorhodopsin from resonance Raman scattering as a probe for photolysis", *Chem. Phys.* **131** (1989), p. 17-29.
[56] L. Song, M. A. El-Sayed, J. K. Lanyi, "Protein catalysis of the retinal subpicosecond photoisomerization in the primary process of bacteriorhodopsin photosynthesis", *Science* **261** (1993), p. 891-894.
[57] S. L. Logunov, M. A. ElSayed, L. Song, J. K. Lanyi, "Photoisomerization quantum yield apparent energy content of the K intermediate in the photocycles of bacteriorhodopsin, its mutants D85N, R82Q, and D212N, and deionized blue bacteriorhodopsin", *J. Phys. Chem.* **100** (1996), p. 2391-2398.

[58] T. Kobayashi, M. Terauchi, T. Kouyama, M. Yoshizawa, M. Taiji, "Femtosecond spectroscopy of acidified and neutral bacteriorhodopsin", in *Laser Applications in Life Sciences*, Proceedings, vol. 1403, SPIE, 1991, p. 407-416.
[59] J. T. M. Kennis, D. S. Larsen, K. Ohta, M. T. Facciotti, R. M. Glaeser, G. R. Fleming, "Ultrafast protein dynamics of bacteriorhodopsin probed by photon echo and transient absorption spectroscopy", *J. Phys. Chem. B* **106** (2002), p. 6067-6080.
[60] K. Inoue, H. Ono, R. Abe-Yoshizumi, S. Yoshizawa, H. Ito, K. Kogure, H. Kandori, "A light-driven sodium ion pump in marine bacteria", *Nat. Commun.* **4** (2013), article no. 1678.
[61] H. E. Kato, K. Inoue, R. Abe-Yoshizumi, Y. Kato, H. Ono, M. Konno, S. Hososhima, T. Ishizuka, M. R. Hoque, H. Kunitomo *et al.*, "Structural basis for Na^+ transport mechanism by a light-driven Na^+ pump", *Nature* **521** (2015), p. 48-53.
[62] I. Gushchin, V. Shevchenko, V. Polovinkin, V. Borshchevskiy, P. Buslaev, E. Bamberg, V. Gordeliy, "Structure of the light-driven sodium pump KR2 and its implications for optogenetics", *FEBS J.* **283** (2016), p. 1232-1238.
[63] P. Skopintsev, D. Ehrenberg, T. Weinert, D. James, R. K. Kar, P. J. M. Johnson, D. Ozerov *et al.*, "Femtosecond-to-millisecond structural changes in a light-driven sodium pump", *Nature* **583** (2020), p. 314-318.
[64] Y. Hontani, K. Inoue, M. Kloz, Y. Kato, H. Kandori, J. T. M. Kennis, "The photochemistry of sodium ion pump rhodopsin observed by watermarked femto- to submillisecond stimulated Raman spectroscopy", *Phys. Chem. Chem. Phys.* **18** (2016), p. 24729-24736.
[65] S. Tahara, S. Takeuchi, R. Abe-Yoshizumi, K. Inoue, H. Ohtani, H. Kandori, T. Tahara, "Ultrafast photoreaction dynamics of a light-driven sodium-ion-pumping retinal protein from *Krokinobacter eikastus* revealed by femtosecond time-resolved absorption spectroscopy", *J. Phys. Chem. Lett.* **6** (2015), p. 4481-4486.
[66] S. Tahara, S. Takeuchi, R. Abe-Yoshizumi, K. Inoue, H. Ohtani, H. Kandori, T. Tahara, "Origin of the reactive and nonreactive excited states in the primary reaction of rhodopsins: pH dependence of femtosecond absorption of light-driven sodium ion pump rhodopsin KR2", *J. Phys. Chem. B* **122** (2018), p. 4784-4792.
[67] M. O. Lenz, R. Huber, B. Schmidt, P. Gilch, R. Kalmbach, M. Engelhard, J. Wachtveitl, "First steps of retinal photoisomerization in proteorhodopsin", *Biophys. J.* **91** (2006), p. 255-262.
[68] T. Nakamura, S. Takeuchi, M. Shibata, M. Demura, H. Kandori, T. Tahara, "Ultrafast pump–probe study of the primary photoreaction process in pharaonis halorhodopsin: halide ion dependence and isomerization dynamics", *J. Phys. Chem. B* **112** (2008), p. 12795-12800.
[69] C.-F. Chang, H. Kuramochi, M. Singh, R. Abe-Yoshizumi, T. Tsukuda, H. Kandori, T. Tahara, "Acid–base equilibrium of the chromophore counterion results in distinct photoisomerization reactivity in the primary event of proteorhodopsin", *Phys. Chem. Chem. Phys.* **21** (2019), p. 25728-25734.
[70] M. Karasuyama, K. Inoue, R. Nakamura, H. Kandori, I. Takeuchi, "Understanding colour tuning rules and predicting absorption wavelengths of microbial rhodopsins by data-driven machine-learning approach", *Sci. Rep.* **8** (2018), article no. 15580.
[71] B. R. Rost, F. Schneider-Warme, D. Schmitz, P. Hegemann, "Optogenetic tools for subcellular applications in neuroscience", *Neuron* **96** (2017), p. 572-603.
[72] P. Nogly, T. Weinert, D. James, S. Carbajo, D. Ozerov, A. Furrer, D. Gashi, V. Borin, P. Skopintsev, K. Jaeger *et al.*, "Retinal isomerization in bacteriorhodopsin captured by a femtosecond x-ray laser", *Science* (2018), article no. eaat0094.
[73] G. Nass Kovacs, J.-P. Colletier, M. L. Grünbein, Y. Yang, T. Stensitzki, A. Batyuk, S. Carbajo, R. B. Doak *et al.*, "Three-dimensional view of ultrafast dynamics in photoexcited bacteriorhodopsin", *Nat. Commun.* **10** (2019), article no. 3177.
[74] S. Schenkl, F. van Mourik, G. van der Zwan, S. Haacke, M. Chergui, "Probing the ultrafast charge translocation of photoexcited retinal in bacteriorhodopsin", *Science* **309** (2005), p. 917-920.
[75] J. Léonard, E. Portuondo-Campa, A. Cannizzo, F. van Mourik, G. van der Zwan, J. Tittor, S. Haacke, M. Chergui, "Functional electric field changes in photoactivated proteins revealed by ultrafast Stark spectroscopy of the Trp residues", *Proc. Natl Acad. Sci. USA* **106** (2009), p. 7718-7723.
[76] S. Tahara, H. Kuramochi, S. Takeuchi, T. Tahara, "Protein dynamics preceding photoisomerization of the retinal chromophore in bacteriorhodopsin revealed by deep-UV femtosecond stimulated Raman spectroscopy", *J. Phys. Chem. Lett.* **10** (2019), p. 5422-5427.
[77] P. Tavan, K. Schulten, "Electronic excitations in finite and infinite polyenes", *Phys. Rev. B* **36** (1987), p. 4337-4358.
[78] K. C. Hasson, F. Gai, P. A. Anfinrud, "The photoisomerization of retinal in bacteriorhodopsin: experimental evidence for a three-state model", *Proc. Natl Acad. Sci. USA* **93** (1996), p. 15124-15129.
[79] A. Muñoz-Losa, M. E. Martín, I. Fdez Galván, M. L. Sánchez, M. A. Aguilar, "Solvent effects on the radiative and nonradiative decay of a model of the rhodopsin chromophore", *J. Chem. Theor. Comput.* **7** (2011), p. 4050-4059.
[80] R. González-Luque, M. Garavelli, F. Bernardi, M. Merchán, M. A. Robb, M. Olivucci, "Computational evidence in favor of a two-state, two-mode model of the retinal chromophore photoisomerization", *Proc. Natl Acad. Sci. USA* **97** (2000), p. 9379-9384.
[81] A. Cembran, R. González-Luque, L. Serrano-Andrés, M. Merchán, M. Garavelli, "About the intrinsic photochemical

properties of the 11-cis retinal chromophore: computational clues for a trap state and a lever effect in Rhodopsin catalysis", *Theor. Chem. Acc.* **118** (2007), p. 173-183.

[82] J. P. Kraack, T. Buckup, M. Motzkus, "Evidence for the two-state-two-mode model in retinal protonated Schiff-bases from pump degenerate four-wave-mixing experiments", *Phys. Chem. Chem. Phys.* **14** (2012), p. 13979-13988.

[83] S. Gozem, H. L. Luk, I. Schapiro, M. Olivucci, "Theory and simulation of the ultrafast double-bond isomerization of biological chromophores", *Chem. Rev.* **117** (2017), p. 13502-13565.

[84] M. Manathunga, X. Yang, Y. Orozco-Gonzalez, M. Olivucci, "Impact of electronic state mixing on the photoisomerization time scale of the retinal chromophore", *J. Phys. Chem. Lett.* **8** (2017), p. 5222-5227.

[85] M. Manathunga, X. Yang, M. Olivucci, "Electronic state mixing controls the photoreactivity of a rhodopsin with all-trans chromophore analogues", *J. Phys. Chem. Lett.* **9** (2018), p. 6350-6355.

[86] H. L. Luk, F. Melaccio, S. Rinaldi, S. Gozem, M. Olivucci, "Molecular bases for the selection of the chromophore of animal rhodopsins", *Proc. Natl Acad. Sci. USA* **112** (2015), p. 15297-15302.

[87] S. Gozem, P. J. M. Johnson, A. Halpin, H. L. Luk, T. Morizumi, V. I. Prokhorenko, O. P. Ernst, M. Olivucci, R. J. D. Miller, "Excited-state vibronic dynamics of bacteriorhodopsin from two-dimensional electronic photon echo spectroscopy and multiconfigurational quantum chemistry", *J. Phys. Chem. Lett.* (2020), p. 3889-3896.

[88] B. Demoulin, S. F. Altavilla, I. Rivalta, M. Garavelli, "Fine tuning of retinal photoinduced decay in solution", *J. Phys. Chem. Lett.* **8** (2017), p. 4407-4412.

[89] S. Smith, J. A. Pardoen, J. Lugtenburg, R. A. Mathies, "Vibrational analysis of the 13-cis-retinal chromophore in dark-adapted bacteriorhodopsin", *J. Phys. Chem.* **91** (1987), p. 804-819.

[90] A. Wand, B. Loevsky, N. Friedman, M. Sheves, S. Ruhman, "Probing ultrafast photochemistry of retinal proteins in the near-IR: bacteriorhodopsin and Anabaena Sensory Rhodopsin versus retinal protonated Schiff base in solution", *J. Phys. Chem. B* **117** (2013), p. 4670-4679.

[91] P. Pratim Roy, Y. Kato, R. Abe-Yoshizumi, E. Pieri, N. Ferré, H. Kandori, T. Buckup, "Mapping the ultrafast vibrational dynamics of all- trans and 13- cis retinal isomerization in Anabaena Sensory Rhodopsin", *Phys. Chem. Chem. Phys.* **20** (2018), p. 30159-30173.

[92] O. Weingart, I. Schapiro, V. Buss, "Photochemistry of visual pigment chromophore models by ab initio molecular dynamics", *J. Phys. Chem. B* **111** (2007), p. 3782-3788.

[93] Q. Wang, R. W. Schoenlein, L. A. Peteanu, R. A. Mathies, C. V. Shank, "Vibrationally coherent photochemistry in the femtosecond primary event of vision", *Science* **266** (1994), p. 422-424.

[94] D. Polli, P. Altoe, O. Weingart, K. M. Spillane, C. Manzoni, D. Brida, G. Tomasello, G. Orlandi, P. Kukura, R. A. Mathies, M. Garavelli, G. Cerullo, "Conical intersection dynamics of the primary photoisomerization event in vision", *Nature* **467** (2010), p. 440-443.

[95] P. J. Johnson, A. Halpin, T. Morizumi, V. I. Prokhorenko, O. P. Ernst, R. J. Miller, "Local vibrational coherences drive the primary photochemistry of vision", *Nat. Chem.* **7** (2015), p. 980-986.

[96] P. J. M. Johnson, M. H. Farag, A. Halpin, T. Morizumi, V. I. Prokhorenko, J. Knoester, T. L. C. Jansen, O. P. Ernst, R. J. D. Miller, "The primary photochemistry of vision occurs at the molecular speed limit", *J. Phys. Chem. B* **121** (2017), p. 4040-4047.

[97] A. Wand, R. Rozin, T. Eliash, K.-H. Jung, M. Sheves, S. Ruhman, "Asymmetric toggling of a natural photoswitch: ultrafast spectroscopy of Anabaena Sensory Rhodopsin", *J. Am. Chem. Soc.* **133** (2011), p. 20922-20932.

[98] G. Bassolino, T. Sovdat, M. Liebel, C. Schnedermann, B. Odell, T. D. W. Claridge, P. Kukura, S. P. Fletcher, "Synthetic control of retinal photochemistry and photophysics in solution", *J. Am. Chem. Soc.* **136** (2014), p. 2650-2658.

[99] K.-H. Jung, V. D. Trivedi, J. L. Spudich, "Demonstration of a sensory rhodopsin in eubacteria", *Mol. Microbiol.* **47** (2003), p. 1513-1522.

[100] A. Kawanabe, H. Kandori, "Photoreactions and structural changes of Anabaena Sensory Rhodopsin", *Sens. Basel.* **9** (2009), p. 9741-9804.

[101] L. Vogeley, O. A. Sineshchekov, V. D. Trivedi, J. Sasaki, J. L. Spudich, H. Luecke, "Anabaena sensory rhodopsin: a photochromic color sensor at 2.0 Å", *Science* **306** (2004), p. 1390-1393.

[102] A. Kawanabe, Y. Furutani, K.-H. Jung, H. Kandori, "FTIR study of the photoisomerization processes in the 13-*cis* and all-*trans* Forms of *Anabaena* sensory rhodopsin at 77 K", *Biochemistry* **45** (2006), p. 4362-4370.

[103] I. Schapiro, S. Ruhman, "Ultrafast photochemistry of anabaena sensory rhodopsin: experiment and theory", *Biochim. Biophys. Acta BBA - Bioenerg.* **1837** (2014), p. 589-597.

[104] A. Strambi, B. Durbeej, N. Ferré, M. Olivucci, "Anabaena sensory rhodopsin is a light-driven unidirectional rotor", *Proc. Natl Acad. Sci. USA* **107** (2010), p. 21322-21326.

[105] D. Agathangelou, Y. Orozco-Gonzalez, M. del Carmen Marin, P. P. Roy, J. Brazard, H. Kandori, K. H. Jung, J. Léonard, T. Buckup, N. Ferre, M. Olivucci, S. Haacke, "Effect of point mutations on the ultrafast photo-isomerization of anabaena sensory rhodopsin", *Faraday Discuss.* **207** (2018), p. 55-75.

[106] Y. Orozco-Gonzalez, M. Manathunga, M. del C Marin, D. Agathangelou, K.-H. Jung, F. Melaccio, N. Ferre, S. Haacke, K. Coutinho, S. Canuto, M. Olivucci, "An average solvent electrostatic configuration protocol for QM/MM free

energy optimization: implementation and application to rhodopsin systems", *J. Chem. Theory Comput.* **13** (2017), p. 6391-6404.

[107] J. Hauer, T. Buckup, M. Motzkus, "Pump-degenerate four wave mixing as a technique for analyzing structural and electronic evolution: multidimensional time-resolved dynamics near a conical intersection", *J. Phys. Chem. A* **111** (2007), p. 10517-10529.

[108] T. Buckup, J. Hauer, J. Mohring, M. Motzkus, "Multidimensional spectroscopy of beta-carotene: vibrational cooling in the excited state", *Arch. Biochem. Biophys.* **483** (2009), p. 219-223.

[109] T. Buckup, J. Léonard, "Multidimensional vibrational coherence spectroscopy", in *Multidimensional Time-Resolved Spectroscopy* (T. Buckup, J. Léonard, eds.), Springer International Publishing, Cham, 2019, p. 207-245.

[110] T. Buckup, M. Motzkus, "Multidimensional time-resolved spectroscopy of vibrational coherence in biopolyenes", *Annu. Rev. Phys. Chem.* **65** (2015), p. 39-57.

[111] P. P. Roy, R. Abe-Yoshizumi, H. Kandori, T. Buckup, "Point mutation of *Anabaena* Sensory Rhodopsin enhances ground-state hydrogen out-of-plane wag Raman activity", *J. Phys. Chem. Lett.* **10** (2019), p. 1012-1017.

[112] M. D. C. Marin, D. Agathangelou, Y. Orozco-Gonzalez, A. Valentini, Y. Kato, R. Abe-Yoshizumi, H. Kandori, A. Choi, K.-H. Jung, S. Haacke, M. Olivucci, "Fluorescence enhancement of a microbial rhodopsin via electronic reprogramming", *J. Am. Chem. Soc.* **141** (2019), p. 262-271.

[113] F. Melaccio, M. Del Carmen Marin, A. Valentini, F. Montisci, S. Rinaldi, M. Cherubini *et al.*, "Toward automatic rhodopsin modeling as a tool for high-throughput computational photobiology", *J. Chem. Theor. Comput.* **12** (2016), p. 6020-6034.

[114] F. Lumento, V. Zanirato, S. Fusi, E. Busi, L. Latterini, F. Elisei, A. Sinicropi, T. Andruniów, N. Ferré, R. Basosi, M. Olivucci, "Quantum chemical modeling and preparation of a biomimetic photochemical switch", *Angew. Chem. Int. Ed. Engl.* **119** (2007), p. 418-424.

[115] A. Sinicropi, E. Martin, M. Ryazantsev, J. Helbing, J. Briand, D. Sharma, J. Léonard, S. Haacke, A. Cannizzo *et al.*, "An artificial molecular switch that mimics the visual pigment and completes its photocycle in picoseconds", *Proc. Natl Acad. Sci. USA* **105** (2008), p. 17642-17647.

[116] B. L. Feringa, "The art of building small: from molecular switches to motors (Nobel lecture)", *Angew. Chem. Int. Ed.* **56** (2017), p. 11060-11078.

[117] T. P. Sakmar, R. R. Franke, H. G. Khorana, "Glutamic acid-113 serves as the retinylidene Schiff base counterion in bovine rhodopsin", *Proc. Natl Acad. Sci. USA* **86** (1989), p. 8309-8313.

[118] M. Gueye, M. Manathunga, D. Agathangelou, Y. Orozco, M. Paolino, S. Fusi, S. Haacke, M. Olivucci, J. Léonard, "Engineering the vibrational coherence of vision into a synthetic molecular device", *Nat. Commun.* **9** (2018), article no. 313.

[119] J. Briand, O. Braem, J. Rehault, J. Léonard, A. Cannizzo, M. Chergui, V. Zanirato, M. Olivucci, J. Helbing, S. Haacke, "Coherent ultrafast torsional motion and isomerization of a biomimetic dipolar photoswitch", *Phys. Chem. Chem. Phys.* **12** (2010), p. 3178-3187.

[120] A. D. Dunkelberger, R. D. Kieda, J. Y. Shin, R. Rossi Paccani, S. Fusi, M. Olivucci, F. Fleming Crim, "Photoisomerization and relaxation dynamics of a structurally modified biomimetic photoswitch", *J. Phys. Chem. A* **116** (2012), p. 3527-3533.

[121] J. Léonard, I. Schapiro, J. Briand, S. Fusi, R. R. Paccani, M. Olivucci, S. Haacke, "Mechanistic origin of the vibrational coherence accompanying the photoreaction of biomimetic molecular switches", *Chem. Eur. J.* **18** (2012), p. 15296-15304.

[122] J. Léonard, J. Briand, S. Fusi, V. Zanirato, M. Olivucci, S. Haacke, "Isomer-dependent vibrational coherence in ultrafast photoisomerization", *New J. Phys.* **15** (2013), p. 105022-105032.

[123] I. Schapiro, M. Gueye, M. Paolino, S. Fusi, G. Marchand, S. Haacke, M. Elena Martin, M. Huntress, V. P. Vysotskiy, V. Veryazov, J. Léonard, M. Olivucci, "Synthesis, spectroscopy and QM/MM simulations of a biomimetic ultrafast light-driven molecular motor", *Photochem. Photobiol. Sci.* **18** (2019), p. 2259-2269.

[124] R. Rozin, A. Wand, K. H. Jung, S. Ruhman, M. Sheves, "pH dependence of Anabaena Sensory Rhodopsin: retinal isomer composition, rate of dark adaptation, and photochemistry", *J. Phys. Chem. B* **118** (2014), p. 8995-9006.

[125] M. Stenrup, E. Pieri, V. Ledentu, N. Ferré, "pH-dependent absorption spectrum of a protein: a minimal electrostatic model of Anabaena Sensory Rhodopsin", *Phys. Chem. Chem. Phys.* **19** (2017), p. 14073-14084.

[126] M. L. Grünbein, M. Stricker, G. Nass Kovacs, M. Kloos, R. B. Doak, R. L. Shoeman, J. Reinstein, S. Lecler, S. Haacke, I. Schlichting, "Illumination guidelines for ultrafast pump–probe experiments by serial femtosecond crystallography", *Nat. Methods* **17** (2020), p. 681-684.

[127] S. Adachi, T. Schatteburg, A. Humeniuk, R. Mitrić, T. Suzuki, "Probing ultrafast dynamics during and after passing through conical intersections", *Phys. Chem. Chem. Phys.* **21** (2019), p. 13902-13905.

[128] A. D. Smith, E. M. Warne, D. Bellshaw, D. A. Horke, M. Tudorovskya, E. Springate, A. J. H. Jones, C. Cacho, R. T. Chapman, A. Kirrander, R. S. Minns, "Mapping the complete reaction path of a complex photochemical reaction", *Phys. Rev. Lett.* **120** (2018), article no. 183003.

[129] J. Hummert, G. Reitsma, N. Mayer, E. Ikonnikov, M. Eckstein, O. Kornilov, "Femtosecond extreme ultraviolet photoelectron spectroscopy of organic molecules in aqueous solution", *J. Phys. Chem. Lett.* **9** (2018), p. 6649-6655.

Comptes Rendus
Physique
2021, 22, nº S2, p. 139-160
https://doi.org/10.5802/crphys.89

Physics of ultra-fast phenomena / *Physique des phénomènes ultra-rapides*

Photoinduced charge density wave phase in 1T-TaS_2: growth and coarsening mechanisms

Onde de densité de charge photoinduite dans 1T-TaS_2 : mécanismes de croissance et de mûrissement

Amélie Jarnac [a], Vincent L. R. Jacques [b], Laurent Cario [c], Etienne Janod [c], Steven L. Johnson [d], Sylvain Ravy [b] and Claire Laulhé [*, a]

[a] Université Paris-Saclay, Synchrotron Soleil, 91190, Saint-Aubin, France

[b] Université Paris-Saclay, CNRS, Laboratoire de Physique des Solides, 91405, Orsay, France

[c] Institut des Matériaux Jean Rouxel, Université de Nantes, CNRS, 2 rue de la Houssinière, 44322 Nantes Cedex 03, France

[d] Institute for Quantum Electronics, Eidgenossische Technishe Hochschule (ETH) Zürich, 8093 Zürich, Switzerland

Current address: Université Paris-Saclay, ONERA, DPHY, F-91123 Palaiseau, France (A. Jarnac)

E-mails: amelie.jarnac@onera.fr (A. Jarnac), vincent.jacques@u-psud.fr (V. L. R. Jacques), Laurent.Cario@cnrs-imn.fr (L. Cario), Etienne.Janod@cnrs-imn.fr (E. Janod), johnson@phys.ethz.ch (S. L. Johnson), sylvain.ravy@cnrs.fr (S. Ravy), claire.laulhe@synchrotron-soleil.fr (C. Laulhé)

Abstract. Recent experiments have shown that the high-temperature incommensurate (I) charge density wave (CDW) phase of 1T-TaS_2 can be photoinduced from the lower-temperature, nearly commensurate CDW state. In a first step, several independent regions exhibiting I-CDW phase modulations nucleate and grow. After coalescence, these regions form a multidomain I-CDW phase that undergoes coarsening dynamics, i.e. a progressive increase of the domain size or I-CDW correlation length. Using time-resolved X-ray diffraction, we show that the wave vector of the photoinduced I-CDW phase is shorter than in the I-CDW phase at equilibrium, and progressively increases towards its equilibrium value as the correlation length increases. We interpret this behaviour as a consequence of a self-doping of the photoinduced I-CDW, following the presence of trapped electrons in the vicinity of CDW dislocation sites. Putting together results of the present and past experiments, we develop a scenario in which the I-CDW dislocations are created during the coalescence of the I-CDW phase regions.

Résumé. Plusieurs expériences récentes ont montré que les impulsions laser dans les domaines optique ou proche infrarouge permettent de déclencher des transitions entre états à onde de densité de charge (ODC) dans 1T-TaS_2. Nous nous intéressons ici à la transition entre l'état à ODC presque commensurable (NC)

* Corresponding author.

et l'état à ODC incommensurable (I), habituellement observé au-dessus de 350 K. Lors de cette transition, plusieurs régions présentant les modulations de l'état I se forment et se développent. Lorsque la coalescence a lieu, ces régions se muent en domaines de la phase I photoinduite de 1T-TaS_2, caractérisés chacun par un phasage particulier de l'ODC I. La phase I ainsi fragmentée en domaines subit alors une dynamique de mûrissement, c'est-à-dire une augmentation progressive de la taille de domaine ou encore de la longueur de corrélation de l'ODC I. En utilisant la diffraction des rayons X résolue en temps, nous montrons que le vecteur d'onde de l'ODC I photoinduite est plus court que dans l'ODC I observée à l'équilibre thermodynamique. Celui-ci s'allonge progressivement vers sa valeur d'équilibre, en même temps que la longueur de corrélation de l'ODC I augmente. Nous attribuons ce comportement à un autodopage de l'ODC I photoinduite, dû à la présence d'électrons piégés au voisinage de dislocations de l'ODC I. En réalisant une synthèse des résultats des différentes expériences menées jusqu'à présent, nous développons un scénario dans lequel les dislocations de l'ODC I sont créées au moment de la coalescence.

Keywords. Photoinduced phase transitions, Pump–probe X-ray diffraction, Charge density wave compounds, Topological defects, Transition metal dichalcogenides.

Mots-clés. Transitions de phase photoinduites, Diffraction pompe–sonde des rayons X, Composés à onde de densité de charge, Défauts topologiques, Dichalcogénures de métaux de transition.

Available online 12th October 2021

1. Introduction

The physics of correlated materials involves couplings between charge, orbital, spin and lattice degrees of freedom, which give rise to a wealth of physical properties as well as complex phase diagrams [1, 2]. Correlated systems display equally fascinating out-of-equilibrium physics, in the form of ultra-fast symmetry changes known as photoinduced phase transitions [3–5], and occurrence of new emergent metastable or transient states with unexpected functionalities [6–11]. Charge density wave (CDW) phases are gapped phases that emerge at low temperatures, mostly in low-dimensional metals. They are characterized by a periodic modulation of both atomic positions and electron density [12]. A significant number of photoinduced phase transitions have been achieved in CDW compounds, most often corresponding to a *suppression* of the CDW order, i.e. a transition between a CDW state and a metallic state free of any structural modulation [13–27]. In layered CDW compounds such as rare-earth tritellurides and transition-metal dichalcogenides, photoinduced developments of CDW orders were also reported [28–37]. These photoinduced CDW orders were found to be either closely related to the ones observed at equilibrium [28–34] or genuinely new states of matter [35–37]. Their observation has highlighted an unforeseen complexity of the free energy surface of such layered materials, and the possibility of controlling transitions between several competing states by light.

In the last decade, it has been recognized that topological defects play a significant role in the photoinduced dynamics of CDW compounds [38]. In $LaTe_3$, the photoinduced suppression of CDW order was shown to be accompanied by a significant decrease of the CDW correlation length, which was attributed to the creation of CDW dislocations [25]. In 1T-TaS_2 at low temperatures, the metastability of the photoinduced "hidden" phase was shown to be due to the emergence of unpaired dislocations, which stabilize chiral domain patterns [36]. Here, we focus on the photoinduced phase transition between the nearly commensurate (NC) and the incommensurate (I) CDW states in 1T-TaS_2. The photoinduced I-CDW state (hereafter denoted I*-CDW) was revealed to be fragmented into nanometric domains that subsequently grow [32, 34]. It is established that this so-called phase-ordering process involves motion of topological defects of the I*-CDW: both domain wall motion [32] and dislocation annihilation [34] were evoked.

1T-TaS_2 is formed by sheets of edge-linked TaS_6 octahedra (Figure 1a) [39]. In the high-symmetry phase ($T > 543$ K), Ta-atoms form a regular hexagonal lattice within a layer. As temperature decreases, three CDW phases stabilize alternately [40, 41], namely the incommensurate (I), nearly-commensurate (NC) and commensurate (C) phases. The first transition to

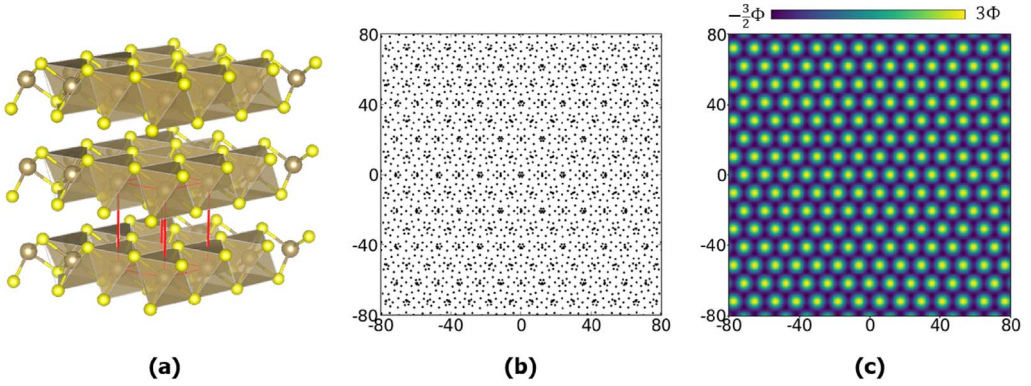

Figure 1. (a) Crystal structure of 1T-TaS_2 [44]. The hexagonal unit-cell is represented in red. (b,c) Ta-plane located at $z = 0$. All the length-scales are in Å. (b) Ta-plane exhibiting modulations of the I phase (350 K < T < 543 K). The Ta-atoms are represented as black dots, their displacements being exaggerated for visualization purposes. (c) Spatial dependence of the I-CDW real order parameter $\alpha(\vec{r}) = \Phi \sum_{j=1}^{3} \cos(\vec{q_I^j} \cdot \vec{r} + \theta_I^j)$, which corresponds to the charge density modulation.

the I-CDW phase occurs below 543 K and is believed to be driven by Fermi surface nesting [42], similarly to the Peierls distortion in one-dimensional systems [12]. The I-CDW phase is a triple-q modulated phase, characterized by the wave vectors $\vec{q_I^1} \approx 0.283\vec{a}^* + (1/3)\vec{c}^*$ and equivalents by 3-fold symmetry (Figure 2a). An atom which lies at a position $\vec{r}$ of the hexagonal lattice in the high temperature phase gets displaced in the I-CDW phase by $\vec{u}(\vec{r}) = \sum_{j=1}^{3} u_I \vec{e}_j \sin(\vec{q_I^j} \cdot \vec{r} + \theta_I^j)$, where $\vec{e}_j$ and θ_I^j are the polarisation and the phase associated with the j^e structural modulation. The amplitude u_I is the same for all three modulation components. The modulated Ta-positions observed in the I-CDW phase of 1T-TaS_2 are represented in Figure 1b. The electronic charge density is also modulated, and written in the form $\rho(\vec{r}) = \rho_0[1 + \alpha(\vec{r})]$, where ρ_0 is the density of conduction electrons and $\alpha(\vec{r}) = \Phi \sum_{j=1}^{3} \cos(\vec{q_I^j} \cdot \vec{r} + \theta_I^j)$ the order parameter of the I-CDW phase, Φ denoting the amplitude of each of the 3 electronic density modulations (Figure 1c) [43]. Note that the three θ_I^j phases may be different, however their sum has to be a multiple of 2π in order to yield peaks in the electron density as observed experimentally [43]. Below 350 K, the modulation wave vectors suddenly rotate by about 12° in the $(\vec{a}^*, \vec{b}^*)$ plane, marking the onset of the NC-CDW state (Figure 2a). At 300 K, the NC phase exhibits modulation vectors $\vec{q_{NC}^1} = 0.245\vec{a}^* + 0.068\vec{b}^* + (1/3)\vec{c}^*$ and equivalents by 3-fold symmetry. The in-plane components of $\vec{q_{NC}^1}$ are close to the commensurate values $(3/13)\vec{a}^* + (1/13)\vec{b}^*$. This commensurate, triple-q in-plane modulation is actually achieved below 180 K in the C-CDW phase.

X-ray diffraction is a perfectly suited method to study the structural evolution of CDWs, thanks to the selectivity and high-resolution in q-space it provides. More specifically: (1) A structural modulation with wave vector $\vec{q}$ gives rise to satellite peaks located at positions $\pm\vec{q}$ with respect to each Bragg peak of the unmodulated lattice (Figure 2a). (2) The integrated intensity of a CDW satellite peak is proportional to both the average of the square of the structural modulation amplitude and the volume fraction of the CDW phase in the sample. (3) After deconvolution of the instrument profile, the width of a CDW satellite peak is inversely proportional to the CDW correlation length. In the case of 1T-TaS_2, previous time-resolved diffraction studies have shown that the photoinduced I*-CDW phase appears within a picosecond after laser excitation [30] through a nucleation and growth process [32,33]. The correlation length of the newly formed I*-CDW phase,

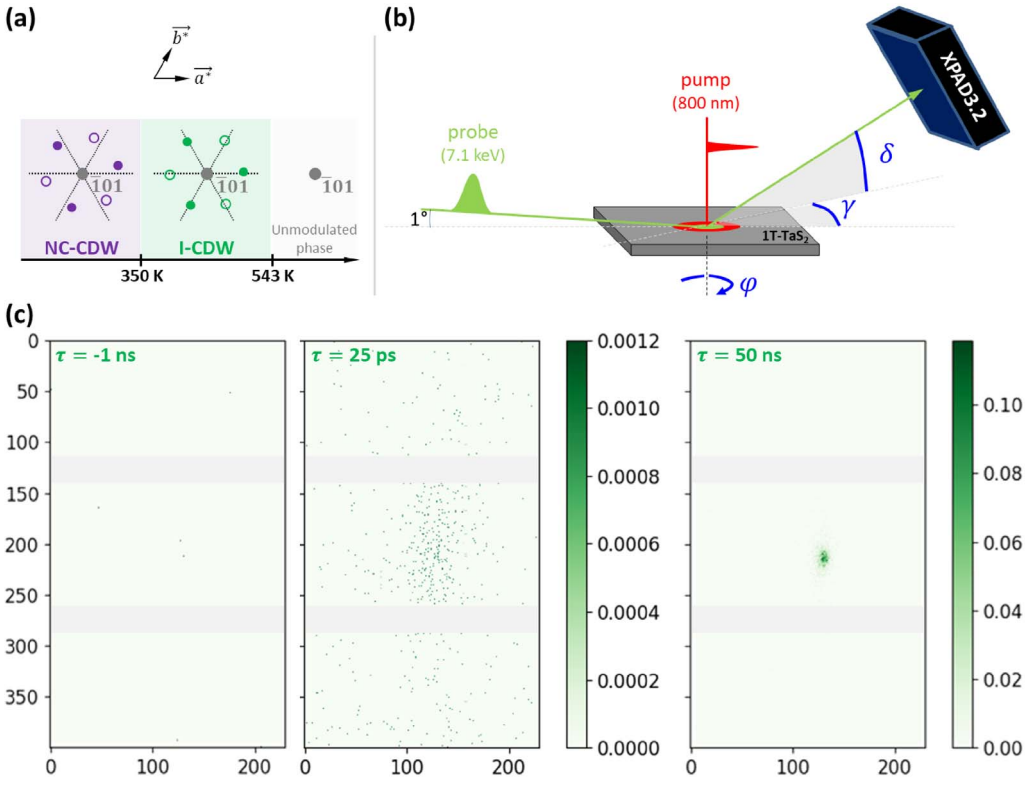

Figure 2. (a) Schematic representation of diffracted intensity in reciprocal space, as a projection in the $(\vec{a}^*, \vec{b}^*)$ plane of 1T-TaS_2. Satellite peaks related to the $\bar{1}01$ lattice peak are represented in purple for the NC phase and in green for the I phase. Their coordinate along c^*-axis can take two possible values: $1 + (1/3)$ (filled circles) and $1 - (1/3)$ (open circles). (b) Experimental setup and definition of the angles φ (sample rotation), δ and γ (detector rotations). (c) Diffracted intensity measured in the vicinity of the reciprocal space position $\bar{1}01 - \vec{q}_I^1$ for various pump–probe delays τ (265 K, absorbed fluence 3.9 mJ/cm^2). These images were obtained by summing diffracted intensities over a 1.75° φ-range. The image axes are graduated in pixel units, the pixel size being 135 µm. The non-sensitive regions of the detector are represented in light grey. The diffracted intensity is color-coded according to the scales displayed at the right of each image (in counts/s).

initially limited to a few nanometres, subsequently increases on timescales ranging from few tens of picoseconds to nanoseconds [32–34]. At this stage, considering together the time evolutions of both the I*-CDW correlation lengths and the volume fraction of the I*-CDW phase is crucial to distinguish between two very different phase development processes: *growth* and *phase ordering*. The *growth* of isolated I*-CDW phase regions from nuclei of the I*-CDW phase is characterized by a concomitant increase of the volume fraction of the I*-CDW phase and of the I*-CDW correlations lengths. After coalescence of the I*-CDW phase regions, a short-range correlated I*-CDW phase is observed in a single region of the sample. The I*-CDW *phase ordering* (or coarsening) that takes place afterwards corresponds to an increase of the I*-CDW correlation length in a constant volume fraction of the I*-CDW phase.

In the following, we present a new data set showing the development of a I*-CDW satellite in 1T-TaS_2 after laser excitation at 800 nm wavelength (Section 3). Based on a joint analysis of

the I*-CDW satellite peak profile and integrated intensity, we give evidence for a coarsening process in the $(\vec{a},\vec{b})$ plane (Section 3.1). For the first time in this coarsening regime, the wave vector of the photoinduced I*-CDW phase $\vec{q}_I^*$ could be tracked as the I*-CDW correlation length increases. We show that the in-plane component of $\vec{q}_I^*$ is initially shorter than in the I-CDW phase at equilibrium, and gradually increases towards its equilibrium value as the correlation length increases (Section 3.2). In Section 4, we discuss the possible scenarios behind this observation, in the framework of self-hole doping by CDW dislocations.

2. Experimental setup and method

The pump–probe time-resolved diffraction experiment took place at the CRISTAL beamline of SOLEIL synchrotron source (Saint Aubin, France). The sample was a platelet-like, (001)-oriented single crystal of 1T-TaS_2, few hundreds of micrometers thick and synthesised as described in Ref. [45].

The NC → I phase transition was triggered by 40 fs, 800 nm laser pulses at normal incidence with respect to the (001) surface plane. The laser fluence, which was calculated as the ratio between the energy of a single laser pulse and the full width half maximum (FWHM) of the laser beam, amounted 6.7 ± 0.8 mJ/cm^2. Given the reflectivity of the sample at 800 nm ($R = 0.417$ [46]), only 58.3% of this laser fluence i.e. 3.9 ± 0.5 mJ/cm^2 was actually absorbed.

The growth of the photoinduced I*-CDW phase was probed by X-ray diffraction at various delays τ after laser excitation, using 7.1 keV, 12 ps X-ray pulses. This relatively short pulse duration was provided during the low-α operation of the storage ring [47]. Intensity decays of the laser pump and X-ray probe beams are described by very different values of penetration depths in 1T-TaS_2: $\delta_X = 7.42$ µm [48] and $\delta_L \approx 30$ nm,[1] respectively. The incidence angle of the X-ray pulses was fixed to 1° with respect to the (001) surface plane, in order to limit the effective penetration depth of the probe to 130 nm and thereby minimize background signal from unpumped regions. The diffraction condition was tuned by rotating the sample about its surface normal, by an angle hereafter denoted φ. The diffraction signal was recorded with the 2D gateable detector XPAD3.2 [49], which can be rotated through both an elevation angle δ and an azimuthal angle γ (Figure 2b).

Determining the time-evolution of the wave vector of the photoinduced I*-CDW requires a very high resolution in reciprocal space. A resolution of about 6×10^{-4} Å^{-1} could be achieved by: (1) using a Si(111)-monochromator ($\Delta E/E = 2.4 \times 10^{-4}$) in conjunction with the low-divergent synchrotron source and (2) setting a relatively long sample-to-detector distance of 82.8 cm, leading to a correspondence of 0.009°/pixel.

At 1° incidence, the X-ray beam footprint on the sample was 1.7 mm × 0.5 mm FWHM. The laser spot on the sample was set to twice that size, i.e. 3.5 mm × 1.0 mm FWHM. The diffraction signals were recorded in a regular pump–probe scheme. The laser pulses were electronically phase-locked to a single electron bunch of the storage ring, using TimBeL boards [50] and an in-phase/quadrature modulator. A repetition rate of 500 Hz was chosen in order to ensure a complete disappearance of the photoinduced I*-CDW phase before the arrival of the following laser pulse, allowing cumulative measurement of the pump–probe cycles. A significant number of scans were performed at negative delays close to the I*-CDW satellite peak position, regularly throughout the experiment, in order to check that no residual I*-CDW peak would form as the number of pump–probe cycles increased.

[1] Both the reflectivity R and the penetration depth δ_L of 800 nm photons in 1T-TaS_2 were calculated from the complex optical index, which itself was deduced from the real and imaginary parts of the dielectric function published in [46].

The sample temperature was regulated by means of a N_2 blower. Cryostats of this type have a limited cooling power, so that the controller temperature and the actual sample temperature may differ, especially in the present case of a laser-heated, millimetric sample. We estimate the actual sample temperature to be about 25 K higher than the controlled temperature, as I-CDW satellite peaks become observable at negative pump–probe delays for temperature setpoints higher than 325 K. The data presented in this article were acquired for a controlled temperature of 265 K.

3. Results

We first demonstrate the occurrence of a photoinduced NC → I phase transition in the chosen experimental conditions (absorbed fluence: 3.9 mJ/cm^2, controller temperature: 265 K). Figure 2c presents images of the diffracted intensity summed over a 1.75° wide φ-range around the I-CDW satellite peak position $\bar{1}01 - \vec{q}_I^1$, for three delays before and after laser excitation. No contribution is observed before laser excitation, which is expected since the sample lies in its NC-CDW phase. Shortly after laser excitation (τ = 25 ps), a diffuse scattering signal appears in the vicinity of the I-CDW satellite peak position, which shows the onset of the photo-induced I* phase. This scattering progressively narrows over time and eventually forms a well-defined diffraction peak at longer delays (τ = 50 ns). These observations are consistent with those previously reported in Refs. [16,30,32–34].

Figure 3 shows the I*-CDW satellite peak profiles as functions of the angles φ, δ and γ, for various delays after laser excitation. The diffracted intensities displayed on the φ-profiles correspond to photon counts summed over the detector area presented in Figure 2c. The δ- and γ-profiles were obtained by first summing all the images taken along a φ-scan, and then projecting photon counts along the horizontal and vertical directions of the detector respectively, assuming a correspondence of 0.009°/pixel.

3.1. *Development of the I*-CDW phase*

The CDW correlation lengths correspond to distances over which both the amplitude and the phase of the CDW are homogeneous. As such, they are of central importance for discussing the CDW growth and phase-ordering processes. It has been emphasized that determining the 3D profile of a CDW satellite peak in reciprocal space allows retrieval of the CDW correlation lengths in all directions of space [33]. In the following, we provide an estimation of the correlation lengths of the I*-CDW, both in the $(\vec{a},\vec{b})$ plane and along $\vec{c}$. Those are hereafter denoted $\xi_{a,b}$ and ξ_c.

We first determined the time-dependent FWHMs of the I*-CDW satellite peak, $\Delta\delta(\tau)$ and $\Delta\gamma(\tau)$, by fitting pseudo-Voigt functions to the profiles along δ and γ, respectively (Figure 3). The contributions of instrumental resolution and sample mosaicity were then removed from the measured satellite peak widths, according to the following expressions: $\Delta\delta'(\tau) = \sqrt{[\Delta\delta(\tau)]^2 - [\Delta\delta_B]^2}$ and $\Delta\gamma'(\tau) = \sqrt{[\Delta\gamma(\tau)]^2 - [\Delta\gamma_B]^2}$. The angular widths $\Delta\delta_B = 0.075°$ and $\Delta\gamma_B = 0.043°$ correspond to those of the nearest Bragg peak $\bar{1}01$. The correlation lengths $\xi_{a,b}$ and ξ_c were finally estimated by using the following equations:

$$\xi_{a,b}(\tau) = \frac{2\pi}{\Delta q_{a^*,b^*}} = \frac{\lambda_X}{2\tan\left[\frac{\Delta\gamma'(\tau)}{2}\right]\cos[\delta(\tau)]} \tag{1}$$

$$\xi_c(\tau) = \frac{2\pi}{\Delta q_{c^*}} = \frac{\lambda_X}{2\tan\left[\frac{\Delta\delta'(\tau)}{2}\right]\cos[\delta(\tau)]}, \tag{2}$$

where λ_X is the X-ray wavelength. $\Delta q_{a^*,b^*}$ and Δq_{c^*} are the FWHMs of the I*-CDW satellite peak in reciprocal space related to the limited I*-CDW correlation lengths (Figure 4).

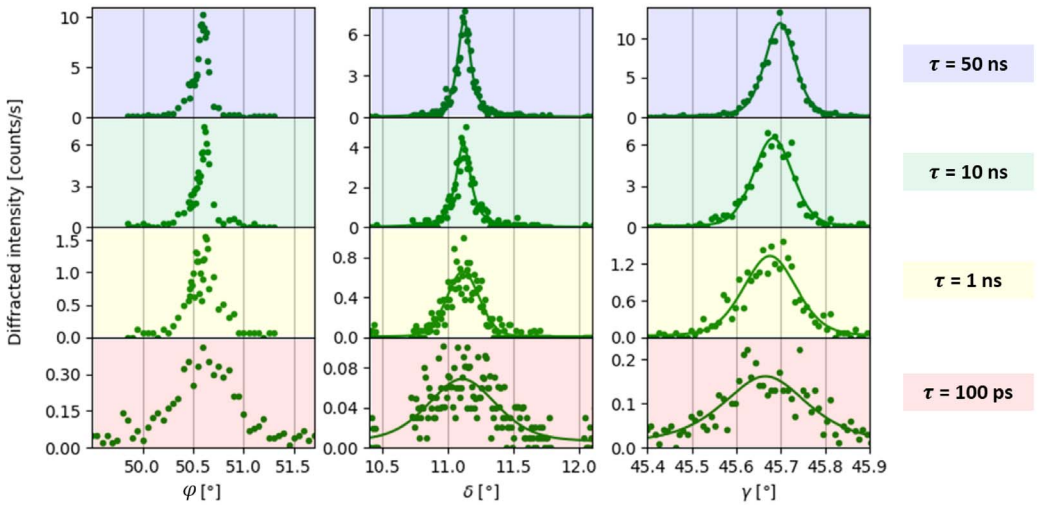

Figure 3. Profiles of the $\bar{1}01-\vec{q}_{I*}^{\,\vec{1}}$ I*-CDW satellite peak as functions of the angles φ, δ and γ, for selected pump–probe delays (265 K, absorbed fluence 3.9 mJ/cm^2). The dots represent measured data and the solid lines their best fit using a pseudo-Voigt function. Those fits allow extracting the peak widths and angular positions as a function of the pump–probe delay τ.

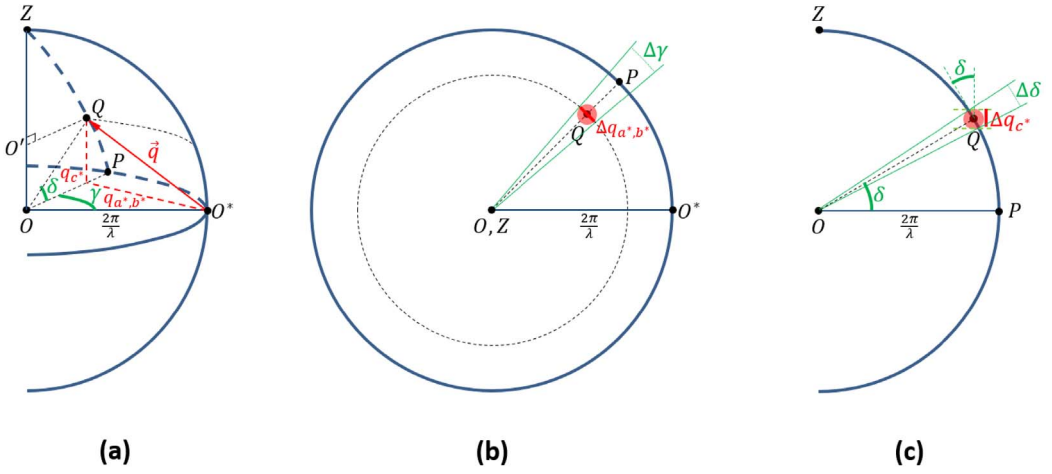

Figure 4. (a) 3D-view of the Ewald's sphere, with the I*-CDW satellite peak fulfilling the diffraction condition. The scattering vector $\vec{q} = -\vec{a}^* + \vec{c}^* - \vec{q}_{I*}^{\,\vec{1}}$ intercepts the Ewald sphere at point Q. (b) Orthogonal projection in the (OO^*P) plane, which allows defining $\Delta q_{a^*,b^*}$ (red line segment). (c) Orthogonal projection in the (OPQ) plane, which allows defining Δq_{c^*} (red line segment). Note that for ease of calculation, the X-ray incidence angle has been approximated to 0 (instead of 1°), i.e. $\vec{c}^*$ is supposed to lie along the OZ direction.

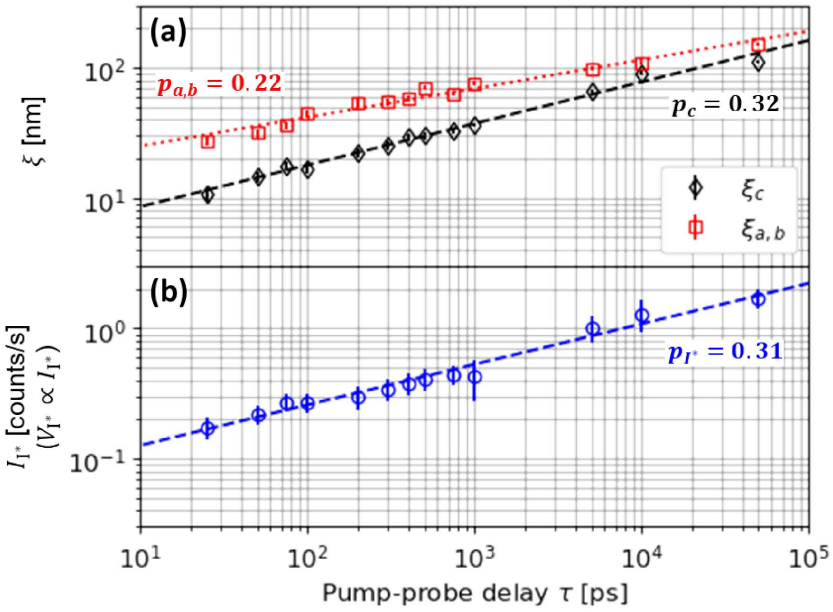

Figure 5. (a) Time-evolution of the I*-CDW correlation lengths, in the $(\vec{a}, \vec{b})$ plane ($\xi_{a,b}$, open squares) and along $\vec{c}$ (ξ_c, open diamonds). (b) Integrated intensity of the $\bar{1}01 - \vec{q}_{I^*}^{\vec{1}}$ satellite peak of the I*-CDW, I_{I^*}. The error bars correspond to $\pm\sigma$ where σ is the standard deviation. Those were determined by propagating the errors on $\Delta\delta(\tau)$ and $\Delta\gamma(\tau)$, which themselves were estimated from the I* satellite peak fitting. Dotted lines mark the best fits of the data using the power-law function $A \times \tau^p$. The optimized values of p are indicated in the figure. The temperature setpoint was 265 K and the absorbed fluence 3.9 mJ/cm^2.

The time-dependent correlation lengths $\xi_{a,b}(\tau)$ and $\xi_c(\tau)$ do not exceed few tens of nm in the pump–probe delay range studied (Figure 5a). Those exhibit a linear behaviour when plotted on a double logarithmic scale, which implies that they exhibit a power-law dependence on time $\xi \propto \tau^p$. Two distinct exponents p are found for $\xi_{a,b}$ and ξ_c: $p_{a,b} = 0.22 \pm 0.04$ and $p_c = 0.32 \pm 0.03$, respectively. The correlation lengths $\xi_{a,b}$ and ξ_c correspond to distances over which the phases $\theta_{I^*}^j$ of the I*-CDW are homogeneous. As a consequence, the observed increase of the I*-CDW correlation lengths stems either from an expansion of regions exhibiting homogeneous CDW-phases $\theta_{I^*}^j$ (growth, Figure 6a), or from a homogenization of the CDW-phases $\theta_{I^*}^j$ within a single region exhibiting I*-CDW order (ordering, Figure 6b). The latter two processes can be distinguished by determining the time-dependence of the volume fraction of the I*-CDW phase, V_{I^*}.[2]

The integrated intensity of the I*-CDW satellite peak I_{I^*} is directly proportional to V_{I^*}. However, it is also directly proportional to the square of the average I*-CDW amplitude Φ_{I^*}. The amplitude Φ_{I^*} increases concomitantly with the I*-CDW gap formed at the Fermi level [42]. Although the latter quantity has never been probed following the photoinduced NC → I phase transition in 1T-TaS_2, pump–probe photoemission experiments have allowed establishing that the typical timescales of formation or recovery of CDW gaps lie below few ps [20, 25, 51–53]. Interestingly,

[2] In this work, the volume fraction of the I*-CDW phase is to be understood as the total volume of the I*-CDW phase region(s) divided by the volume probed by X-rays.

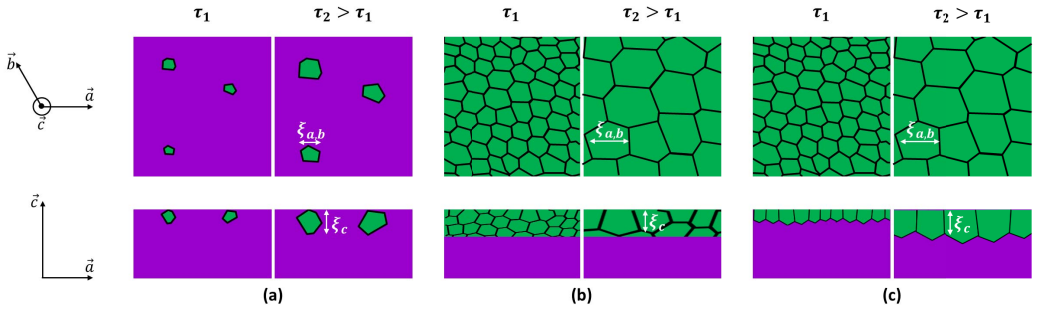

Figure 6. Schematic representation of the three scenarios that have been reported for the development of the I*-CDW phase (times after laser excitation: τ_1 and $\tau_2 > \tau_1$). The top and bottom rows show views of the 1T-TaS_2 crystal along its c-axis and along a direction normal to the c-axis, respectively. (a) Growth of isolated I*-CDW phase regions. In this case, the volume of the I*-CDW phase is directly proportional to ${\xi_{a,b}}^2 \times \xi_c$ [33]. (b) Coarsening of I*-CDW domains in a large I*-CDW region. In this case, the volume of the I*-CDW phase is constant [32]. (c) Growth of the I*-CDW phase region along $\vec{c}$, and domain coarsening in the $(\vec{a}, \vec{b})$ plane. In this case, the volume of the I*-CDW phase is directly proportional to ξ_c [present work].

a previous ultrafast electron diffraction study unveiled two characteristic time scales of the photoinduced NC → I phase transition in 1T-TaS_2 [30] (pump wavelength 775 nm). The first characteristic time scale, of 1.5 ps, was attributed to the nucleation of the I* phase, i.e. the increase of Φ_{I^*} towards its equilibrium value in finite regions of the sample. The second characteristic time scale, of few tens of ps, was attributed to the growth of the I* phase nucleated regions. Given these results, it is reasonable to assume that in the delay range $\tau \geq 25$ ps investigated in this work, Φ_{I^*} has reached its maximum value throughout the I*-CDW regions. Under the latter hypothesis, the volume fraction of the I*-CDW phase can be directly inferred from the integrated intensity of the I*-CDW satellite peak, using $V_{I^*} \propto I_{I^*}$. The dependence of V_{I^*} on pump–probe delay is given in Figure 5b, on a double logarithmic scale. It keeps increasing in the (0–50 ns) delay range investigated, following a power-law scaling $V_{I^*} \propto \tau^{0.31}$, which indicates a continuous expansion of the volume fraction of the I*-CDW phase in the sample. The scenario of a pure phase-ordering process, in which the correlation length increases in a fixed volume fraction of the I*-CDW phase (Figure 6b), is thus very unlikely. In the case where I*-CDW regions would grow without being in contact (Figure 6a), we expect the integrated intensity of the I*-CDW satellite peak to be proportional to ${\xi_{a,b}}^2 \times \xi_c$ and, therefore, to τ^{p_g} with $p_g = 2 \times p_{a,b} + p_c = 0.8 \pm 0.1$. This exponent is inconsistent with our findings ($p_{I^*} = 0.31 \pm 0.02$). We conclude that none of the scenarios depicted in Figures 6a,b matches with the experimental observations. A model thus has to be built, where (1) both the I*-CDW correlation lengths and the volume fraction of the I*-CDW phase increase, and (2) the correlated volume and the volume fraction of the I*-CDW phase grow at different rates. Noticing that V_{I^*} and ξ_c have the same time-dependence ($p_{I^*} \approx p_c$), we propose that the I*-CDW phase is developed in a layer of thickness $\xi_c(\tau)$ at the surface of the sample. The volume fraction of the I*-CDW phase then grows concomitantly with ξ_c, according to the power-law function τ^{p_c}. On the other hand, one can assume that the I*-CDW phase has already developed over the entire $(\vec{a}, \vec{b})$ plane. It is divided into domains exhibiting each a different set of CDW-phases $\theta^j_{I^*}$, and undergoes coarsening along the $\vec{a}$ and $\vec{b}$ directions (Figure 6c). We exclude the possibility that isolated regions of the I*-CDW phase, growing at a rate $\tau^{p_{I^*}}$, would host several CDW-phase domains growing at a rate τ^{p_g}. Indeed, previous experiments have shown that

before coalescence, both the nucleated I*-CDW phase regions and the correlated volume grow at the same rate [33], thereby establishing that the CDW-phases are homogeneous within isolated I*-CDW regions. Finally, let us note that if our experiment shows a proportionality between the c-axis correlation length and the volume fraction of the I* phase, this does not necessarily mean that the thickness of the I* phase is equal to the time-dependent $\xi_c(\tau)$ correlation length (Figure 6c). Namely, a scenario where the ξ_c correlation length would be a fixed fraction of the thickness of the I*-CDW layer cannot be excluded. We however consider it unlikely, as it would imply that coarsening and growth along the c-axis, which are markedly different processes, happen at the same rate.

It is interesting to discuss the proposed scenario (Figure 6c) in the framework of the previous findings of Haupt *et al.* [30]: they report that the time needed to achieve a complete transition to the I-CDW phase over a 22 nm thick 1T-TaS_2 sample decreases from ~500 ps to ~200 ps as the incident fluence increases from 1.3 mJ/cm^2 to 2.1 mJ/cm^2. In our experiment, the sample is much thicker than the laser penetration depth, so that we cannot expect a development of the I phase over the whole sample. Nevertheless, it is possible to estimate the time needed for the I* phase to get fully developed across a 20 nm thickness of our 1T-TaS_2 sample, $\tau_{20\,\mathrm{nm}}$. Assuming the scenario depicted in Figure 6c, $\tau_{20\,\mathrm{nm}}$ simply corresponds to the delay at which ξ_c reaches 20 nm, that is $\tau_{20\,\mathrm{nm}} = 140$ ps (Figure 5b). The latter delay is consistent with the ones reported by Haupt *et al.*, given the incident fluence used in the present work (6.7 ± 0.8 mJ/cm^2).

3.2. *Time evolution of the I*-CDW wave vector*

The defect structures that lead to short range correlated CDW states can modify both the spatial distribution of electrons and the density of states [54] and, in turn, the wave vectors of the I*-CDW phase $\vec{q}^{\,j}_{I^*}$. In the following, we give evidence for a progressive increase of the $(\vec{a}^*, \vec{b}^*)$-plane component of $\vec{q}^{\,1}_{I^*}$ towards its equilibrium value, which we will relate to CDW dislocation annihilation processes in Section 4.

The wave vector of the photoinduced I*-CDW at time τ, $\vec{q}^{\,1}_{I^*}(\tau)$, has coordinates $(h_{I^*}(\tau) - h_B, k_{I^*}(\tau) - k_B, l_{I^*}(\tau) - l_B)$ in the time-dependent basis $(\vec{a}^*(\tau), \vec{b}^*(\tau), \vec{c}^*(\tau))$ of the reciprocal space, where $(h_{I^*}(\tau), k_{I^*}(\tau), l_{I^*}(\tau))$ are the coordinates of a satellite peak and (h_B, k_B, l_B) those of the corresponding lattice peak. In order to study the dynamics of $\vec{q}^{\,1}_{I^*}(\tau)$, one has thus to determine the time-evolution of both the reciprocal lattice vectors and the $(h_{I^*}(\tau), k_{I^*}(\tau), l_{I^*}(\tau))$ coordinates.

3.2.1. *Time evolution of the underlying crystal lattice*

Assuming that the lattice remains hexagonal at all times after laser excitation, the set of vectors $(\vec{a}^*(\tau), \vec{b}^*(\tau), \vec{c}^*(\tau))$ can be entirely determined from the orientation matrix of the crystal (3 rotation parameters) and the values of the a and c cell parameters. We evaluated the latter 5 parameters for all the pump–probe delays investigated, by using the GHKL computation library [55] along with the angular positions of both $\bar{1}01$ and $\bar{1}02$ Bragg peaks.

The experimental values of the angles $\varphi(\tau)$, $\delta(\tau)$ and $\gamma(\tau)$ were determined as the first moments of the normalized intensity distributions, which are partly shown in Figure 7. One can observe that the angular positions of the $\bar{1}01$ and $\bar{1}02$ Bragg peaks exhibit similar time evolutions (Figure 8a). The peak angles $\varphi(\tau)$ and $\delta(\tau)$ increase and decrease, respectively, by a few hundredth of degrees within 50 ps. Both angles then remain constant up to 1 ns, and progressively recover their initial values in the τ-range (1–50 ns). The angle $\gamma(\tau)$ does not exhibit any significant changes throughout the whole pump–probe cycle. The orientation matrix calculated from the angular positions of the two lattice reflections $\bar{1}01$ and $\bar{1}02$ is found to be constant over time.

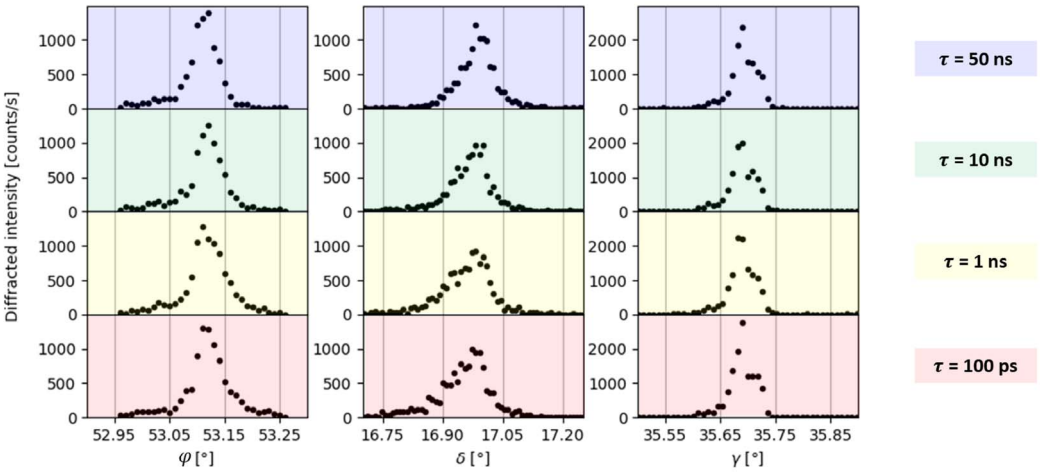

Figure 7. Profiles of the $\bar{1}01$ lattice peak as functions of the angles φ, δ and γ, for selected pump–probe delays (265 K, absorbed fluence 3.9 mJ/cm^2).

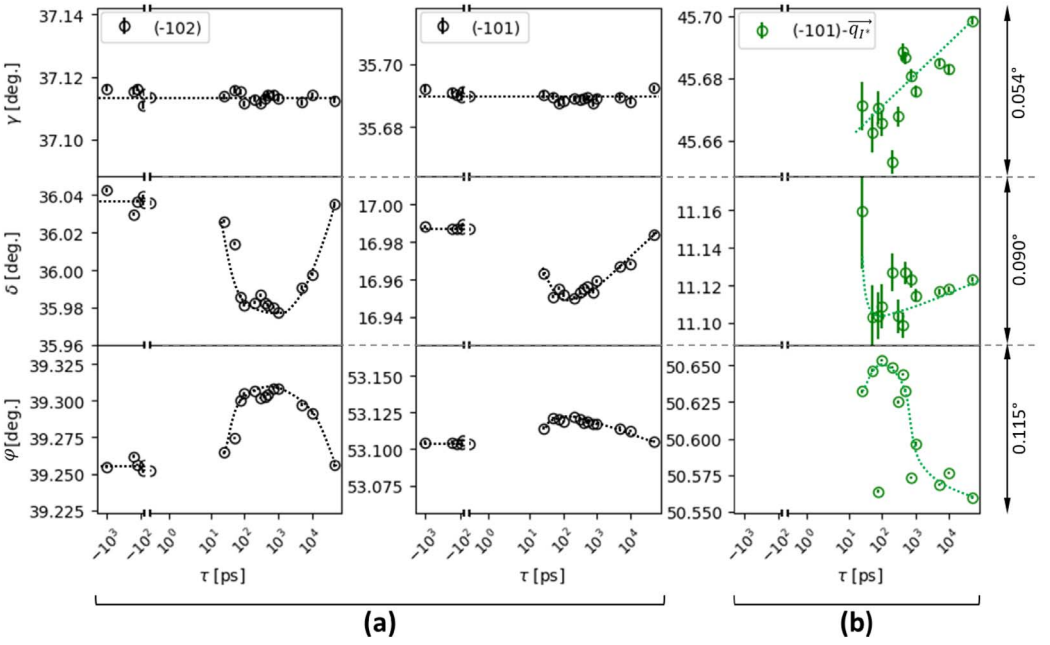

Figure 8. Time-evolution of the angles φ, δ and γ for the $\bar{1}01$ and the $\bar{1}02$ lattice peaks (a), and for the $\bar{1}01 - \vec{q}^{\bar{1}}_{I^*}$ satellite peak (b). The error bars correspond to $\pm\sigma$ where σ is the standard deviation. Those take into account the accuracy of the diffractometer (0.001°) as well as the propagation of statistical errors when determining the first moments of the intensity distributions (φ angle values and (a) panel). The error bars presented in panel (b) for δ and γ angles were calculated using the accuracy of the diffractometer and the errors estimated from the I* satellite peak fitting. The dotted lines are guides for the eye. The temperature setpoint was 265 K and the absorbed fluence 3.9 mJ/cm^2.

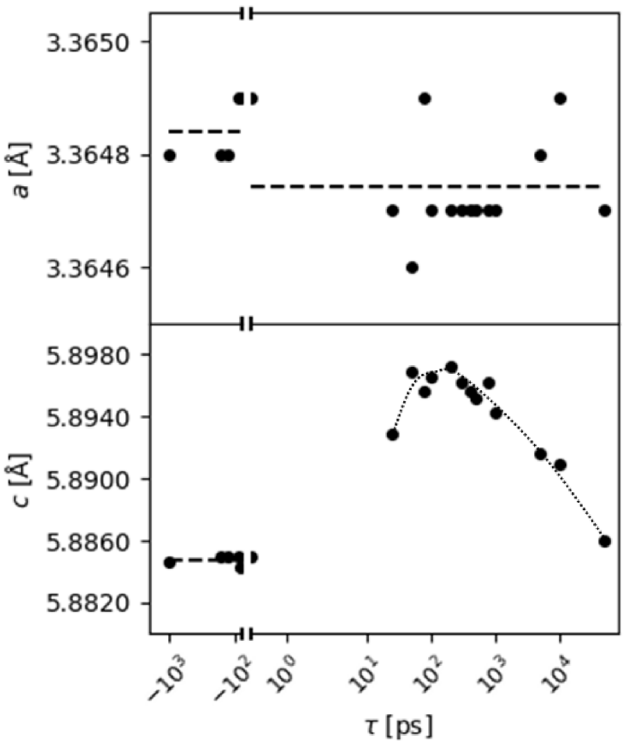

Figure 9. Time-evolution of the cell parameters a and c, as determined by using the GHKL library with the measured diffraction angles of the $\bar{1}01$ and the $\bar{1}02$ lattice peaks. The dashed lines indicate averaged values of the a and c parameters before laser excitation ($\tau < 0$), as well as the averaged value of a after laser excitation ($\tau > 0$). The dotted line is a guide for the eye. The base temperature was 265 K and the absorbed fluence 3.9 mJ/cm^2.

The time-dependent cell parameters deduced from measurements on the $\bar{1}01$ Bragg peak are reported in Figure 9. The shifts of $\varphi(\tau)$ and $\delta(\tau)$ mentioned above appear to be due to a transient lattice expansion along the c-axis, i.e. in the direction perpendicular to the sample's surface. This phenomenon is generally observed in laser-excited solids and stems from the propagation of a laser-induced strain wave [56]. A very small contraction of the lattice in the $(\vec{a}, \vec{b})$ plane could also be detected after laser excitation ($\langle \Delta a/a \rangle = -3 \times 10^{-5}$), which can be attributed to longitudinal-to-transverse strain coupling (Poisson effect) [57].

3.2.2. *Dynamics of the I*-CDW satellite peak*

The orientation matrices and cell parameters being known for all pump–probe delays, we now turn to the determination of the time-dependent coordinates of the forming I*-CDW satellite peak $(h_{I^*}(\tau), k_{I^*}(\tau), l_{I^*}(\tau))$. The $\varphi(\tau)$ angular positions of the I*-CDW satellite peak were determined from the calculation of the first moments of the diffraction profiles, as was done for the $\bar{1}01$ and $\bar{1}02$ Bragg peaks. The same method could not be safely used to extract the $\delta(\tau)$ and $\gamma(\tau)$ values, as part of the satellite peak intensity falls into dead-zones of the detector (Figure 2). We thus determined those latter two angles by fitting a pseudo-Voigt function to the respective diffraction profiles (Figure 3). Figure 8b shows the time-evolution of the $\varphi(\tau)$, $\delta(\tau)$ and $\gamma(\tau)$ angles of the I* satellite peak. The data are noisier than those related to the lattice peaks (Figure 8a), despite the

fact that we adapted the total counting times to get sufficient statistics on the I* satellite peak intensities. This indicates drifts in some of the experimental parameters over the 33 hour period during which we acquired the series of measurements on the time-dependence of the I* satellite peak. The time-dependence of the $\delta(\tau)$ angle of the I*-CDW satellite peak is found to exhibit qualitatively the same features as the ones measured for the lattice peaks. On the other hand, time evolutions of the $\varphi(\tau)$ and $\gamma(\tau)$ angles differ significantly for the lattice and satellite peaks. The $\varphi(\tau)$ angle of the I* satellite peak is found to increase in the first 50 ps, as for the lattice peaks. However, its subsequent decrease is about ten times faster. Moreover, in marked contrast with the constant $\gamma(\tau)$ angle observed for lattice peaks, we report a continuous increase of the $\gamma(\tau)$ angle of the I*-CDW satellite peak over time. Hence, we give evidence for distinct dynamics of the satellite and lattice diffraction peaks, which in turn indicates a *time-dependence* of the I*-CDW wave vector $\vec{q}_{I^*}^{\,\parallel}$.

The time-dependent coordinates of the forming I*-CDW satellite peak $(h_{I^*}(\tau), k_{I^*}(\tau), l_{I^*}(\tau))$ were calculated by using the GHKL library [55] and the previously determined time-dependent basis of the reciprocal space, $(\vec{a}^*(\tau), \vec{b}^*(\tau), \vec{c}^*(\tau))$. The coordinates of $\vec{q}_{I^*}^{\,\parallel}$ were then deduced from $(h_{I^*}(\tau), k_{I^*}(\tau), l_{I^*}(\tau))$, by subtracting the coordinates of the nearest lattice peak $\bar{1}01$. The CDW wave vectors of 1T-TaS_2 are usually divided into two components, $\vec{q}_{\mathrm{CDW}}^{\,\perp}$ and $\vec{q}_{\mathrm{CDW}}^{\,\parallel}$ (Figure 10a). The c^*-axis component of the CDW wave vector $\vec{q}_{\mathrm{CDW}}^{\,\perp}$ is related to the stacking of the 2D-CDWs from one layer to the other. In both the I and NC phases of 1T-TaS_2, it is determined by interlayer Coulombic interactions which yield a $3c$ stacking period and $\|\vec{q}_{\mathrm{CDW}}^{\,\perp}\| = 1/3$ [58,59]. The $(\vec{a}^*, \vec{b}^*)$-plane component $\vec{q}_{\mathrm{CDW}}^{\,\parallel}$ determines both the period and the orientation of the 2D hexagonal lattices of charge modulation. The time-dependences of the polar coordinates of $\vec{q}_{I^*}^{\,\parallel}$, $q_{I^*}^{\parallel}$ and α_{I^*}, are represented in Figures 10b and c respectively (black circles). The coordinates $q_I^{\parallel}$ and α_I of the I-CDW wave vector measured at equilibrium (385 K, no laser excitation) are also reported for comparison purposes (red dotted lines). The values of $q_I^{\parallel}$ and α_I found for the I-CDW at equilibrium are in agreement with previous reports [40,59–61]. We find that the I-CDW develops in the $(\vec{a}, \vec{b})$ plane with a wave vector component $q_I^{\parallel} = 0.2827(1)$. Structural modulations in the $(\vec{a}, \vec{b})$ plane are observed in directions slightly off the main hexagonal axes. We find an angle α_I of 0.1(2)°, which falls in the range of previously reported values: 0° [59,60], 0.38(2)° [40] and 1° [61]. The large dispersion of α_I values reported so far indicates that the I-CDW tilt angle might be sample-dependent. At the onset of the I*-CDW formation ($\tau = 25$ ps), $q_{I^*}^{\parallel}$ is found 0.3% smaller than $q_I^{\parallel}$ (Figure 10b). The orientation of the in-plane I*-CDW modulation with respect to the hexagonal axes also differs from the one observed in the I phase at equilibrium (Figure 10c). Both parameters $q_{I^*}^{\parallel}$ and α_{I^*} evolve in time to reach their reference values, albeit on different timescales: few tens of ns for $q_{I^*}^{\parallel}$, about 1 ns for α_{I^*}).

Let us note that due the limited penetration depth of the 800 nm photons in 1T-TaS_2 ($\delta_L \approx$ 30 nm, see Section 2) and the resulting inhomogeneous excitation profile, it is expected that the cell parameters a and c exhibit a significant depth-dependence over the 130 nm probed region. The values of a and c given in Figure 9, which are deduced from lattice peaks, correspond to an average over the entire probe depth of 130 nm. On the other hand, the satellite peak signal originates from the I* phase region, which is confined within the depth ξ_c below the sample's surface. Its actual position in reciprocal space depends on the a and c parameters averaged over the depth $\xi_c < 130$ nm, rather than on those presented in Figure 9. Despite this major limitation, the two conclusions given above about the dynamics of the I*-CDW wave vector hold:

(i) The a parameter averaged over a 130 nm depth decreases (Figure 9), which means that we may have underestimated the decrease of a over the depth ξ_c. In turn, we may have underestimated the averaged value of $a^* = 4\pi/a\sqrt{3}$ over the depth ξ_c, and thus

overestimated $q^{\parallel}_{I^*}/a^*$. Hence, our observation of a *shorter* I*-CDW wave vector with respect to the equilibrium value cannot be explained by this experimental artefact.

(ii) The orientation of the $\vec{a}^*$ and $\vec{b}^*$ vectors remains unchanged at all delays across the 130 nm probe depth (see Section 3.2.1). There are thus no reasons to evoke a rotation of the reciprocal space vectors over the depth ξ_c. As a result, the rotation of $\vec{q}^{\parallel}_{I^*}$ with respect to $\vec{a}^*$ can neither be explained by the differing diffracting volumes of the satellite and lattice peaks.

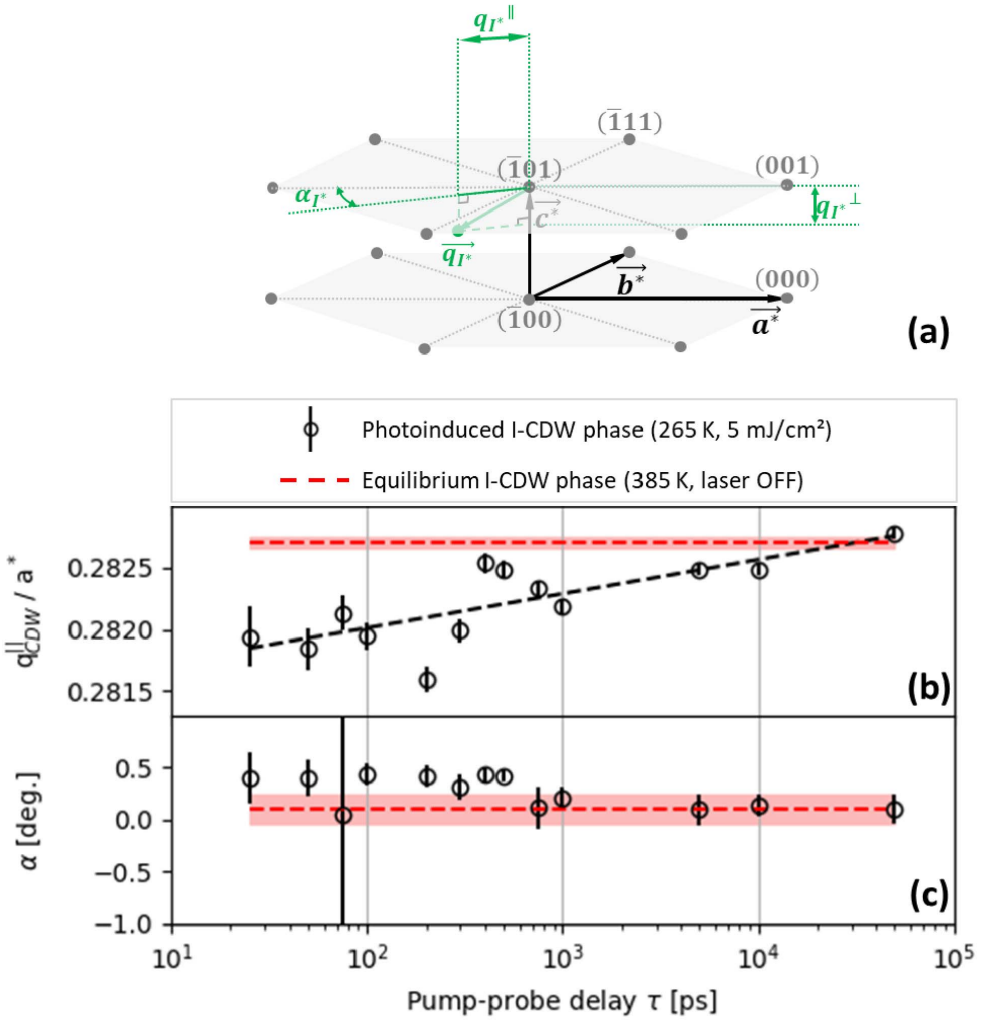

Figure 10. (a) Graphical definition of the I*-CDW wave vector components. (b,c) Time evolution of $\vec{q}^{\parallel}_{I^*}$ (black circles): (b) $\|\vec{q}^{\parallel}_{I^*}\|$ in a^* units, and (c) angle between $\vec{q}^{\parallel}_{I^*}$ and $-\vec{a}^*$, α_{I^*}. Values corresponding to the equilibrium I-CDW wave vector are also reported on panels (b,c), using red dashed lines. The error bars correspond to $\pm\sigma$ where σ is the standard deviation. Those were determined by propagating the errors on the $\varphi(\tau)$, $\delta(\tau)$ and $\gamma(\tau)$ angles of both the I* satellite peak and the $\bar{1}01$ lattice peak.

We emphasize that the observed dynamics of the I*-CDW wave vector cannot be attributed to a simple change of the average lattice temperature following laser excitation. Indeed, the wave vector of the I-CDW was shown to be temperature-independent in the range (350–420 K) [59,60]. For $\tau \leq 1$ ns, the I*-CDW thus *intrinsically* differs from the equilibrium I-CDW, not only by its limited correlation length, but also by its orientation and its larger periodicity in the $(\vec{a},\vec{b})$ plane ($q^{\parallel}_{I^*} < q^{\parallel}_{I}$). In equilibrium conditions, it is widely accepted that $\vec{q^{\parallel}_{I}}$ corresponds to a nesting vector of the 2D Fermi surface of 1T-TaS_2, lying close to one of the MK directions of reciprocal space [42, 62]. Given the local linear dispersion of the electronic state energies along the MK direction [63], a shorter nesting vector can be observed in the case where the Fermi energy is lowered consecutive to hole-doping. Shortening of the $\vec{q^{\parallel}_{I^*}}$ wave vector in 1T-TaS_2 has already been observed in chemically hole-doped samples [62]. As for the photoinduced I*-CDW phase, we propose that hole-doping is achieved in the pump–probe delay range $\tau \leq 30$ ns, owing to the presence of CDW dislocations. We further develop this idea in the following discussion. Understanding the larger value of α_{I^*} as compared to α_I is certainly a more complex task. The 1°-wide range of α_I reported in different samples of 1T-TaS_2 at equilibrium suggest that defects may play a role on the actual orientation of the I-CDW. A possibility would be that the CDW dislocations mentioned above influences the I*-CDW orientation.

4. Discussion

In the following, we first expose a detailed description of the mechanism of the photoinduced NC → I phase transition in 1T-TaS_2, based on past electron and X-ray diffraction studies. Considering the sequence of nucleation, growth, coalescence and phase ordering processes, we discuss the appearance of two kinds of topological defects, namely extended domain walls and dislocations. Their influence on the phase ordering kinetics as well as on the CDW period in the photoinduced I*-CDW phase of 1T-TaS_2 is finally examined in light of the present experimental results.

4.1. *Nucleation and growth of I*-CDW phase regions*

The development of the I*-CDW phase starts by the formation of several nuclei that subsequently grow [30]. Assuming that the I*-CDW phase regions are free from defects, their size limits the I*-CDW correlations lengths (Figure 6a) and one can write: $V_{I^*} \propto {\xi_{a,b}}^2 \times \xi_c$. Such a situation was evidenced in Ref. [33], where both V_{I^*} and the correlation lengths $\xi_{a,b}$ and ξ_c could be determined simultaneously, as in the present study. Since the I*-CDW period is incommensurate with that of the underlying lattice, there is an infinite number of energetically equivalent I*-CDW states, each corresponding to a distinct set of CDW phases $\theta^j_{I^*}$ ($j = 1,2,3$) [43]. Hence, in the early step of the photoinduced I*-CDW phase development, one can reasonably assume that isolated, defect-free I*-CDW phase regions appear, each being characterized by a distinct set of CDW phases.

4.2. *Coalescence*

At some point in the growth process of the isolated I*-CDW regions, coalescence is expected to occur. In a simple scenario, one can propose that the isolated I*-CDW regions then become CDW-phase domains in a single extended I*-CDW phase region, as sketched in Figures 6b and 11. Interestingly, the presence of CDW-phase domains was demonstrated experimentally in the equilibrium I-CDW phase, in freshly synthesized 1T-TaS_2 samples [64]. It was interpreted as resulting from the rapid quench performed at the end of the synthesis in order to avoid the formation of 2H-TaS_2 [39]. Ultrafast laser excitation and temperature quench, which both induce a sudden

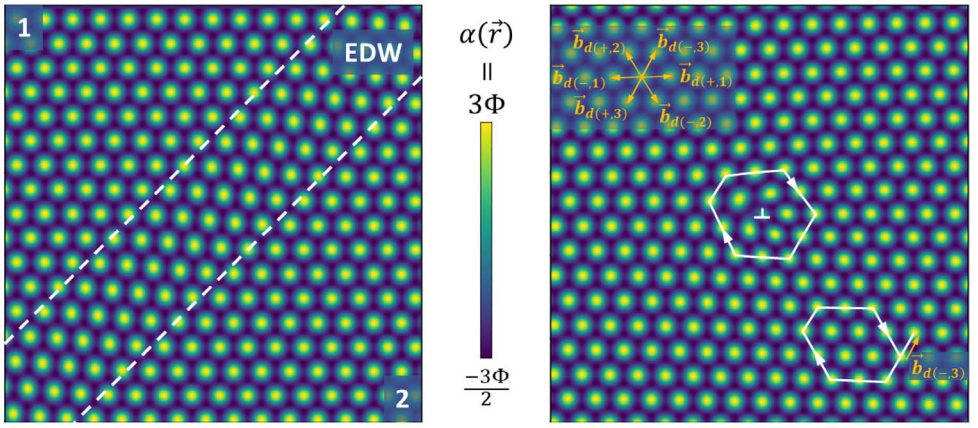

Figure 11. Spatial dependence of the I-CDW order parameter $\alpha(\vec{r})$ in a layer of 1T-TaS_2. (a) An extended domain wall (EDW) separates region 1 where the CDW-phases are $\theta_I^1 = \theta_I^2 = \theta_I^3 = 0$, and region 2 where $\theta_I^1 = -\pi$, $\theta_I^2 = \pi$ and $\theta_I^3 = 0$. (b) A dislocation is marked by the symbol $\perp$. Building the Burgers circuits around the dislocation and in a dislocation-free zone allows one to determine the Burgers vector of the dislocation, $\vec{b}_{d(-,3)}$. The 6 possible Burgers vectors of a I-CDW dislocation are depicted in the upper left part of the figure.

change of the atomic potential, are indeed expected to give rise to similar distributions of the CDW-phases $\theta_{I^*}^j(\vec{r})$. Let us note that the variation of the CDW-phases $\theta_{I^*}^j$ across CDW-phase domain boundaries causes an increase of the total internal energy that scales with the CDW-phase gradients squared [43]. As a consequence, the I*-CDW-phase domains are more likely separated by extended domain walls (Figure 11a) than by the sharp domains walls represented in Figure 6b, extended domains walls allowing a reduction of the CDW-phase gradients.

In addition to the elastic deformations of the I*-CDW described above, edge dislocations are susceptible to form in the CDW hexagonal lattice [43]. In analogy with edge dislocations in atomic lattices, it is expected that their Burgers vectors $\vec{b}_d$ link a maximum of the charge density with one of its six nearest neighbours, yielding 6 possibilities (Figure 11b): $\vec{b}_d(\pm, j) = \pm 2\pi / \| \vec{q}_{I^*}^{\parallel} \| \times \vec{q}_{I^*}^{\parallel j}$ ($j = 1,2,3$). Such dislocations were indeed found to appear in a time-dependent Ginzburg–Landau simulation of the formation of the I*-CDW [34]. This simulation showed that dislocations have already been formed 20 ps after laser excitation. However, the results available make it difficult to discuss whether the dislocations are created during coalescence of individual I*-CDW phase regions after a nucleation-growth process, or by another source of strain on the I*-CDW. In a scenario where dislocations are created during coalescence of defect-free I*-CDW phase regions in 1T-TaS_2, their Burgers vectors are expected to depend both on the orientation of the interfaces and on the CDW-phase differences between the regions. The possible configurations are in this case infinite, yielding a random distribution of each of the 6 types of dislocations.

4.3. *Phase ordering*

4.3.1. *Models for phase ordering*

Both extended domain walls and edge dislocations can evolve in time to let the correlation length increase (so-called phase-ordering processes).

When extended domain walls are present, the free energy is lowered by a reduction of the total domain wall area, through coarsening of the domain pattern. In this case, the average domain size (or I*-CDW correlation length) obeys a power-law scaling to time, following the Allen–Cahn growth law $\xi_{I^*} \propto \tau^{0.5}$ suitable for systems with non-conserved order parameters [65].

As mentioned previously, edge dislocations may also be present and limit the correlation length ξ_{I^*}. In this case, phase-ordering proceeds through a reduction of their total number, via pair annihilation of dislocations with opposite Burgers vectors. This process is driven by an attractive elastic interaction force with $1/r$ dependence (Peach–Koehler force) [66]. The problem of defect–antidefect pair annihilation has been studied theoretically in isotropic two-dimensional media where randomly distributed dislocations with $\vec{b}_d$ and $-\vec{b}_d$ Burgers vectors are present [67]. The surface density of defects is shown to decrease with a τ^{-1} behaviour. The correlation length ξ, defined as the average distance between two defects, then increases following $\tau^{0.5}$. In the case of a layer of 1T-TaS_2 the situation is more complex, as three types of defect-antidefect pairs coexist: $\vec{b}_{d(+,j)}$ and $\vec{b}_{d(-,j)}$ with $j = 1,2,3$. Dislocations with Burgers vectors $\vec{b}_{d(\pm,j)}$ and $\vec{b}_{d(\pm,j')}$ $(j' \neq j)$ are susceptible to interact elastically without being annihilated, which gives a *diffusive character* to their motions. In a diffusive motion regime and two-dimensional space, the surface density of randomly distributed defects is shown to decrease following a $\tau^{-0.5}$ power law [68]: correlation lengths then increase with a $\tau^{0.25}$ behaviour.

Both extended domain walls and edge dislocations are expected to be present in the photoinduced I*-CDW phase of 1T-TaS_2, each type of defect evolving according to its own dynamics. The growth kinetics of the CDW-phase domains is thus susceptible to strongly depend on the relative numbers of both types of defects. According to the above-mentioned models, domain coarsening following a τ^p power law is likely to be observed, with $0.25 \leq p \leq 0.5$. However, it is not excluded that the p exponent evolves with time, if the relative proportions of extended domain walls and edge dislocations change as a consequence of their distinct dynamics.

4.3.2. *Phase ordering as observed in the photoinduced I*-CDW phase*

The phase ordering process corresponds to an increase of the correlation length in a single region where the order parameter has already reached its equilibrium value. It thus translates into a coarsening of the domain pattern. In CDW systems, experimental evidence for phase ordering requires simultaneous measurement and analysis of the intensity and width of a CDW satellite peak. To our knowledge, coarsening of the CDW-phase domains was unambiguously observed only in the present work and in Ref. [32]. The data presented in this work show that, in the (25 ps–50 ns) range of pump–probe delays studied, the photoinduced I*-CDW phase undergoes phase-ordering in the $(\vec{a},\vec{b})$ plane with a $\tau^{0.22(4)}$ length-scaling. In Ref. [32], the I*-CDW phase was found to undergo phase-ordering in the $(\vec{a},\vec{b})$ plane with a $\tau^{0.5}$ length-scaling in the (100–500 ps) pump–probe delay range. Both experiments reveal domain coarsening, with correlation lengths increasing according to power laws in time τ^p. While the p exponents both fall in the range predicted by theoretical models, those differ significantly from one experiment to the other.

These markedly different behaviours might originate from the different excitation wavelengths and absorbed fluences used in Ref. [32] (1550 nm, 6.9 mJ/cm^2) and in the present work (800 nm, 3.9 mJ/cm^2), which results in differing depth-dependent profiles of absorbed energy density and, in turn, in differing profiles of quasi-equilibrium temperature once the excitation energy is transferred to the lattice after few picoseconds. Recalling that the growth kinetics of nucleated regions depends on temperature [69], one could propose that at the time of coalescence, the relative speeds of the I*-CDW phase fronts strongly differ in both experiments. This, in turn, could yield different distributions of extended domain walls and CDW-dislocations in the short-range correlated I*-CDW state, thereby influencing the coarsening dynamics.

Note that in the thick samples used for X-ray diffraction studies, the I*-CDW develops only close to the surface owing to the limited penetration depth of either the 800 nm or the 1550 nm photons of the pump pulse. Growth in the c-axis direction might be hindered by the small excitation depth, with possible repercussions on the growth or coarsening in the $(\vec{a},\vec{b})$ plane. In this respect, another explanation for the observation of the distinct coarsening dynamics following 800 nm (this work) and 1550 nm excitations (Ref. [32]) could stem from the differing excitation depths δ_L of 800 nm and 1550 nm photons, which amount 30 nm and 45 nm respectively.

Overall, the results presented in this work and Ref. [32] indicate that the kinetics of domain coarsening might depend on several parameters including the type of defects created in the I*-CDW and their distribution, as well as the limited extent of the I*-CDW in the c-axis direction. Determining the exact role of each of those parameters in the kinetics of phase ordering calls for additional experiments in thin samples (10 nm), using various excitation wavelengths and laser fluences.

4.3.3. *CDW dislocations and self-doping in the photoinduced I*-CDW phase*

Edge dislocations in CDWs are characterized by a local cancellation of the CDW-amplitude and a dipolar charge distribution associated with the π CDW-phase shift [66], which yields bound electronic states with energies distributed just below the Fermi energy (intra-CDW-gap states) [70]. Electrons trapped in those states do not belong to the CDW condensate, tantamount to a self-hole-doping in presence of CDW edge dislocations. The transient shortening of $q^{\parallel}_{I^*}$, which we attributed to a transient hole-doping of the photoinduced I*-CDW in Section 3.2.2, thus likely originates from the presence of dislocations in the I*-CDW phase. As coarsening occurs, the number of dislocations progressively decreases through pair-annihilation, thereby reducing the density of states of the intra-CDW-gap trapping sites. This, in turn, would explain the regular increase of $q^{\parallel}_{I^*}$ in the pump–probe delay range (25 ps–50 ns), towards its equilibrium value. It is interesting to note that in the experiment of Ref. [33], where the growth of isolated and *defect-free* I*-CDW regions was observed over an extended delay range (50 ps–10 ns), no significant changes of $q^{\parallel}_{I^*}$ could be detected despite a q-resolution comparable to the present experiment. This further supports the idea that the dynamics of $q^{\parallel}_{I^*}$ observed in the present work is related to the time-evolution of defects of the I*-CDW, in the form of I*-CDW dislocation annihilations.

The proportion of trapped electrons in the photoinduced I*-CDW phase can be inferred from the $q^{\parallel}_{I}$ dependence observed in chemically hole-doped samples. In 1T-$(Ta_{1-x}Ti_x)S_2$ for instance, Ta-atoms bring one conduction electron each, while Ti-atoms do not bring any: x then represents the fraction of holes among conduction electrons. Wilson *et al.* determined that $q^{\parallel}_{I}(x) = q^{\parallel}_{I}(x=0) \times [1 - 0.5327x]$ for $x \leq 0.25$ [62]. In 1T-TaS_2 at $\tau = 25$ ps, when the I*-CDW wave vector exhibits its smallest length, the ratio $q^{\parallel}_{I^*}/q^{\parallel}_{I}$ amounts 0.9969 (Figure 10b). This translates into a fraction $x_t(\tau = 25\text{ ps}) = 0.58\%$ of trapped electrons among conduction electrons or, equivalently, a surface density of trapped electrons $\rho_t(\tau = 25\text{ ps}) = (x_t(\tau = 25\text{ ps}))/(a^2 \times \sin(120)) = 5.9 \times 10^{-2}$ nm^{-2}. The average number of trapped electrons per dislocation can also be estimated. The I*-CDW correlation length in the $(\vec{a},\vec{b})$ plane allows calculating the surface density of dislocations: $\rho_d(\tau = 25\text{ ps}) = 4/\pi\xi^2_{a,b} = 1.4 \times 10^{-3}$ nm^{-2}. It follows that about 40 electrons would be trapped at each dislocation site.

Putting together the elements given in Section 3.2.2 and above, the complete scenario would be the following. The photoinduced I*-CDW phase differs from the I-CDW phase observed at equilibrium by the presence of topological defects, namely extended domain walls and CDW dislocations, which are formed at the time of coalescence of the nucleated I*-CDW phase regions. The dipolar charge distributions associated with CDW dislocations trap a fraction of the conduction electrons into intra-CDW-gap states, which lowers the Fermi energy and shrinks the

Fermi surface. The I-CDW modulation, which is driven by nesting of the Fermi surface, then exhibits a shorter wave vector $\vec{q}^{\parallel}_{I^*}$ as compared to the equilibrium I-CDW phase. As for the dynamics, the correlation lengths of the I*-CDW phase progressively increase on the ns timescale, owing to, among others, CDW dislocation annihilations. This causes a reduction of the density of intra-CDW-gap states and, in turn, an increase of the Fermi energy towards its equilibrium value. Concomitantly, the Fermi surface expands and the nesting vector $\vec{q}^{\parallel}_{I^*}$ elongates as shown in Figure 10b.

5. Summarizing conclusion and outlook

Based on the results of the present experiment and those of Refs. [32, 33], we built an improved description of the mechanisms at work behind the photoinduced NC → I phase transition in 1T-TaS_2. The photoinduced I*-CDW phase appears in the form of nuclei which subsequently grow. At this stage, the I*-CDW correlation lengths were shown to be limited by the size of the isolated I*-CDW regions [33], which highlights the absence of defects within those. The incommensurate nature of the I*-CDW enables an infinite number of energetically equivalent possibilities to position the charge density maxima relative to the underlying atomic lattice. Each isolated I*-CDW region is thus characterized by a distinct set of CDW-phases $(\theta^1_{I^*}, \theta^2_{I^*}, \theta^3_{I^*})$. When coalescence occurs, a single I*-CDW phase region emerges. It is fragmented into CDW-phase domains, reminiscent of the isolated I*-CDW regions with distinct CDW-phases. At this stage, the I*-CDW correlation length corresponds to the average distance between defects in the charge density modulation. CDW-phase accommodations between two adjacent domains can be achieved by two types of defects: extended domain walls and CDW-dislocations. Domain wall motions and dislocation annihilations allow the correlation lengths to increase, in a so-called phase-ordering process. In this regime, a self-similar growth of the CDW-phase domain pattern is observed with τ^p length-scaling (this work and Ref. [32]). p-exponents in the range (0.22–0.5) can be retrieved from the available experimental data, which compares reasonably well with the results of existing theories on coarsening [65, 67, 68].

In the present work, we have shown that the photoinduced I*-CDW phase differs from the I-CDW phase at equilibrium, not only by its limited correlation length, but also by a larger period of the CDW modulation (shorter wave vector of the CDW). We propose that the increased period of the I*-CDW modulation would be due to a smaller number of conduction electrons involved in the collective CDW state, some of them being trapped at CDW-dislocation sites. In this view, the I*-CDW appears as a hole-doped I-CDW.

This and previous works [32] indicate that the kinetics of phase ordering in the photoinduced I*-CDW phase could be influenced by the distribution of extended domain walls and CDW-dislocations. The latter distribution arises from complex interactions between nucleated regions at the time of coalescence, which likely depend on the quasi-equilibrium temperature reached once the laser pulse energy is transferred to the lattice. The next challenge will certainly consist in achieving a complete description of defect formation in the photoinduced I*-CDW. In this view, performing wavelength-dependent studies at short timescales, when coalescence of the initially formed I*-CDW regions occurs, would be of high interest.

Acknowledgements

We wish to warmly thank Philippe Hollander (SOLEIL synchrotron) for his continuous efforts toward improving laser operation at CRISTAL beamline, as well as Frédéric Picca (SOLEIL synchrotron) for his precious help at the time of integrating functionalities of the GHKL library into our analysis scripts. We acknowledge SOLEIL for provision of synchrotron radiation at CRISTAL beamline (proposal number 20171529).

References

[1] E. Dagotto, "Correlated electrons in high-temperature superconductors", *Rev. Mod. Phys.* **66** (1994), p. 763-840.

[2] M. Imada, A. Fujimori, Y. Tokura, "Metal–insulator transitions", *Rev. Mod. Phys.* **70** (1998), p. 1039-1263.

[3] K. Nasu, *Photoinduced Phase Transitions*, World Scientific Publishing, Singapore, 2004.

[4] K. Yonemitsu, K. Nasu, "Theory of photoinduced phase transitions in itinerant electron systems", *Phys. Rep.* **465** (2008), p. 1-60.

[5] J. Zhang, R. D. Averitt, "Dynamics and control in complex transition metal oxides", *Annu. Rev. Mater. Res.* **44** (2014), p. 19-43.

[6] D. N. Basov, R. D. Averitt, D. Hsieh, "Towards properties on demand in quantum materials", *Nat. Mater.* **16** (2017), p. 1077-1088.

[7] E. Janod, J. Tranchant, B. Corraze, M. Querre, P. Stoliar, M. Rozenberg, T. Cren, D. Roditchev, V. T. Phuoc, M.-P. Besland, L. Cario, "Resistive switching in mott insulators and correlated systems", *Adv. Funct. Mater.* **25** (2015), p. 6287-6305.

[8] A. Singer, S. K. K. Patel, R. Kukreja, V. Uhlíř, J. Wingert, S. Festersen, D. Zhu, J. M. Glownia, H. T. Lemke, S. Nelson, M. Kozina, K. Rossnagel, M. Bauer, B. M. Murphy, O. M. Magnussen, E. E. Fullerton, O. G. Shpyrko, "Photoinduced enhancement of the charge density wave amplitude", *Phys. Rev. Lett.* **117** (2016), article no. 056401.

[9] V. L. R. Jacques, C. Laulhé, N. Moisan, S. Ravy, D. L. Bolloc'h, "Laser-induced charge-density-wave transient depinning in chromium", *Phys. Rev. Lett.* **117** (2016), article no. 156401.

[10] P. Stoliar, J. Tranchant, B. Corraze, E. Janod, M.-P. Besland, F. Tesler, M. Rozenberg, L. Cario, "A leaky-integrate-and-fire neuron analog realized with a mott insulator", *Adv. Funct. Mater.* **27** (2017), article no. 1604740.

[11] C. Adda, B. Corraze, P. Stoliar, P. Diener, J. Tranchant, A. Filatre-Furcate, M. Fourmigué, D. Lorcy, M.-P. Besland, E. Janod, L. Cario, "Mott insulators: a large class of materials for leaky integrate and fire (LIF) artificial neuron", *J. Appl. Phys.* **124** (2018), article no. 152124.

[12] G. Grüner, *Density Waves in Solids*, Perseus Publishing, Cambridge, MA, 2000.

[13] F. Schmitt, P. Kirchmann, U. Bovensiepen, R. Moore, L. Rettig, M. Krenz, J.-H. Chu, N. Ru, L. Perfetti, D. Lu, M. Wolf, I. Fisher, Z.-X. Shen, "Transient electronic structure and melting of a charge density wave in $TbTe_3$", *Science* **321** (2008), p. 1649-1652.

[14] A. Tomeljak, H. Schäfer, D. Städter, M. Beyer, K. Biljakovic, J. Demsar, "Dynamics of photoinduced charge-density-wave to metal phase transition in $K_{0.3}MoO_3$", *Phys. Rev. Lett.* **102** (2009), article no. 066404.

[15] R. Yusupov, T. Mertelj, V. V. Kabanov, S. Brazovskii, P. Kusar, J.-H. Chu, I. R. Fisher, D. Mihailovic, "Coherent dynamics of macroscopic electronic order through a symmetry-breaking transition", *Nat. Phys.* **6** (2010), p. 681-684.

[16] M. Eichberger, H. Schäfer, M. Krumova, M. Beyer, J. Demsar, H. Berger, G. Moriena, G. Sciaini, R. J. D. Miller, "Snapshots of cooperative atomic motions in the optical suppression of charge density waves", *Nature* **468** (2010), p. 799-802.

[17] S. Hellmann, M. Beye, C. Sohrt, T. Rohwer, F. Sorgenfrei, H. Redlin, M. Kallaäne, M. Marczynski-Bühlow, F. Hennies, M. Bauer, A. Föhlisch, L. Kipp, W. Wurth, K. Rossnagel, "Ultrafast melting of a charge-density wave in the mott insulator 1T-TaS_2", *Phys. Rev. Lett.* **105** (2010), article no. 187401.

[18] T. Rohwer, S. Hellmann, M. Wiesenmayer, C. Sohrt, A. Stange, B. Slomski, A. Carr, Y. Liu, L. Avila, M. Kalläne, S. Mathias, L. Kipp, K. Rossnagel, M. Bauer, "Collapse of long-range charge order tracked by time-resolved photoemission at high momenta", *Nature* **471** (2011), p. 490-493.

[19] E. Möhr-Vorobeva, S. L. Johnson, P. Beaud, U. Staub, R. Desouza, C. Milne, G. Ingold, J. Demsar, H. Schaefer, A. Titov, "Nonthermal melting of a charge density wave in $TiSe_2$", *Phys. Rev. Lett.* **107** (2011), article no. 036403.

[20] S. Hellmann, T. Rohwer, M. Kalläne, K. Hanff, C. Sohrt, A. Stange, A. Carr, M. Murnane, H. Kapteyn, L. Kipp, M. Bauer, K. Rossnagel, "Time-domain classification of charge-density-wave insulators", *Nat. Commun.* **3** (2012), article no. 1069.

[21] T.-R. T. Han, Z. Tao, S. D. Mahanti, K. Chang, C.-Y. Ruan, C. D. Malliakas, M. G. Kanatzidis, "Structural dynamics of two-dimensional charge-density waves in $CeTe_3$ investigated by ultrafast electron crystallography", *Phys. Rev. B* **86** (2012), article no. 075145.

[22] N. Erasmus, M. Eichberger, K. Haupt, I. Boshoff, G. Kassier, R. Birmurske, H. Berger, J. Demsar, H. Schwoerer, "Ultrafast dynamics of charge density waves in $4H_b$–$TaSe_2$ probed by femtosecond electron diffraction", *Phys. Rev. Lett.* **109** (2012), article no. 167402.

[23] P. Zhu, J. Cao, Y. Zhu, J. Geck, Y. Hidaka, S. Pjerov, T. Ritschel, H. Berger, Y. Shen, R. Tobey, J. P. Hill, X. J. Wang, "Dynamic separation of electron excitation and lattice heating during the photoinduced melting of the periodic lattice distortion in 2H-$TaSe_2$", *Appl. Phys. Lett.* **103** (2013), article no. 071914.

[24] T. Huber, S. O. Mariager, A. Ferrer, H. Schäfer, J. A. Johnson, S. Grübel, A. Lübcke, L. Huber, T. Kubacka, C. Dornes, C. Laulhé, S. Ravy, G. Ingold, P. Beaud, J. Demsar, S. L. Johnson, "Coherent structural dynamics of a prototypical charge-density-wave-to-metal transition", *Phys. Rev. Lett.* **113** (2014), article no. 026401.

[25] A. Zong, A. Kogar, Y.-Q. Bie, T. Rohwer, C. Lee, E. Baldini, E. Ergeçen, M. B. Yilmaz, B. Freelon, E. J. Sie, H. Zhou,

J. Straquadine, P. Walmsley, P. E. Dolgirev, A. V. Rozhkov, I. R. Fisher, P. Jarillo-Herrero, B. V. Fine, N. Gedik, "Evidence for topological defects in a photoinduced phase transition", *Nat. Phys.* **15** (2019), p. 27-31.

[26] A. Zong, P. E. Dolgirev, A. Kogar, E. Ergeçen, M. B. Yilmaz, Y.-Q. Bie, T. Rohwer, I.-C. Tung, J. Straquadine, X. Wang, Y. Yang, X. Shen, R. Li, J. Yang, S. Park, M. C. Hoffmann, B. K. Ofori-Okai, M. E. Kozina, H. Wen, X. Wang, I. R. Fisher, P. Jarillo-Herrero, N. Gedik, "Dynamical slowing-down in an ultrafast photoinduced phase transition", *Phys. Rev. Lett.* **123** (2019), article no. 097601.

[27] M. Trigo, P. Giraldo-Gallo, M. E. Kozina, T. Henighan, M. P. Jiang, H. Liu, J. N. Clark, M. Chollet, J. M. Glownia, D. Zhu, T. Katayama, D. Leuenberger, P. S. Kirchmann, I. R. Fisher, Z. X. Shen, D. A. Reis, "Coherent order parameter dynamics in $SmTe_3$", *Phys. Rev. B* **99** (2019), article no. 104111.

[28] S. Sun, L. Wei, Z. Li, G. Cao, Y. Liu, W. J. Lu, Y. P. Sun, H. Tian, H. Yang, J. Li, "Direct observation of an optically induced charge density wave transition in 1T-$TaSe_2$", *Phys. Rev. B* **92** (2015), article no. 224303.

[29] T.-R. T. Han, F. Zhou, C. D. Malliakas, P. M. Duxbury, S. D. Mahanti, M. G. Kanatzidis, C.-Y. Ruan, "Exploration of metastability and hidden phases in correlated electron crystals visualized by femtosecond optical doping and electron crystallography", *Sci. Adv.* **1** (2015), article no. e1400173.

[30] K. Haupt, M. Eichberger, N. Erasmus, A. Rohwer, J. Demsar, K. Rossnagel, H. Schwoerer, "Ultrafast metamorphosis of a complex charge-density wave", *Phys. Rev. Lett.* **116** (2016), article no. 016402.

[31] L. L. Guyader, T. Chase, A. H. Reid, R. K. Li, D. Svetin, X. Shen, T. Vecchione, X. J. Wang, D. Mihailovic, H. A. Dürr, "Stacking order dynamics in the quasi-two-dimensional dichalcogenide 1T-TaS_2 probed with mev ultrafast electron diffraction", *Struct. Dyn.* **4** (2017), article no. 044020.

[32] C. Laulhé, T. Huber, G. Lantz, A. Ferrer, S. O. Mariager, S. Grübel, J. Rittmann, J. A. Johnson, V. Esposito, A. Lübcke, L. Huber, M. Kubli, M. Savoini, V. L. R. Jacques, L. Cario, B. Corraze, E. Janod, G. Ingold, P. Beaud, S. L. Johnson, S. Ravy, "Ultrafast formation of a charge density wave state in 1T-TaS_2: observation at nanometer scales using time-resolved X-ray diffraction", *Phys. Rev. Lett.* **118** (2017), article no. 247401.

[33] G. Lantz, C. Laulhé, S. Ravy, M. Kubli, M. Savoini, K. Tasca, E. Abreu, V. Esposito, M. Porer, A. Ciavardini, L. Cario, J. Rittmann, P. Beaud, S. L. Johnson, "Domain-size effects on the dynamics of a charge density wave in 1T-TaS_2", *Phys. Rev. B* **96** (2017), article no. 224101.

[34] S. Vogelgesang, G. Storeck, J. G. Horstmann, T. Diekmann, M. Sivis, S. Schramm, K. Rossnagel, S. Schäfer, C. Ropers, "Phase ordering of charge density waves traced by ultrafast low-energy electron diffraction", *Nat. Phys.* **14** (2018), p. 184-190.

[35] L. Stojchevska, I. Vaskivskyi, T. Mertelj, P. Kusar, D. Svetin, S. Brazovskii, D. Mihailovic, "Ultrafast switching to a stable hidden quantum state in an electronic crystal", *Science* **344** (2014), p. 177-180.

[36] Y. A. Gerasimenko, P. Karpov, I. Vaskivskyi, S. Brazovskii, D. Mihailovic, "Intertwined chiral charge orders and topological stabilization of the light-induced state of a prototypical transition metal dichalcogenide", *NPJ Quantum Mater.* **4** (2019), article no. 32.

[37] A. Kogar, A. Zong, P. E. Dolgirev, X. Shen, J. Straquadine, Y.-Q. Bie, X. Wang, T. Rohwer, I.-C. Tung, Y. Yang, R. Li, J. Yang, S. Weathersby, S. Park, M. E. Kozina, E. J. Sie, H. Wen, P. Jarillo-Herrero, I. R. Fisher, X. Wang, N. Gedik, "Light-induced charge density wave in $LaTe_3$", *Nat. Phys.* **16** (2019), p. 159-163.

[38] D. Mihailovic, "The importance of topological defects in photoexcited phase transitions including memory applications", *Appl. Sci.* **9** (2019), article no. 890.

[39] J. A. Wilson, F. J. di Salvo, S. Mahajan, "Charge-density waves and superlattices in the metallic layered transition metal dichalcogenides", *Adv. Phys.* **24** (1975), p. 117-201.

[40] T. Ishiguro, H. Sato, "Electron microscopy of phase transformations in 1T-TaS_2", *Phys. Rev. B* **44** (1991), no. 5, p. 2046-2060.

[41] A. Spijkerman, J. L. de Boer, A. Meetsma, G. A. Wiegers, S. van Smaalen, "X-ray crystal-structure refinement of the nearly commensurate phase of 1T-TaS_2 in (3 + 2)-dimensional superspace", *Phys. Rev. B* **56** (1997), no. 21, p. 13757-13767.

[42] K. Rossnagel, "On the origin of charge-density waves in selected layered transition-metal dichalcogenides", *J. Phys. Condens. Matter* **23** (2011), article no. 213001.

[43] W. L. McMillan, "Landau theory of charge-density waves in transition-metal dichalcogenides", *Phys. Rev. B* **12** (1975), p. 1187-1196.

[44] K. Momma, F. Izumi, "Vesta 3 for three-dimensional visualization of crystal, volumetric and morphology data", *J. Appl. Crystallogr.* **44** (2011), p. 1272-1276.

[45] S. Ravy, C. Laulhé, J. P. Itié, P. Fertey, B. Corraze, S. Salmon, L. Cario, "High-pressure X-ray diffraction study of 1T-TaS_2", *Physica B* **407** (2012), p. 1704-1706.

[46] A. Beal, H. Hughes, W. Liang, "The reflectivity spectra of some group va transition metal dichalcogenides", *J. Phys., C, Solid State Phys.* **8** (1975), p. 4236-4248.

[47] M.-A. Tordeux, J. Barros, A. Bence, P. Brunelle, N. Hubert, M. Labat, A. Nadji, L. Nadolski, P. Lebasque, J.-P. Pollina, C. Evain, "Low-alpha operation for the soleil storage ring", in *Proceedings of the 2012 International Particle Accelerator Conference (IPAC12)*, JACoW - Joint Accelerator Conferences Website, Geneva, 2012, p. 1608-1610.

[48] B. Henke, E. Gullikson, J. Davis, "X-ray interactions: photoabsorption, scattering, transmission, and reflection at e = 50–30000 eV, z = 1–92", *At. Data Nucl. Data Tables* **54** (1993), p. 181-342.
[49] K. Medjoubi, S. Hustache, F. E. Picca, J. Bérar, N. Boudet, F. Bompard, P. Breugnon, J.-C. Clémens, A. Dawiec, P. Delpierre, B. Dinkenspiler, S. Godiot, J.-P. Logier, M. Menouni, C. Morel, M. Nicolas, P. Pangaud, E. Vigeolas, "Performance and applications of the CdTe- and Si-XPAD3 photon counting 2D detector", *J. Instrum.* **6** (2011), article no. C01080.
[50] J.-P. Ricaud, P. Betinelli-Deck, J. Bisou, X. Elattaoui, C. Laulhé, P. Monteiro, L. S. Nadolski, G. Renaud, S. Ravy, M. Silly, F. Sirotti, "The timbel synchronization board for time-resolved experiments at synchrotron soleil", in *Proceedings of the 2011 International Conference on Accelerator and Large Experimental Physics Control Systems (ICALEPCS2011)*, JACoW - Joint Accelerator Conferences Website, Geneva, 2011, p. 1036-1038.
[51] L. Perfetti, P. A. Loukakos, M. Lisowski, U. Bovensiepen, H. Berger, S. Biermann, P. S. Cornaglia, A. Georges, M. Wolf, "Time evolution of the electronic structure of 1T-TaS_2 through the insulator–metal transition", *Phys. Rev. Lett.* **97** (2006), article no. 067402.
[52] L. Perfetti, P. A. Loukakos, M. Lisowski, U. Bovensiepen, M. Wolf, H. Berger, S. Biermann, A. Georges, "Femtosecond dynamics of electronic states in the mott insulator 1T-TaS_2 by time resolved photoelectron spectroscopy", *New J. Phys.* **10** (2008), article no. 053019.
[53] L. Rettig, R. Cortés, J.-H. Chu, I. R. Fisher, F. Schmitt, R. G. Moore, Z.-X. Shen, P. S. Kirchmann, M. Wolf, U. Bovensiepen, "Persistent order due to transiently enhanced nesting in an electronically excited charge density wave", *Nat. Commun.* **7** (2016), article no. 10459.
[54] P. Monceau, "Electronic crystals: an experimental overview", *Adv. Phys.* **61** (2012), p. 325-581.
[55] F. E. Picca, Ghkl's documentation [https://people.debian.org/~picca/hkl/hkl.html], Université Paris-Saclay (Synchrotron SOLEIL), 91190, Saint-Aubin, France.
[56] C. Thomsen, H. T. Grahn, H. J. Maris, J. Tauc, "Surface generation and detection of phonons by picosecond light pulses", *Phys. Rev. B* **34** (1986), p. 4129-4138.
[57] S. Lee, G. J. Williams, M. I. Campana, D. A. Walko, E. C. Landahl, "Picosecond X-ray strain rosette reveals direct laser excitation of coherent transverse acoustic phonons", *Sci. Rep.* **6** (2016), article no. 19140.
[58] K. Motizuki (ed.), *Structural Phase Transitions in Layered Transition Metal Compounds*, Springer, Netherlands, 1986.
[59] C. B. Scruby, P. M. Williams, G. S. Parry, "The role of charge density waves in structural transformations of 1T-TaS_2", *Philos. Mag.* **31** (1975), p. 255-274.
[60] K. Nakanishi, H. Takatera, Y. Yamada, H. Shiba, "The nearly commensurate phase and effect of harmonics on the successive phase transitions in 1T-TaS_2", *J. Phys. Soc. Japan* **43** (1977), p. 1509-1517.
[61] J. van Landuyt, G. van Tendeloo, S. Amelinckx, "Electron diffraction study of inter- and intrapolytypic phase transition in transition metal dichalcogenides. III. complementary diffraction studies and lattice imaging of the deformation waves", *Phys. Status Solidi A* **36** (1976), p. 757-777.
[62] J. A. Wilson, F. J. di Salvo, S. Mahajan, "Charge-density waves in metallic, layered, transition-metal dichalcogenides", *Phys. Rev. Lett.* **32** (1974), p. 882-885.
[63] L. F. Mattheiss, "Band structures of transition-metal-dichalcogenide layer compounds", *Phys. Rev. B* **8** (1973), p. 3719-3740.
[64] J.-D. Su, A. R. Sandy, J. Mohanty, O. G. Shpyrko, M. Sutton, "Collective pinning dynamics of charge-density waves in 1T-TaS_2", *Phys. Rev. B* **86** (2012), article no. 205105.
[65] A. J. Bray, "Theory of phase-ordering kinetics", *Adv. Phys.* **51** (2002), p. 481-587.
[66] D. Feinberg, J. Friedel, "Elastic and plastic deformations of charge density waves", *J. Phys. (France)* **49** (1988), p. 485-496.
[67] H. Toyoki, "Pair annihilation of pointlike topological defects in the ordering process of quenched systems", *Phys. Rev. A* **42** (1990), p. 911-917.
[68] D. Toussaint, F. Wilczek, "Particle-antiparticle annihilation in diffusive motion", *J. Chem. Phys.* **78** (1983), p. 2642-2647.
[69] P. Papon, J. Leblond, P. H. E. Meijer, *The Physics of Phase Transitions: Concepts and Applications*, Springer, Netherlands, 2006.
[70] K. Maki, X. Z. Huang, "Phase vortices in charge-density-wave conductors", *Phys. Rev. B* **37** (1988), p. 8668-8673.

Comptes Rendus
Physique
2021, 22, nº S2, p. 161-184
https://doi.org/10.5802/crphys.44

Physics of ultra-fast phenomena / *Physique des phénomènes ultra-rapides*

Light-control of materials via nonlinear phononics

Alaska Subedi [a, b]

[a] CPHT, CNRS, Ecole Polytechnique, IP Paris, F-91128 Palaiseau, France

[b] Collège de France, 11 place Marcelin Berthelot, 75005 Paris, France

E-mail: alaska.subedi@polytechnique.edu

Abstract. Nonlinear phononics is the phenomenon in which a coherent dynamics in a material along a set of phonons is launched after its infrared-active phonons are selectively excited using external light pulses. The microscopic mechanism underlying this phenomenon is the nonlinear coupling of the pumped infrared-active mode to other phonon modes present in a material. Nonlinear phonon couplings can cause finite time-averaged atomic displacements with or without broken crystal symmetries depending on the order, magnitude and sign of the nonlinearities. Such coherent lattice displacements along phonon coordinates can be used to control the physical properties of materials and even induce transient phases with lower symmetries. Light-control of materials via nonlinear phononics has become a practical reality due to the availability of intense mid-infrared lasers that can drive large-amplitude oscillations of the infrared-active phonons of materials. Mid-infrared pump induced insulator–metal transitions and spin and orbital order melting have been observed in pump–probe experiments. First principles based microscopic theory of nonlinear phononics has been developed, and it has been used to better understand how the lattice evolves after a mid-infrared pump excitation of infrared-active phonons. This theory has been used to predict light-induced switching of ferroelectric polarization as well as ferroelectricity in paraelectrics and ferromagnetism in antiferromagnets, which have been partially confirmed in recent experiments. This review summarizes the experimental and theoretical developments within this emerging field.

Keywords. Nonlinear phononics, Ultrafast control, Light-matter interaction, Mode-selective control, Light-induced phonon dynamics.

Available online 18th March 2021

1. Introduction

Light is a popular probe that is widely used to investigate the structure and properties of materials. However, light has seldom been used to coherently control materials, notwithstanding its use as a source of heat. New methods for modifying crystal structures can lead to previously unexplored structures with unusual physical properties. Therefore, there is much interest in developing a technique to control materials using light in the hope that this can be used to stabilize hitherto unknown structures that have not been accessed using pressure, heterostructuring or isovalent chemical doping.

On the practical side, light-control of materials requires intense laser sources that excite materials and examine the excited state. Such pump–probe laser setups were pioneered in chemistry laboratories, and their development was instigated by the dream of controlling chemical reactions by selectively exciting bond-specific vibrations using ultrashort laser pulses [1]. In a thermodynamically activated chemical reaction, statistical laws imply that indiscriminately imparted energy to the reactants cause large amplitude atomic vibrations along the weak bonds, which then get ruptured. By using an intense laser pulse to induce large amplitude vibrations along a stronger bond-stretching mode, it has been shown that it is possible to modify the chemical reaction pathway and obtain a different set of products [2]. However, bond-selective light-control of chemical reactions has only been successful in relatively simple molecules with few atoms [3]. In complex molecules, it has been found that the vibrational energy in the pumped mode is quickly redistributed to other modes present in the molecule, and the pumped mode dissipates and dephases before the amplitude of its vibration becomes large [4].

Vibrational energy redistribution occurs due to nonlinear couplings between the vibrational modes of a molecule [5, 6]. Two-dimensional (2D) pump–probe spectroscopy techniques have been developed that can simultaneously measure the oscillations of the pumped mode and other modes that are nonlinearly coupled to it [7]. This has allowed the determination of the nature and magnitude of the nonlinear couplings, as well as the dissipation and dephasing times of the vibrations. The nonlinear couplings between different vibrational modes appear as off-diagonal peaks in 2D pump–probe spectroscopy measurements. In addition to the lowest-order $Q_1 Q_2$ coupling between two vibrational mode coordinates Q_1 and Q_2, higher-order $Q_1 Q_2^2$ nonlinearity has also been inferred from the measurements [8, 9]. It has also been noted that $Q_1 Q_2^2$ nonlinearity causes Frank–Condon-like displacement along the vibrational coordinates in the excited state [10].

Although nonlinear couplings between vibrational modes are an impediment to bond-selective chemistry in large molecules, they do lead to observation of coherent vibrations of nonlinearly coupled modes in 2D pump–probe spectroscopy. The discussion of a similar effect in crystalline solids due to nonlinear coupling between phonons starts with the proposal of ionic Raman scattering in the 1970s [11, 12]. These studies showed that infrared-active (IR-active) phonons can play the role of an intermediate state in a Raman scattering process in the presence of a $Q_R Q_{IR}^2$ nonlinear coupling between a Raman-active phonon mode Q_R and an IR-active phonon mode Q_{IR}.

Ionic Raman scattering has not yet been observed in light scattering experiments. However, Först *et al.* observed coherent oscillations at frequencies corresponding to Raman-active phonon modes in their time-resolved reflectivity measurements after a mid-IR pump in metallic $La_{0.7}Sr_{0.3}MnO_3$ [13]. They proposed that these oscillations occur because Raman-active modes are coherently excited when an IR-active phonon mode is externally pumped due to $Q_R Q_{IR}^2$ nonlinearities, and this phenomenon has been called stimulated ionic Raman scattering. In that study, oscillations of the pumped mode were not measured via time-resolved spectroscopy experiments to show that IR-active phonon excitations, and not electronic excitations, are responsible for the coherent oscillations of the Raman-active phonons. However, coherent oscillations at Raman-active phonon frequencies have been observed in insulating $ErFeO_3$ [14] and $LaAlO_3$ [15] in time-resolved spectroscopy experiments after a mid-IR pump, and these experiments do show that the amplitude of the oscillations are largest when the pump frequency is tuned to the frequency of the IR-active phonon mode. Moreover, oscillations of the pumped mode as well as the nonlinearly coupled low-frequency mode have been simultaneously observed after a mid-IR pump in time-resolved second harmonic generation (SHG) experiment on $LiNbO_3$ [16], which conclusively demonstrates the phenonmenon of stimulated ionic Raman scattering.

Först *et al.* have also noted that a Raman-active phonon mode experiences a force proportional to gQ_{IR}^2 in the presence of a nonlinear coupling term $gQ_{\mathrm{R}}Q_{\mathrm{IR}}^2$ with coupling constant g [13]. Since the force is proportional to the square of the IR-active phonon coordinate, total force exerted on the Raman-active mode has a nonzero time-averaged value while the IR-active mode is oscillating. This causes the lattice to get displaced along the Raman-active phonon coordinate when the IR-active mode is pumped, and this phenonmena has been termed nonlinear phononics. Time-resolved X-ray diffraction experiments on $La_{0.7}Sr_{0.3}MnO_3$ and $YBa_2Cu_3O_{6.5}$ after an intense mid-IR excitation have found intensity modulation of Bragg peaks of less than 0.5%, and it has been argued that these modulations are due to lattice displacement along Raman-active phonon coordinates [17, 18]. In $YBa_2Cu_3O_{6.5}$, this corresponds to bond length changes of less than 1 pm. Furthermore, these materials are metallic, and oscillations of the pumped mode have not been measured in these experiments to rule out electronic excitation as a cause of the structural changes. More convincing evidence of light-induced displacement due to nonlinear phononics has been proposed [19] and then observed in ferroelectric $LiNbO_3$, which has a high-frequency IR-active phonon with a large oscillator strength [16]. In this material, a strong reduction and sign reversal of the electric dipole moment and a simultaneous oscillation at the frequency of the pumped IR-active mode has been observed in pump–probe SHG experiments. This demonstrates that a coherent displacement of the lattice along a phonon coordinate is feasible at least in insulators that have IR-active phonons with a large oscillator strength.

Coherent lattice displacements due to nonlinear phononics after mid-IR excitations have been attributed to be the cause of insulator–metal transitions in $Pr_{1-x}Ca_xMnO_3$ ($x = 0.3, 0.5$) [20, 21] and $NdNiO_3$ [22], orbital order melting in $La_{0.5}Sr_{1.5}MnO_3$ [23, 24], and magnetic order melting in $NdNiO_3$ [25]. Although phase transitions in these materials occur after a mid-IR pump, neither coherent lattice displacements nor excitations of the pumped IR-active phonon was demonstrated in any of these experiments. Therefore, it is not yet known if lattice displacements due to nonlinear phononics can be large enough to modify the physical properties of materials. Most of the currently reported phase transitions due to mid-IR excitations involve melting of order. Since light pulses always impart heat, it may be infeasible to unambiguously show that melting of order is due to nonlinear phononics because it might not be possible to disentangle the effects of heating and light-induced phonon excitations. Light-control of materials properties via nonlinear phononics can only be conclusive when it involves breaking of symmetries that are present in the equilibrium phase. Light-induced breaking of inversion symmetry in oxide paraelectrics has been theoretically predicted [26], and Nova *et al.* have observed metastable ferroelectricity in $SrTiO_3$ after a mid-IR pump [27]. However, the same effect in $SrTiO_3$ has also been achieved using terahertz pump [28]. So it is not yet clear if the observed mid-IR pump induced ferroelectricity is caused by lattice displacements due to nonlinear phononics.

Mid-IR pump terahertz probe experiments have been performed on several superconductors [29–32]. The reflected electric field transients of probe pulses are enhanced by a few percent in these experiments, and the nonequilibrium state with enhanced reflectivity relaxes to the normal state within 1–2 ps. Although the low-frequency optical conductivity of a short-lived state is not a well defined quantity, the Fourier transform of the reflected electric field transients have been analyzed in terms of frequency-domain optical conductivity. The increased time-dependent reflectivity after a mid-IR pump appears as a low-frequency peak in the imaginary part of the reconstructed optical conductivity $\sigma_2(\omega)$, and this has been interpreted as a signature of light-induced superconductivity. In a true superconducting state, the real part of the optical conductivity $\sigma_1(\omega)$ should concomitantly decrease at low frequencies. However, the reconstructed $\sigma_1(\omega)$ shows an increase at low frequencies. Moreover, there have been no two-dimensional spectroscopy experiments to show that an IR-active phonon mode is actually being pumped while the metastable state with increased reflectivity gets transiently realized, making the connection of

nonlinear phononics phenomena in these experiments rather tenuous. In fact, the reconstructed $\sigma_2(\omega)$ shows a superconductivity-like behaviour after a mid-IR pump in samples where even the IR-active phonon is not observed in optical spectroscopy experiments [32], suggesting that the observed light-induced effect is due to electronic excitations. Since light-induced superconductivity is not apparent in the raw data and only manifests after data analysis, this subject will not be discussed in this review. Readers interested in this subject are pointed to reviews that discuss the mid-IR pump experiments in superconductors in detail [33–35].

Light-induced structural dynamics in crystals has been theoretically studied using molecular dynamics [36] and time-dependent density functional theory calculations [37]. These methods have the advantage of taking into account the light-induced changes in all the dynamical degrees of freedom present in the material. But it is cumbersome to extract the relevant nonlinear couplings between the pumped IR-active mode and coupled Raman-active modes from these methods, which hinders the understanding of the microscopic processes that cause the light-induced phenomena. Subedi *et al.* started the use of a theoretical framework to study nonlinear phononics that is based on symmetry principles to identify the symmetry-allowed nonlinear couplings, first principles calculations of the coefficients of these nonlinear terms, and solution of the equations of the motions for the coupled phonon coordinates [38]. This framework was used to explain the light-induced phenonmena observed in the pioneering mid-IR pump experiments in the manganites [13,20]. Calculations based on this framework was used to reconstruct the mid-IR pump-induced changes in the structure of $YBa_2Cu_3O_{6.5}$ [18] and explain the observation of symmetry-breaking Raman-active modes in orthoferrites [39]. A mechanism for ultrafast switching of ferroelectricity was proposed using this method [19], and a recent observation of momentary reversal of ferroeletricity in $LiNbO_3$ has partially confirmed this prediction [16]. Light-induce ferroelectricity [26] and ferromagnetism [40] have also been proposed, the latter prediction based solely on symmetry arguments. Recent mid-IR pump experiments have observed long-lived metastable ferroelectricity in $SrTiO_3$ [27] and ferromagnetism in $DyFeO_3$ [41] and CoF_2 [42], but the precise mechanisms for these phenomena need to be clarified with further experimental studies. Other theoretical predictions based on the nonlinear phonon couplings that await experimental confirmations include indirect-to-direct band gap switching [43], phono-magnetic analogs of opto-magnetic effects [44], cavity control of nonlinear phonon interactions [45], and excitation of an optically silent mode in $InMnO_3$ [46].

Recent successes in light-control of materials using mid-IR pulses show that nonlinear phononics has an important role to play at the frontier of materials physics. This is further underscored by the construction of several free electron laser sources that have recently come online or are in the process of being built. There have been several reviews of this field that have focused on the experimental aspects of the field [33–35, 47–49]. This review attempts to summarize the experimental and theoretical developments in the field of nonlinear phononics, emphasizing how theoretical calculations have helped the experimentalists drive this field forward.

2. Theoretical approach

In nonlinear phononics experiments, experimentalists are equipped with a light source that can strongly excite some set of IR-active phonons of a material, and they want to understand how the structure and physical properties of the material changes after the phonon excitation. In another situation, experimentalists know a phonon mode associated with an order parameter, and they want to identify the IR-active phonons that should be pumped to alter the ordered state by coherently displacing the lattice along the phonon coordinate of the order parameter. Subedi *et al.* initiated the use of a microscopic theory to quantify the nonlinear couplings between the IR- and Raman-active phonons and predict the light-induced structural dynamics from first

principles [38]. This framework relies on (i) symmetry principles to determine which phonon modes can couple to the pumped IR-active phonon, (ii) first principles calculation of the energy surface as a function of the coupled phonon coordinates to extract their nonlinear couplings, and (iii) solution of the coupled equations of motions for the phonon coordinates.

The first step in a nonlinear phononics experiment is the identification of phonons of a material. Since light couples to phonons near the Brillouin zone center, the phonons relevant to a nonlinear phononics experiment are measured using optical reflectivity and Raman scattering experiments. In addition to measuring the frequencies, these experimental methods also yield information about the symmetry of the phonons. In the theory side, density functional theory (DFT) based methods can calculate forces on atoms, and these can be used to construct dynamical matrices. Diagonalization of the dynamical matrices produces phonon frequencies and their irreducible representation (irrep) can be determined by studying how the corresponding eigenvectors transform under the symmetry operations of the point group of the material. In this way, the phonon frequencies and their symmetries can be reconciled between experiment and theory.

The ability to pump a particular set of phonons in a material depends on the frequency and power of the available laser source. The pump-induced response of a material is usually investigated by analyzing the reflected, transmitted or scattered probe pulses. The phonons that are nonlinearly coupled to the pumped IR-active mode are observed as oscillations in the amplitude of the detected probe pulse. Although the response along the coupled phonon modes can easily be detected after a pump, extraction of nonlinear couplings from experimental data has so far proven to be difficult. Additionally, coherent change in lattice can also be inferred from time-resolved diffraction experiments, but a complete determination of the structural changes has been impractical because this requires measuring changes in numerous diffraction peaks as a function of time after a pump. The usefulness of the DFT-based microscopic theory of nonlinear phononics lies in the ability to calculate nonlinear couplings from first principles, which makes it possible to efficiently calculate and predict pump-induced structural changes.

To extract the nonlinear phonon couplings between two modes, the calculated phonon eigenvectors are used to generate a large number of structures as a function of the two phonon coordinates. DFT calculations are run again to calculate total energies of these structures. The total energies are then collected and fit with a polynomial to extract the coefficients corresponding to the nonlinear terms in the expansion of the total energy as a function of the phonon coordinates. Although a generic polynomial can be used to fit the calculated total energy surface, polynomials with only symmetry-allowed terms are used in the fitting to reduce the sources of numerical noise. The symmetry allowed terms are determined by noting that the total energy is a scalar and has the trivial irrep. For the cubic order coupling $Q_{\mathrm{R}}Q_{\mathrm{IR}}^2$, it implies that an IR-active mode can only couple to a Raman mode with the irrep A_g in centrosymmetric crystals because the square of an irrep is the trivial irrep A_g. However, if two different IR modes are pumped simultaneously, then their coupling to the A_g mode is forbidden with the $Q_{\mathrm{R}}Q_{\mathrm{IR}_1}Q_{\mathrm{IR}_2}$ term because the product of two different odd irreps cannot equal the trivial irrep. For example, if phonons with the irreps B_{2u} and B_{3u} of a material with the point group mmm are pumped simultaneously, only Raman-active modes with the irrep B_{1g} can nonlinearly couple to them because $B_{1g} \subseteq B_{2u} \otimes B_{3u}$. For the quartic term $Q_{\mathrm{R}}^2Q_{\mathrm{IR}}^2$, any Raman mode can couple to the pumped mode because the square of any irrep is the trivial irrep.

After the nonlinear coefficients present in the polynomial fit of the calculated energy surface as a function of phonon coordinates are extracted, the phonons are treated as classical oscillators to study their light-induced dynamics. The coupled equations of motion for phonon coordinates are numerically solved in the presence of a forcing term of the form $F(t) = Z_\alpha^* F_0 \sin(\Omega t)\mathrm{e}^{-t^2/\sigma^2}$. Here, Z_α^* is the component of the mode effective charge along the direction α, and it is related to the Born effective charge tensor $Z_{\kappa,\alpha\beta}^*$ of atom κ with mass m_κ and the eigendisplacement vector

$w_{\kappa,\beta}$ by the expression $Z^*_\alpha = \Sigma_{\kappa,\beta} Z^*_{\alpha\beta} w_{\kappa,\beta}/\sqrt{m_\kappa}$ [26]. The mode effective charge can be calculated from first principles and is related to the LO–TO splitting that can be experimentally measured. Hence, except for the damping of the phonon modes that are roughly 10–20% of the respective phonon frequencies, all the quantities necessary for calculating the light-induced dynamics can be determined from first principles.

3. Coherent lattice displacement due to cubic-order coupling

3.1. *Coherent displacement in $Pr_{0.7}Ca_{0.3}MnO_3$*

An insulator–metal transition in $Pr_{0.7}Ca_{0.3}MnO_3$ after an excitation with a mid-IR laser was reported by Rini *et al.* in 2007 [20]. This was the first report of a pump–probe experiment in a transition metal oxide using a mid-IR pump that could excite the high-frequency IR-active phonons of the material causing changes in the metal-oxygen bond distances. The observed insulator–metal transition was understood in terms of the modification of the electronic bandwidth associated with the changes in these bond distances. In 2012, Först *et al.* proposed that nonlinear phonon coupling of the type $Q_R Q_{IR}^2$ can cause a coherent lattice displacement along the Raman-active phonon coordinate Q_R when the IR-active phonon coordinate Q_{IR} is externally pumped [13]. Subedi *et al.* theoretically investigated whether this nonlinear phononics phenonmenon can explain the observed insulator–metal transition in $Pr_{0.7}Ca_{0.3}MnO_3$ and found that externally exciting an IR-active phonon mode of this material can cause a lattice displacement along a low-frequency Raman-active phonon coordinate [38].

Optical spectroscopy shows that there is an IR-active phonon mode with a large oscillator strength in this material at 573 cm^{-1} [50]. In their experiment, Rini *et al.* used a mid-IR laser with a frequency near 573 cm^{-1} to pump this highest-frequency IR-active phonon of the material. For computational efficiency, Subedi *et al.* studied this phenomenon on the parent compound $PrMnO_3$. They started by calculating the zone center phonon frequencies and eigenvectors of this material. The calculated frequencies of the three highest IR-active phonon modes are 633, 640, and 661 cm^{-1} with irreps B_{1u}, B_{2u}, and B_{3u}, respectively. Since the product of an irrep with itself is the trivial irrep A_g, any of the seven A_g phonon modes present in the material can couple with an IR-active mode with a cubic-order $Q_R Q_{IR}^2$ nonlinear coupling. The irreps of the pumped IR-active mode and the A_g mode that couples to the pumped mode was not reported in the experimental study [20]. So total energies $E(Q_R, Q_{IR})$ as a function of the Q_R and Q_{IR} coordinates were calculated for each pair of A_g and high-frequency IR-active phonon modes. The $A_g(9)$ and B_{1u} modes showed a large nonlinear coupling, and the calculated energy surface of this pair is shown in Figure 1 (bottom). The high-frequency B_{1u} mode involves changes in the bond length between the apical O and Mn of the MnO_6 octahedra. The $A_g(9)$ mode has a relatively low calculated frequency of 155 cm^{-1} and involves rotation of the MnO_6 octahedra about the c axis as shown in Figure 1 (top). The in-plane angle between the corner-shared octahedra become closer to 90° for positive values of the $A_g(9)$ coordinate, while the distortion increases for negative values.

The calculated energy surface between $A_g(9)$ and B_{1u} modes fits the following polynomial

$$\begin{aligned} E(Q_R, Q_{IR}) = {} & \tfrac{1}{2}\Omega_R^2 Q_R^2 + \tfrac{1}{2}\Omega_{IR}^2 Q_{IR}^2 + \tfrac{1}{3} a_3 Q_R^3 + \tfrac{1}{4} b_4 Q_{IR}^4 \\ & - \tfrac{1}{2} g Q_R Q_{IR}^2, \end{aligned} \tag{1}$$

with Q_R and Q_{IR} now denoting the coordinates of the $A_g(9)$ and B_{1u} modes, respectively. Since the pump-induced dynamics causes large displacements along the phonon coordinates, they can be regarded as classical oscillators. The effect of an external pump on the IR-active mode can be treated by the presence of a driving term $F(t) = F\sin(\Omega t)e^{-t^2/2\sigma^2}$, where F, σ, and Ω are the

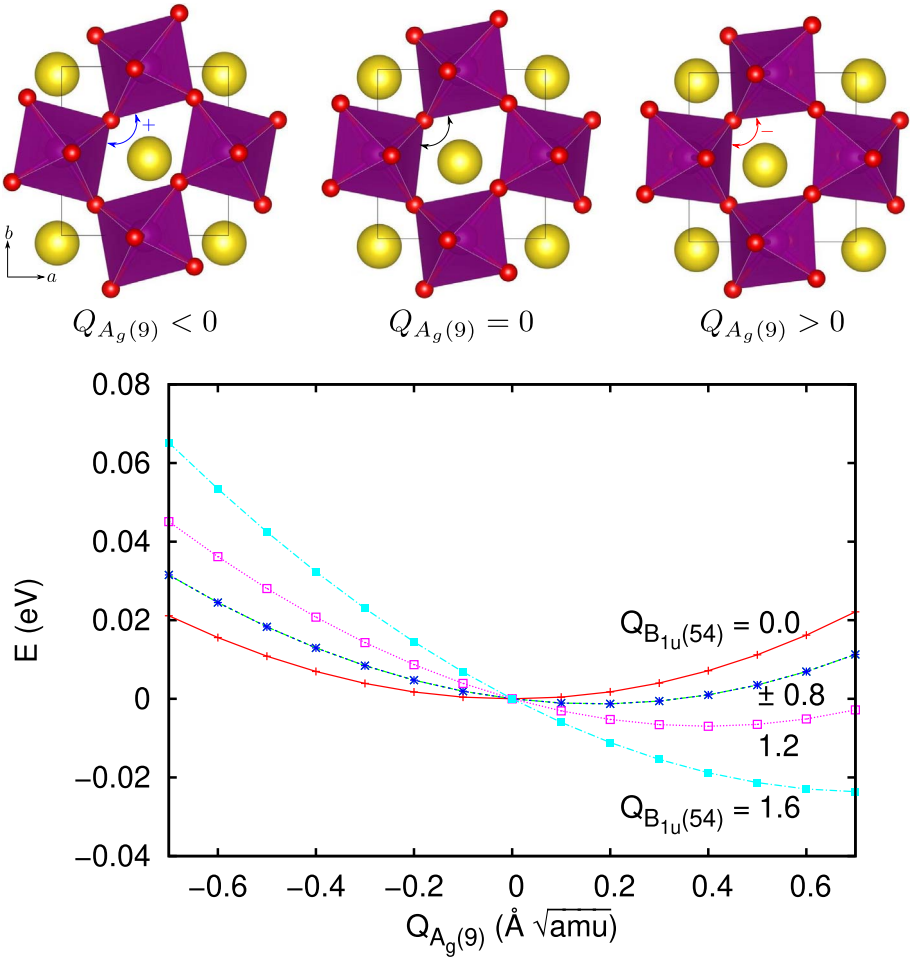

Figure 1. Top: sketch of the atomic displacements corresponding to the $A_g(9)$ Raman-active phonon mode of $PrMnO_3$ A positive value of the $A_g(9)$ coordinate brings the angle between octahedra closer to 90°. Bottom: total energy as a function of the $A_g(9)$ coordinate for several values of the B_{1u} coordinate. For visual clarity $E(Q_R, Q_{IR}) - E(0, Q_{IR})$ is plotted so that all curves coincide at $Q_R = 0$. Reproduced from [38].

amplitude, time-width and frequency of the pump pulse, respectively. The zero of the time delay t is typically chosen such that $t = 0$ when the pump and probe pulses are superposed. The coupled equations of motions for the two phonon coordinates in the absence of damping terms then read

$$\begin{aligned} \ddot{Q}_{IR} + \Omega_{IR}^2 Q_{IR} &= g Q_R Q_{IR} - b_4 Q_{IR}^3 + F(t) \\ \ddot{Q}_R + \Omega_R^2 Q_R &= \tfrac{1}{2} g Q_{IR}^2 - a_3 Q_R^2. \end{aligned} \tag{2}$$

For a finite pump amplitude F, the oscillation of the Q_{IR} coordinate has a time dependence $Q_{IR}(t) \propto F\Omega_{IR}\sigma^3 \cos\Omega_{IR} t$ [38]. Due to the cubic-order coupling between the two modes, the Raman coordinate experiences a forcing field $gQ_{IR}^2/2 \propto gF^2\Omega_{IR}^2\sigma^6(1 - \cos 2\Omega_{IR} t)$, which has a finite time-averaged value. Therefore, unlike the pumped IR-active mode, the Raman mode vibrates about a displaced position. Numerical solution of these coupled equations of motion also confirms this picture. Figures 2(a) and (b) show the dynamics of the Q_R coordinate with and

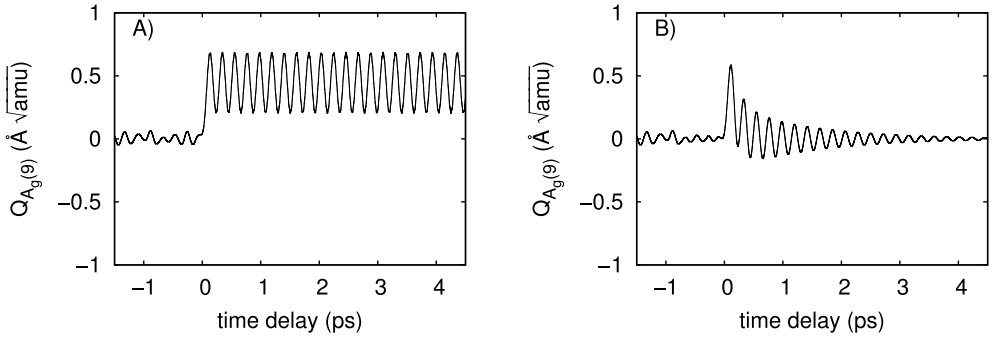

Figure 2. Dynamics of the $A_g(9)$ Raman mode. Left panel: dynamics without damping. Right panel: dynamics with damping values of 5% for both $A_g(9)$ and B_{1u} modes. Reproduced from [38].

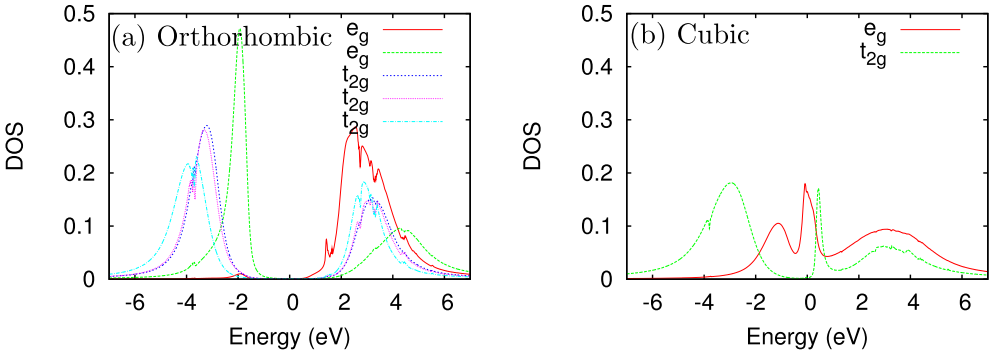

Figure 3. DFT+DMFT orbitally resolved density of states of Mn-d states in $PrMnO_3$ for the equilibrium orthorhombic (insulating) and cubic (metallic) crystal structures. Reproduced from [38].

without damping terms. In both cases, the Q_R coordinate oscillates about a displaced position while the Q_{IR} mode is also oscillating with a finite amplitude.

Since the lattice displaces along the positive value of the $A_g(9)$ coordinate while the B_{1u} is pumped, the rotation of the MnO_6 octahedra in the ab plane gets reduced. This should bring the system closer to the metallic phase because reduced octahedral rotation enhances hopping of the Mn d electrons via oxygen sites. Subedi *et al.* performed combined density functional theory and dynamical mean field theory (DMFT) electronic structure calculations on the cubic and equilibrium structures of $PrMnO_3$ to understand how the electronic structure changes as the octahedral rotation is suppressed. The calculated partial density of states of the Mn t_{2g} and e_g orbitals for the two structures are shown in Figure 3. They show that the distorted equilibrium structure is insulating, while the cubic structure is metallic. This suggests that light-induced suppression of the octahedral rotation due to nonlinear phononics might cause insulator–metal transition in this material.

Has it been conclusively shown that the observed mid-IR pump-induced insulator–metal transition in $Pr_{0.7}Ca_{0.3}MnO_3$ is due to displacement of the lattice along the Raman coordinate? It is worthwhile to point out that any magnetic, optical, and electrical perturbations easily cause insulator–metal transition in $Pr_{0.7}Ca_{0.3}MnO_3$ [51–53]. There have been no experiments to measure the oscillations of the pumped IR- and Raman-active modes using 2D spectroscopy to

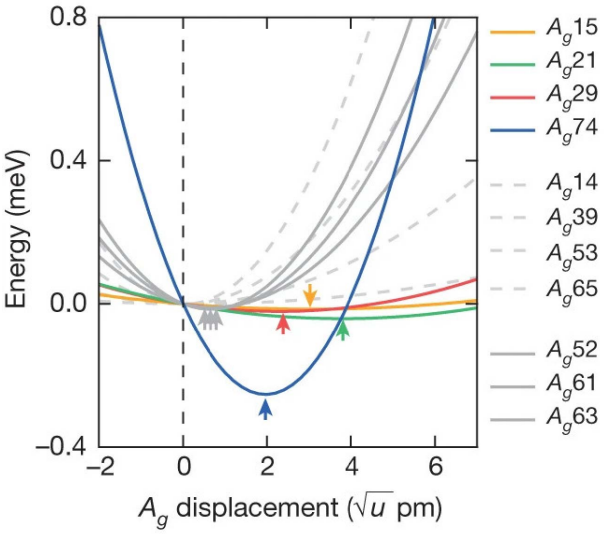

Figure 4. Calculated total energy of all the A_g modes for a frozen B_{1u} displacement of 0.14 Å $\sqrt{u}$ (u, atomic mass unit), corresponding to a change in the apical O–Cu distance of 2.2 pm. Arrows indicate the potential minima. Reproduced from [18].

show that these phonons are excited in the experiment, nor have the light-induced changes in the structure been studied using time-resolved X-ray diffraction spectroscopy. Moreover, since the light-induced transition is from an insulating to a metallic phase, heating effects cannot be ruled out as the cause of the transition unless the timescale for thermal redistribution of the pumped vibrational energy is disentangled from the timescale of any displacement along the Raman coordinate. As a result, it may be practically impossible to conclusively prove that pump-induced insulator–metal transition in this material is due to a displacement along the Raman coordinate.

3.2. *Coherent displacement in ortho-II* $YBa_2Cu_3O_{6.5}$

A mid-IR pump-induced increase in reflectivity has been observed in several cuprates, and this fact from raw data has been interpreted as a signature of light-induced transient superconductivity [29–31]. Mankowsky *et al.* have performed a combined time-resolved X-ray diffraction and first-principles lattice dynamics study to find out if the light-induced effect observed in $YBa_2Cu_3O_{6.5}$ is due to structural changes caused by nonlinear phononics [18]. Optical spectroscopy experiments show that this material has an IR-active phonon with a frequency of 640 cm^{-1} [54]. This mode has the irrep B_{1u}. Mankowsky *et al.* pumped this mode with an intense mid-IR laser pulse and measured changes in the diffraction intensity of four Bragg peaks as a function of time using time-resolved X-ray diffraction experiment. The intensities either increased or decreased promptly after a mid-IR pump. Since the intensity of a Bragg peak is proportional to the square of the structure factor, which is a function of atomic positions, this implies that the crystal structure of the material coherently changes after the pump. However, ortho-II $YBa_2Cu_3O_{6.5}$ has 25 atoms, and they were not able to fully resolve the light-induced changes in the crystal structure by measuring the changes in intensities of only four Bragg peaks.

There are 11 A_g modes in this material, and all of them can couple to the pumped B_{1u} mode with a cubic-order $Q_R Q_{IR}^2$ coupling. Mankowsky *et al.* calculated the total energy surface for each

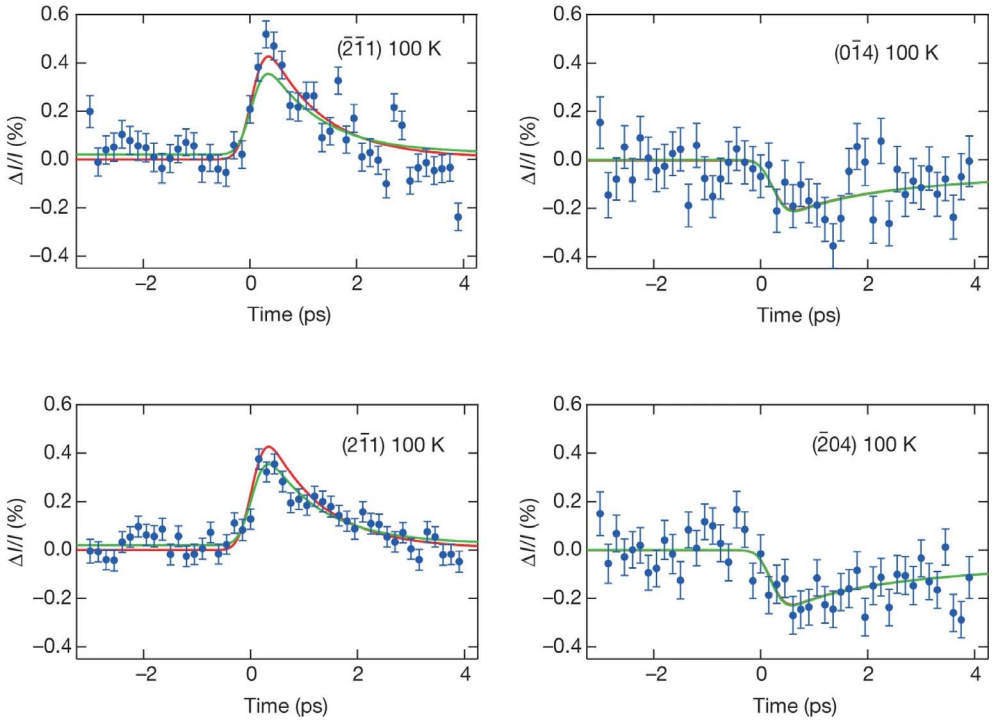

Figure 5. Time-dependent diffracted peak intensity (I) for four Bragg reflections. The solid curves are fit to the experimental data which were done by adjusting the B_{1u} amplitude and relaxation times. The relative amplitudes and signs of the curves are determined from the calculated structure using only the four most strongly coupled modes (green) or all A_g modes (red). Reproduced from [18].

pair of B_{1u} and A_g modes. The total energies of the seven A_g modes for a B_{1u} displacement of 0.14 Å $\sqrt{\text{amu}}$ are shown in Figure 4. The calculated energy curves show that four A_g modes show significant coupling to the pumped B_{1u} mode, and these modes involve out-of-plane motion of the apical O and Cu ions. The rest of the A_g modes that are weakly coupled involve in-plane motions of the O ions in the CuO_2 plane. The presence of these nonlinearities was also independently confirmed by the calculations of Ref. [55]. Changes in the intensities of the four Bragg peaks measured in the time-resolved X-ray diffraction experiment were calculated considering the displacement of the lattice along these A_g coordinates. The measured and calculated changes in the intensities of the Bragg peaks as a function of time are shown in Figure 5. With only the B_{1u} pump amplitude and the decay time as the fitting parameters, the changes in the crystal structure due to displacement along the A_g coordinates could independently reproduce the pump-induced changes in intensities of the four measured Bragg peaks. In the transient structure corresponding to the B_{1u} amplitude of 0.3 Å $\sqrt{\text{amu}}$ estimated for the pump intensity utilized in the the experiment, the apical O–Cu distance decreases and the O–Cu–O buckling increases. There is also an increase of the intra-bilayer distance and a decrease of the inter-bilayer distance. The changes in the distances are around 1 pm, and DFT calculations show that these cause practically no modification of the electronic structure for the estimated pump-induced amplitude of the B_{1u} mode in the experiment [18]. This suggests that structural changes due to nonlinear phononics do not cause the observed light-induced enhancement of reflectivity in this material.

3.3. *Excitation of Raman modes with nontrivial irreps in $ErFeO_3$*

$ErFeO_3$ is an insulator with a band gap of 2.1 eV, and it shows resonances at 540 and 567 cm^{-1} in the optical conductivity spectra corresponding to phonons with irreps B_{3u} and B_{2u}, respectively [56]. When either the B_{3u} or B_{2u} mode of this material was externally pumped with light polarized along a or b axes, respectively, Nova *et al.* observed oscillations at the frequency of 112 cm^{-1} corresponding to an A_g Raman-active phonon mode [14]. This reflects the cubic-order $Q_R Q_{IR}^2$ coupling between the pumped IR-active and A_g modes. In addition, they measured two B_{1g} phonons with frequencies of 112 and 162 cm^{-1} when the B_{3u} and B_{2u} modes were simultaneously pumped. The excitation of the B_{1g} phonons is due to a cubic-order $Q_{B_{1g}} Q_{B_{2u}} Q_{B_{3u}}$ coupling that is allowed by symmetry because $B_{1g} \subseteq B_{2u} \times B_{3u}$. Juraschek *et al.* studied the dynamics of these phonons in $ErFeO_3$ using theoretical framework described above and found large symmetry-allowed cubic-order couplings between the Raman- and IR-active phonons that explains the observed pump-induced Raman oscillations [39].

The observation of stimulated oscillations of Raman phonons due to nonlinear phonon couplings in $ErFeO_3$ is interesting because the band gap of this material is large enough that the role of electronic excitations in causing the light-induced dynamics can reasonably be ruled out. The observation of Raman oscillations at only two frequencies also raises an interesting question. Why are not the oscillations of other Raman A_g and B_{1g} modes observed? It can be conjectured that the respective nonlinear couplings are small or that the energy from the pumped IR modes flows mostly to low frequency Raman modes. It would be illuminating to perform experimental and theoretical studies that can clarify this issue. It would also be interesting to perform time-resolved X-ray diffraction experiment to find out whether the lattice displaces along the Raman-active phonon coordinates after a mid-IR pump in this material.

3.4. *Transient switching of ferroelectricity*

Although the capability to pump the IR-active phonons of transition metal oxides has been available since 2007 [20], a mechanism for switching ferroelectric order using nonlinear phononics was not discussed until 2015 [19]. The main reason for this delay in tackling this problem was a conceptual misunderstanding. Since the 1970s, nonlinear phonon couplings had been discussed in terms of ionic Raman scattering where excited IR-active phonons couple to Raman phonons via $Q_R Q_{IR}^2$ or $Q_R Q_{IR_1} Q_{IR_2}$ couplings [11, 12]. In centrosymmetric crystals, only Raman-active phonons, which do not break inversion symmetry, can couple to IR-active phonons at this order. Because the atomic displacement pattern associated with a ferroelectric order parameter derives from an unstable IR-active phonon, lattice displacements that change the ferroelectric order parameter via nonlinear phononics was not explored. In 2015, Subedi pointed out that any phonon mode Q_P that modifies the ferroelectric polarization is both Raman and IR active due to the lack of inversion symmetry in ferroelectric materials [19]. Thus, a cubic-order coupling is allowed between Q_P and any IR-active phonon that can be externally pumped. The question is whether the coupling is large and causes displacement along the direction that switches the ferroelectric order. This question was answered in the affirmative for the case of $PbTiO_3$.

The displacement patterns of the lowest (Q_P) and highest (Q_{IR}) frequency phonon modes of $PbTiO_3$ are shown in Figure 6 (top). The calculated total energy as a function of the Q_P coordinate for several values of the Q_{IR} coordinate is shown in Figure 6 (bottom). The minimum of the energy curve for the Q_P coordinate shifts towards the switching direction for both positive and negative values of the Q_{IR} coordinate, which reflects the presence of a $Q_P Q_{IR}^2$ nonlinear coupling term. There is an asymmetry in energy as a function of the Q_P coordinate because of the presence of a large Q_P^3 anharmonicity. Due to this anharmonic term, the minimum of

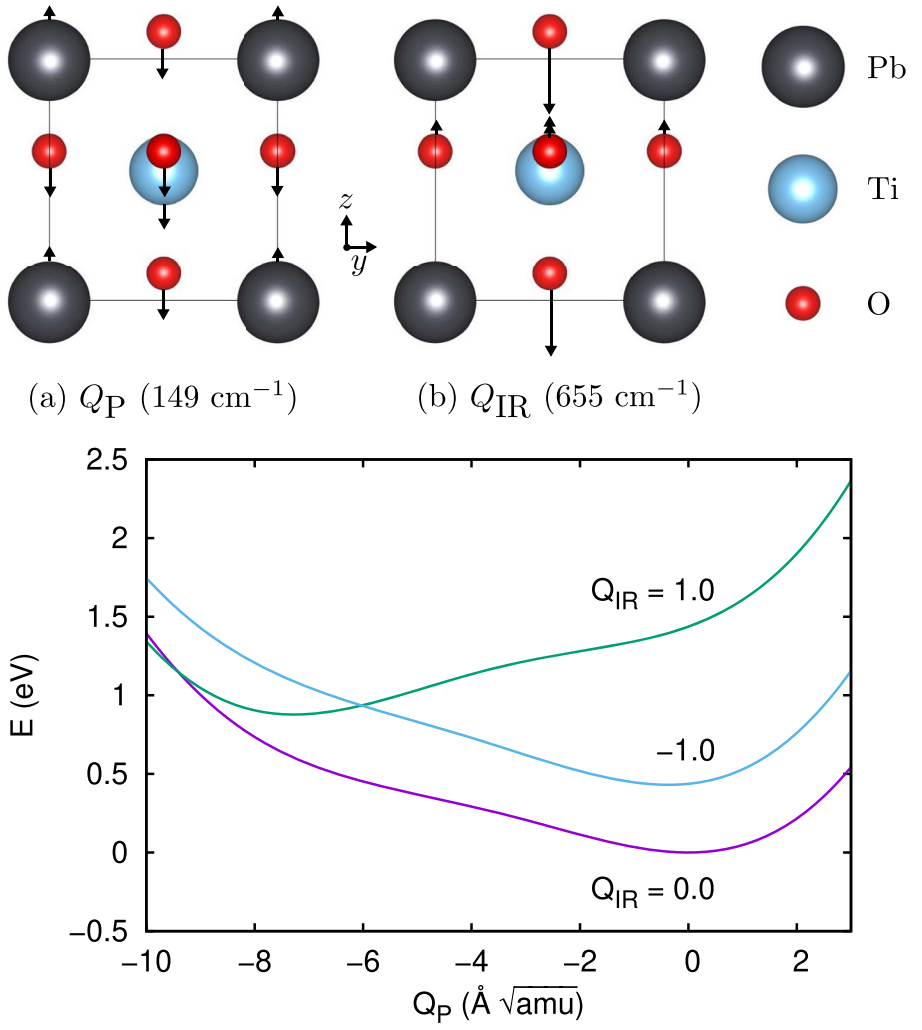

Figure 6. Top: displacement patterns of (a) lowest-frequency Q_{P} and (b) highest-frequency Q_{IR} modes of the ferroelectric phase of $PbTiO_3$. Bottom: total energy as a function of the Q_{P} coordinate for several values of the Q_{IR} coordinate. Reproduced from [19].

the Q_{P} coordinate suddenly jumps to a large negative when the value of the Q_{IR} coordinate is continuously increased to large positive values. This causes an abrupt reversal of the ferroelectric polarization without the magnitude of the polarization getting reduced to a value of zero. This phenonmena is seen in the numerical solutions of the coupled equations of motions for the Q_{P} and Q_{IR} coordinates in the presence of an external pump on the Q_{IR} mode as shown in Figure 7.

The phenomenon of light-induced switching of ferroelectrics via nonlinear phononics proposed by theory was partially confirmed by Mankowsky *et al.* [16]. They performed time-resolved measurements of SHG intensity and phase of an 800 nm probe pulse after a mid-IR excitation in $LiNbO_3$ with a pump duration of 150 fs. Their result is shown in Figure 8. For pump fluences smaller than 50 mJ/cm^2, the SHG intensity decreased to a finite value before returning to the equilibrium value. Above a threshold fluence of 60 mJ/cm^2, the intensity vanished completely,

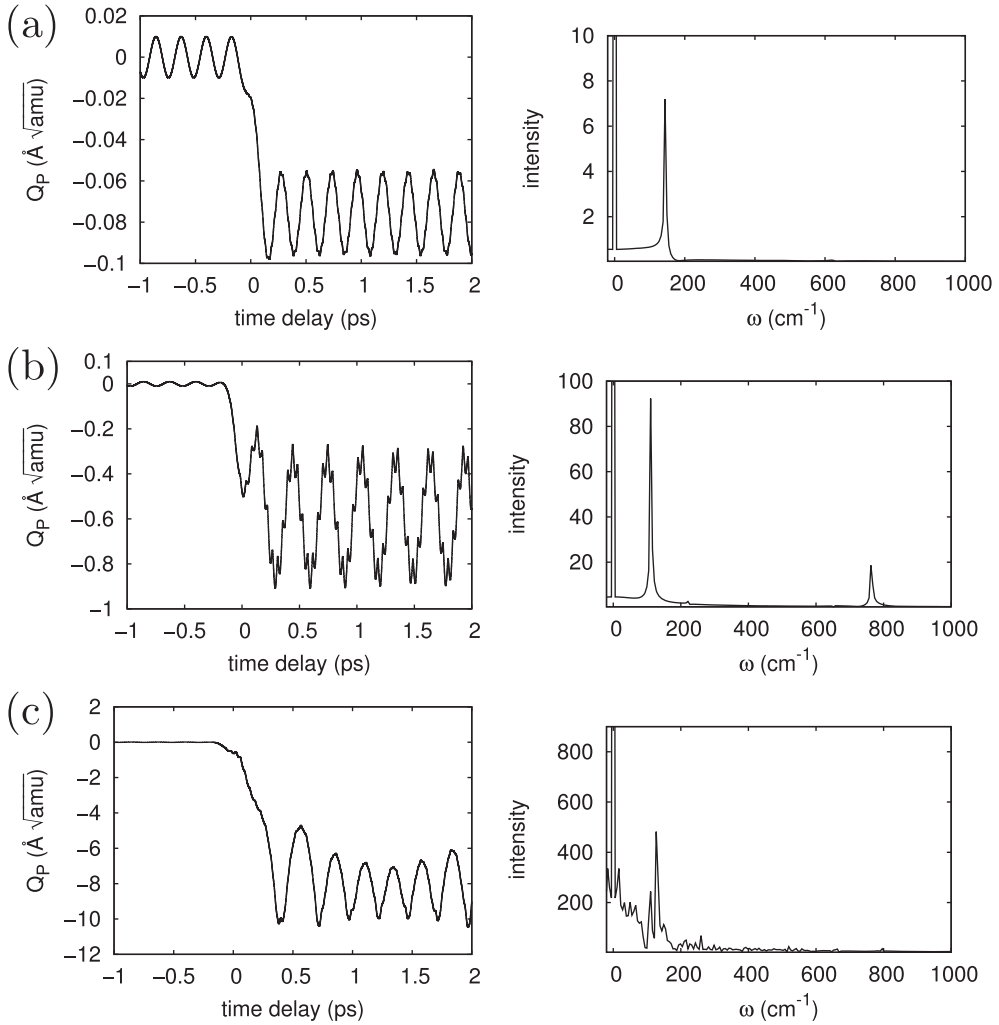

Figure 7. Dynamics of the Q_P mode for three different pump amplitudes. Left panels: displacements along Q_P coordinate as function of time delay. Right panels: Fourier transform of the positive time delay oscillations. Damping effects have been neglected. Reproduced from [19].

increased to a finite value, vanished completely again, and then relaxed to the equilibrium value. Their measurement of the phase of the second-harmonic signal showed that the phase changed by 180° whenever the SHG intensity vanished completely, which implies a temporary and partial reversal of the ferroelectric polarization. Furthermore, as can be seen in Figure 8, the SHG intensity also showed small modulations corresponding to the oscillations of the pumped IR-active phonon, and this indicates that the IR-active phonon is coherently oscillating while the polarization reversal is taking place. The state with switched polarization lasted only for 200 fs. Similar experiments with longer pump pulses are necessary to ascertain whether the switching lasts for the duration of the pump pulse or the pump only causes large-amplitude oscillations of the Q_P coordinate. In any case, even though Mankowsky *et al.* were not able to permanently switch the electric polarization, their experiment confirms the theoretical prediction that a cubic-order

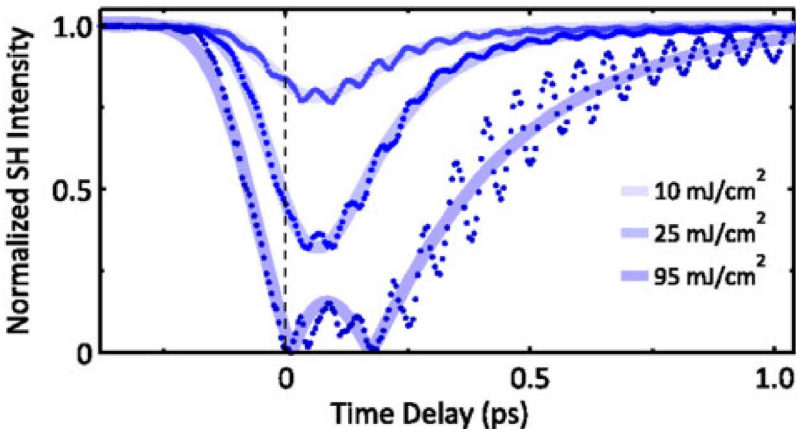

Figure 8. Time-resolved second-harmonic intensity of $LiNbO_3$ after a mid-IR pump. The intensity is normalized to its value before excitation. Reproduced from [16].

nonlinear phonon coupling with a large magnitude and an appropriate sign exists in oxide ferroelectrics that can reverse the electric polarization.

4. Symmetry breaking due to quartic coupling

4.1. *Quartic coupling between a Raman and an IR phonon modes*

Only cubic nonlinearities between phonon modes were discussed in the literature prior to 2014. This was presumably because higher order nonlinearities were thought to be small when the total energy of a crystal is expanded as a function of phonon coordinates. Subedi *et al.* pointed out that quartic nonlinearities between two phonon modes can be large when cubic nonlinearity is not allowed by symmetry [38]. In fact, a $Q_R^2 Q_{IR}^2$ term is the lowest order nonlinearity allowed by symmetry when Q_R has a non-trivial irrep.

Such a large quartic order coupling was found in La_2CuO_4 between its $B_{1g}(18)$ and $B_{3u}(41)$ phonon modes [38]. The $B_{1g}(18)$ mode changes the in-plane rotations of the CuO_6 octahedra as shown in Figure 9 (top), and the $B_{3u}(41)$ mode involves in-plane stretching of the Cu–O bonds. The $B_{1g}(18)$ mode breaks the m_x and m_y mirror symmetries. Therefore, the structures generated by the positive and negative values of the $B_{1g}(18)$ coordinates are related by these symmetries, and the total energy is symmetric as a function of the $B_{1g}(18)$ coordinate. Similarly, the $B_{3u}(41)$ mode breaks the m_z and inversion symmetries, and the total energy is also symmetric as a function of the $B_{3u}(41)$ coordinate.

The calculated total energy surface as a function of the $B_{1g}(18)$ and $B_{3u}(41)$ coordinates is shown in Figure 9 (bottom). It fits the expression

$$E(Q_R, Q_{IR}) = \tfrac{1}{2}\Omega_R^2 Q_R^2 + \tfrac{1}{2}\Omega_{IR}^2 Q_{IR}^2 + \tfrac{1}{4} a_4 Q_R^4 + \tfrac{1}{4} b_4 Q_{IR}^4 - \tfrac{1}{2} g Q_R^2 Q_{IR}^2, \quad (3)$$

where Q_R and Q_{IR} denote the coordinates of the $B_{1g}(18)$ and $B_{3u}(41)$ modes, respectively. As expected, the calculated energy surface is even with respect to both $B_{1g}(18)$ and $B_{3u}(41)$ coordinates, which is in contrast to the $Q_R Q_{IR}^2$ nonlinearity that is even only with respect to the IR phonon coordinate. The energy curve of the $B_{1g}(18)$ coordinate softens as the value of the $B_{3u}(41)$ coordinate is increased, and it develops a double well beyond a threshold value of the $B_{3u}(41)$ coordinate. In (3), this is reflected by a positive value of the coupling coefficient g.

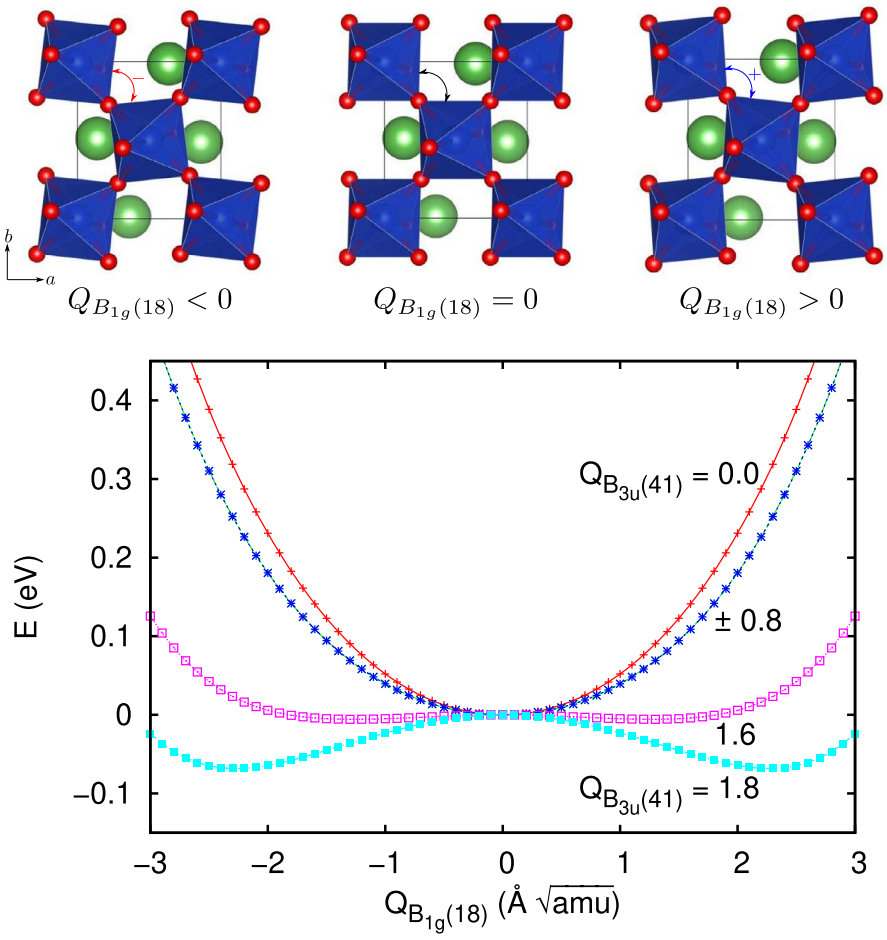

Figure 9. Top: sketch of the atomic displacements corresponding to the $B_{1g}(18)$ Raman-active phonon mode of La_2CuO_4. Bottom: total energy as a function of the $B_{1g}(18)$ coordinate for several values of the $B_{3u}(41)$ coordinate. For visual clarity $E(Q_R, Q_{IR}) - E(0, Q_{IR})$ is plotted so that all curves coincide at $Q_R = 0$. Reproduced from [38].

Since a finite value of the $B_{3u}(41)$ coordinate decreases the curvature of the energy curve of the $B_{1g}(18)$ coordinate, this implies that frequency of the $B_{1g}(18)$ mode changes while the $B_{3u}(41)$ is coherently oscillating. Furthermore, the $B_{1g}(18)$ mode should oscillate at a displaced position at one of the local minima of the double-well potential beyond a critical value of the amplitue of $B_{3u}(41)$ mode. This picture was confirmed by solving the coupled equations of motion of these modes, which are

$$\begin{aligned} \ddot{Q}_{IR} + \Omega_{IR}^2 Q_{IR} &= g Q_R^2 Q_{IR} - b_4 Q_{IR}^3 + F(t) \\ \ddot{Q}_R + \Omega_R^2 Q_R &= \tfrac{1}{2} g Q_R Q_{IR}^2 - a_4 Q_R^3. \end{aligned} \tag{4}$$

Here $F(t) = F \sin(\Omega t) e^{-t^2/2\sigma^2}$ is the external pump term on the $B_{3u}(41)$ coordinate, and F, σ, and Ω are the amplitude, width and frequency of the pump light pulse, respectively. Numerical solutions of these equations revealed four qualitatively different behavior for the oscillations of the $B_{1g}(18)$ mode, as depicted in Figure 10. The Raman mode oscillates about its local minimum below a threshold value F_c of the external pump (Figure 10(a)). Near this threshold,

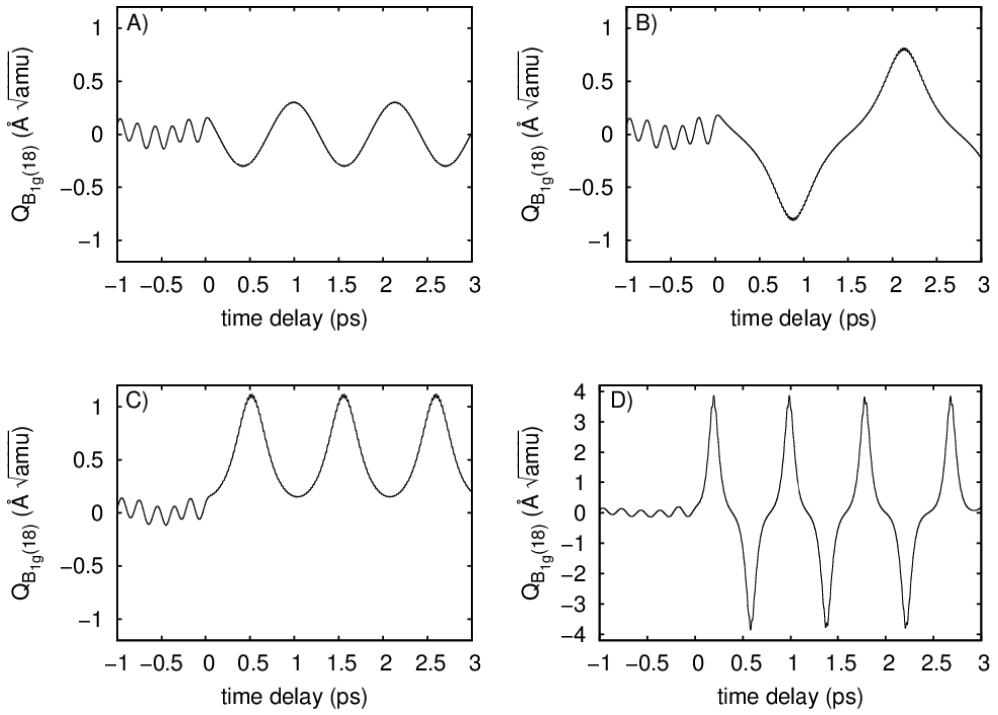

Figure 10. Dynamics of the $B_{1g}(18)$ coordinate due to a quartic nonlinearity in La_2CuO_4. Damping effects have been neglected. Reproduced from [38].

there is a narrow range where it makes a long period oscillation about the local maximum of the double well potential, which is analogous to the Kapitza phenomenon for a vibrating pendulum (Figure 10(b)). As the pump amplitude is increased further, it oscillates at a displaced position in one of the minima of the double well (Figure 10(c)). At even larger values of the pump amplitude, it again oscillates about the equilibrium position with a large amplitude that encompasses both minima of the double well potential (Figure 10(d)).

Since $B_{1g}(18)$ mode breaks the m_x and m_y mirror symmetries, the oscillations about the displaced position in Figure 10(c) describe a light-induced dynamical symmetry breaking of the crystal. This is a non-perturbative effect that occurs above a critical threshold of the pump field. Although intense pump pulses with peak fields greater than 10 MV/cm are available these days, experimental studies of this phenomenon in La_2CuO_4 have not yet been reported in the literature.

4.2. *Light induced ferroelectricity due to quartic coupling between two IR phonon modes*

Quartic nonlinearities of the type $Q_1^2 Q_2^2$ are allowed by symmetry between any two phonon coordinates Q_1 and Q_2 because the square of an irrep is the trivial irrep. Therefore, two IR-active phonon modes can also couple with each other. Subedi showed that such a nonlinearity can lead to transiently induced ferroelectricity in strained $KTaO_3$ [26]. This phenomenon was illustrated for the case of 0.6% compressively strained $KTaO_3$ by studying the dynamics of its two lowest-frequency IR-active phonons when its highest-frequency IR-active phonon mode is pumped. The two lowest-frequency phonon modes in this system have the irreps A_{2u} and E_u. The A_{2u} mode with calculated frequency $\Omega_{l_z} = 20$ cm^{-1} involves atomic motions along the z axis, whereas the

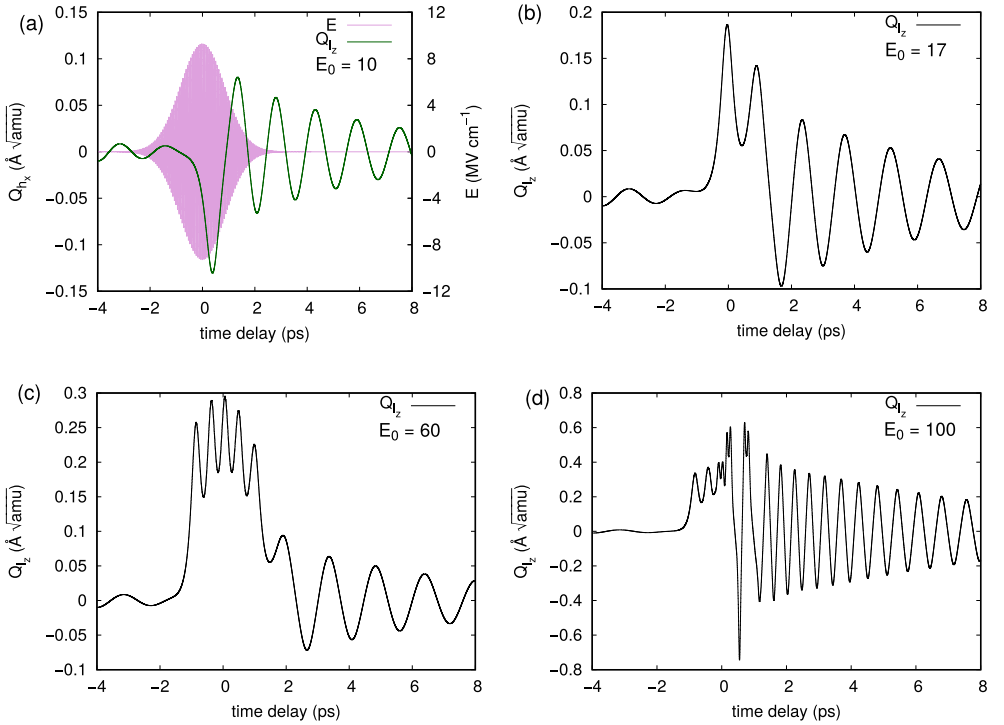

Figure 11. Dynamics of the Q_{l_z} coordinate of strained $KTaO_3$ after Q_{h_x} coordinate has been pumped by an external pulse E with duration of 2 ps. The dynamics for four different values of the peak electric field E_0 (MV·cm^{-1}) of the pump pulse are shown. Damping effects are taken into account in this study. Reproduced from [26].

doubly degenerate E_u mode with frequency $\Omega_{l_x} = \Omega_{l_y} = 122$ cm^{-1} causes the atoms to move in the xy plane. The highest-frequency mode that should be pumped to induce ferroelectricity has the irrep E_u with frequency $\Omega_{h_x} = \Omega_{h_y} = 556$ cm^{-1}.

Total energy calculations as a function of the phonon coordinates showed that the highest-frequency mode couples to the two lowest-frequency modes in this system with large quartic nonlinearities. The coupling is such that the energy curve of the low-frequency E_u coordinate Q_{l_x} stiffens, whereas the energy curve of the low-frequency A_u coordinate Q_{l_z} softens when the highest-frequency coordinate Q_{h_x} has a finite value. The calculated total energies as a function of these three coordinates were fit to a polynomial. These coordinates were treated as classical oscillators, and the fitted polynomial was used as their potential energy. The coupled equations of motion in the presence of an external pump were numerically solved for several values of pump intensities, and four such solutions for the Q_{l_z} coordinate is shown in Figure 11. Similar to the case of $Q_R^2 Q_{IR}^2$ coupling in La_2CuO_4 discussed in the previous section, here also the lowest-frequency Q_P coordinate oscillates about a local minimum above a pump threshold (Figures 11(b) and (c)). Since the displacement along the Q_P coordinate breaks inversion symmetry, these calculations show that light-induced ferroelectricity can be stabilized due to the $Q_P^2 Q_{IR}^2$ nonlinear coupling.

Nova *et al.* have pumped the highest-frequency IR-active phonon of paraelectric $SrTiO_3$ [27]. They did not observe any second harmonic signal of an optical probe pulse from the sample after it was pumped by a single mid-IR pulse, indicating that the sample remained paraelectric after the mid-IR pump. However, when the sample was exposed to a mid-IR pump for several minutes, the formation of a metastable ferroelectric state was inferred from a finite second harmonic

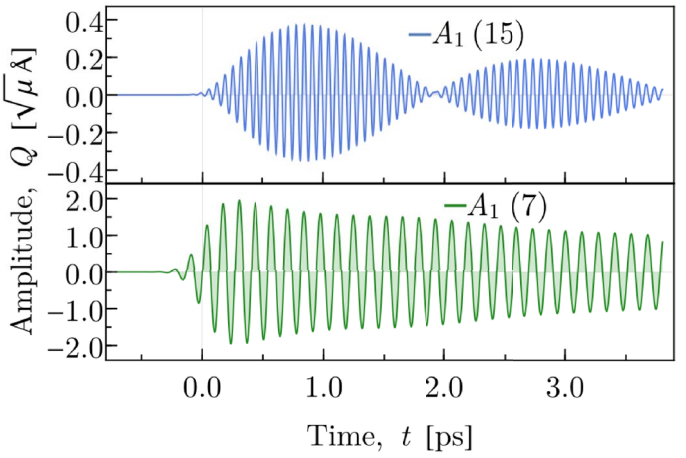

Figure 12. Dynamics of the high-frequency Q_{IR_2} coordinate (denoted by $A_1(15)$) after the low-frequency Q_{IR_1} coordinate (denoted by $A_1(7)$) is externally pumped. Reproduced from [57].

signal of the probe pulse. The metastable ferroelectric state persisted for several hours after being exposed to the mid-IR irradiation. Intriguingly, similar metastable ferroelectric state was obtained by using teraherz pump [28]. This suggests that nonlinear phononics may not be the cause of transient ferroelectricity in the experiment of Nova *et al.*

5. Phonon upconversion due to ionic Raman scattering

Majority of the experimental and theoretical investigations of the nonlinear phononics phenomena have focused on pumping the high-frequency IR-active phonons of materials to induce dynamics along their low-frequency phonon modes. Juraschek and Maehrlein proposed that a phenomenon analogous to sum frequency Raman scattering can occur due to a $Q_{\mathrm{IR}_1}Q^2_{\mathrm{IR}_2}$ nonlinearity in a material with two IR-active phonons with the relation $\Omega_{\mathrm{IR}_1} = \Omega_{\mathrm{IR}_2}/2$ [57]. They found that when the low-frequency coordinate Q_{IR_1} is resonantly pumped, the cubic nonlinearity can cause oscillations of the high-frequency coordinate Q_{IR_2}.

They considered the simplest form of nonlinear lattice potential $V(Q_{\mathrm{IR}_1}, Q_{\mathrm{IR}_2}) = (1/2)\Omega^2_{\mathrm{IR}_1}Q^2_{\mathrm{IR}_1} + (1/2)\Omega^2_{\mathrm{IR}_2}Q^2_{\mathrm{IR}_2} + cQ_{\mathrm{IR}_1}Q^2_{\mathrm{IR}_2}$. This leads to the coupled equations of motions

$$\begin{aligned} \ddot{Q}_{\mathrm{IR}_1} + \gamma_{\mathrm{IR}_1}\dot{Q}_{\mathrm{IR}_1} + (\Omega^2_{\mathrm{IR}_1} + 2cQ_{\mathrm{IR}_2})Q_{\mathrm{IR}_1} &= Z_{\mathrm{IR}_1}E(t), \\ \ddot{Q}_{\mathrm{IR}_2} + \gamma_{\mathrm{IR}_2}\dot{Q}_{\mathrm{IR}_2} + \Omega^2_{\mathrm{IR}_2}Q_{\mathrm{IR}_2} &= cQ^2_{\mathrm{IR}_1}(t). \end{aligned} \tag{5}$$

Here, γ_{IR_1} and γ_{IR_2} describe the damping of the Q_{IR_1} and Q_{IR_2} coordinates, respectively, and Z_{IR_1} denotes the mode effective charge of the low-frequency Q_{IR_1} coordinate. The results of numerical solutions of these equations in the presence of a finite driving field $E(t)$ with frequency $\omega_0 = \Omega_{\mathrm{IR}_1}$ is shown in Figure 12, which shows the high-frequency Q_{IR_2} mode oscillating due to sum-frequency upconversion.

Kozina *et al.* have experimentally demonstrated this phenomenon in $SrTiO_3$ [58]. When they pumped the lowest-frequency transverse optic TO_1 phonon of this material, they also observed lattice oscillations at higher frequencies corresponding to the transverse optic TO_2 and TO_3 modes in time-resolved X-ray diffraction experiments. The TO_1 mode has a frequency of 1.5–2.5 THz depending on the sample temperature, whereas the TO_2 and TO_3 modes have frequencies of 5.15 and 7.6 THz, respectively. This indicates that the phonon upconversion mechanism

proposed by Juraschek and Maehrlein works even when the frequencies of the high-frequency phonon modes are not integer multiples of the frequency of the pumped low-frequency phonon mode.

6. Control of magnetism via nonlinear phononics

6.1. *Magnon excitation via nonlinear magneto-phonon coupling in $ErFeO_3$*

$ErFeO_3$ is an antiferromagnetic insulator with a small residual ferromagnetic moment that arises due to a canting associated with the Dzyaloshinskii–Moriya interaction. Earlier in this review, the observation of the A_g and B_{1g} phonon modes after a mid-IR pump by Nova *et al.* was discussed [14]. Interestingly, they also observed oscillations corresponding to a low-frequency magnon when the B_{2u} and B_{3u} IR-active phonons were simultaneously excited. The B_{2u} and B_{3u} modes are polarized along the b and a axes, respectively. Since a finite value of their respective coordinates Q_{2u} and Q_3u leads to a formation of finite electrical dipole moments along the b and a axes, respectively, simultaneous excitation of these modes using a circularly polarized pulse should give rise to circulating charges inside the lattice. Nova *et al.* proposed that this generates an effective magnetic field that excites the low-frequency magnon. Their scenario has been supported by a microscopic theory based on first principles calculations [59].

6.2. *Modifying the magnetic state of a material*

Nonlinear phononics can coherently modify atomic distances inside a crystal. In magnetic materials, this can also alter exchange interactions, and a modified magnetic state might get stabilized in the light-induced transient state. Fechner *et al.* have theoretically proposed that the equilibrium antiferromagnetic ordering of Cr_2O_3 gets modified to another antiferromagnetic ordering with ferromagnetically coupled nearest-neighbor spins when its high-frequency IR-active phonon mode with the irrep A_u is externally pumped [60]. This occurs because the Cr–Cr distances increase in the transient state as a result of the displacement along an A_g Raman mode due to a $Q_{\mathrm{R}}Q_{\mathrm{IR}}^2$ nonlinearity. Similar modification of the equilibrium magnetic state to a hidden antiferromagnetic state has been proposed in the rare-earth titantes by Gu and Rondinelli [61] and Khalsa and Benedek [62].

More interestingly, Radaelli has proposed that ferroelectricity and ferromagnetism can be induced in piezoelectric and piezomagnetic materials, respectively, by simultaneously pumping the orthogonal components Q_{IR}^x and Q_{IR}^y of a doubly degenerate IR-active mode with the irrep E_u [40]. The metastable states occur because the simultaneous pumping of the orthogonal components causes a displacement along a Raman-active phonon mode with a nontrival irrep due to a $Q_{\mathrm{R}}^{xy}Q_{\mathrm{IR}}^xQ_{\mathrm{IR}}^y$ nonlinearity. It was shown that the displacement along the Raman coordinate Q_{R}^{xy}, which transforms as xy, is given by

$$\begin{aligned} Q_{\mathrm{IR}}^{xy} &\propto 2Q_{\mathrm{IR,max}}^xQ_{\mathrm{IR,max}}^y\cos\Delta\phi \\ &\propto 2E_xE_y\cos\Delta\phi. \end{aligned} \tag{6}$$

Here $Q_{\mathrm{IR,max}}^x$ and $Q_{\mathrm{IR,max}}^y$ are the amplitudes of the Q_{IR}^x and Q_{IR}^y modes, respectively. E_x and E_y are the magnitudes of the electric fields used to pump the Q_{IR}^x and Q_{IR}^y modes, respectively, and $\Delta\phi$ is their phase difference. Because the displacement along the Q_{IR}^{xy} coordinate is proportional to $\cos\Delta\phi$, Q_{IR}^{xy} has a finite value only when the orthogonal components of E_u are pumped in-phase or out-of-phase. Furthermore, the displacement along Q_{R}^{xy} coordinate switches direction wherever the phase difference changes by π. Thus, the $Q_{\mathrm{R}}^{xy}Q_{\mathrm{IR}}^xQ_{\mathrm{IR}}^y$ nonlinearity can induce ferroelectricity or ferromagnetism if the ferroelectric polarization or ferromagnetic moment is proportional to the Q_{R}^{xy} coordinate, and the direction of the induced ferroelectric or ferromagnetic

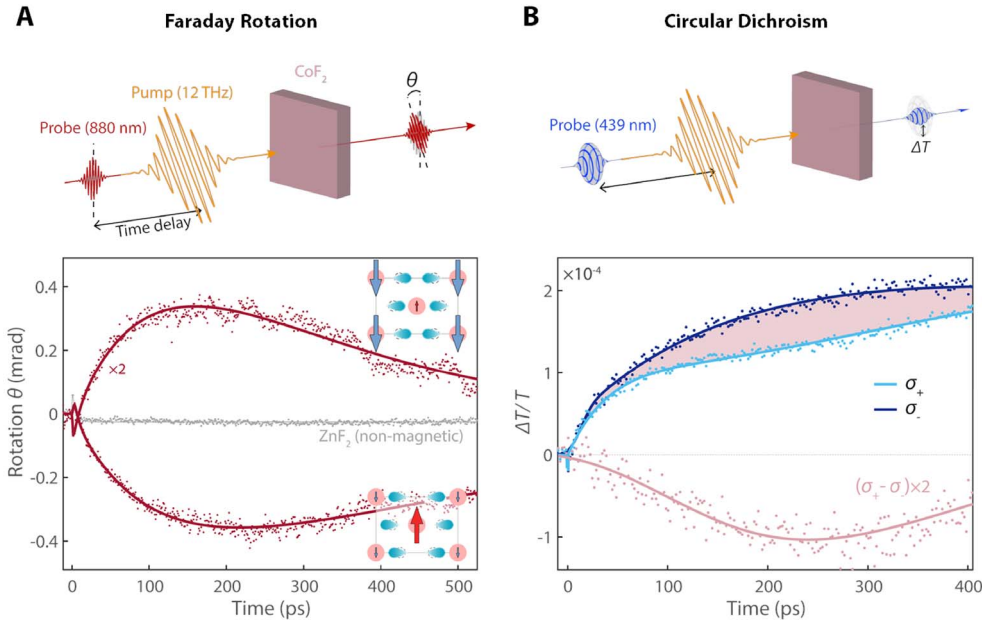

Figure 13. A (top): Depiction of mid-IR pump-Faraday rotation probe setup. A (bottom): Faraday rotation in CoF_2 after a 12 THz pump for two polarizations of the pump pulses (+45° and −45°. B (top): Depiction of mid-IR pump-circular dichroism probe setup. B (bottom): The relative change in transmission for left (dark blue) and right (light blue) circular polarized probe pulses. Reproduced from [42].

moment can be controlled by changing the phase difference of the pump pulse. Radaelli has suggested that peizoelectric BPO_4 and piezomagnetic CoF_2 are candidate materials where this type of ferroelectricity and ferromagnetism can be induced, respectively, using nonlinear phononics.

Disa *et al.* have recently demonstrated this phenomena in CoF_2 [42]. This material is a compensated antiferromagnet below $T_N = 39$ K, and an application of a strain along the [110] direction induces a ferrimagnetic state with a finite magnetic moment. They were able to stabilize a similar ferrimagnetic state by simultaneously pumping the orthogonal components of its high-frequency IR-active phonon with the irrep E_u, which should displace the lattice along a Raman-active phonon with the irrep B_{2g} due to the $Q_{\mathrm{R}}^{xy} Q_{\mathrm{IR}}^{x} Q_{\mathrm{IR}}^{y}$ nonlinearity. A displacement along the B_{2g} mode causes one set of Co–F distances in the material to lengthen while Co–F distances in another sublattice shortens, and this is responsible for the uncompensation of Co moments. The presence of a finite net magnetic moment in the transient state was confirmed by time-resolved measurements of the Faraday rotation and circular dicroism of probe pulses. As shown in Figure 13, a pump-induced magnetic signal was immediately observed, which changed sign after 7 ps. After the sign reversal, the magnetic signal continued to grow until it reached its maximum value at 200 ps. The reason for such a long-lived magnetic signal has not been completely understood. One possibility proposed by Disa *et al.* is that the transient displacement along the Raman-active phonon coordinate is reinforced by induced magnetic moment. Time-resolved X-ray diffraction studies should help in understanding this long-lived metastable state by clarifying the nature of the structural distortions in the light-induced phase. In particular, oscillations and displacements along the B_{2g} coordinate should be observed while the Q_{IR}^{x} and Q_{IR}^{y} coordinates are simultaneously oscillating to confirm that the transient ferrimagnetism is due to nonlinear phononics.

7. Conclusions

In summary, nonlinear phononics is an emerging field that has the potential to develop as a powerful method for controlling materials by stabilizing novel crystal structures that cannot be accessed in equilibrium. This is made possible by coherent atomic displacements along a set of phonon coordinates after a selective excitation of the IR-active phonons of a material, and it contrasts with the incoherent atomic motions that result from heating. Nonlinear coupling of the pumped IR-active phonon to other phonons is the microscopic mechanism responsible for the coherent lattice displacement. Intense mid-IR pump pulses are now available, and mid-IR light-induced control of materials properties have been demonstrated in pump–probe experiments. Nevertheless, this field is still in infancy compared to the pump–probe experimental activities that are performed in chemistry laboratories. 2D pump–probe spectroscopy experiments are routinely used by chemists to directly observe simultaneous excitations of the pumped vibrational mode as well as other modes that are excited due to nonlinear couplings. The nonlinearity between different vibrational modes are reflected by the presence of off-diagonal signals in 2D spectroscopy, and they can be used to quantify the nonlinear couplings. Mid-IR pump-second harmonic probe experiments similar to 2D spectroscopy have been recently performed on the wide band gap insulator $LiNbO_3$, and they have demonstrated simultaneous oscillations of the pumped IR-active mode while the lattice gets displaced along a Raman-active phonon coordinate. Several mid-IR pump induced phase transitions have been attributed to coherent lattice displacements due to nonlinear phononics, including insulator–metal transitions and melting of spin and orbital orders. Mid-IR pump-induced increase in reflectivity have also been reported in several superconductors, and they have been interpreted as signatures of light-enhanced superconductivity. However, excitations of the pumped mode have not been experimentally demonstrated in these experiments. More experimental studies that directly measure the nonlinear phonon couplings between the pumped phonon and other active phonon degrees of freedom would put this field on a stronger footing.

A microscopic theory based on first principles calculations of nonlinear phonon couplings has been developed to study the dynamics of a material when its IR-active phonons are selectively pumped. In addition to the cubic nonlinearities discussed in the 1970s, quartic nonlinearities with large coupling coefficients that can stabilize a symmetry-broken phase beyond a threshold value of the pump intensity has been found using this theoretical approach. Theoretical studies have also proposed light-induced reversal of ferroelectric polarization, ferroelectricity in paraelectrics and ferromagnetism in antiferromagnets, and these predictions have been partially confirmed by experiments. Cavity control of nonlinear couplings and phono-magneto analog of opto-magneto effect have been shown to be feasible by calculations. Their experimental realizations would confirm that nonlinear phononics is truly a novel way to control the physical properties of materials.

Acknowledgements

I am grateful to Antoine Georges and Andrea Cavalleri for previous collaborations on this subject. I have also benefited from helpful discussions with Michael Först, Roman Mankowsky, Tobia Nova, Matteo Mitrano, Srivats Rajasekaran and Yannis Laplace on this topic.

References

[1] A. H. Zewail, “Laser selective chemistry — is it possible?”, *Phys. Today* **33** (1980), p. 27-33.
[2] R. N. Zare, “Laser control of chemical reactions”, *Science* **279** (1998), no. 5358, p. 1875-1879.

[3] W. S. Warren, H. Rabitz, M. Dahleh, "Coherent control of quantum dynamics: The dream is alive", *Science* **259** (1993), p. 1581-1589.
[4] N. Bloembergen, A. H. Zewail, "Energy redistribution in isolated molecules and the question of mode-selective laser chemistry revisited", *J. Phys. Chem.* **88** (1984), p. 5459-5465.
[5] C. S. Parmenter, "Vibrational redistribution within excited electronic states of polyatomic molecules", *Faraday Discuss. Chem. Soc.* **75** (1983), p. 7-22.
[6] D. J. Nesbitt, R. W. Field, "Vibrational energy flow in highly excited molecules: Role of intramolecular vibrational redistribution", *J. Phys. Chem.* **100** (1996), p. 12735-12756.
[7] S. Woutersen, P. Hamm, "Nonlinear two-dimensional vibrational spectroscopy of peptides", *J. Phys. Condens. Matter* **14** (2002), no. 39, article no. R1035–R1062.
[8] M. Khalil, A. Tokmakoff, "Signatures of vibrational interactions in coherent two-dimensional infrared spectroscopy", *Chem. Phys.* **266** (2001), p. 213-230.
[9] M. Khalil, N. Demirdöven, A. Tokmakoff, "Coherent 2D IR spectroscopy: Molecular structure and dynamics in solution", *J. Phys. Chem.* **107** (2003), p. 5258-5279.
[10] N. Huse, K. Heyne, J. Dreyer, E. T. J. Nibbering, T. Elsaesser, "Vibrational multilevel quantum coherence due to anharmonic couplings in intermolecular hydrogen bonds", *Phys. Rev. Lett.* **91** (2003), article no. 197401.
[11] R. F. Wallis, A. A. Maradudin, "Ionic Raman effect. II. The first-order ionic Raman effect", *Phys. Rev. B* **3** (1971), p. 2063-2075.
[12] T. P. Martin, L. Genzel, "Ionic Raman scattering and ionic frequency mixing", *Phys. Status Solidi B* **61** (1974), no. 2, p. 493-502.
[13] M. Först, C. Manzoni, S. Kaiser, Y. Tomioka, Y. Tokura, R. Merlin, A. Cavalleri, "Nonlinear phononics as an ultrafast route to lattice control", *Nat. Phys.* **7** (2011), p. 854-866.
[14] T. F. Nova, A. Cartella, A. Cantaluppi, M. Först, D. Bossini, R. V. Mikhaylovskiy, A. V. Kimel, A. Cavalleri, "An effective magnetic field from optically driven phonons", *Nat. Phys.* **13** (2016), p. 132-136.
[15] J. R. Hortensius, D. Afanasiev, A. Sasani, E. Bousquet, A. D. Caviglia, "Ultrafast strain engineering and coherent structural dynamics from resonantly driven optical phonons in $LaAlO_3$", *NPJ Quant. Mater.* **5** (2020), article no. 95.
[16] R. Mankowsky, A. von Hoegen, M. Först, A. Cavalleri, "Ultrafast reversal of the ferroelectric polarization", *Phys. Rev. Lett.* **118** (2017), article no. 197601.
[17] M. Först, R. Mankowsky, H. Bromberger, D. M. Fritz, H. Lemke, D. Zhu, M. Chollet, Y. Tomioka, Y. Tokura, R. Merlin, J. P. Hill, S. L. Johnson, A. Cavalleri, "Displacive lattice excitation through nonlinear phononics viewed by femtosecond X-ray diffraction", *Solid State Commun.* **169** (2013), p. 24-27.
[18] R. Mankowsky, A. Subedi, M. Först, S. O. Mariager, M. Chollet, H. T. Lemke, J. S. Robinson, J. M. Glownia, M. P. Minitti, A. Frano *et al.*, "Nonlinear lattice dynamics as a basis for enhanced superconductivity in $YBa_2Cu_3O_{6.5}$", *Nature (London)* **516** (2014), p. 71-73.
[19] A. Subedi, "Proposal for ultrafast switching of ferroelectrics using midinfrared pulses", *Phys. Rev. B* **92** (2015), article no. 214303.
[20] M. Rini, R. Tobey, N. Dean, J. Itatani, Y. Tomioka, Y. Tokura, R. W. Schoenlein, A. Cavalleri, "Control of the electronic phase of a manganite by mode-selective vibrational excitation", *Nature (London)* **449** (2007), p. 72-74.
[21] V. Esposito, M. Fechner, R. Mankowsky, H. Lemke, M. Chollet, J. M. Glownia, M. Nakamura, M. Kawasaki, Y. Tokura, U. Staub, P. Beaud, M. Först, "Nonlinear electron–phonon coupling in doped manganites", *Phys. Rev. Lett.* **118** (2017), article no. 247601.
[22] A. D. Caviglia, R. Scherwitzl, P. Popovich, W. Hu, H. Bromberger, R. Singla, M. Mitrano, M. C. Hoffmann, S. Kaiser, P. Zubko *et al.*, "Nonlinear electron–phonon coupling in doped manganites", *Phys. Rev. Lett.* **108** (2012), article no. 136801.
[23] R. I. Tobey, D. Prabhakaran, A. T. Boothroyd, A. Cavalleri, "Ultrafast electronic phase transition in $La_{1/2}Sr_{3/2}MnO_4$ by coherent vibrational excitation: Evidence for nonthermal melting of orbital order", *Phys. Rev. Lett.* **101** (2008), article no. 197404.
[24] M. Först, R. I. Tobey, S. Wall, H. Broberger, V. Khanna, A. L. Cavalieri, Y.-D. Chuang, W. S. Lee, R. Moore, W. F. Schlotter *et al.*, "Driving magnetic order in a manganite by ultrafast lattice excitation", *Phys. Rev. B* **84** (2011), article no. 241104(R).
[25] M. Först, A. D. Caviglia, R. Scherwitzl, R. Mankowsky, P. Zubko, V. Khanna, H. Bromberger, S. B. Wilkins, Y.-D. Chuang, W. S. Lee *et al.*, "Spatially resolved ultrafast magnetic dynamics initiated at a complex oxide heterointerface", *Nat. Mater.* **14** (2015), p. 883-888.
[26] A. Subedi, "Midinfrared-light-induced ferroelectricity in oxide paraelectrics via nonlinear phononics", *Phys. Rev. B* **95** (2017), article no. 134113.
[27] T. F. Nova, A. S. Disa, M. Fechner, A. Cavalleri, "Metastable ferroelectricity in optically strained $SrTiO_3$", *Science* **364** (2019), p. 1075-1079.
[28] X. Li, T. Qiu, J. Zhang, E. Baldini, J. Lu, A. M. Rappe, K. A. Nelson, "Terahertz field-induced ferroelectricity in quantum paraelectric $SrTiO_3$", *Science* **364** (2019), p. 1079-1082.

[29] D. Fausti, R. I. Tobey, N. Dean, S. Kaiser, A. Dienst, M. C. Hoffmann, S. Pyon, T. Takayama, H. Takagi, A. Cavalleri, "Light-induced superconductivity in a stripe-ordered cuprate", *Science* **331** (2011), p. 189-191.
[30] S. Kaiser, C. R. Hunt, D. Nicoletti, W. Hu, I. Gierz, H. Y. Liu, M. Le Tacon, T. Loew, D. Haug, B. Keimer, A. Cavalleri, "Optically induced coherent transport far above Tc in underdoped $YBa_2Cu_3O_{6+\delta}$", *Phys. Rev. B* **89** (2014), article no. 184516.
[31] W. Hu, S. Kaiser, D. Nicoletti, C. R. Hunt, I. Gierz, M. C. Hoffmann, M. Le Tacon, T. Loew, B. Keimer, A. Cavalleri, "Optically enhanced coherent transport in $YBa_2Cu_3O_{6.5}$ by ultrafast redistribution of interlayer coupling", *Nat. Mater.* **13** (2014), p. 705-711.
[32] M. Mitrano, A. Cantaluppi, D. Nicoletti, S. Kaiser, A. Perucchi, S. Lupi, P. Di Pietro, D. Pontiroli, M. Ricc, S. R. Clark, D. Jaksch, A. Cavalleri, "Possible light-induced superconductivity in K_3C_{60} at high temperature", *Nature (London)* **530** (2016), p. 461-464.
[33] R. Mankowsky, M. Först, A. Cavalleri, "Non-equilibrium control of complex solids by nonlinear phononics", *Rep. Prog. Phys.* **79** (2016), article no. 064503.
[34] D. Nicoletti, A. Cavalleri, "Nonlinear light-matter interaction at terahertz frequencies", *Adv. Opt. Photon. 8* (2016), p. 401-464.
[35] A. Cavalleri, "Photo-induced superconductivity", *Contemp. Phys.* **59** (2018), p. 31-46.
[36] T. Qi, Y.-H. Shin, K.-L. Yeh, K. A. Nelson, A. M. Rappe, "Collective coherent control: Synchronization of polarization in ferroelectric $PbTiO_3$ by shaped THz fields", *Phys. Rev. Lett.* **102** (2009), article no. 247603.
[37] Y. Shinohara, K. Yabana, Y. Kawashita, J.-I. Iwata, T. Otobe, G. F. Bertsch, "Coherent phonon generation in time-dependent density functional theory", *Phys. Rev. B* **82** (2010), article no. 155110.
[38] A. Subedi, A. Cavalleri, A. Georges, "Theory of nonlinear phononics for coherent light control of solids", *Phys. Rev. B* **89** (2014), article no. 220301(R).
[39] D. M. Juraschek, M. Fechner, N. A. Spaldin, "Ultrafast structure switching through nonlinear phononics", *Phys. Rev. Lett.* **118** (2017), article no. 054101.
[40] P. G. Radaelli, "Breaking symmetry with light: Ultrafast ferroelectricity and magnetism from three-phonon coupling", *Phys. Rev. B* **97** (2018), article no. 085145.
[41] D. Afanasiev, J. R. Hortensius, B. A. Ivanov, A. Sasani, E. Bousquet, Y. M. Blanter, R. V. Mikhaylovskiy, A. V. Kimel, A. D. Caviglia, "Ultrafast control of magnetic interactions via light-driven phonons", *Nat. Mater.* (2021), p. 1-5.
[42] A. S. Disa, M. Fechner, T. F. Nova, B. Liu, M. Först, D. Prabhakaran, P. G. Radaelli, A. Cavalleri, "Polarizing an antiferromagnet by optical engineering of the crystal field", *Nat. Phys.* **16** (2020), p. 937-941.
[43] M. Gu, J. M. Rondinelli, "Ultrafast band engineering and transient spin currents in antiferromagnetic oxides", *Sci. Rep.* **6** (2016), article no. 25121.
[44] D. M. Juraschek, P. Narang, N. A. Spaldin, "Phono-magnetic analogs to opto-magnetic effects", *Phys. Rev. Res.* **2** (2020), article no. 043035.
[45] D. M. Juraschek, T. Neuman, J. Flick, P. Narang, "Cavity control of nonlinear phononics", https://arxiv.org/abs/1912.00122, 2019.
[46] D. M. Juraschek, Q. N. Meier, P. Narang, "Parametric excitation of an optically silent Goldstone-like phonon mode", *Phys. Rev. Lett.* **124** (2020), article no. 117401.
[47] M. Först, R. Mankowsky, A. Cavalleri, "Mode-selective control of the crystal lattice", *Acc. Chem. Res.* **48** (2015), p. 380-387.
[48] M. Buzzi, M. Först, A. Cavalleri, "Measuring non-equilibrium dynamics in complex solids with ultrashort X-ray pulses", *Phil. Trans. R. Soc. A* **377** (2019), no. 2145, article no. 20170478.
[49] P. Salén, M. Basini, S. Bonetti, J. Hebling, M. Krasilnikov, A. Y. Nikitin, G. Shamuilov, Z. Tibai, V. Zhaunerchyk, V. Goryashko, "Matter manipulation with extreme terahertz light: Progress in the enabling THz technology", *Phys. Rep.* **836-837** (2019), p. 1-74.
[50] Y. Okimoto, Y. Tomioka, Y. Onose, Y. Otsuka, Y. Tokura, "Optical study of $Pr_{1-x}Ca_xMnO_3$ ($x = 0.4$) in a magnetic field: Variation of electronic structure with charge ordering and disordering phase transitions", *Phys. Rev. B* **59** (1999), p. 7401-7408.
[51] Y. Tomioka, A. Asamitsu, H. Kuwahara, Y. Moritomo, Y. Tokura, "Magnetic-field-induced metal-insulator phenomena in $Pr_{1-x}Ca_xMnO_3$ with controlled charge-ordering instability", *Phys. Rev. B* **53** (1996), article no. R1689–R1692.
[52] K. Miyano, T. Tanaka, Y. Tomioka, Y. Tokura, "Photoinduced insulator-to-metal transition in a perovskite manganite", *Phys. Rev. Lett.* **78** (1997), p. 4257-4260.
[53] A. Asamitsu, Y. Tomioka, H. Kuwahara, Y. Tokura, "Current switching of resistive states in magnetoresistive manganites", *Nature (London)* **388** (1997), p. 50-52.
[54] C. C. Homes, T. Timusk, D. A. Bonn, R. Liang, W. N. Hardy, "Optical properties along the c-axis of $YBa_2Cu_3O_{6+x}$, for $x = 0.50 \rightarrow 0.95$ evolution of the pseudogap", *Physica C* **254** (1995), no. 3-4, p. 265-280.
[55] M. Fechner, N. A. Spaldin, "Effects of intense optical phonon pumping on the structure and electronic properties of yttrium barium copper oxide", *Phys. Rev. B* **94** (2016), article no. 134307.

[56] G. V. Subba Rao, C. N. R. Rao, J. R. Ferraro, "Infrared and electronic spectra of rare earth perovskites: Ortho-chromites, -manganites and -ferrites", *Appl. Spectrosc.* **24** (1970), p. 436-445.
[57] D. M. Juraschek, S. F. Maehrlein, "Sum-frequency ionic Raman scattering", *Phys. Rev. B* **97** (2018), article no. 174302.
[58] M. Kozina, M. Fechner, P. Marsik, T. van Driel, J. M. Glownia, C. Bernhard, M. Radovic, D. Zhu, S. Bonetti, U. Staub, M. C. Hoffmann, "Terahertz-driven phonon upconversion in $SrTiO_3$", *Nat. Phys.* **15** (2019), p. 387-392.
[59] D. M. Juraschek, M. Fechner, A. V. Balatsky, N. A. Spaldin, "Dynamical multiferroicity", *Phys. Rev. Mater.* **1** (2017), article no. 014401.
[60] M. Fechner, A. Sukhov, L. Chotorlishvili, C. Kenel, J. Berakdar, N. A. Spaldin, "Magnetophononics: Ultrafast spin control through the lattice", *Phys. Rev. Mater.* **2** (2018), article no. 064401.
[61] M. Gu, J. M. Rondinelli, "Nonlinear phononic control and emergent magnetism in Mott insulating titanates", *Phys. Rev. B* **98** (2018), article no. 024102.
[62] G. Khalsa, N. A. Benedek, "Ultrafast optically induced ferromagnetic/anti-ferromagnetic phase transition in $GdTiO_3$ from first principles", *NPJ Quant. Mater.* **3** (2018), article no. 15.

Comptes Rendus

Physique

Objet de la revue

Les *Comptes Rendus Physique* sont une revue électronique évaluée par les pairs de niveau international, qui couvre l'ensemble des domaines de la physique et de l'astrophysique. Ils publient principalement des numéros thématiques, mais également des articles originaux de recherche, des annonces préliminaires, des articles de revue, des mises en perspective historiques, des textes à visée pédagogique ou encore des actes de colloque, sans limite de longueur, en anglais ou en français. Ils proposent également des numéros spéciaux consacrés à certains aspects récents et/ou significatifs de la discipline, dont les auteurs sont choisis parmi les chercheurs les plus actifs sur le sujet et dont la coordination est assurée par des rédacteurs en chef invités.

Les *Comptes Rendus Physique* sont diffusés selon une politique vertueuse de libre accès diamant, gratuit pour les auteurs (pas de frais de publications) comme pour les lecteurs (libre accès immédiat et pérenne).

À propos de la revue

Toutes les informations concernant la revue, y compris le texte des articles publiés qui est en accès libre intégral, figurent sur le site https://comptes-rendus.academie-sciences.fr/physique/.

Informations à l'attention des auteurs

Pour toute question relative à la soumission des articles, les auteurs peuvent consulter le site https://comptes-rendus.academie-sciences.fr/physique/.

Contact

Académie des sciences
23, quai de Conti, 75006 Paris, France
Tél. : (+33) (0)1 44 41 43 72
CR-Physique@academie-sciences.fr

Comptes Rendus
de l'Académie des sciences

Physique

Volume 22, nº S2, 2021

Special issue / *Numéro thématique*
Physics of ultra-fast phenomena / *Physique des phénomènes ultra-rapides*

Guest editors / *Rédacteurs en chef invités*
Éric Collet (Université Rennes 1, CNRS, France)
Sylvain Ravy (Université Paris-Saclay, CNRS, France)

Cover illustration / *Illustration de couverture*
Éric Collet

1878-1535 (electronic)

Académie des sciences — Paris

COMPTES RENDUS
DE L'ACADÉMIE DES SCIENCES

Physique

Volume 22, nº S2, 2021